LIBRARY
TECHNICAL REPORT SECTION
NAVAL POSTGRADUATE SCHOOL
MONTEREY, CALIFORNIA 93940

NPS61-78-003

NAVAL POSTGRADUATE SCHOOL

Monterey, California

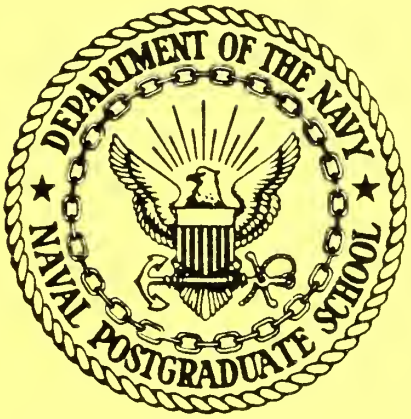

OPTICAL RESOLUTION IN THE TURBULENT ATMOSPHERE OF THE MARINE BOUNDARY LAYER

E. C. Crittenden, Jr., A. W. Cooper, E. A. Milne,
G. W. Rodeback, R. L. Armstead, S. H. Kalmback,
D. Land and B. Katz *

February 1978

Final Report for Period July 1973 - September 1977

Approved for public release; distribution unlimited.

Prepared for: Naval Sea Systems Command
PMS 405
Washington, D.C. 20362

* Naval Surface Weapon Center, White Oak, MD

FEDDOCS
D 208.14/2:
NPS-61-78-003

NAVAL POSTGRADUATE SCHOOL
Monterey, California

Rear Admiral Tyler Dedman
Superintendent

Jack R. Borsting
Provost

The work reported herein was supported in part by the Naval Sea Systems Command, PMS 405.

Reproduction of all or part of this report is authorized.

This report was prepared by:

NPS61-78-003

REPORT DOCUMENTATION PAGE

READ INSTRUCTIONS BEFORE COMPLETING FORM

1. REPORT NUMBER: NPS61-78-003	2. GOVT ACCESSION NO.
3. RECIPIENT'S CATALOG NUMBER	
4. TITLE (and Subtitle): Optical Resolution in the Turbulent Atmosphere of the Marine Boundary Layer	5. TYPE OF REPORT & PERIOD COVERED: Final Report, 1 JUL 73 - 30 Sep 77
	6. PERFORMING ORG. REPORT NUMBER
7. AUTHOR(s): E. C. Crittenden, Jr., A. W. Cooper, E. A. Milne, G. W. Rodeback, R. L. Armstead, S. H. Kalmbach, D. Land and B. Katz	8. CONTRACT OR GRANT NUMBER(s)
9. PERFORMING ORGANIZATION NAME AND ADDRESS: Naval Postgraduate School, Monterey, CA 93940	10. PROGRAM ELEMENT, PROJECT, TASK AREA & WORK UNIT NUMBERS
11. CONTROLLING OFFICE NAME AND ADDRESS: Naval Sea Systems Command, PMS 405, Washington, D.C. 20362	12. REPORT DATE: 24 February 1978
	13. NUMBER OF PAGES: 186
14. MONITORING AGENCY NAME & ADDRESS (if different from Controlling Office)	15. SECURITY CLASS. (of this report): Unclassified
	15a. DECLASSIFICATION/DOWNGRADING SCHEDULE

16. DISTRIBUTION STATEMENT (of this Report)

Approved for public release; distribution unlimited.

17. DISTRIBUTION STATEMENT (of the abstract entered in Block 20, if different from Report)

18. SUPPLEMENTARY NOTES

19. KEY WORDS (Continue on reverse side if necessary and identify by block number)

Modulation Transfer Function (MTF)
Optical Transfer Function (OTF)
Resolution
Turbulence
Atmospheric MTF

20. ABSTRACT (Continue on reverse side if necessary and identify by block number)

The effects of atmospheric turbulence on the performance of imagers and beam projection systems have been found to be well expressed in terms of a model for the modulation transfer function (MTF) depending on the wavelength, range, and a properly path-position weighted value of C_n^2, the turbulence structure constant for optical index. The short-term average and long-term MTF and image wander (wave front tilt) can be predicted in the above parameters in most cases. For non-Kolmogorov turbulence,

Summary

The effects of turbulence on the performance of imagers or on beam forming optical systems are well expressed by the optical transfer function (OTF), or its essential equivalents, the modulation transfer function (MTF), or the mutual coherence function (MCF) for the atmosphere. The program has shown that these quantities can be adequately expressed in terms of the Fried model by means of a single number, the turbulence structure constant for optical index, C_n^2, provided that a properly path-weighted value is obtained. The behavior as a function of wavelength and range is also well understood. The quantity C_n^2, which varies with the micrometeorology, can be determined in its properly path-weighted form with a slit-scanning telescope system developed at NPS. A portable system is available which includes an on-line data processing system that gives immediate numerical and graphical results for the properties of the atmosphere, together with performance prediction for a given optical system. The direct optical measurement of weighted C_n^2 for the path avoids the necessity of making a large number of measurements of C_T^2 at points along the path. Measurement of C_n^2 by the slit-scanner method also obtains a direct result that is independent of the assumptions as to the statistical form of the turbulence.

Prediction of anticipated C_n^2 in terms of micro- and large scale meteorology is the subject of a companion program at NPS. Progress in this area is reported in a set of companion reports.

The weighting needed in the path-position weighted value of C_n^2 heavily emphasizes the region near the imaging or beam forming optics. Anomolies in the distribution of C_n^2 due to air flow around obstructions near the otpics is a common problem. Direct evaluation with a system such as the NPS equipment becomes important for installations such as shipboard optics where the

heavily weighted part of the path is the shipboard end.

Work on this project has shown that, in most cases, any one of the quantities, the short-term (image centered) MTF, the long-term MTF, and the image wander (wave front tilt) can be used to measure the weighted C_n^2. However, situations exist in which a C_n^2 measurement is applicable only to its particular mode of measurement, i.e. long-term, short-term MTF, or wander, with different values of C_n^2 needed for each mode. This appears to occur under non-Kolmogorov turbulence conditions where an excess or deficiency of large scale vortices exists. The short term MTF is the preferred measurement because usually the other modes can be predicted from it, it is generally the primary quantity desired, and it can be measured from a moving platform such as shipboard.

Scintillation can yield values of C_n^2, but unfortunately the path-weighting differs from that needed to determine the effects on image resolution. The weighting obtained from scintillation emphasizes the path center rather than the end nearest the optics and can be misleading in cases of pronounced nonuniformities in C_n^2 along the path. Spatial filtering can modify the weighting in the direction of that needed for MTF but always gives zero weight to the immediate telescope vicinity.

Extension of scintillation techniques at NPS is providing results on extinction, with improvements in averaging over conventional methods. During the coming year the systems will be extended for use at sea for shore-to-ship, ship-to-ship, and kytoon-to-ship, the latter yielding slant-path extinction results.

TABLE OF CONTENTS

I. Introduction 1

II. Applicability of MTF to a High Energy Laser and a Pointer/Tracker 5

III. Theoretical Considerations

A. General 8

B. Turbulence Effects on OTF and Wander 10

C. Path-Position Weighting of C_n^2 for OTF 13

D. Mutual Coherence Function, MCF 14

E. Approximate Method for Transform 15

F. Turbulence and Scintillation 15

G. Path-Position Weighting of C_n^2 for Scintillation 16

H. Effects of Fog/Aerosol Scattering on OTF 18

IV. General Plan of Experimental Program 19

A. General Considerations 19

B. MTF and Wander 19

C. Scintillation 20

D. C_T^2 21

E. Meteorology 21

F. Extinction 21

G. Location of Experiments - Ranges 22

V. Measurement Techniques 28

A. MTF - OTF or MCF 28

1. Long-Term, Short-Term, and Wander 28

2. On-Line Data Reduction 43

3. Optical Equipment 43

4. Portable MTF equipment 46

B. Comparison of Slit-Scanning Imager and Shearing Interferometer

1. Shearing Interferometer 49

2. Data Reduction - MTF from Shearing Interferometer vs. OTF from Slit-Scanner 57

C. Scintillation Measurements of C_n^2 60

1. C_n^2 Data Reduction 60

2. Beam Forming, Chopping, Demodulation, and Calibration 62

3. Gyro Tracking System 70

(Table of Contents, Cont'd)

4. Shipmotion Problems - Fan-scan Modulation, Demodulation 73
5. Aperture Averaging and Saturation Corrections 77

D. Extinction 82
1. Alignment, monitoring, detection, and calibration 82
2. Demodulation 86
3. Data Reduction 87
4. Subtraction of Absorption - McClatchey Codes 89
5. Prediction of Extinction from Nephelometer Data 91
6. Nephelometer Measurements 91

E. DF Laser 92

VI. Results 95
A. MTF 95
1. Curve Shape 95
2. C_n^2 from Long-Term, Short-Term MTF, and Wander 111
3. Variation of MTF with Wavelength 120
4. Variation of MTF with Range and Path-Weighting of C_n^2, and Comparison with C_n^2 from Scintillation and C_T^2. 122
5. Comparison of MTF from Slit-Scanner and Shearing Interferometer 129
6. Isotropy of Optical Turbulence 132

B. Scintillation 133
1. Aperture Averaging 133
2. Effects of Wavelength 151
3. Saturation Effects 154
4. Temporal Frequency Distribution 158
5. Scintillation C_n^2 vs. C_T^2 166
6. Variation of C_n^2 with height. 172

C. Extinction 176
1. Comparison with NOSC Aircraft Nephelometer Results. 176

VII. References 180

VIII. Appendices 184
A. Abel Inversion 184
B. Data Compendium - In Separate Volume

List of Illustrations

		Page No.
III-1.	Relative Weighting of C_n^2 as a Function of Position Along the Path, for MTF and for Scintillation.	17
IV-1.	Optical Ranges across Monterey Bay	24
IV-2.	Mobile Laboratory	26
IV-3.	Instrument Van	27
V-1.	Typical Line-Spread Functions	29
V-2.	Observed Line-Spread Function for Instrument Alone, 10.6 micrometers	30
V-3a.	Point-Spread Image Function for an 18 inch Circular Aperture with a Central Obscuration Ratio of 0.33 Wavelength, 10.6 micrometers	31
V-3b.	Line-Spread Function for the Point-Spread Function of Fig. V-3a	32
V-4.	Transform of the Observed Line-Spread Function of Fig. V-2	34
V-5.	Magnification Calibration Signal. Grating Placed at Entrance Aperture	35
V-6.	Short-Exposure and Long-Exposure Line-Spread Functions	37
V-7a.	Fourier Transforms of the Curves of Fig. V-6	38
V-7b.	MTF for Curves of Fig. V-7a. Curves of V-7a divided by the Modulus of the Transform of the Instrument Line-Spread Function	39
V-8.	Wander Displacement as a Function of Time	40
V-9.	Frequency Spectrum of Wander	41
V-10.	Portable MTF System	47
V-11.	Aperture Displacement in the Shearing Interferometer	50
V-12.	Diffraction Limited MTF for Unobstructed Circular Aperture	50
V-13.	Shearing Interferometer Signal	53
V-14.	Probability Density vs. Log-Intensity for Scintillation	63

(Illustration, Cont'd) Page No.

V-15. Functional Diagram for Scintillation (or Extinction) Measurements 65
V-16. Chopper/Demodulator Waveforms 66
V-17. Demodulator Calibration Curve 69
V-18. Optical Tracking System for Gyro-Platform 71
V-19. Gyro-System 74
V-20. "Fan-Scan" Transmitter Optical System 76
V-21. Transmitter and Monitoring System for Extinction 83
VI-A-1. Long-Term MTF, 0.4880 micrometers 96
VI-A-2. Long-Term MTF, 0.6328 micrometers 97
VI-A-3. Long-Term MTF, 1.06 micrometers 98
VI-A-4. Long-Term MTF, 10.6 micrometers 99
VI-A-5. Short-Term MTF, 0.4880 micrometers 101
VI-A-6. Short-Term MTF, 0.6328 micrometers 102
VI-A-7. Short-Term MTF, 1.06 micrometers 103
VI-A-8. Short-Term MTF, 10.6 micrometers 104
VI-A-9. MTF for two Wavelengths and three Turbulence Levels, Near Diffraction Limit 106
VI-A-10. Short-Term OTF for 10.6 μm. 107
VI-A-11. Short-Term OTF for 10.6 μm 108
VI-A-12. C_n from Short-Term MTF vs. C_n from Long-Term MTF 112
VI-A-13. C_n Short-Term MTF vs. C_n from Wander 113
VI-A-14. Long-Term OTF, 0.6328 μm. 115
VI-A-15. Long-Term OTF, 10.6 μm 116
VI-A-16. Short-Term OTF 0.6328 μm with Low Wander C_n 117
VI-A-17. Short-Term OTF 10.6 μm with Low Wander C_n 118
VI-A-18. Log C_n vs. Time of Day for a Variety of Types of Measurement, 22 September 1977 123
VI-A-19. Log C_n vs Time of Day for a Variety of Types of Measurement, 21 September 1977 125
VI-A-20. C_n from MTF and C_n from Scintillation vs. Time of Day, 16 December 1976 126

(Illustrations, Cont'd) Page No.

VI-A-21. C_n from MTF and C_n from Scintillation vs. Time of Day, 17 December 1976 127

VI-A-22. C_n from Shearing Interferometer vs. C_n from Slit-Scanning Imager 131

VI-B-1. Laboratory Aperture Averaging Experiment 134

VI-B-2. Average Value of $\sigma_{\ell I}(D)-\sigma_{\ell I}(23\ mm)$ vs. Aperture Diameter for 22 October 1973 135

VI-B-3. Average Value of $\sigma_{\ell I}(D)-\sigma_{\ell I}(23\ mm)$ vs. Aperture Diameter for 27 October 1973 136

VI-B-4. Propagation Paths Used for Aperture Averaging Studies 139

VI-B-5. Aperture Factor vs. Reduced Aperture 143

VI-B-6. G(D) vs. Aperture Diameter D, 5-6 March 1976 145

VI-B-7. G(D) vs. Aperture Diameter D, 30 March 1976 146

VI-B-8. G(D) as. a Function of Reduced Aperture 147

VI-B-9. Empirical vs. Theoretical

$$\theta \text{ vs } \frac{D}{(4\ z/k)^{\frac{1}{2}}}$$ 148

VI-B-10. $\theta(D) = G(D)_{min}/G(D)$ vs. Reduced Aperture Data Taken at Sea 149

VI-B-11. Scintillation, Monterey Bay, 22 May 1975 152

VI-B-12. C_n vs. Time for Scintillation at Two Wavelengths 153

VI-B-13. C_n as a Function of Time for Four Wavelengths 155

VI-B-14. Standard Deviation of Log-Intensity vs. $(Range)^{11/12}$ 156

VI-B-15. Relative Spectral Power vs. Frequency for Scintillation, Wind Velocity 8 m/sec 160

VI-B-16. Relative Spectral Power vs. Frequency for Scintillation, Wind Velocity 0.5 m/sec 161

VI-B-17. $Log_{10}W(f)$ as a Function of Frequency 162

VI-B-18. Temporal Frequency Spectra for Several Aperture Diameters (Large) 163

VI-B-19. Temporal Frequency Spectra for Several Aperture Diameters (Small) 164

(Illustrations, Cont'd) Page No.

VI-B-20. Met.Measurements of C_n vs. Time of Day 168

VI-B-21. Optical Measurements of C_n vs. Meteorological Measurements of C_n. Wind Greater than 6 mph 169

VI-B-22. Optical Measurements of C_n vs. Meteorological Measurements of C_n. Wind less than 3 mph 170

VI-B-23. Optical Measurements of C_n vs. Meteorological Measurements of C_n. All Wind Velocities, 3 May 171

VI-B-24. Standard Deviation of Log-Intensity vs. Time for 16 ft. and 40 ft. above Ocean Surface 174

VI-C-1. Measured Extinction across Monterey Bay, and Extinction Calculated from Aerosol Spectrum Plotted as a Function of Time 178

VIII-1. The Processes Involved in Calculating a Real System Spot Distribution

List of Tables

		Page No.
V-C-1.	Range for Saturation of Scintillation as a Function of Wavelength	81
VI-A-1.	Values of C_n, from MTF and Wander for Curves of Figs. VI-A-1 to VI-A-8	121
VI-A-2.	Additional Values of C_n from MTF and Wander	121
VI-B-1.	Summary Matrix of Experiments Conducted Concerning Aperture Averaging of Scintillation	138
VI-B-2.	$\sigma_{\ell I}$ for Aperture Averaging of Scintillation, 7-8 February 1976	141
VI-B-3.	$\sigma_{\ell I}$ for Aperture Averaging of Scintillation, 10 February 1976	142
VI-B-4.	Comparison of C_{nO} from Scintillation with C_{nT} from Thermal Fluctuation	167
VI-B-5.	Height Dependence of Standard Deviation of Log-Intensity, $\sigma_{\ell I}$	175

I. Introduction

This report describes the results of a program primarily designed to evaluate the effects of atmospheric turbulence on the propagation of optical radiation in a marine environment. The program is interdisciplinary, involving not only the optical properties but also the meteorological and oceanographic parameters known to have a bearing on the optical properties.

Atmospheric turbulence adversely affects the propagation of a laser beam or the performance of an imaging system. The objective of this work has been to verify theoretical models for this behavior and to provide the basis for prediction of performance of optical systems in terms of the prevalent meteorological conditions. The general program also involves prediction of the turbulence level and determination of the relationship of the micrometeorology to the macrometeorology. Work in these areas is carried out by the meteorology group, with the bulk of their results appearing in other related reports. Some of their results will be included in this report, when they relate directly to the optical results.

Fog-aerosol concentrations also have an important impact on optical transmission, by causing extinction of the beam and by reducing the resolution as a result of scattered background light. The resolution results reported here are obtained in a manner designed to minimize the effects of fog/aerosol scattering. Work is in progress, in a continuing effort, to evaluate the fog/aerosol extinction effects. This will be the subject of later reports.

The fundamental property of a medium that determines the propagation of optical radiation is its index of refraction. At constant atmospheric pressure the index of refraction is proportional to the density of the medium, which in turn is porportional to the temperature. Hence temperature fluctuations

in the medium translate into index of refraction fluctuations. With an air flow over the ocean surface the velocity usually increases with height. This shear in the atmosphere leads to turbulence. As there is usually a vertical temperature gradient, the turbulence causes temperature fluctuations and hence index fluctuations.

The instantaneous deviations of index of refraction cause the focused spot of a laser beam, or the focused image in an imager, to be displaced, distorted, and broadened relative to the diffraction-limited case. For severe turbulence or long path lengths, the beam can be broken up or bear little resemblance to the original beam or object. In addition, the internal dynamics of turbulence cause the individual deviations in the index of refraction to change with time. This has the effect of causing the focused beam or image to wander. The average of many such images is an image which is further broadened.

The principal motivation for this work is to provide prediction capability for the effects of the atmosphere on laser weapons. The effects of heat absorbed in the optical path from the laser beam are not included, but are treated in other projects and can be folded into the overal behavior.

Because of reciprocity, (Yura, 1973) the results obtained here are equally applicable either to imaging systems, or to beam projection systems. Imaging systems have been used for the measurements carried out in this work because the optical equipment is simpler and less bulky than for beam projection systems. The problem has also been simplified, with little loss of generality, by utilizing one-dimensional treatment for most of the steps in the image analysis. The two-dimensional image of a point source is called the "point spread" function, and its two-dimensional Fourier transform is the two-dimensional Optical Transfer Function (OTF) of the optical system. However,

the number of calculations involved in dealing with a two-dimensional transfer function is large. In order to simplify the calculations, the point spread function has been reduced to a one-dimensional "line-spread" function by scanning the image of a point source, produced in a telescope, with a slit. The Fourier transform of this image is the one-dimensional OTF of the overall optical system including both atmosphere and optics. This OTF completely expresses the behavior of the system, provided that the images have circular or elliptic symmetry. Although individual images may be asymmetric, the average of a number of images has the required symmetry. All the calculations can be carried out quickly in one dimension. The final results can be inverted with the Abel transform (Griem, 1964; Magnus and Oberhettinger, 1949)to give the two-dimensional performance.

The system of atmosphere plus optics has been treated here as a linear system from which the properties of the measuring system can be unfolded by factoring the Fourier transforms. This yields the OTF of the atmosphere, independent of the measuring optics. The results are directly applicable to prediction of the behavior of a laser weapon projection system. The process of inversion to two dimensions and prediction of the beam profile cross-section is described later, in Appendix A, this report.

The effects of atmospheric turbulence can also be expressed in terms of another function, the mutual coherence function (MCF). The atmospheric MCF and the OTF are, in fact, the same function, but expressed in terms of different variables. The MCF is the primary quantity of concern for coherent detection. Thus, studies involving the behavior of imaging also yield results relevant to the coherence problem as well.

Propagation through the turbulent atmosphere also leads to intensity fluctuations, or scintillation, of the light intensity

received at a point on the wavefront. This property can also be used to determine the turbulence level. Such measurements have been carried out in this work and are reported in Section VI. B. The values of turbulence level obtained from scintillation are useful in cases of uniform turbulence. However, they need careful treatment in cases of non-uniform turbulence because the path-position weighting differs from the weighting needed to express the resolution (OTF).

The work reported here verifies a theoretical model of Fried (Fried, 1966) within the limits of experimental error, if a modification is included for the short-term MTF near diffraction limited conditions. The dependence of OTF on a properly weighted value of C_n^2, on range, and on wavelength, as well as the internal consistency of short-term and long-term MTF, and wander have been tested. The expected behavior has been verified except for cases where the turbulence vortex size distribution may be non-Kolmogorov. In such cases a separate value of C_n^2, applicable for each of short-term, long-term MTF, and wander can handle the situation.

In addition to the primary equipment used for most of the measurements described in this report, a portable OTF system has been constructed and utilized in the field and is available for measurements on optical ranges wherever a need exists. This system, together with the on-line data processing system, can provide immediate predictions of the effects of the atmosphere on an imaging or beam projection system under test.

II. Applicability of MTF to a High Energy Laser and a Pointer/Tracker

Knowledge of the MTF of the atmosphere is necessary for prediction of the beam cross-sectional profile on target and the spot wander for a high energy laser and its beam projection system. The MTF permits prediction of the effects of atmospheric turbulence on low-to-medium power laser beams. At higher powers, effects due to beam-heating must also be incorporated, but the turbulence effects are still present, requiring the MTF as the means of expressing the behavior. The effects of atmospheric turbulence also cause degradation of the image resolution of the pointer/tracker, as well as causing a time dependent displacement of the image center, or image wander. Knowledge of the MTF of the atmosphere, and an associated weighted value of C_n^2 for the optical path, permit prediction of the performance of the imager after folding in the properties of the idealized perfect system.

For a beam-forming system, the predicted average beam cross-section on target can be calculated from the atmospheric MTF and the properties of the laser and its beam projection system. Considering the system as linear, the MTF of the entire system is the MTF of the atmosphere times the Fourier transforms of the line-spread functions of the laser output pattern, and of the defocus, diffraction, and aberration broadenings of the projection system. Fourier inversion of MTF for the entire system gives the overall line-spread function. Use of the Abel inversion (Appendix A) then yields the two-dimensional spot pattern, expressed as a function of radius. In turn, the fraction of output power within a given radius is readily calculated.

For an imaging system, such as the imaging portion of the pointer/tracker, the real behavior for operation through the turbulent atmosphere is obtained by utilization of the MTF of the atmosphere and the Fourier transform for the optical system.

The image profile of a point source for the entire real system is unfolded from the combined transform in a manner similar to that for the high energy laser projection system.

The atmospheric MTF thus becomes a central parameter in High Energy Laser and Pointer/Tracker behavior. Work reported in this report has verified a model for predicting the wander, and the short and long term average MTF curves at any wavelength in terms of a weighted value of C_n^2 for the optical path. The slit scan telescope has also been shown to be a capable and effective way of measuring the properly path-position weighted C_n^2 needed to predict the MTF values or spot wander. Measurement of the weighted C_n^2 is also simplified by the demonstrated internal consistency between short term MTF, long term MTF and spot wander. The short term (image-centered) average MTF can be obtained for moving targets or unstable platforms by use of a system with tracking optics, making C_n^2 available under otherwise difficult circumstances.

A portable slit-scan telescope system for measuring MTF and weighted C_n^2 has been constructed and utilized at the Naval Postgraduate School. The system is equipped with on-line data processing equipment to obtain immediate MTF and C_n^2 values with hard copy printouts, together with predicted performance results for any optical system for which the system constants are available. This portable system is available for use on ranges wherever needed.

Work has been initiated, and is continuing in an on-going project, to evaluate the effects of aerosols and fog on optical extinction for transmission through the atmosphere in the marine environment, particularly for slant paths measured from shipboard.

Companion work has also been carried out to determine the meteorological parameters responsible for C_n^2 values observed in the field, with the overall objective of providing advance prediction of HEL performance under a variety of circumstances. That

work is reported in full in several separate reports [Davidson, 1977-1, 2]. The results directly related to optical properties are included in this report.

III. Theoretical Considerations

A. General

Turbulence and a vertical temperature gradient in the atmosphere result in a random fluctuation in temperature about an average value. Similarly, turbulence and a vertical humidity gradient also lead to humidity fluctuations. The optical index of refraction depends on both the temperature and the humidity, so that the index, in turn, undergoes fluctuations around its mean value under such circumstances.

A quantity useful in characterizing optical turbulence effects is the average of the square of the difference of the index of refraction at two points $\underline{r_1}$ and $\underline{r_2}$ separated by a distance r, i.e.:

$$\left\langle [n(\underline{r_1}) - n(\underline{r_2})]^2 \right\rangle$$

For isotropic turbulence, the quantity C_n, expressed by the relationship (Tatarski, 1961):

$$\left\langle [n(\underline{r_1}) - n(\underline{r_2})]^2 \right\rangle = r^{2/3} C_n^2 \qquad \ell_o << r << L_o$$

is called the "index of refraction turbulence structure constant". The quantity C_n has the dimensions of length$^{-1/3}$. The relationship above, involving $r^{2/3}$, is determined basically by a dimensional argument. It holds within the "inertial sub-range",

$$\ell_o << r << L_o ,$$

where ℓ_o and L_o are respectively the inner and outer scales of turbulence. These scales correspond roughly to the size of the smallest eddies of turbulence, about a millimeter, and the largest eddies, often taken to be the order of the height above the ground, or sea surface, of the point, or propagation path of interest.

The quantity C_n, defined as a property at a point in the atmosphere, affects the optical properties in terms of a path-integrated value along the optical path. A properly path-position weighted mean value of C_n, with the weighting function depending

on the particular optical property, becomes the central parameter of interest to the optical properties of the atmosphere due to turbulence.

Values of C_n at specific points in the atmosphere can be determined from measurements of the temperature and humidity fluctuations. We will look first at the temperature fluctuation component. The index of refraction, n, is related to the absolute temperature, T, by

$$n - 1 = 79 \times 10^{-6}\ p/T$$

with the pressure p in millibars. The average of the square of the temperature fluctuation can be shown to follow an equation similar to that for index fluctuation, leading to definition of the temperature turbulence structure constant C_T^2 in terms of:

$$\left\langle [T(\underline{r}_1) - T(\underline{r}_2)]^2 \right\rangle = C_T^2\ r^{2/3}$$

Using the expression for index in terms of p and T above, this leads to (Ochs, et al, 1969):

$$C_n = 79 \times 10^{-6}\ (p/T^2)\ C_T$$

For humidity fluctuation the index variation at optical wavelengths is much less than for the microwave region where the effects are large. Friehe has studied the optical humidity effects in detail, (Friehe, 1975). The contribution of humidity fluctuation to C_n can be positive or negative, relative to the temperature contribution, depending on the signs of the gradients of temperature and humidity. Over the ocean the humidity effects tend to be small, with Friehe reporting the largest contribution at 17% of the temperature contribution in one set of experiments.

C_n can be determined at a given point by direct measurement of the temperature and humidity fluctuations. Such measurements are described briefly later in this report and in more detail in reports of the associated meteorological group at the

NPS (Davidson et al, 1977, 1 and Davidson et al, 1977, 2). Generally the effect of humidity fluctuation on C_n is expected to be a small fraction of the effect of temperature. Point measurements of C_n have generally been made here in terms of C_T only, with humidity contribution omitted. The point results have usually indicated large variations of C_n along the optical path. As a result, the point values have been used to indicate order of magnitude agreement with the path-weighted integrated values obtained from optical measurements, and the small loss of accuracy due to omission of humidity has not seemed critical.

B. Turbulence Effects on OTF and Wander

Turbulence in the atmosphere, as expressed by a path-integrated C_n value, determines the performance of imaging or beam-forming optical systems, and this performance can be used to measure the path-integrated C_n.

The effects of atmospheric turbulence on the performance of an imaging or beam projection system are usually treated (Fried, 1966; Lutomirski and Yura, 1974) by considering the atmosphere-plus-optics combination as a linear system, with the image being the response of the system to the object. If there were no sources of image degradation between the object and the image, a point object would have a point as its image. However, diffraction, caused by the finite aperture of the system, is always present. Within the present context, refraction and diffraction caused by the index of refraction inhomogeneities in the atmosphere are also present. These effects cause the ideal point response to a point object to be smeared out. If the point spread function is transitionally invariant, i.e., the point spread function has the same shape regardless of its position in the image plane, then the image function becomes the convolution of the object function and the point spread function. In this case the convolution theorem of Fourier transform theory yields:

$$i(\nu_x,\nu_y) = H(\nu_x,\nu_y) \cdot o(\nu_x,\nu_y)$$

where $i(\nu_x,\nu_y)$, $H(\nu_x,\nu_y)$, and $o(\nu_x,\nu_y)$ are the two-dimensional Fourier transforms of the image function, point spread function, and object function respectively and the ν values are the spatial frequencies. The quantity $H(\nu_x,\nu_y)$ is known as the optical transfer function (OTF) and its modulus is called the modulation transfer function (MTF). The optical transfer function is thus the fundamental quantity which contains the effects of the atmospheric turbulence. The modulation transfer function is also used to characterize the effects of turbulence, but it lacks some information on phase deformations.

For isotropic turbulence and circularly symmetric optics, the OTF is a function of $\nu_x = \nu_y = |\nu|$. In this case, a one-dimensional treatment is adequate. Physically, a one-dimensional image signal is obtained by scanning the image of a point object with a slit. Then the point spread function is replaced by the line-spread function: $h(x) = \int h(x,y)\, dy$ and $i(\nu) = H(\nu) \cdot o(\nu)$.

Theoretical studies (Fried, 1966; Lutomirski and Yura, 1971) for an imaging system which include the effects of atmospheric turbulence show that the total optical transfer function can be expressed as the product of the transfer function for the optics and the transfer function for the atmosphere,

$$H_{tot}(\nu) = H_{opt}(\nu) \cdot H_{atm}(\nu).$$

The transfer function for the optics in the case of a circular aperture is well known and is illustrated in Fig. III-1, for the case of no central obscuration, and for the case of a central obscuration ratio (D_{obs}/D) of 0.32, one of the geometries employed. In the work reported here, the instrument line-spread function has been experimentally measured for each set of instrument conditions. This measured line-spread function includes, besides diffraction, the effects of finite slit width, residual geometrical aberrations, electronic and recording frequency limitations and any unpredicted errors in the system. In most cases the system was primarily diffraction limited. The details of

unfolding the atmospheric OTF from the observed line-spread function are reported in a later section.

Models for the transfer function describing the effects of atmospheric turbulence have been considered by several authors in the past decade (Tatarski, 1961; Hufnagel and Stanley, 1964; Fried, 1966; Lutomirski and Yura, 1971; Lutomirski et al, 1973; Lutomirski and Yura, 1974). Because of the stochastic nature of turbulence, quantities which relate to it can be understood only by means of an ensemble average. The problem of calculating the atmospheric OTF is considered in two limiting situations, the short term or short exposure (S.E.) and the long term or long exposure (L.E.). The short term OTF describes images obtained in the limit of time intervals sufficiently short that the turbulence can be considered frozen. The average short term OTF is then the average of the OTF's corresponding to many such images. The long term OTF results simply from taking an image of sufficiently long term which sees effectively all possible turbulence configurations. The average long term OTF is, therefore, the same as that from a single long time integrated exposure, since every turbulence configuration has been taken into account (properly weighted).

Another method of distinguishing the long and short exposure OTF's is of particular practical significance as it allows the measurement of each. If one observes a series of line-spread images, one would find that each image is broadened over the diffraction limit imposed by the optics and that the center of the area of each image appears to wander. The first effect is called image spread and the second image wander. The short exposure OTF is obtained by taking the average (and then the Fourier transform) of successive line-spread functions in which each line-spread function is shifted such that the center of the area of each curve has a common origin. This procedure in effect removes the image wander. The long exposure OTF is obtained by including the image wander; i.e., by not performing this shift in origin.

The long exposure OTF is seen to be the result of image spread (the short term OTF) plus image wander.

Several theoretical models have been proposed from which the L.E. OTF can be derived and all lead to the same result. On the other hand the only theoretical treatment of the S.E. OTF thus far is that of Fried (Fried, 1966). The result for both cases can be summarized by the following expression:

$$M(f) = \langle H(f) \rangle = \exp\{-57.64\ \beta\ C_n^2\ z_o\ \lambda^{-1/3}\ f^{5/3}[1 - \alpha(\tfrac{f\lambda}{D})^{1/3}]\}$$

where

λ = wavelength

f = angular spatial frequency (cycles/radian), = $F\nu$

ν = linear spatial frequency, cycles/meter

F = focal length of system

D = diameter of optics,

z_o = range

$$\alpha = \begin{cases} 0 \text{ for the L.E. OTF} \\ 1/2 \text{ for the far-field S.E. OTF, } D << (z\lambda)^{1/2} \\ 1 \text{ for the near-field S.E. OTF, } D \gtrsim (z\lambda)^{1/2} \end{cases}$$

$$\beta = \begin{cases} 1 \text{ for a plane wave} \\ 3/8 \text{ for a spherical wave} \end{cases}$$

Use of the quantity, f, the angular spatial frequency appearing in this expression, avoids the necessity to know the focal length or magnification of a system. It might be noted that most experimental situations which employ a diverging laser beam as the light source or object can be considered to correspond to the spherical wave model. Plane waves are rarely encountered (an example of a plane wave is starlight incident on the earth's atmosphere) and if the spherical wave model does not apply, one must then employ the full mathematical apparatus of the finite beam, a much more complicated situation.

C. Path-position weighting of C_n^2 for OTF

The expression (in the preceding section), for the OTF applies to the case where C_n is independent of the position along the propagation path. If C_n varies along the path, this equation generalizes for the L.E. spherical-wave OTF to

$$M(f) = \exp\{-57.64\,\lambda^{-1/3} f^{5/3} \int_o^{z_o} C_n^2 \cdot (z/z_o)^{5/3} \cdot dz\}$$

That is, C_n^2 is replaced a weighted mean C_n^2 given by

$$C_n^2 = \frac{1}{z_o} \int_o^{z_o} C_n^2 \cdot (z/z_o)^{5/3}\, dz$$

The experimentally determined OTF can be used to infer this weighted mean for C_n^2.

The above equation expresses the path weighting of C_n^2 indicated in Fig. III-1 in which the path region nearest the imaging, or beam projecting system at $z = z_o$ has the largest contribution. The opposite end of the path has zero contribution.

D. Mutual Coherence Function, MCF

It is of interest to note that the function M(f) which is the relevant quantity to characterize atmospheric turbulence in imaging systems is the same function that enters in descriptions of the effects of turbulence on the coherence of a propagating wave (Hufnagel and Stanley, 1964). Expressed as a function of the length variable $\rho = F\nu\lambda = f\lambda$, the function $M(\rho)$ is called the mutual coherence function (MCF). Hence studies of the OTF with an imaging system also provide information concerning laser propagation. The mutual coherence function is frequently written

$$M(\rho) = \exp\left[-(\rho/\rho_o)^{5/3}\right] ,$$

where ρ_o is called the coherence length and applies to the long exposure situation. The quantity ρ_o is sometimes used to characterize a propagation path in terms of the turbulence along the path.

E. Approximate Method for Transform

For the long term MTF, i.e., with α equal to zero, the long term MTF has the general form:

$$M(f) = \exp\left[-(f/f_o)^{5/3}\right]$$

In the data reported in this report the shape of the M(f) curves is fitted very well by this form, under a wide variety of conditions. For this function, the relationship between f_e, the 1/e point, and x_e, the 1/e point for its transform, the line-spread function for the atmosphere, is:

$$x_e f_e = 0.60$$

or for the half height values

$$x_{\frac{1}{2}} f_{\frac{1}{2}} = 0.40$$

This relationship provides a very simple but approximate method for obtaining f_e for the OTF of the atmosphere from the value of x_e for the long term line-spread function. The utility of this approximation would be principally for cases where the atmospheric image broadening is very large, where the instrument broadening can be neglected. For small broadening, Fourier transform techniques are needed to remove the instrument broadening. None of the data reported in this report were reduced by the above approximate method.

F. Turbulence and Scintillation

A different path-integrated value of C_n from that obtained from the OTF can be obtained from scintillation. If the intensity of a laser beam, which has propagated through a turbulent medium, is observed at a point, the intensity appears to fluctuate or scintillate in a random way. It has been shown that the values of the logarithm of the amplitude follow a Gaussian distribution. The variance of the log amplitude of these fluctuations can be related to C_n^2 as well as to the wavelength and the propagation pathlength z_o by the expression, (Lutomirski, et al, 1973; Fried, 1967).

$$\sigma^2_{\ell nA} = 0.124\ k^{7/6}\ C_n^{\ 2}\ z_o^{\ 11/6}\ .$$

where $k = 2\pi/\lambda$

This formula holds only for small intensity fluctuations such that the log intensity fluctuation standard deviation $\sigma_{\ell nI}$, which is twice the log amplitude fluctuation standard deviation $\sigma_{\ell nA}$, is less than about 0.8, i.e.:

$$\sigma_{\ell nI} = 2\sigma_{\ell nA} \lesssim 0.8$$

For higher levels of turbulence or greater pathlengths, such that this condition is not fulfilled, $\sigma_{\ell nI}$ is observed to level off at a value of about unity (saturation) and, for still greater turbulence or range, to decrease slowly (supersaturation). No good theory for the region of saturation yet exists. Thus one may infer values of C_n by measuring the log intensity variance $\sigma_{\ell nI}$, though the method is valid only in the region below saturation.

G. Path-position Weighting of $C_n^{\ 2}$ for Scintillation

The equation above is applicable under the assumption that the turbulence levels along the propagation path are constant. If this is not the case, such that $C_n = C_n(z)$, a function of the position z along the path, then the equation above generalizes for spherical waves (Lutomirski, et al, 1973) to:

$$\sigma^2_{\ell nA} = 0.56\ k^{7/6} \int_o^{z_o} C_n^{\ 2} \cdot (z_o - z)^{5/6} \cdot (z/z_o)^{5/6} \cdot dz$$

$$= 0.56\ k^{7/6} \int_o^{z_o} C_n^{\ 2} \cdot w \cdot dz$$

This method thus determines a path-averaged value of $C_n^{\ 2}$ but with the particular weighting, $w(z)$, given by $w(z) = (z_o - z)^{5/6} \cdot (z/z_o)^{5/6}$. This weighting emphasizes the middle of the path length with no contribution from the ends, as indicated in Fig. III-1.

Use of one-dimensional spatial filtering can alter the path-position weighting profile. This technique has been used by othe with a star as the source, for plane waves, to obtain information on the vertical distribution of $C_n^{\ 2}$ in the atmosphere (Ochs,1976).

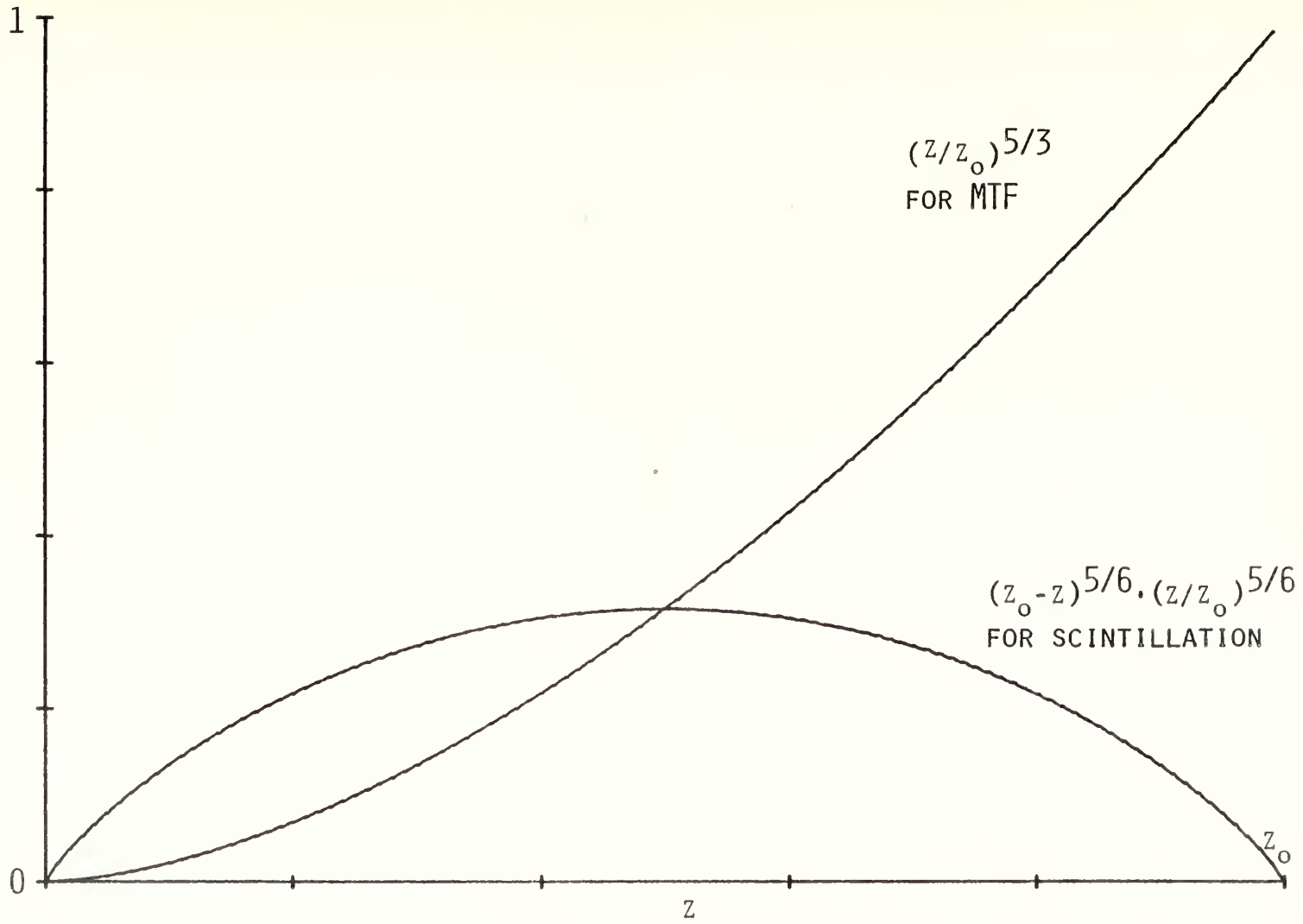

FIG. III-1. RELATIVE WEIGHTING OF C_N^2 AS A FUNCTION OF POSITION ALONG THE PATH, FOR MTF AND FOR SCINTILLATION. THE TELESCOPE END OF THE PATH IS AT THE RIGHT.

Although this helps move the peak weighting nearer the telescope, the relative weight is still zero at the telescope. On this account scintillation-determined C_n^2 seems to be of marginal utility in application to MTF.

H. Effects of Fog/Aerosol Scattering on OTF

The principal thrust of this work has been to evaluate the effects of turbulence on the MTF of the atmosphere. The scattering of a laser beam due to aerosols and fog is also capable, in principle, of degrading the MTF. This can occur in three ways. First the MTF can be reduced by an increase in the background level because of the scattering of sky light into the field of view of the telescope. This was largely eliminated in this work by use of narrow band interference filters passing the laser wavelength, but suppressing the background. The second mechanism is a broadening of the image by small angle scatter of the laser beam. Added to this is a third mechanism of multiple large angle scattering to return some laser beam light to the field of view. Estimates of the latter two effects (Livingston, et al, 1975), in terms of the theoretical mechanisms of scattering, indicate that scattering would make negligible contribution to the observed atmospheric MTF as observed with an imaging system. The techniques used here are such as to largely cancel the effects of scattering. The zero background level is determined in the wings of each line-spread function obtained from slit scanning. This tends to cancel any scattering of substantially larger angle than the turbulence broadening. In view of the possibility of missing some scattering by this technique, a number of measurements were made with the source rapidly chopped. In no case was any background scatter observed, presumably because its level was below that detectable compared to the primary line-spread function.

IV. General Plan of Experimental Program

A. General Considerations

The general objective has been that of acquiring a basis for prediction of the optical properties of imagers and beam projectors which must work through the real atmosphere, with emphasis on the atmosphere over the ocean. The program has been interdisciplinary, with all measurements, as far as possible, made under conditions where all the parameters affecting optical behavior are measured simultaneously. The work was carried out by three closely associated but identifiable groups working in the areas of meteorology, fog/aerosols, and optics. The work reported here in this report is primarily optical. Some of the work of the other two groups is included here, where the results have direct interaction with the optical results reported here. Additional material concerning meteorology and fog/aerosols is reported in separate reports (Davidson 1977 and 1978).

B. MTF and Wander

The performance of an imaging system, or of a beam projection system such as the HEL and pointer/tracker, through the atmosphere can be characterized and predicted in terms of the MTF of the atmosphere. Consequently, an understanding of the MTF has been the central problem. The experimental program has been designed to provide verification of theoretical models involving all the factors that determine resolution as expressed by MTF. In addition, the experiments have been designed to provide evolution of field test techniques and equipment capable of providing immediate data, with on-line data reduction, for results applicable to HEL performance in the field.

As indicated in Section III, the MTF is expected to depend on the level of turbulence, as expressed by a path-weighted value of C_n^2, and on the wavelength and range. A number of experiments have been carried out to measure the effects of

these parameters on the MTF. These have been carried out under maritime conditions on nearly horizontally paths, to provide as nearly uniform C_n^2 as possible. The ranges used are described in Section IV. E.

Measurements of MTF yield long term and short term MTF and wander. The experiments were designed to test the internal consistency among these three types of measurements. The consistency has proved to be good enough that one type of measurement can be made and the other results calculated from those measurements. This broadens the capability to carry out measurements, because the short term (image centered) MTF can be measured from an unstable platform and for moving sources, by active tracking in the optical system.

Values of MTF can also be measured by a different technique utilizing a "shearing interferometer". A set of experiments was carried out to compare our results with those from a shearing interferometer operated by another group (Lincoln Lab.). The results indicated that both methods measure basically the same phenomena and obtain the same results. However the particular data processing employed by the Lincoln Lab group is such that the average of MTF is obtained, whereas our data processing produces the average of OTF, the modulus of which is what we call the MTF. The Lincoln Lab average is strictly applicable to speckle interferometry results whereas our results are applicable to image or beam projection prediction. Our results can be processed to reproduce the Lincoln Lab results. The results are very little different in practice, although differing in principle. The differences lie mostly in the high spatial frequency region, out of the range of much significance to HEL.

C. Scintillation

A value of C_n^2, but path-weighted differently than for C_n^2 obtained from MTF, was also determined in all the experiments,

by means of scintillation measurements along the same optical path as the MTF measurements. Experiments were also designed and carried out to verify the expected behavior of scintillation results with receiver aperture diameter, saturation of signal, and variation with wavelength. Variation of C_n^2 with height above the sea surface was also determined by scintillation measurements.

D. C_T^2

Point values of C_n^2 were also measured at points on the optical path in terms of thermal C_T^2. These measurements were made by the MET group, with sensors carried at various levels aboard the ACANIA, and by sensors placed at the land ends of the optical paths for ship-to-shore or shore-to-shore measurements.

E. Meteorology

Variation in meteorological conditions provided a wide range of C_n^2, from high to low, from very uniform in space and time, to rapidly varying behavior. The meteorological conditions associated with the values of C_n^2 encountered in the course of the experiments and the problems of predicting C_n^2 have been the subject of a companion project at NPS. Some of these results are incorporated in this report when they bear directly on the optical results. The remainder of the results appear in separate reports (Davidson, 1977, 1978).

F. Extinction

Since measurement of MTF and scintillation inherently involve measurement of the light intensity received at the end of a long optical path, it seemed appropriate to extend these measurements to become absolute intensity measurements, and in that way to determine the optical transmission of the atmosphere. Such work was begun during fiscal 77 and reached the quantitative stage at the end of the fiscal year, with one significant test run for shore-to-shore measurements in September, 1977.

Measurements were made from Pt. Pinos to Marina, across Monterey Bay, with a path length of 13.16 km. Measurements were made at wavelengths of 0.4880 μm (blue), 0.6328 μm (red) and 1.06 μm (near IR). Extension to longer wavelengths is under development, and is being continued in fiscal 78. Development is progressing along several lines: (a) Extension to longer wavelengths, (b) Implementation of shore-to-ship techniques, and (c) Development of slant path kytoon-to-ship techniques.

Extension to longer wavelengths is being carried out by stabilization of a CO_2 laser to operate on single line output for shore-to-shore operation. A DF laser may also be utilized For the shorter paths of shore-to-ship, techniques utilizing black body sources are under development. This will permit filling a gap left by available lasers in the 3-5 μm region.

Development of ship-to-shore techniques has required some improvement in the gyro-platform system. The optical systems are also being rebuilt to accomodate larger angular instability than previously. These systems will also be capable of utilizing the black body sources to be located onshore, and will allow complete spectral coverage for extinction measurements from visible to 14 μm.

Development of slant path kytoon-to-ship techniques includes some of the new ship-to-shore techniques, for the receiver optics. It also involves some new light sources for use on the kytoon, which can support only about 15 pounds. The light sources will be omnidirectional flashlamps, triggered by the laser ranger pulses that determine the distance to the kytoon.

G. Location of Experiments

Most of the experiments were carried out on Monterey Bay with a variety of optical paths from Pt. Pinos, or from Pt. Alones, to points along the eastern shore of Monterey Bay, and to the NPS

Research Vessel ACANIA. The ship made it possible to use short ranges and to vary the length and orientation of the optical path during an experimental sequence. The ship was also utilized to make measurements of the micrometeorology at points along the optical path, or at one end of the path. The optical paths employed are indicated in Fig. IV-1.

The land-to-land paths vary from 4.03 km to 18.8 km. Use of the ACANIA for ship-to-land measurements permitted short paths from about 0.3 to 5 km, under ocean atmospheric conditions. The maximum path length for ship-to-land measurements was determined by the sea state and the stability of the optical gyro platform. The ACANIA was usually placed off Pt. Pinos in such a position as to provide an optical path perpendicular to the wind. The prevailing wind is from the northwest. Some optical measurements were also made during storm conditions when the wind came from the southwest.

The longer land-to-land paths, from Pt. Pinos to the shore, are approximately perpendicular to the prevailing wind and are fairly free from acceleration of the wind due to shore effects. The shortest land-to-land path, from the Holiday Inn to Hopkins Marine Station (4.03 km), although very convenient in terms of facilities available, is somewhat affected by the shore on its western end. Data taken on that path have been used primarily for inter-comparison of path-integrated values obtained by several different methods, rather than for comparison with micrometeorological data.

The optical paths utilized are essentially parallel to the ocean surface at a height of about 6m. On the longer ranges the curvature of the earth makes it impossible to maintain a constant height above the water. This factor limits the useful long range path to less than about 20 km. For that range the curvature of the earth and refraction due to the density gradient for constant temperature cause the center of the path to be about 6m

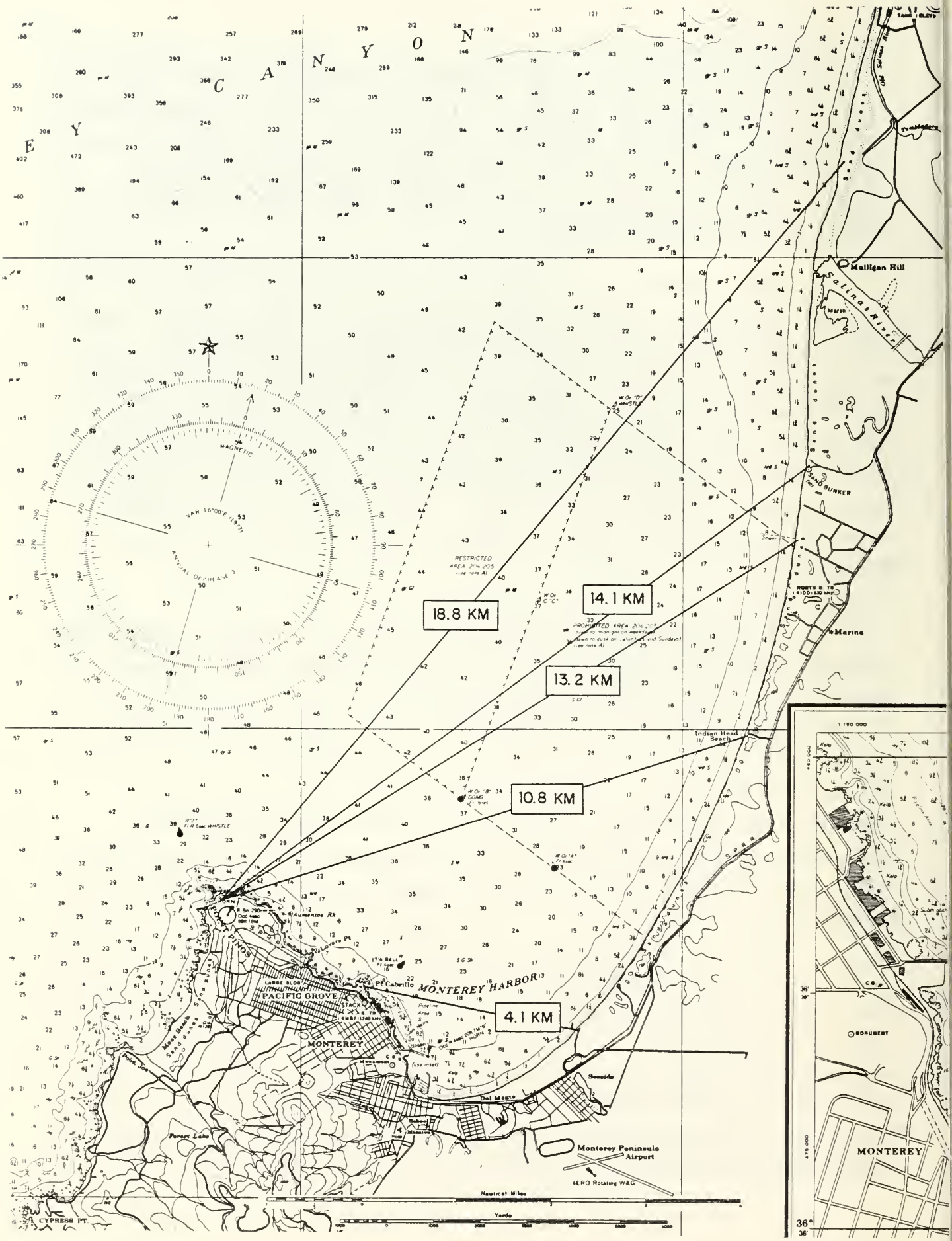

Fig. IV-1. Optical Ranges Across Monterey Bay.

closer to the water than at the two ends. This height varies as the square of the range length. The vertical thermal gradient also affects the curvature of the beam, and needs to be included in the height calculation. The thermal gradient was available from data taken on the ship. The height correction Δh is: $\Delta h = (\text{Range})^2 \times 1.22 \times 10^{-7}$ dt/dh when dt/dh is the vertical temperature gradient.

The shore stations are a mobile lab, converted from a Greyhound bus, and a lab van. In the earlier work, a small trailer was used. The mobile lab is shown in Fig. IV-2. It contains the scanning telescope, laser transmitters and scintillation receivers, and instruments for determining the temperature fluctuation, C_T, at a single height. The optical equipment is supported on a framework resting directly on the ground. On-line scintillation data-reduction equipment is also located in the bus. The 2-1/2 ton lab van is located at the opposite end of the land-to-land path from that of the bus. This van contains laser transmitters at a number of wavelengths, also supported on a framework resting directly on the ground. The van is shown in Fig. IV-3.

Several runs were also made off San Nicolas Island near the beginning of the project. Unfortunately, the results of those runs are marginal, as not all of the factors affecting measurement of MTF were under control at that time. They did, however, serve as useful equipment checkout runs.

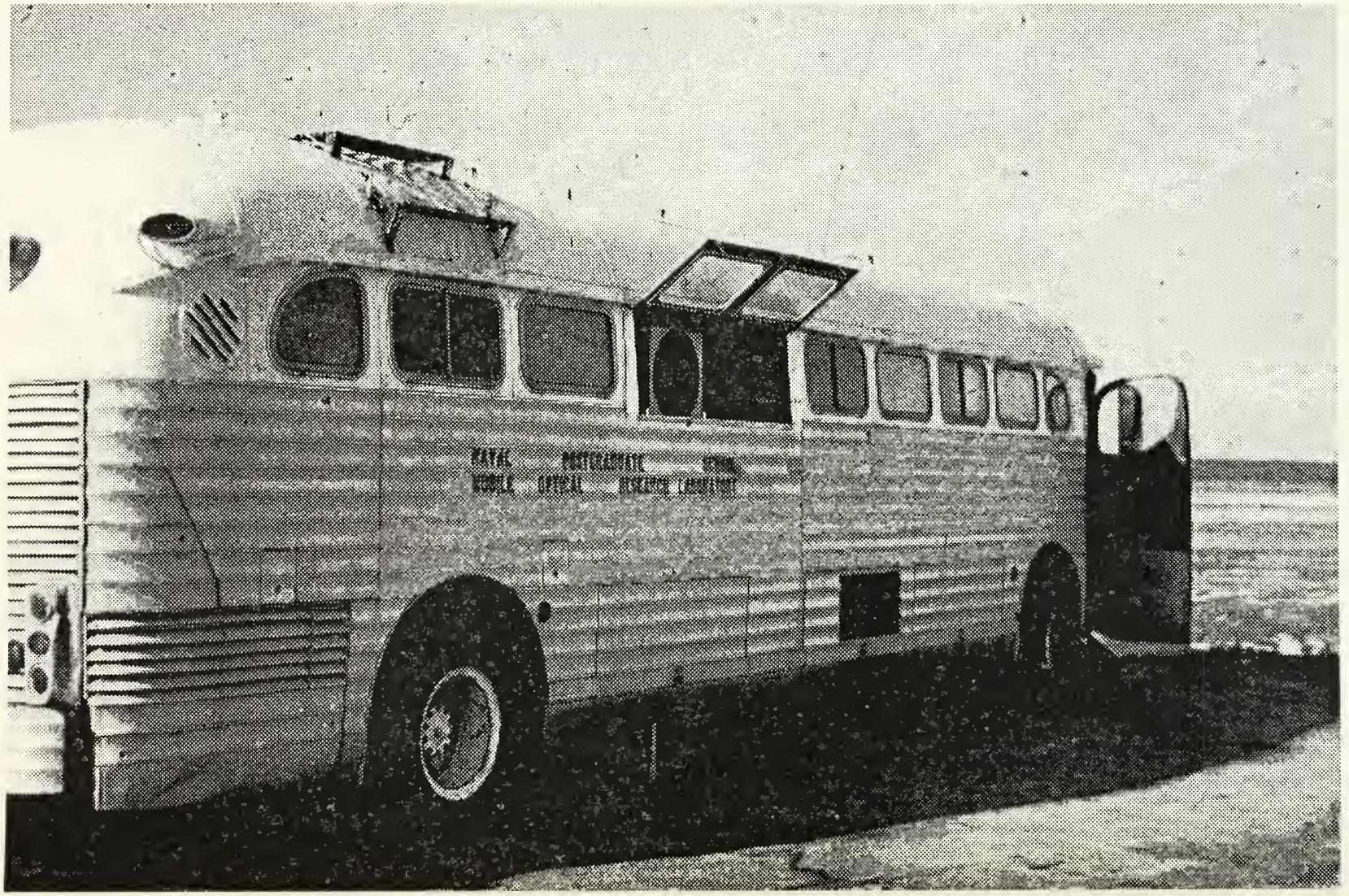

Fig. IV-2. Mobile Laboratory.

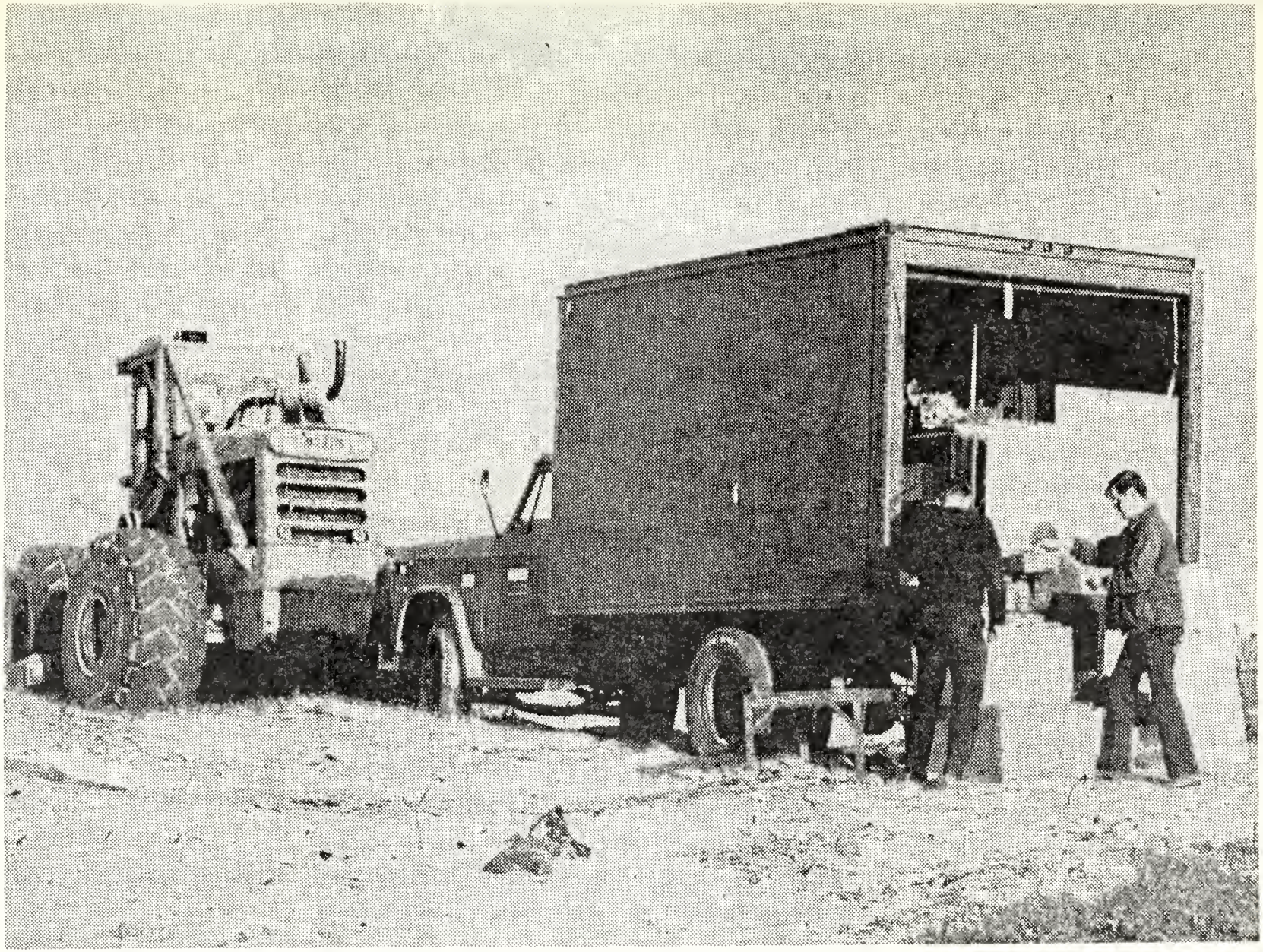

Fig. IV-3. Instrument Van.

V. Measurement Techniques

A. MTF - OTF or MCF

1. Measurement of long and short exposure MTF, and wander, by the Slit Scanning Imager (SSI).

General Principles of Operation

a). The optical system utilized in measuring the MTF is described in detail later in Section V.A 3. Briefly, an image is formed in the focal plane of a telescope, and this image scanned across a slit. The radiation passing through the slit is detected by an appropriate photodetector and converted to an electrical signal. The image is scanned linearly with a fast return servodriven deflection mirror so that the line-spread function appears as a linear function of time. In the early work, this signal and a trigger signal were recorded on a frequency modulated tape recorder and the signals processed later by computer in the laboratory. The band-pass of the recorder is 15 kHz, just adequate to handle the frequencies occurring for diffraction-limited images at the 50 Hz repetition rate employed. (Some early work was done at 25 Hz with a more limited recorder). The recent work has utilized direct on-line data reduction with a minicomputer system, described in a later section. Typical line-spread functions are shown in Fig. V-1. for individual scans.

The image line-spread function, h, for the system alone, is obtained by providing a collimated beam in the laboratory with diameter equal to, or greater than, the telescope input aperture. The total optical path is kept as short as possible - in practice just the internal paths of the instruments. A typical line-spread function for the system alone is shown in Fig. V-2. The calculated ideal two dimensional image point-spread function is shown in Fig. 3a for the 18 inch aperture, with a central obscuration ratio of 0.33. The calculated ideal line-spread function is shown in Fig. 3b. This function represents the integral over the area of a finite slit lying across the two dimensional point-spread image pattern, as a function of the position of the slit. This function does not have the zeroes exhibited by the point spread function, as shown in 3a, except at infinity.

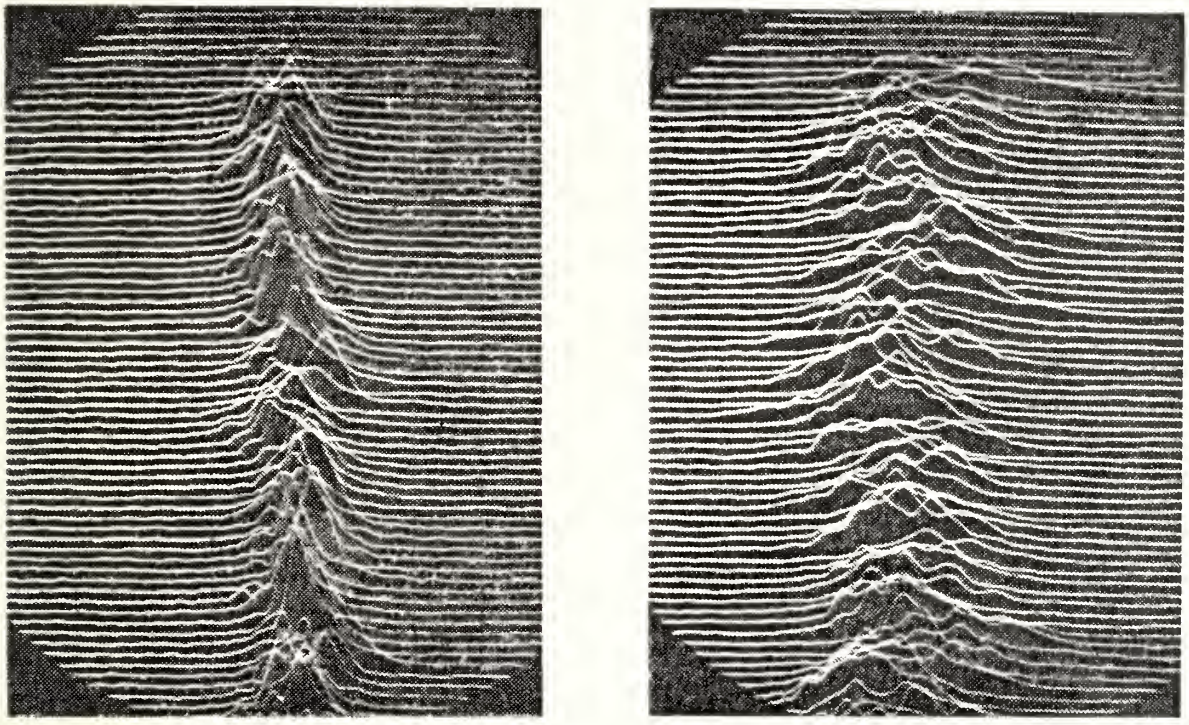

$C_n^2 = 9.6 \times 10^{-16}\ m^{-2/3}$ $C_n^2 = 30 \times 10^{-16}\ m^{-2/3}$

Fig. V-1. Typical Line-Spread Functions

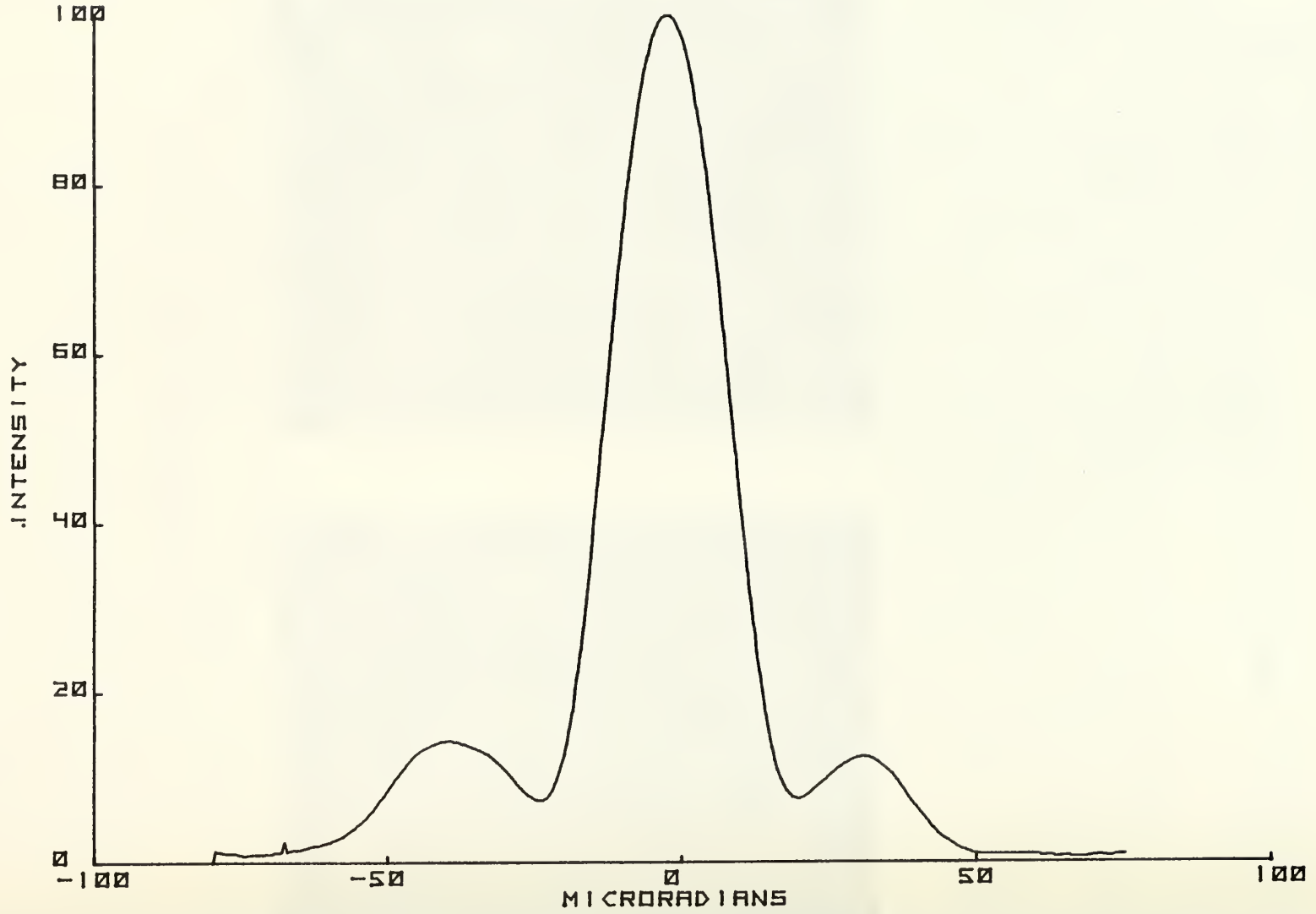

FIG. V-2. OBSERVED LINE-SPREAD FUNCTION FOR INSTRUMENT ALONE, 10.6 MICROMETERS.

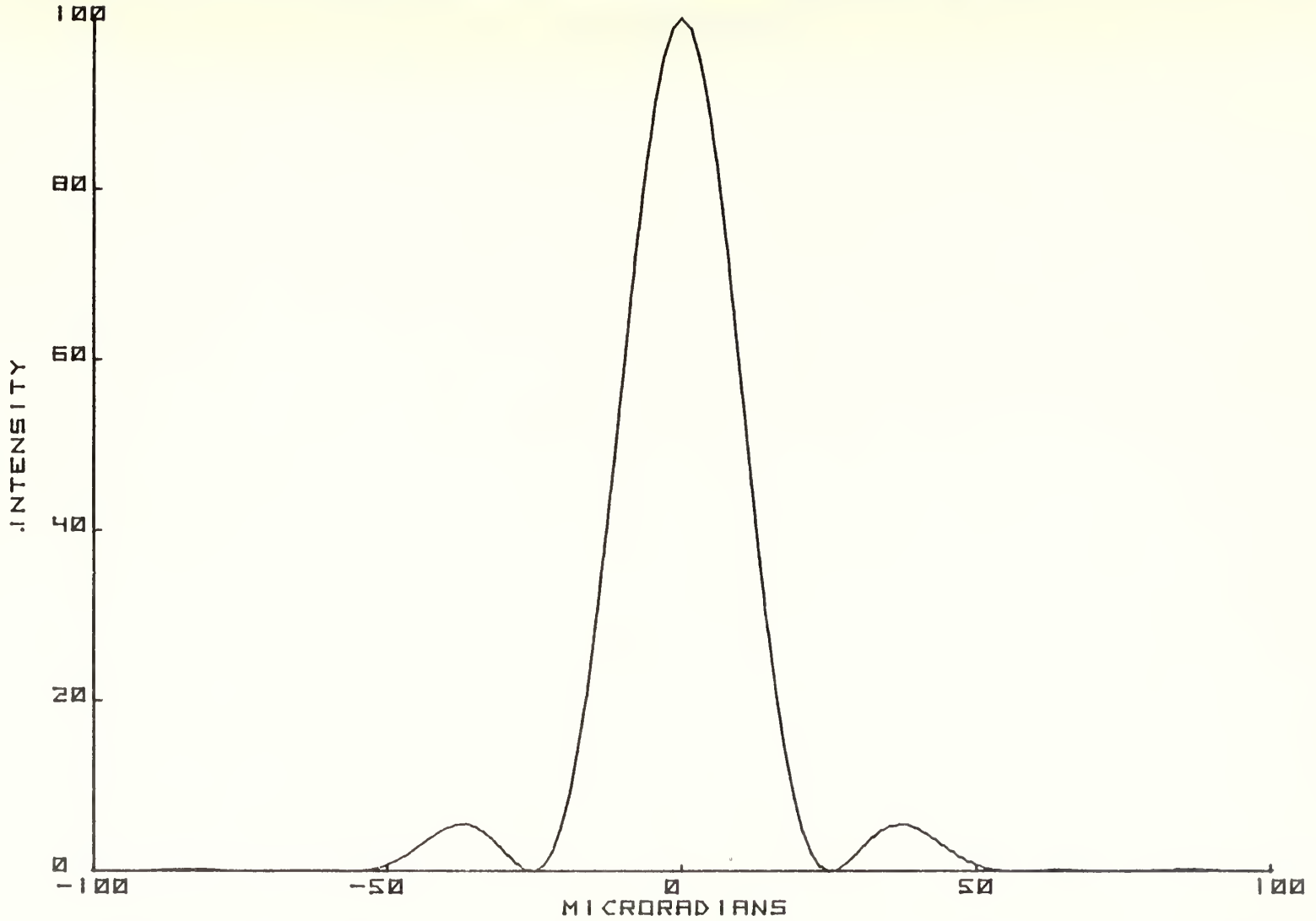

FIG. V-3A. POINT-SPREAD IMAGE FUNCTION FOR AN 18 INCH CIRCULAR APERTURE WITH A CENTRAL OBSCURATION RATIO OF 0.33. WAVELENGTH, 10.6 MICROMETERS.

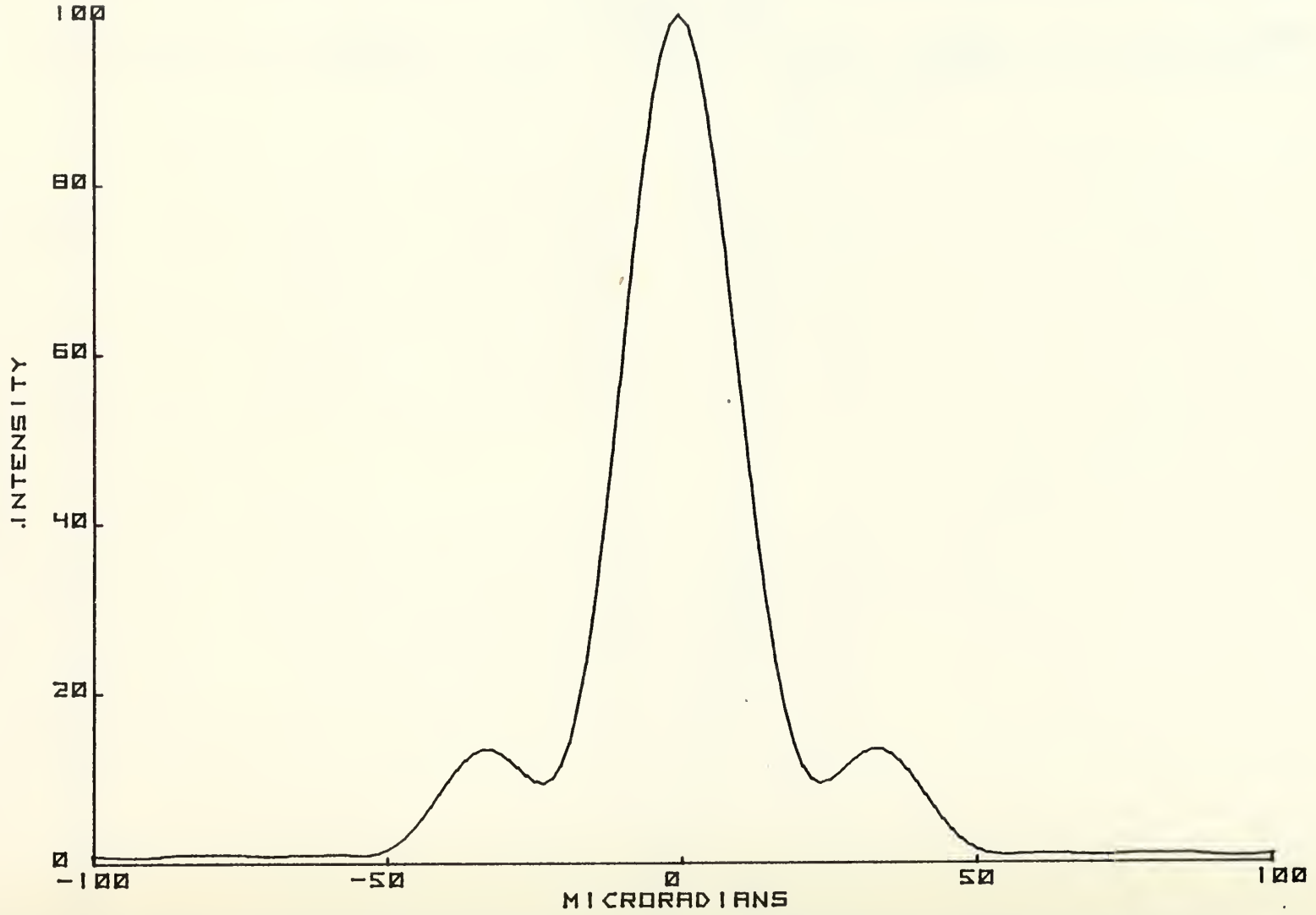

FIG. V-3B. LINE-SPREAD FUNCTION FOR THE POINT-SPREAD FUNCTION OF FIG. V-3A.

The observed instrument line-spread functions coincide with ideal calculated functions for diffraction limited operation and finite slit widths. Separate calibrations are needed for each slit width and each wavelength. The observed instrument line-spread function is symmetrical, and centered, so the transform is real. That is, it has no imaginary component, and the modulus of the transform is the same as the transform (except for alteration in algebraic sign in successive components). A curve of the modulus of the transform for the instrument alone is shown in Fig. V-4. This modulus is used to divide into the transform of field observations to obtain the MTF of the atmosphere. The transforms of the images observed through the atmosphere usually have small imaginary components, since the image functions are often not quite symmetrical. The real and imaginary parts are retained in the computer and are divided by the real transform of the instrument function to obtain a complex transfer function for the atmosphere. This permits the reconstruction of the broadening function for the atmosphere. The modulation transfer function (MTF) is the modulus obtained from the real and imaginary parts.

b). Calibration of Magnification

The magnification of the system is calibrated by inserting a grating, consisting of bars, in front of the entire telescope, so as to produce a diffraction pattern in the image plane. The calculated spacing of these peaks is used to determine the angular spacing as a function of distance in the focal plane. Such a calibration signal is shown in Fig. V-5.

Normally a grating calibration was taken in the field, on a periodic basis. This was used in data reduction to verify the calibration and, if necessary, used to alter the calibration when conditions were slightly changed. This was carried out by changing the sampling rate in the computer to maintain the same equivalent calibration.

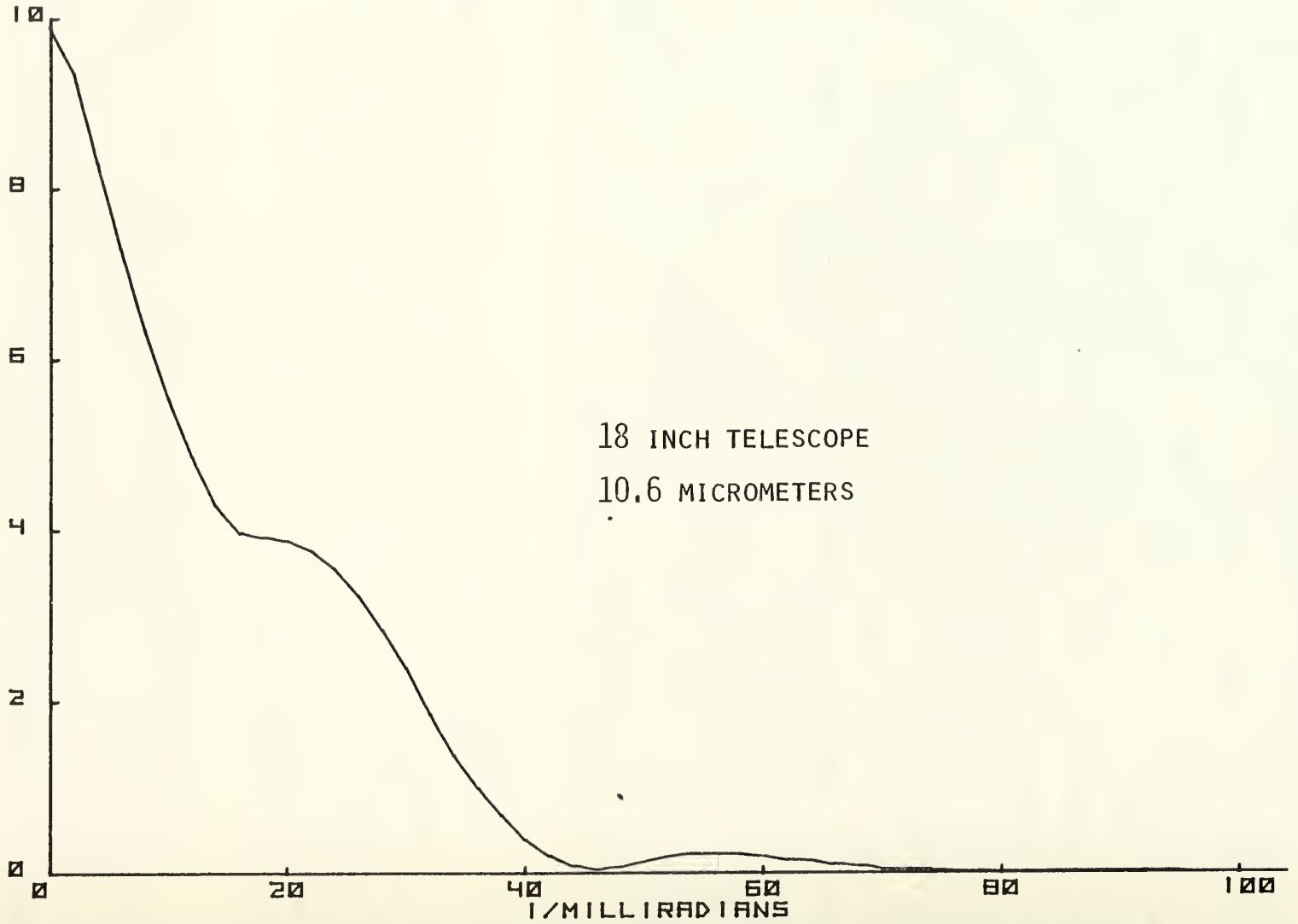

FIG. V-4. TRANSFORM OF THE OBSERVED INSTRUMENT LINE SPREAD FUNCTION OF FIG. V-2.

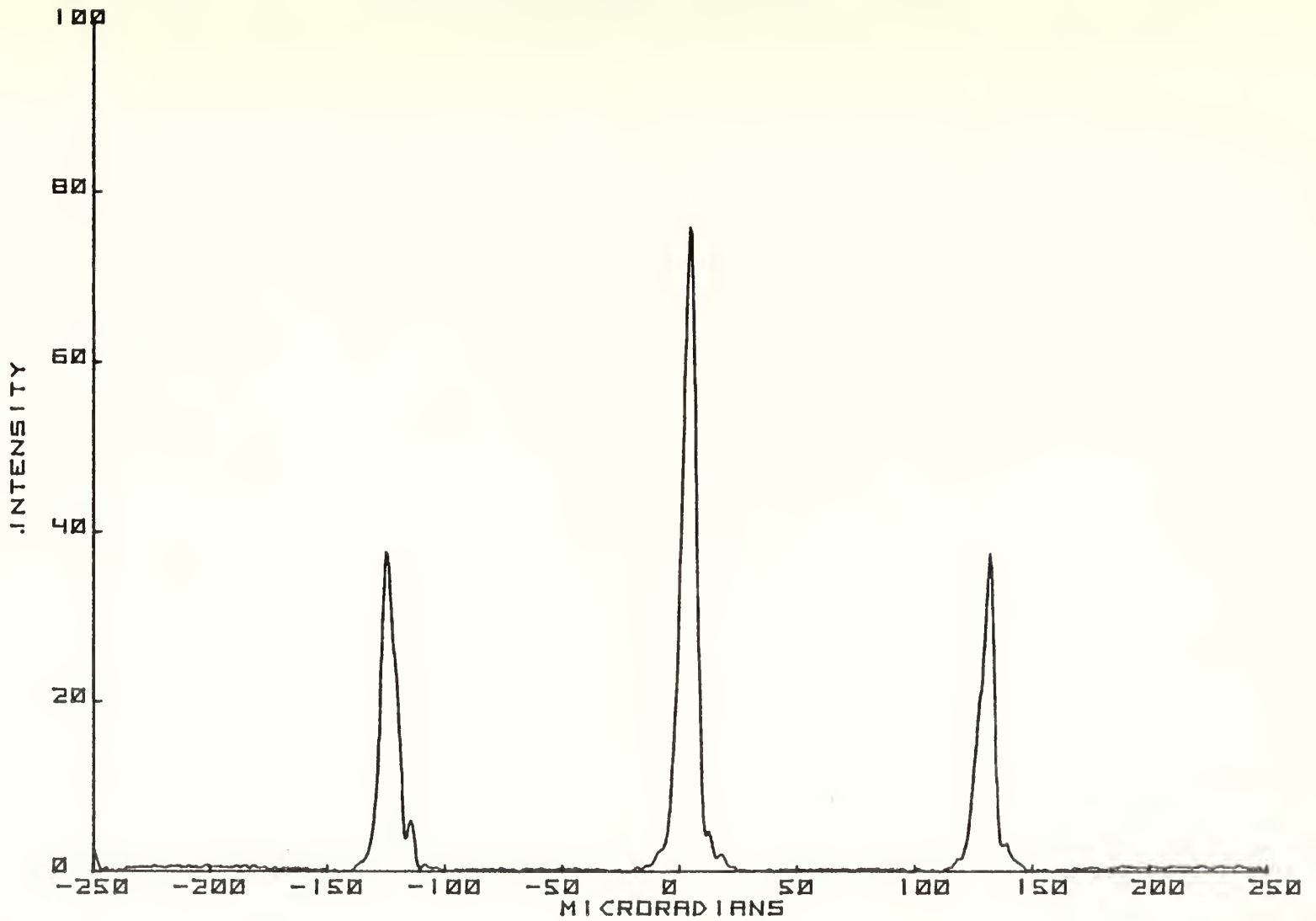

FIG. V-5. MAGNIFICATION CALIBRATION SIGNAL. GRATING PLACED AT ENTRANCE APERTURE.

c). Data Acquisition and Reduction

Briefly, the line-spread functions were sampled and digitized. For early data this was done at 400 points and the center 256 points utilized in the calculation. Now the function is sampled and digitized at 1024 points and the full 1024 points are utilized. In the process of data reduction each successive line-spread function is sampled, the center of its area calculated, and the amount, necessary to shift this to make all area centers coincide, is stored in the computer for later use in determining image-wander and its frequency spectrum. Two line-spread function averages are obtained, one with the centers shifted to align, and one unshifted. The shifted has been called the "short exposure" or "short-term" line-spread function since it bears some relationship to an actual short exposure line-spread function. However, it differs from the latter because the noise has been reduced by averaging. The long exposure or "long term" line-spread function is the unshifted average line-spread function. A short exposure and a long exposure line-spread function are shown in Fig. V-6. Fig. V-7a shows the Fourier transforms of these functions. Fig. V-7b shows the MTF's after dividing by the instrument functions. An example of the wander, or position shifts, stored in memory in the course of obtaining the short term line-spread function is shown in Fig. V-8. A frequency analysis of this gives frequency components as indicated in Fig. V-9. The original signals which are averaged to obtain the preceding figures are modulated by noise produced by transmission through the atmosphere. Representative individual curves are similar to those shown in Fig. V-1 . Those are two sets of observations under conditions with different values of C_n, as determined from scintillation. The values of C_n are shown in the figure captions. The randomly occurring modulation, due to the atmosphere, averages out in the process of averaging the line-spread functions so that the line-spread function used in obtaining a transform is ordinarily quite symmetric and smooth.

A path-averaged optical turbulence structure constant of the atmosphere, C_n^2 is obtained by a curve fitting of the data

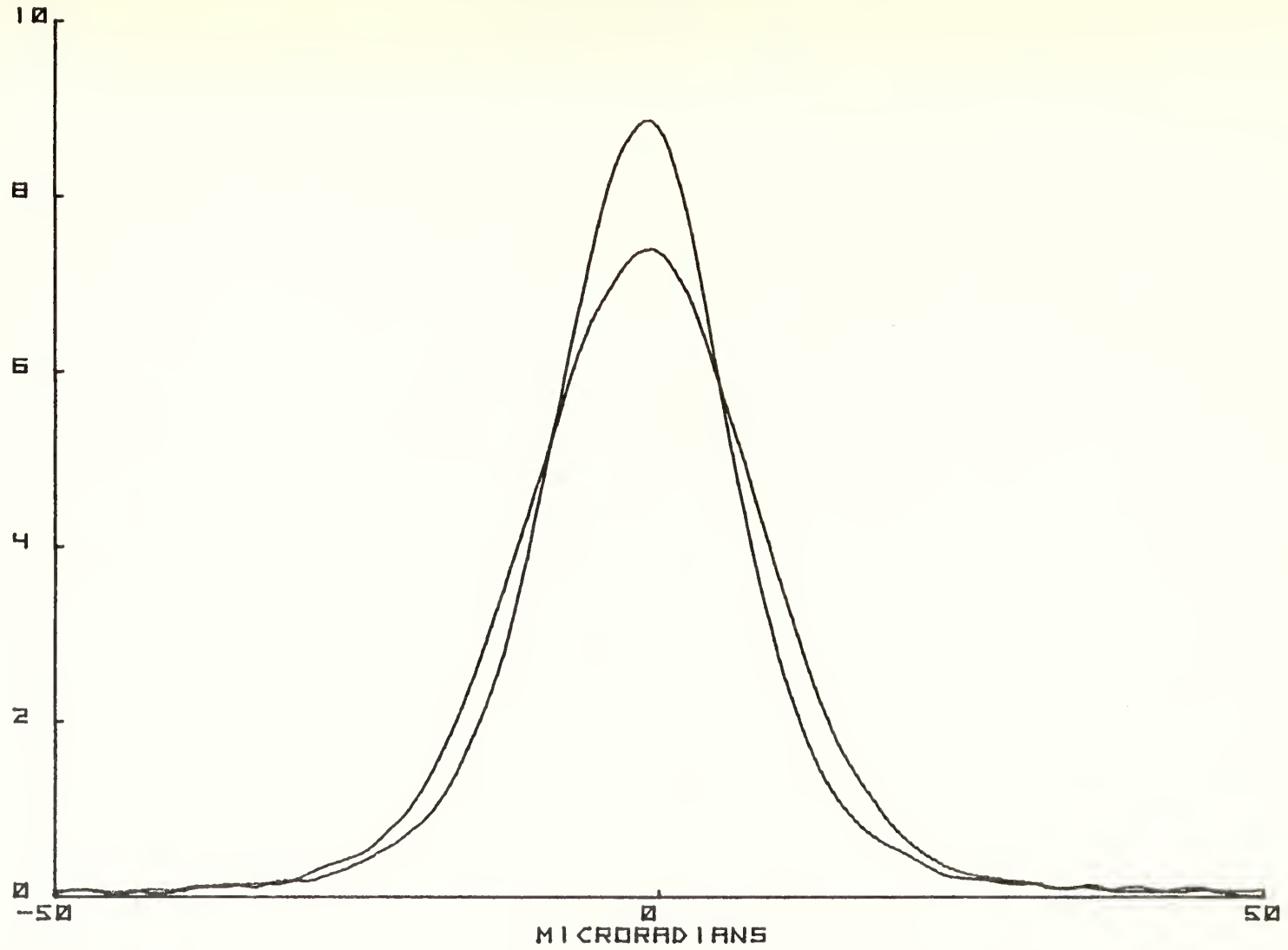

FIG. V-6. SHORT EXPOSURE AND LONG EXPOSURE LINE-SPREAD FUNCTIONS, 0.6328 μM 1100, 21 SEPTEMBER, 1977, RANGE 13.16 KM, MARINA-PT. PINOS

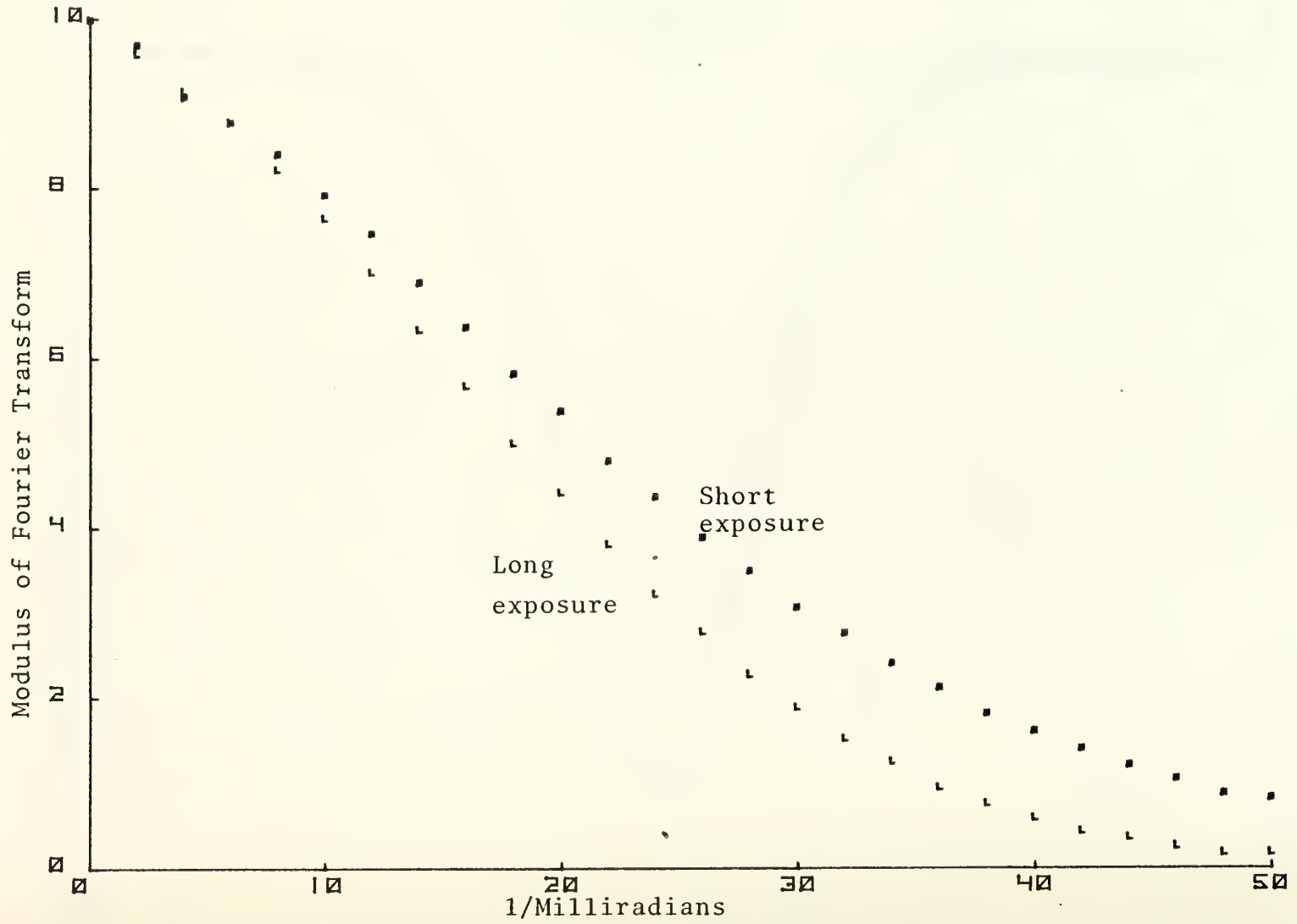

FIG. V-7A. FOURIER TRANSFORMS OF THE CURVES OF FIG. V-6.

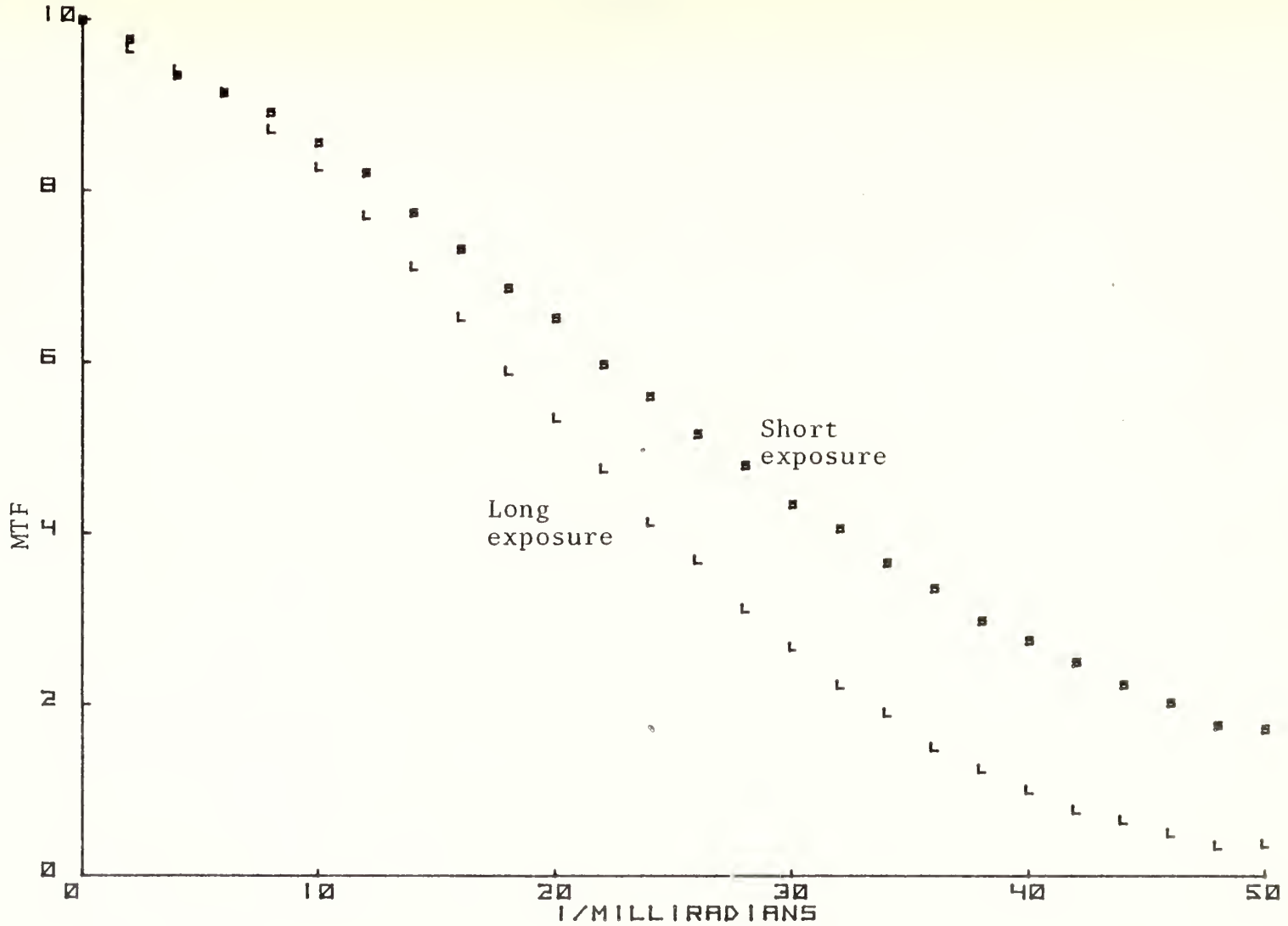

FIG. V-7B. MTF FOR CURVES OF FIG. V-7A - CURVES OF V-7A DIVIDED BY THE MODULUS OF THE TRANSFORM OF THE INSTRUMENT LINE SPREAD FUNCTION.

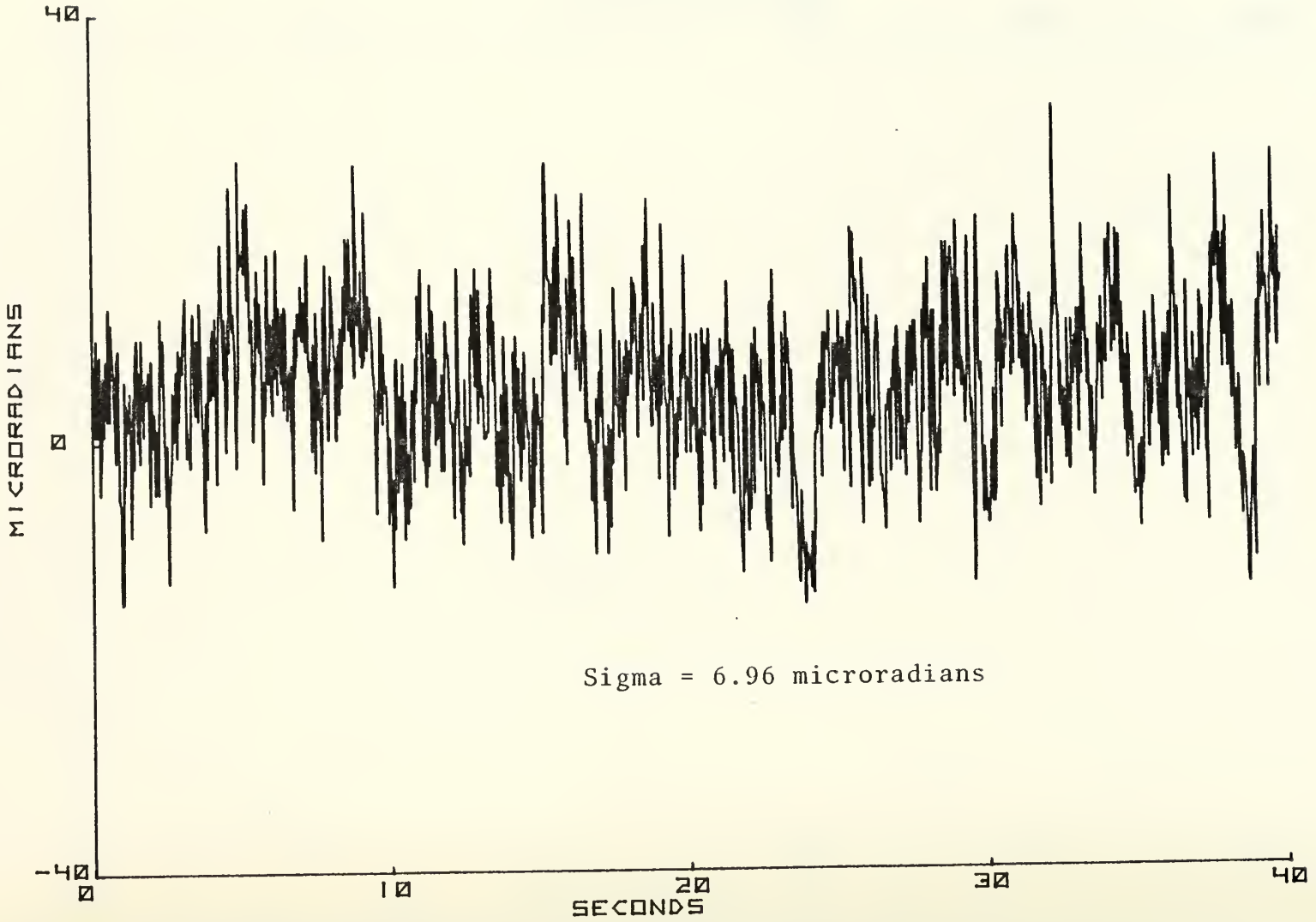

Fig. V-8. Wander displacement as a function of time

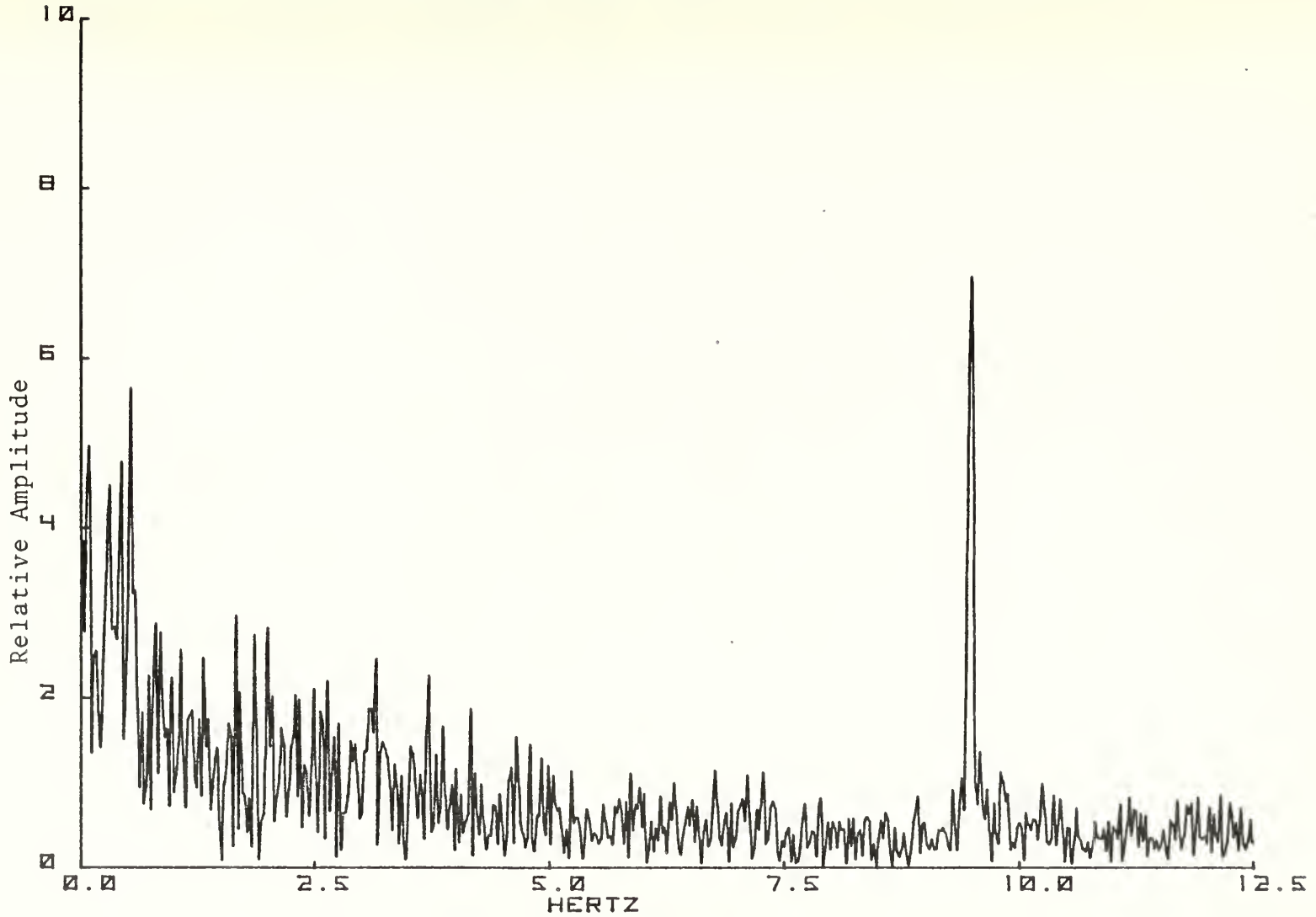

Fig. V-9. Frequency spectrum of the wander shown in Fig. V-8. The strong spike at about 9 Hz results from vibration of the telescope frame caused by wind buffetting. This occurred only when the wind blew directly into the telescope opening. Such data is discarded, for C_n^2 measurement, using long-term MTF or wander.

points, using Fried's model (Fried, 1966) as discussed earlier in Section III:

$$M = \exp\{-21.6\, C_n^2\, z_o (f)^{5/3}\, \lambda^{-1/3} [1 - \alpha\, (\tfrac{f\lambda}{D})^{1/3}]\}$$

where M = MTF

z_o = range

$f = F\nu$ = angular spatial frequency, cycles/radian

ν = spatial frequency, cycles/meter

F = focal length of the optical system

λ = wavelength

α = 1, short term, near field (for far field, α decreases to 1/2. The majority of our experiments lie in the near field, $\alpha \simeq 1$)

α = 0 long term

D = diameter of optics

C_n^2 is obtained by a linear regression of:

$$\ell n\ M \text{ vs. } -21.6\, z_o\, (f)^{5/3}\, \lambda^{-1/3} [1 - \alpha\, (\tfrac{f\lambda}{D})^{1/3}]$$

The calculation is carried out twice, once for short term and once for long term. (Except in cases where tracking requires using the short term only). The experimental data and the fitted curve are then plotted for a visual display of goodness of fit, on a CRT display. This can be converted to hard copy in about two minutes on a HP plotter.

A value of C_n is also obtained from the wander recorded during the short term averaging operation. The expression utilized is:

$$C_n = 1.046\, \sigma\, D^{1/6}\, z_o^{-1/2}$$

where σ = standard deviation of the angle of arrival at the telescope

D = diameter of the optics

z_o = range

2. On-line Data Reduction

The on-line data reduction unit is a Nicolet Instrument Co. Nic-80 data processor. This is a data averager followed by a 12K 20-bit-word digital computer and a Tektronix CRT display unit. Originally the input-output device was a teletype. Since the teletype is slow, not easily portable, and requires a human interface to transfer the data from the Nic-80 to the programmable calculator plotter for the final output, it has been eliminated, and the Nic-80 has been interfaced directly to the Hewlett Packard 9825 programmable calculator. The HP-9825 now acts as the controller and input-output device to the Nic-80 as well as plotter.

The Nic-80 digitizes the analog signal from the detector, processes the raw data to obtain the experimental MTF, wander, C_n, or extinction constant, depending upon the experiment. The processed experimental data is then transferred to the HP-9825 which is better suited for floating point calculations. The HP-9825 calculates the best fit curve and plots out the results in final form.

3. Optical Equipment for MTF-Slit Scanning Imager (SSI)

A series of imaging slit scanners have been used in the course of this work. First tests were made with a 6" aperture Newtonian system. This was soon replaced with a 10" aperture Newtonian system to improve the diffraction limited resolution, particularly at 10.6 μm. Considerable data were taken with this system, including the comparison with the shearing interferometer. This system was replaced with an 18" diameter system which improved the resolution of the atmospheric MTF at 10.6 μm. The 18" system is a Cassegrainian system with equivalent focal length of 6.5 meters and an overall length of about 1.5 meters. It has a 6" central obscuration for the secondary mirror. The optical components are Cervit, providing excellent thermal stability. In all the systems the optical path was turned 90 degrees twice with optically flat mirrors mounted on servo motors, to provide up-down tracking, as well as right-left tracking, plus saw-tooth

scan of the image across a slit. This scan produces the line-spread function as a function of time. A trigger signal associated with initiation of each scan indexes the position of the image.

The light passing through the slit is split with a glass dichroic splitter, reflecting infrared of wavelength longer than 2.5 μm into a cryogenically cooled IR detector. Two interchangeable IR detectors are used, InSb for 3-5 μm, and HgCdTe for 10.6 μm. A Germanium field lens is used to image the slit on the detector. The transmitted light through the dichroic splitter passes through field lenses and an interchangeable set of interference filters to a silicon detector. The latter was at first a UDT PIN detector. This was later replaced with a GE avalanche multiplier detector to improve the signal-to-noise ratio.

The telescope optics are supported on a rigid framework with hydraulically extendable legs, reaching directly to the ground through the floor of the instrument vehicle, isolating the telescope from mechanical vibration. The telescope mounting enclosure is kept closed except when actually in use for measurements, to reduce salt spray contamination of the optical surfaces. It is necessary to wash the optical surfaces after each run of several day's duration. The scattering due to salt particles does not alter the measured MTF, because it is large angle scattering. However, it gradually reduces the signal-to-noise ratio.

Tracking is necessary when the sources are on shipboard. Right-left tracking (perpendicular to the vertical slit) is accomplished by an analog tracking circuit which calculates the centroid of the line-spread function for each scan and centers the next scan on that basis. Up-down tracking (parallel to the slit) is accomplished by reflecting light from one side of the slit structure where the image reaches once during each scan. This light falls on a split photocell and is used to servo the other 90

degree turning mirror to center the image in the direction parallel to the slit. Both the long-wave IR system and the visible to short IR system may be operated simultaneously, so the short wave system provides the tracking for both detectors. The tracking is not needed for land-to-land data.

The signals from the silicon and IR detectors are pre-amplified at the detectors to drive cables to high-gain low-noise PAR 113 amplifiers. These signals are either tape-recorded, together with the trigger signal, or processed immediately with the on-line equipment.

The sources for the MTF system are lasers transmitted from the ship, or from the source van at the opposite shore station. The lasers are diverged to provide a spot size at the MTF telescope about 20-50 meters wide. This provides uniform illumination over the aperture of the telescope and closely approximates light diverging as a spherical wave from a point source. The MTF telescope then images this point source. The lasers are operated in the cw mode for this purpose. From shipboard, three different laser wavelengths can be transmitted simultaneously through the gyro tracking platform. That tracking system is locked onto a beacon signal transmitted from the shore telescope instrument van. The beacon ismounted on the shore telescope structure so that the manual tracking of the telescope, needed to keep it pointing in the right general direction, also keeps the ship illuminated by the beacon signal.

The four laser wavelengths utilized for MTF measurements are Argon ion blue at 0.4880 μm, red HeNe at 0.6328 μm, NdYAG IR at 1.06 μm, and CO_2 IR at 10.6 μm. A DF chemical laser was assembled from purchased head components and NPS pumping and power supply components. This is now operating, but is bulky and hazardous to operate in the field. As the wavelength variation of MTF has been satisfactorily verified with the other wavelengths, bracketing the 3.8 μm of the DF laser, it seems unwarranted to

spend the effort at this point to adapt it for field use.

In the absence of the 3.8 μm laser, some effort was applied to measure MTF using a black body source at 3.8 μm. Images were resolved at distances of 2 km. However, the data were compromised by uncertainties concerning the apparent source size for the black body on the moving ship platform.

In addition, the data available from the four laser wavelengths was by that time conclusive as regards the wavelength variation of MTF, so continuation of the black body work was assigned very low priority and has not been continued.

4. Portable MTF Equipment

In view of the results, reported later in Section VI. A 3 that the wavelength variation is well expressed by the Fried expression, and that the path position weighting goes as expected, it seemed appropriate to design and construct a portable system which could be easily transported to an optical test site to provide data on the MTF and the weighted C_n^2. Such a system has been constructed. It consists of a Celestron 8" diameter Schmidt telescope with an equivalent focal length of 160" with a times 2 Barlow lens. The system has a central obscuration ratio of 0.344. The telescope is equipped with up-down and right-left tracking, and linear scan across a slit, for generating the line-spread function. The field lenses pass the light through a narrow-band interference filter before falling on the detector, which is a GE silicon avalanche multiplier. A photograph of the telescope system is shown in Fig. V-10. The auxiliary equipment is the same as for the larger telescopes utilized in the instrument van. This includes the scan servos, amplifiers and on-line data processing equipment, together occupying a volume about that of an office desk.

The system need only be operated at a single wavelength, since the results reported elsewhere in this report indicate that

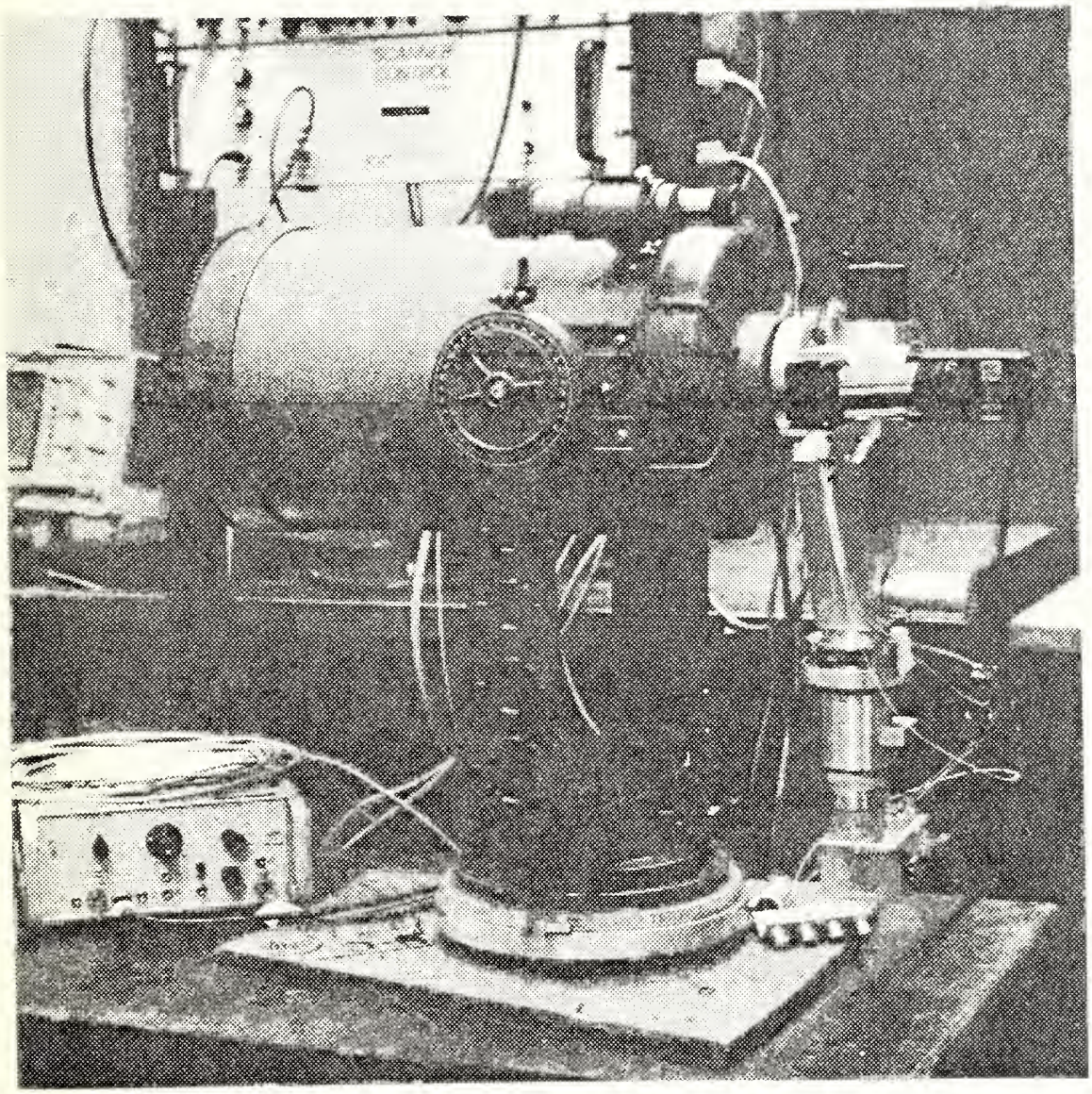

Fig. V-10. Portable MTF System.

the atmospheric MTF can be predicted for any wavelength, once it is known at one wavelength. Since the atmospheric effects on MTF are larger at short wavelength, it is desirable to operate at a short wavelength. This made it possible to utilize the excellent optics of a Schmidt telescope system since the limitation of the wavelength to less than 2.5 μm by the front glass corrector is thus not a problem.

For moving targets or unstable platforms, the portable system can operate to produce a short term MTF, while removing the image motion by tracking. The consistency indicated by the data elsewhere in this report, means that the short term MTF can be used to predict the long term MTF or wander, and only one of these three quantities need be determined.

The portable system is capable of providing a value of MTF path-weighted C_n^2 instantaneously, and a plot of MTF versus spatial frequency in a few minutes. The on-line data system can also produce a plot of predicted radial distribution, or a curve of energy within a given radius for a beam projector system, in a few minutes, when provided with the system constants.

The portable system is available for use on optical ranges wherever needed. It requires only a single diverged laser as a point source at the opposite end of the range.

V. B. Comparison of Slit-scan Imager and Shearing Interferometer MTF Values

1a. Shearing Interferometer

As a means of making a comparison of MTF measured by the slit scanning imager with an independent measurement of MTF, a joint test run was made with a shearing interferometer operated by a group from Lincoln Laboratory*. The shearing interferometer is described in the literature (Kelsall, 1973) but a brief description of its operating principles seems appropriate here.

Determination of MTF with a shearing interferometer bears a close relationship to the process by which the MTF of an optical system can be calculated, employing Fourier theory. For an imaging system with a given input aperture, and incoherent detector, the diffraction limited MTF is given by the autocorrelation of the entrance aperture for lateral displacement. (Goodman, 1968; Born and Wolf, 1970). This becomes the ratio of the area of overlap to the area of the aperture, for displacement of a shape identical to the aperture, across the aperture. The geometrical situation involved in this displacement is indicated in Fig. V-11 . The lateral displacement is the process of shearing for a shearing interferometer. For a circular aperture, the "shear", s, defined by Kelsall, is the ratio of the displacement, u, to the radius of the aperture, D/2, or:

$$s = \frac{u}{D/2} = 2\,u/D \qquad \text{where } D = \text{aperture diameter}$$

The spatial frequency, ν, in cycles per unit length, corresponding to a shear, s, is given by:

$$\nu = \frac{s}{2} \cdot \frac{D}{\lambda F} \qquad \text{where } F = \text{focal length of the primary imaging lens.}$$

In terms of the angular spatial frequency, f, where $f = F\nu$ in cycles per radian:

---

*The Lincoln Laboratory group brought their shearing interferometer to Monterey for the joint experiment. We are indebted to D. Kelsall, E.S. Cotton, L.C. Marquet and W. Stiehl for their contributions to this work.

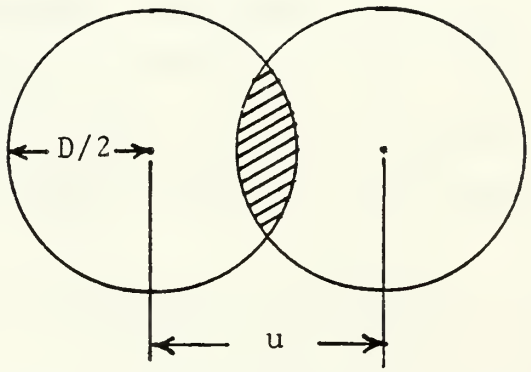

FIG. V-11. APERTURE DISPLACEMENT IN THE SHEARING INTERFEROMETER.

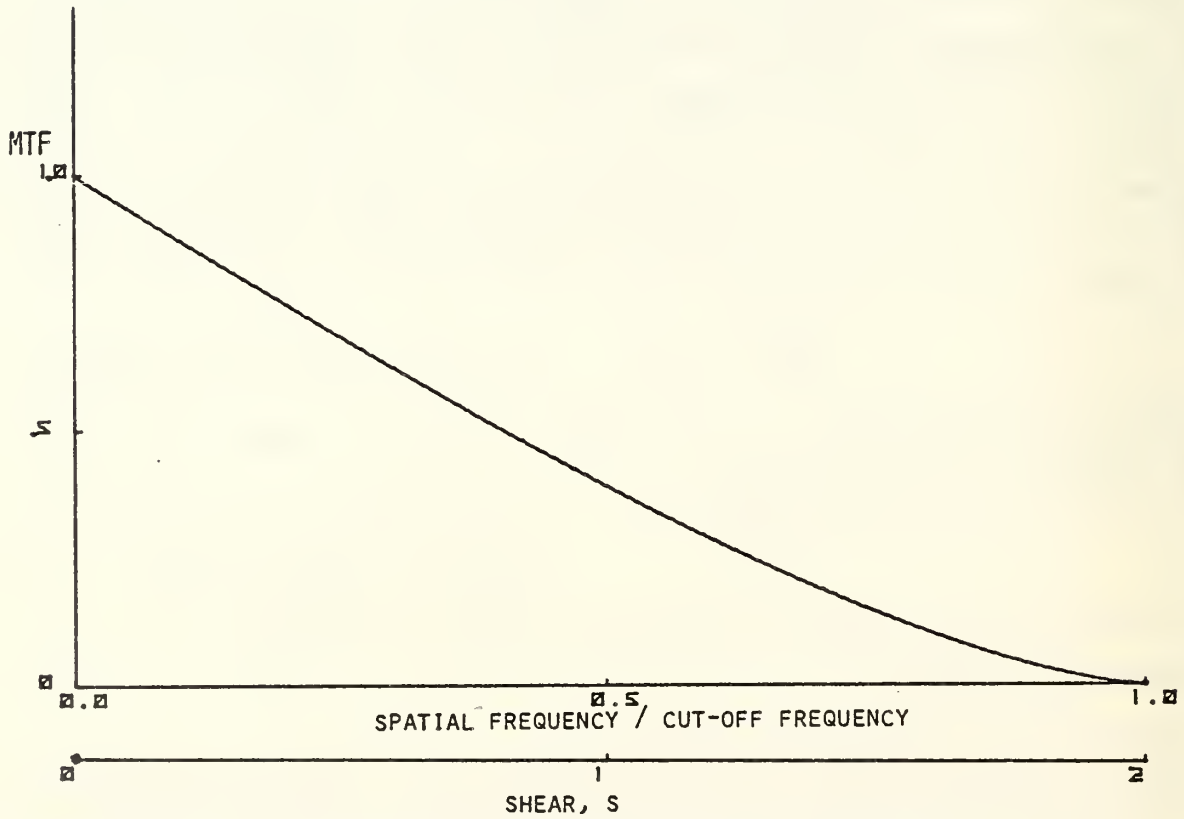

FIG. V-12. DIFFRACTION LIMITED MTF FOR UNOBSTRUCTED CIRCULAR APERTURE

$$f = (s/2) \cdot (D/\lambda)$$

For a diffraction limited system with a circular aperture, the MTF becomes:

$$(MTF) = \frac{2}{\pi}\left[\cos^{-1}\left(\frac{\nu}{\nu_c}\right) - \frac{\nu}{\nu_c}\sqrt{1 - \left(\frac{\nu}{\nu_c}\right)^2}\right]$$

Where ν_c is the diffraction limit or cut-off spatial frequency

$$\nu_c = \frac{D}{F\lambda} \qquad \text{in length}^{-1}$$

or the corresponding cut-off for angular spatial frequency:

$$f_c = D/\lambda \qquad \text{in radians}^{-1}$$

The spatial frequency scale can be expressed in terms of the shear, s, which varies from zero at the origin to 2 at the cut-off. The MTF, resulting from diffraction at a circular aperture, is plotted as a function of both spatial frequency, ν, and shear, s, in Fig. V-12.

The shearing interferometer measures MTF by physically carrying out the same general procedure as described above. The light entering the input aperture of an optical system is split into two beams of parallel light. The input light must be coherent; a laser source. Usually the optical system includes a telescope to provide a small cross-section beam for the shearing operation but permit a large input aperture. The two beams resulting from the splitting are then laterally offset relative to each other by a "shear", provided by a rotating plate or other system which can vary the offset. The two beams are then recombined to form an interference pattern, with its total intensity measured by a photo-detector. The shear is varied linearly with time by the rotating plate system. This system also varies the relative path length in the two beams linearly with time, so that the interference between the two parts of the beams which overlap varies with time. This time varying interference produces a "carrier" signal at the photocell. A band-pass frequency filter in the photocell amplifier circuit limits the system to respond only to frequencies

near this carrier frequency. The amplitude of the oscillating signal received is thus proportional to the area of overlap of the two beams where interference is producing oscillating light intensity. The dc component present from the non-overlapping area is eliminated by the band-pass filter. The envelope of the oscillating signal is then the MTF of the system, displayed in time as a function of "shear", which in turn,is proportional to the spatial frequency. The signal varies in time as shown in the sketch in Fig. V-13 . The upper boundary envelope is the MTF curve, with the zero spatial frequency point at the center of the pattern. The curve from the center to the right is the usual MTF curve. The left part of the pattern is a mirror image curve of the same MTF.

A more sophisticated approach to the theory of the instrument shows that the device indeed does measure the MTF of a telescope system. The result also includes the MTF of the atmosphere intervening between the point laser source and the telescope. The theory is given in the paper by Kelsall (1973). In brief summary, the more complete theory goes as follows.

1b. Shearing Interferometer Theory

Let A(x,y) be the amplitude of the collimated laser beam on emergence (along the z axis) from the entrance aperture of the shearing interferometer. This beam is split into two beams which are guided by reflection along separate paths inside the interferometer. The instrument recombines them so that their centers are not coincident, but are displaced laterally by a "shear distance" u. In addition, one of the beams travels farther than the other by distance δ , introducing a phase difference and facilitating a measure of the MTF, as will be explained below. The resultant combined beam is focused and the total intensity measured by a photodetector.

The amplitude of the recombined, sheared beams is

$$\frac{1}{\sqrt{2}}\left[A(x,y) + e^{-i\kappa\delta}A(x-u,y)\right] ,$$

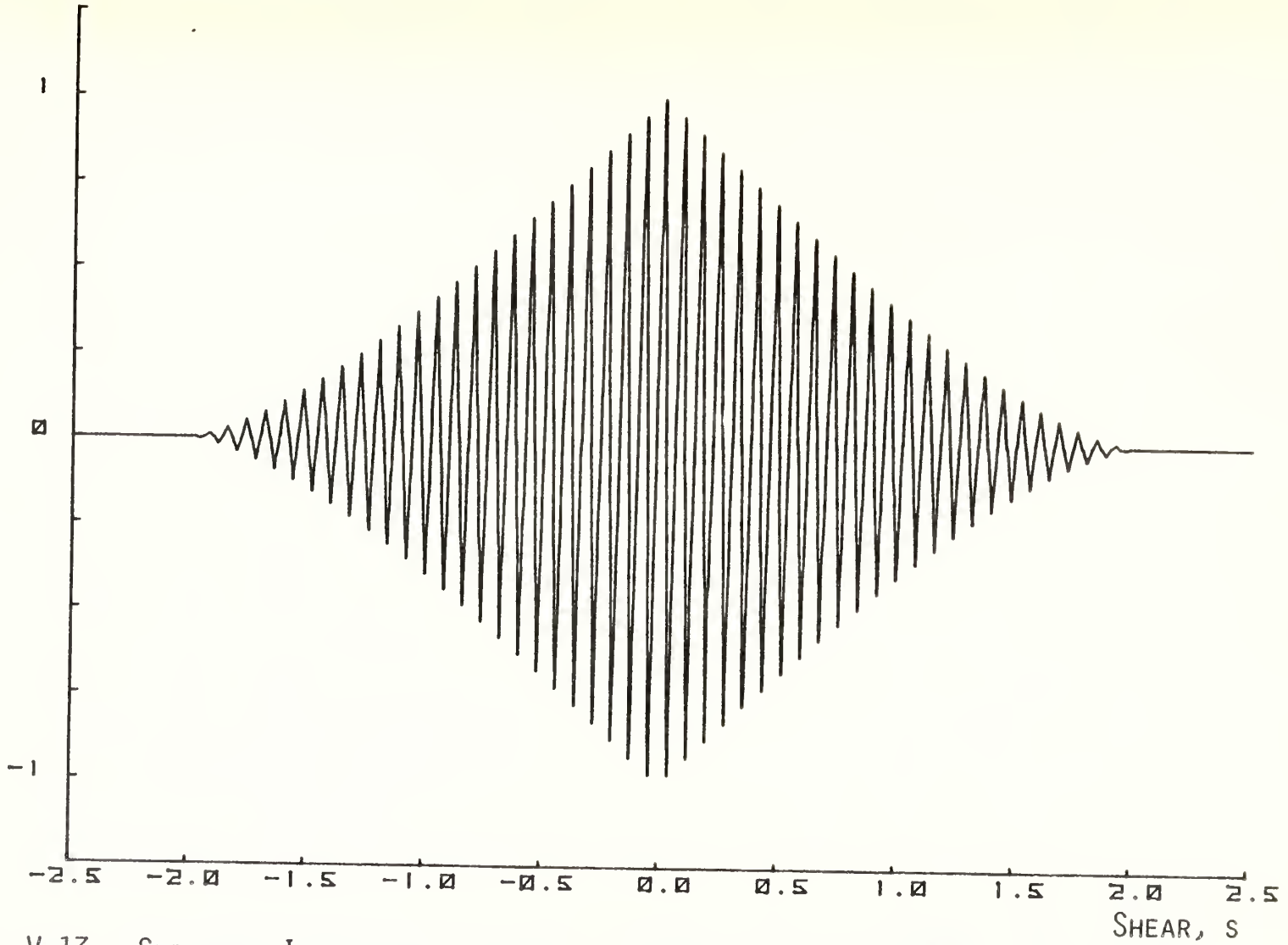

FIG. V-13. SHEARING INTEROMETER SIGNAL. THE ENVELOPE IS THE MTF. (IDEAL CASE)

where $\kappa = \frac{2\pi}{\lambda}$ is the wavenumber of the radiation. The total flux $F(\delta,y)$ in the interferogram is

$$F(\delta,u) = \tfrac{1}{2} \int d\,x\,dy \left| A(x,y) + e^{-i\kappa\delta} A(x-u,y) \right|^2 d\,x\,dy$$

which may be rewritten as

$$F(\delta,u) = \int d\,x\,dy |A(x,y)|^2 \left\{ 1 + \mathrm{Re}\left[\frac{e^{i\kappa\delta} \int d\,x\,dy\; A(x,y)\; A^*(x-u,y)}{\int d\,x\,dy |A(x,y)|^2} \right] \right.$$

where "Re" means "real part of". Apart from the phase factor $e^{i\kappa\delta}$, the expression in the square brackets is the one-dimensional pupil autocorrelation function along the shear axis. This is the complex optical transfer function (OTF), so that

$$\frac{F(\delta,u)}{F_o} = 1 + \mathrm{Re}\left[e^{i\kappa\delta} \cdot (\mathrm{OTF}) \right]$$

where $F_o = \int d\,x\,dy |A(x,y)|^2$, a constant.

Since OTF = (MTF) $\cdot$ $e^{i\psi}$,

$\frac{F(\delta,u)}{F_o} = 1 + (\mathrm{MTF}) \cdot \cos(\kappa\delta + \psi)$, where the modulation transfer function, MTF, is real.

The instrument changes δ linearly with time, giving a carrier signal of frequency $\kappa \frac{d(\delta)}{dt}$ radians/sec. The MTF forms the envelope of this oscillation and may be read off directly. The relation between the offset, u, and the spatial frequency in cycles per unit length is $\nu = \frac{u}{\lambda F}$, where F is the focal length of the primary imaging lens.

OTF Relationship to Pupil Function

If $V_o(x_o,y_o)$ is the field amplitude in the object plane of an optical system and $V_i(x_i,y_i)$ is the amplitude in the image plane, then assuming unit magnification, they are related by convolution with a "diffraction function" $h(x_i - x_o, y_i - y_o)$

according to

$$V_i(x_i,y_i) = \int V_o(x_o,y_o)h(x_i - x_o, y_i - y_o)\, dx_o dy_o$$

This function h is the response in the image plane to a point source in the object plane, and can be shown (Born and Wolf, 1970) to be the Fourier transform of the pupil function P(x',y'). Specifically,

$$h(x,y) \equiv \frac{1}{(\lambda R)^2} \int P(x',y')\, e^{i(x'x + y'y)/(\lambda R)} dx'dy' \ ,$$

where R is the image distance (also the object distance). Taking the Fourier transform of this equation yields

$$F[h] = (2\pi)^2\, P(-\mu\lambda R, -\nu\lambda R) \ ,$$

where

$$F[h] \equiv \int h(x,y)e^{i(\mu x + \nu y)} dxdy$$

If the illumination is incoherent, then the intensities in the object and image plane are related by

$$I_i(x_i,y_i) = |h|^2 * I_o(x_o,y_o) \ ,$$ where the asterisk means convolution.

Taking the Fourier transform of both sides of this equation, using the convolution theorem and denoting the spatial frequency spectrum of intensity by $\mathcal{I}(\mu,\nu)$ gives

$$\mathcal{I}_i(\mu,\nu) = F\left[|h|^2\right] \mathcal{I}_o(\mu,\nu)$$

so that $F\left[|h|^2\right]$ is the OTF for incoherent illumination. However,

$$F\left[|h(\vec{x})|^2\right] \equiv \int h(\vec{x})h^*(\vec{x})e^{i\vec{\mu}\cdot\vec{x}}\, d\vec{x} \ ,$$

where $\vec{\mu} \equiv (\mu,\nu)$ and $\vec{x} = (x,y)$.

Equivalently,

$$F\left[|h(\vec{x})|^2\right] = \int h(\vec{x})h^*(\vec{x}')e^{i\vec{\mu}\cdot\vec{x}}\delta(\vec{x}-\vec{x}')d\vec{x}'d\vec{x}$$

Using the two-dimensional delta function representation

$$\delta(\vec{x}-\vec{x}') = \left(\frac{1}{2\pi}\right)^2 \int e^{i\vec{\mu}'\cdot(\vec{x}-\vec{x}')}d\vec{\mu}'$$

gives

$$F\left[|h|^2\right] = \left(\frac{1}{2\pi}\right)^2 \int h(\vec{x})h^*(\vec{x}')e^{i\vec{\mu}\cdot\vec{x}}\, e^{i\vec{\mu}'\cdot(\vec{x}-\vec{x}')}d\vec{x}\, d\vec{x}'\, d\vec{\mu}'$$

Integrating over $\vec{x}$ first gives

$$F\left[|h|^2\right] = \int P(-\vec{\mu}R\lambda - \vec{\mu}'R\lambda)\, h^*(\vec{x}')e^{-i\vec{\mu}'\cdot\vec{x}'}\, d\vec{x}'\, d\vec{\mu}'$$

$$F\left[|h|^2\right] = (2\pi)^2 \int P(-\vec{\mu}R\lambda - \vec{\mu}'R\lambda)\, P^*(-\vec{\mu}'R\lambda)\, d\vec{\mu}'$$

$$-F\left[|h|^2\right]\frac{(R\lambda)^2}{(2\pi)^2} = \int P(\vec{\omega} - \vec{\mu}R\lambda)\, P^*(\vec{\omega})\, d\vec{\omega}\ ,$$

which is the pupil autocorrelation function for an offset $\vec{\mu}R\lambda$. The conclusion is that, except for some constant factors which get normalized away in practice, the OTF for incoherent illumination is the pupil autocorrelation function, for lateral pupil displacement vector $\vec{\mu}R\lambda$, corresponding to the spatial frequency pair $\vec{\mu} = (\mu,\nu)$.

2. Data Reduction;MTF from Shearing Interferometer vs. OTF from Slit Scanner

As discussed in Section V. B.1, the shearing interferometer yields a curve of the MTF for each repetitive cycle of the instrument. Each MTF curve is already in the form of a modulus, and is always positive. Averaging a series of these curves then gives an average instantaneous MTF. This average modulus is called the MTF, in the usage employed in the field of "speckle interferometry" (Korff, 1973). This differs from the usage of the term MTF employed elsewhere in this report (and rather generally in the field of imaging devices).

In contrast, the slit scanning imager yields a series of line-spread functions for the raw data, as described earlier. These functions are then averaged so as to yield a short exposure, image centered, average, or so as to yield a long exposure average (without centering). Each of these averages is then processed to yield an OTF of the atmosphere by taking the Fourier transform of the averaged line-spread function and dividing by the instrument function. The moduli of these OTF's are the short exposure and long exposure MTF values respectively. This meaning of the term MTF, applied either to the short exposure or long exposure case, is the term commonly used in (non-speckle) imaging work. This MTF is often called the OTF although it actually is the modulus of the average OTF. This use distinguishes this quantity from the MTF as used in the field of speckle interferometry, where the MTF means the average of successive instantaneous MTF modulus values.

In comparing the results from the slit scanner and the shearing interferometer it is the short exposure slit scanner MTF which is appropriate for comparison with the shearing interferometer result. However, the results from the two methods are not expected to be identical because the shearing interferometer averages the modulus, which is always positive. In contrast, the slit scanner does the equivalent of averaging the OTF values.

These individual OTF's are the transforms of the line-spread functions and, because individual functions are asymmetric, have both positive and negative terms in the real and imaginary parts. Some cancellation occurs in the averaging and the resulting average OTF, converted to its modulus, the MTF, will always lie below the value obtained when individual modulus curves are averaged, the latter having only positive values. Thus, the slit-scanner MTF value will lie below the shearing interferometer MTF value. The difference is meaningful and implies that speckle interferometry can extract some additional information (Korff, 1973). However, the slit-scanner MTF is the one applicable to conventional imagers.

Besides the above fundamental difference in the physical quantities measured, the two methods are not expected to yield identical results for two additional reasons: first, the instrument broadening has not been removed for the shearing interferometer, and second, the normalization used before averaging differs in the two methods.

The diffraction, aberration, and finite slit width effects are removed from the NPS slit scanner data by Fourier processing. For the shearing interferometer data, the instrument broadening was not removed by data processing. However, that equipment was essentially diffraction limited only, so that the adverse effects are not serious as long as the atmospheric degradation is large. This was the case for most of the data taken in the comparison experiment.

Looking in detail at the normalization process, the average of successive shearing interferometer MTF curves was taken by the Lincoln Laboratory group, after normalizing the zero spatial frequency point on each MTF curve to unity. This weights all MTF curves equally. This was necessary because successive shearing interferometer MTF curves differ in amplitude as a result of scintillation. This would alter the weighting of each curve

unless normalization is applied.

For the NPS slit scanning imager, the line-spread functions are not usually normalized before averaging because the results without normalizing correspond more closely to the situation encountered in the majority of practical imaging or tracking devices. However, to permit as direct comparison as possible, some of the NPS data was normalized in such a way as to correspond to the normalization used for the shearing interferometer. This involves normalizing the line-spread function curves to constant area under each curve. No significant difference resulted from this normalization, so most of the NPS line-spread data was processed without normalization in this comparison. The NPS slit scanning data can be processed in a variety of ways, and in that respect is more flexible than the shearing interferometer data.

In spite of the above differences between the slit scanner and the shearing interferometer, the two results are expected to differ only slightly, and primarily at high spatial frequencies. Although the results differ in principle, it has been useful to compare the results from the two methods, for confirmation of the general range of MTF obtained.

V. C. Scintillation Measurements of C_n^2

1. C_n^2 Data Reduction

As has been discussed in Section II, the amplitude of radiation, received at a point on an advancing wave front through the atmosphere, fluctuates in magnitude and phase. The magnitude fluctuation is called scintillation and can serve as a means for determining a particular path averaged value of C_n^2. The weighting with path position emphasizes the center region of the path and so does not yield the same average as that for MTF. Nevertheless it can serve as a means of obtaining an additional piece of information about C_n^2.

Determination of the path averaged C_n^2 involves measuring the variance, σ^2, of the fluctuation of the logarithm of the intensity of light received through a small aperture. If the aperture is other than infinitestimal, a correction is needed for "aperture averaging", i.e., the fluctuations decrease in magnitude with increasing aperture size. If the turbulence level or the range, are large, a saturation effect also occurs with the maximum value of the variance limited to about 0.6. For stronger turbulence the variance reaches about unity and then decreases. These two effects are discussed in a following section.

Measurement of the standard deviation σ of the fluctuation of log-intensity is accomplished by passing the received electrical signals, that are proportional to the intensity, through an electronic analog circuit which yields signals proportional to the logarithm of the input signal. These signals are then sampled periodically at about 4 kHz and a probability density curve obtained either in a PIP 400 nuclear pulse height analyzer, a Ubiquitous Model 202C, or in the Nicolet "LAB-80" data processor.

The optical structure constant, C_n, is obtained from this probability density distribution. This distribution has been found to be adequately described by a Gaussian shape except

perhaps under saturation conditions in storm turbulence (Elliott, 1977). For the Gaussian shape:

$$1.\quad y = \text{Const}\ e^{-(x - \bar{x})^2/2\sigma^2}$$

where:

$x = \ell n\ I$ log intensity

$\bar{x} = \overline{\ell n\ I}$ mean of log intensity

σ = standard deviation of the distribution

y = probability density

Const = $1/\sigma\sqrt{2\pi}$ if normalized

The structure constant is related to the standard deviation, range, and wavelength, (Lutomirski et al, 1973; Fried, 1967) for spherical wave fronts, by:

$$2.\quad C_N = \frac{1.420\sigma}{K^{7/12} z_o^{11/12}}$$

where:

$K = 2\pi/\lambda$

λ = wavelength in meters

z_o = range in meters

C_N = structure Const, meters$^{-1/3}$

Originally photographs were taken of the probability density display on an oscilloscope. The standard deviation σ and hence C_N were obtained by measuring the full width at half maximum (FWHM) of the distribution from these photographs.

$$3.\quad \sigma = \frac{\text{FWHM}}{2\sqrt{2\ \ell n\ 2}} = \frac{\text{FWHM}}{2.355}$$

The scale for the abscissa is determined by feeding calibration voltages of 0.5, 1.0, 2.0 and 4.0 volts into the log converter instead of the scintillation signal. This gives equally spaced lines on the probability density curve displayed on the oscilloscope. The spacing between these lines is $\ell n\ 2 = .693$.

We have more recently interfaced the probability density analyzer to a Hewlett Packard programmable calculator and plotter. The data is first plotted and then fitted by a best fit Gaussian to obtain σ. The fitting is obtained as follows. If we take the

logarithm of equation (1), we obtain

$$4.\quad \ln y = \ln C - \frac{(x - \bar{x})^2}{2\sigma^2}$$

$$5.\quad = \left(-\frac{1}{2\sigma^2}\right) x^2 + \left(\frac{\bar{x}}{\sigma}\right) x + \ln C - \frac{\bar{x}^2}{2\sigma^2}$$

$$6.\quad = ax^2 + bx + c$$

where:

$$a = -\frac{1}{2\sigma^2}, \qquad b = \frac{\bar{x}}{\sigma}, \qquad c = \ln C - \frac{\bar{x}^2}{2\sigma^2}$$

which is quadradic in x. The calculator finds ℓn y, and then fits the resulting points of ℓn y with a quadradic regression. Each point is weighted by $\sqrt{y_i}$. Sigma is calculated from the fitting constant, a, by $\sigma = \sqrt{\frac{-1}{2a}}$

A representative computer plot and fitted Gaussian is shown in Fig.V-

2. Beam forming, Chopping, and Demodulation

a. Beam forming and Chopping

In order to obtain sufficient intensity at ranges up to 20 km; it is necessary to transmit a fairly narrow laser beam. This is accomplished by means of divergence control optics placed in the beam of the laser. The light passes through a microscope lens of about 5 mm focal length, to produce a crossover. In the extinction work reported later in this report, a spatial-filter pinhole is placed at this crossover. For scintillation measurements, this pinhole has usually been omitted because strict uniformity is not as critical at the receiving telescope, and the higher intensity present without the pinhole is desirable. A chopper disk is placed in the vicinity of the crossover. This provides pulses at about 4 kHz with approximately equal on, and off, time interval. A second lens, with focal length about 7 cm, brings the rapidly diverging beam from the crossover to a beam divergence of a few milliradians. This divergence is controlled by micrometer screw motion parallel to the system axis. Two additional micrometer screws also provide for motion of the lens perpendicular to the system axis, to precisely align the beam with a finder telescope and other lasers on the same mounting platform.

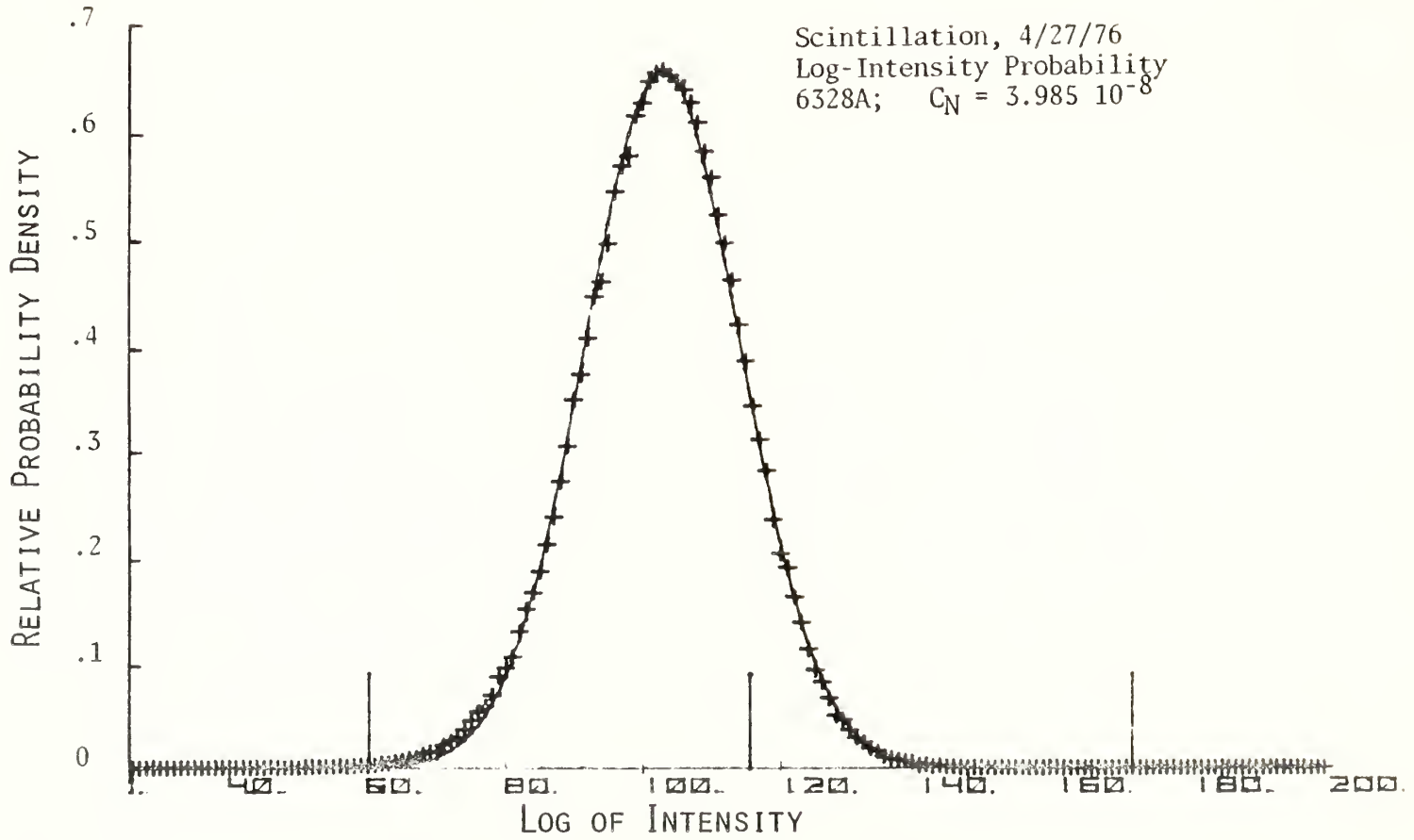

Fig. V-14. Probability Density vs Log-intensity for scintillation.

The entire platform can be moved with training and elevation screws to place the transmitted laser patterns on the receiver optics at the opposite end of the range. Four lasers are mounted on this platform. Three are chopped by a common chopper and the fourth, the CO_2 laser, is separately chopped. The laser platform is, in turn, mounted on a rigid table with legs extending through the instrument van floor to the ground, for vibration isolation.

2b. Pulsed Signal Demodulation

The arrangement used for land-to-land scintillation illustrates the main features of the circuitry. A functional diagram is shown in Fig. V-15.

The source laser is operated continuously. This is chopped by a rotating wheel at approximately 3600 Hz. The resulting light pulses have about equal time on and off. Land-to-ship measurements use the "fan-scan" chopping technique which yields a somewhat different shaped light pulse, with consequences to be discussed later in Section V. C4.

The light received at the far end of the range produces an electrical signal from a dropping resistor in series with a silicon photovoltaic/or avalanche cell, or a HgCdTe photoconductive cell for the case of 10.6 μm. The signal is fed directly to an FET source follower, reducing input circuit capacitance and serving as an impedance matcher. This drives a 50 ohm cable to a PAR 113 low noise amplifier#. This amplifier gain is set to provide output pulses no higher than 7 volts (saturates at 9 volts).

The principle functions of the "Chopper" Demodulator are indicated in Fig. V-16. The amplified pulses (a) are sampled (c) at a time near the mid-portion of their peak duration. A sample-and-hold circuit stretches out the sample peak voltage

#Model 113, Low-Noise Preamplifier manufactured by Princeton Applied Research Corporation.

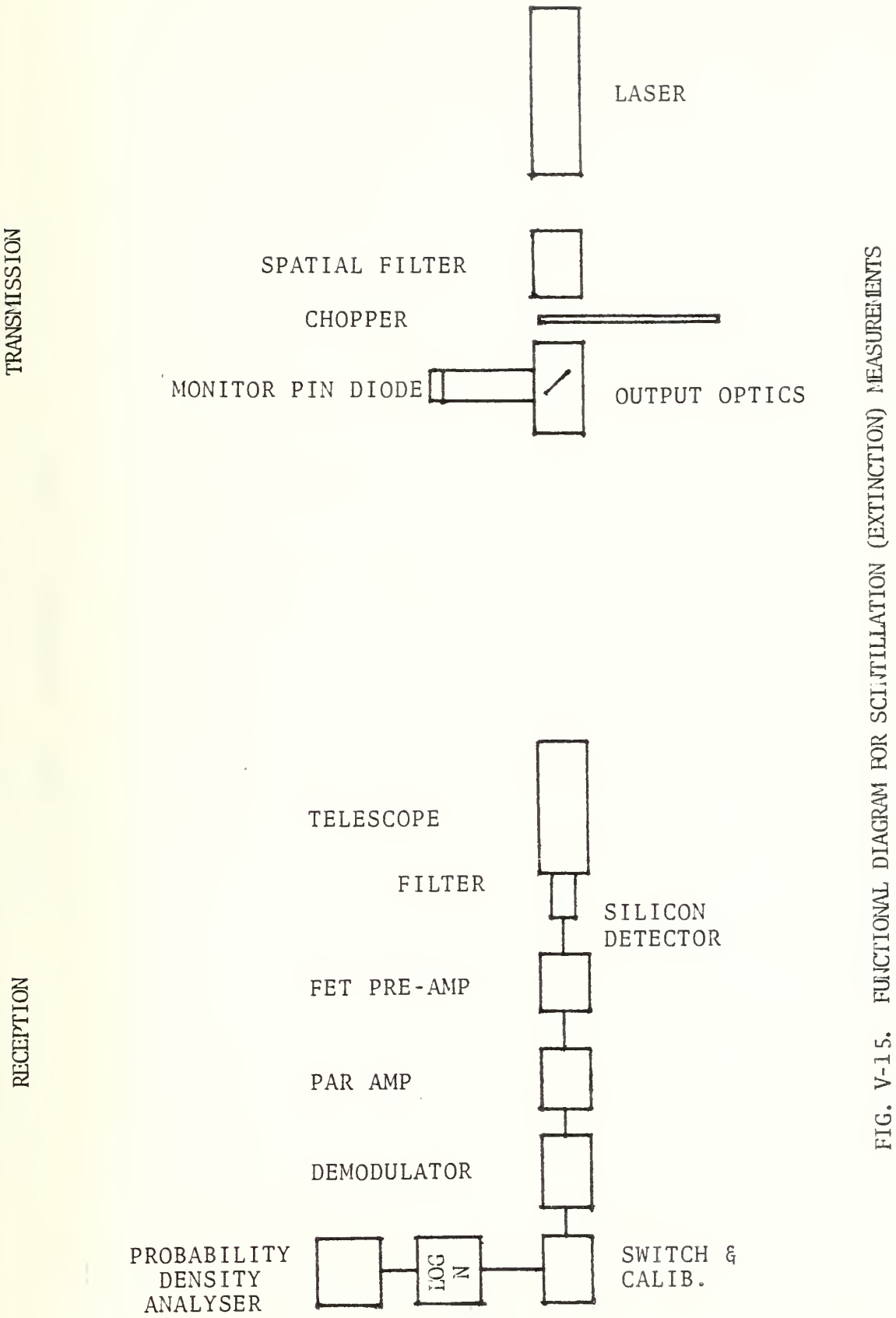

FIG. V-15. FUNCTIONAL DIAGRAM FOR SCINTILLATION (EXTINCTION) MEASUREMENTS

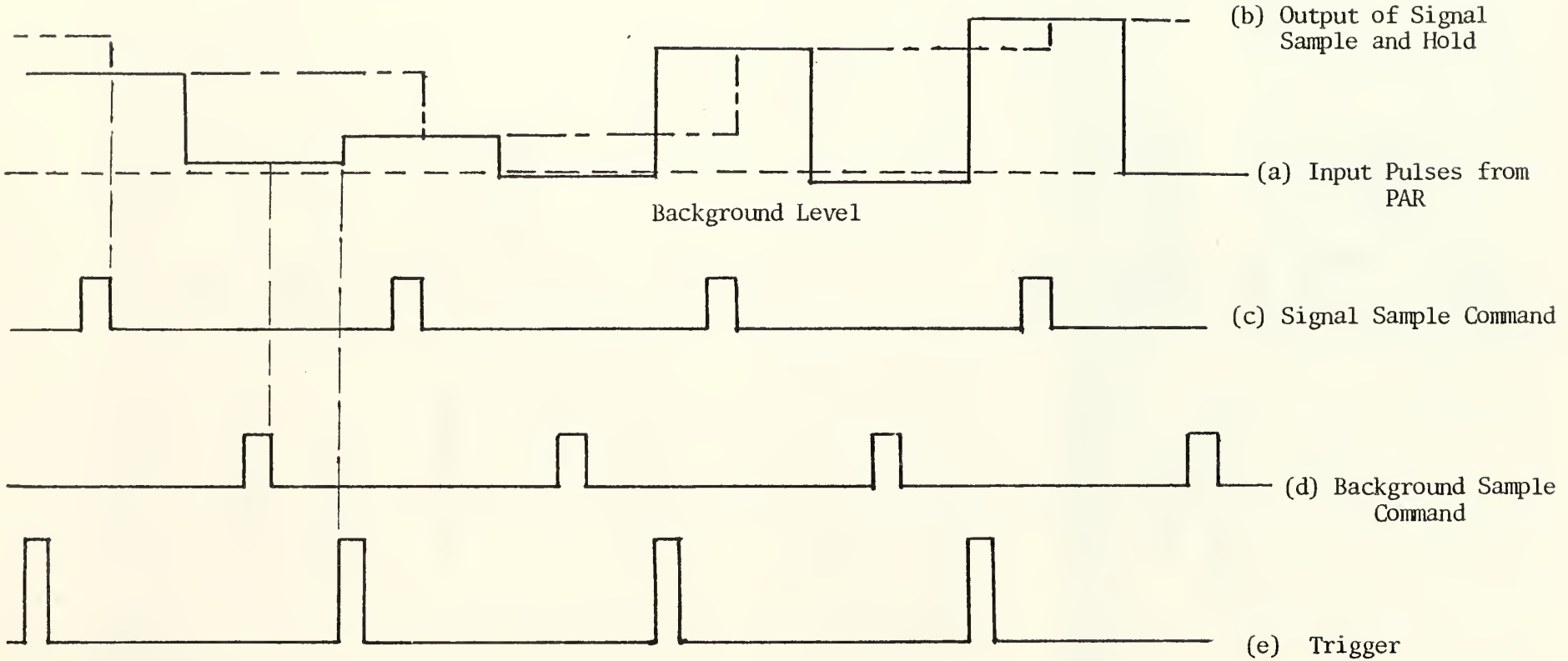
(b) Output of Signal Sample and Hold
(a) Input Pulses from PAR
Background Level
(c) Signal Sample Command
(d) Background Sample Command
(e) Trigger

FIG. V-16. "CHOPPER" DEMODULATOR WAVEFORMS

in time until the next pulse is sampled (b). For example, signal pulse #2 is sampled during sample command pulse #2. The hold operation takes place at the cessation of the command pulse.+ A similar sample-and-hold operation is carried out for the background portion of the received voltage pulse (a) and (d). The resulting sampled background voltage is then subtracted from the sampled peak pulse signal voltage by a differential instrumentation amplifier. The resulting difference in voltage is thus a measure of the intensity of the received signal relative to the no-signal condition (background). This output voltage of the demodulator thus varies from pulse to pulse resulting from the scintillation encountered by the transmitted beam. The frequency components of the "cw" constructed signal are low enough to be handled by the logarithmic converter which follows. The output of the logarithmic converter is then fed to the probability density analyzer. That circuit is triggered by pulses from the demodulator circuit to sample the logarithmic signal once for each arriving optical pulse.

2c. Demodulator Calibration

Ideally, the demodulator should provide a stretched output voltage which is exactly proportional to the peak value of the input pulse height, with no offset voltage. The above requirements are satisfactorally met by the circuitry we have been using and the performance is checked by the following procedures:

Each demodulator is provided with a separate pulse generator whose pulses reasonably approximate those to be demodulated for the experiments, both in shape and in timing. These calibration pulses of constant peak height are accurately attenuated with a ten-turn helipot. For calibration, the attenuated pulses are switched to the input of the demodulator, and the demodulator

---

+The trigger pulse (e) is generated from the leading edge of the input pulse by several stages of amplification with FET amplifiers. This pulse is then used to generate the two sample command pulses shown. Their time delays relative to the trigger are adjustable to conform to the time widths of the on-off portions of the transmitted signals.

output is read with a digital voltmeter to the nearest 10 mv. A plot of the demodulator output versus the attenuator dial-setting is constructed. In Fig. V-17, such a plot is shown for the fan-scan demodulator. A log-log plot of the data used in the above figure indicates a departure from the straight-line fit of about 10 mv, when the output voltage is as low as 0.1 volt.

The linearity and offset of the helipot itself is iniitally checked using a constant d.c. voltage across the helipot. Any bias in the demodulator circuit is removed by bias adjustments in the instrument-amplifier output of the demodulator. For the monitor demodulator, bias is removed by adjustment of the input clamp voltage.

2d. Log-converter and Probability Density Analyzer Calibration

The log-converter and probability density analyzer are calibrated by applying known d.c. voltages at the input of the log-converter. These are manually switched and held on for sufficient time for the probability analyzer to build up a spike corresponding to each applied voltage. Ordinarily, voltages increasing by a factor of two for each step-increase are applied by preset voltage dividers.

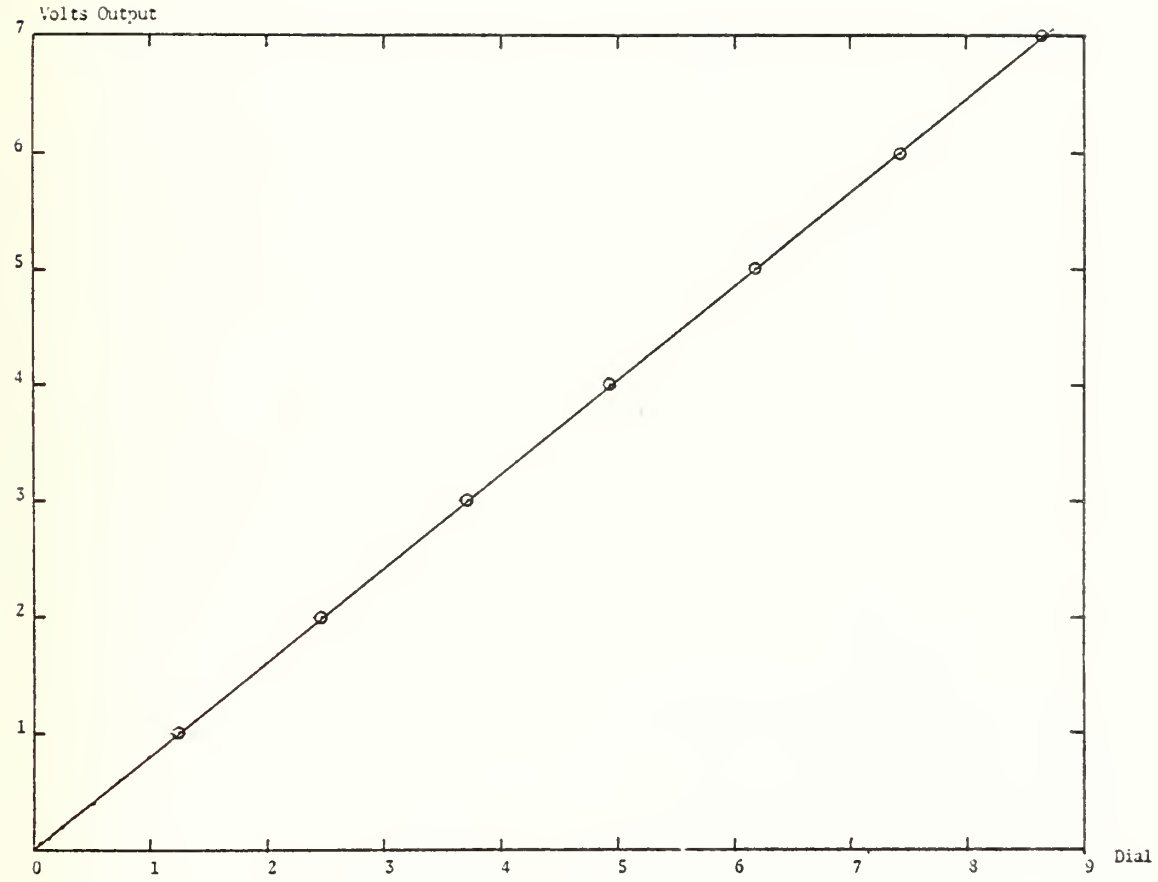

FIG.V-17. DEMODULATOR CALIBRATION CURVE

V. C 3. Gyro Stabilized Shipboard Optical Platform

Use of the ACANIA as one end of the optical path required development and construction of a gyro-stabilized platform and tracking system. At the outset it seemed that a stable platform would be available by conversion from other Navy use. A number of possible alternatives were pursued but were not practical without large conversion expense. As a result, a system was developed at NPS. A number of progressively improved systems were developed and utilized. The present system is capable of stabilizing optical systems up to about 20 kg in mass and providing stability to a few hundred microradians for ship roll up to $\pm$ 30°.

The system utilizes a 20 kg rotor at 3600 rpm, mounted in 2 axis gimbals which have a vertical axis and an axis perpendicular to the light beam. Torques to precess the gyro are applied by two-phase 60 Hz brushless ball bearing torque motors. Drum and wire couplings provide smooth, nearly frictionless, torque with 10:1 mechanical advantage. One winding of each of the AC motors is provided with a fixed 60 Hz amplitude and phase. The second (quadrature) winding is provided with a 60 Hz signal at 90° phase. The amplitude is capable of varying through zero. The signal is generated by an analog error signal computer.

The gyro optical system tracks a chopped 0.6328 μm laser beacon located onshore. The optical system is shown in Fig. V-18. The light from the beacon onshore is reflected at mirror A to be parallel to the gyro vertical gimbal axis. That mirror is rotated with the gyro head, about the vertical gimbal axis, but is driven at a ratio 1:2 for rotation of the gyro head about the horizontal gimbal axis (perpendicular to the page, in the figure). The outgoing laser beams transmitted from ship-to-shore also reflect from mirror A. This causes most errors in misalignment in the system to be cancelled. After reflection from mirror A, the incoming light from the beacon onshore then reflects in mirror B, which is fixed in the ship's frame of reference. The outgoing laser beams pass through a hole in the center of mirror B.

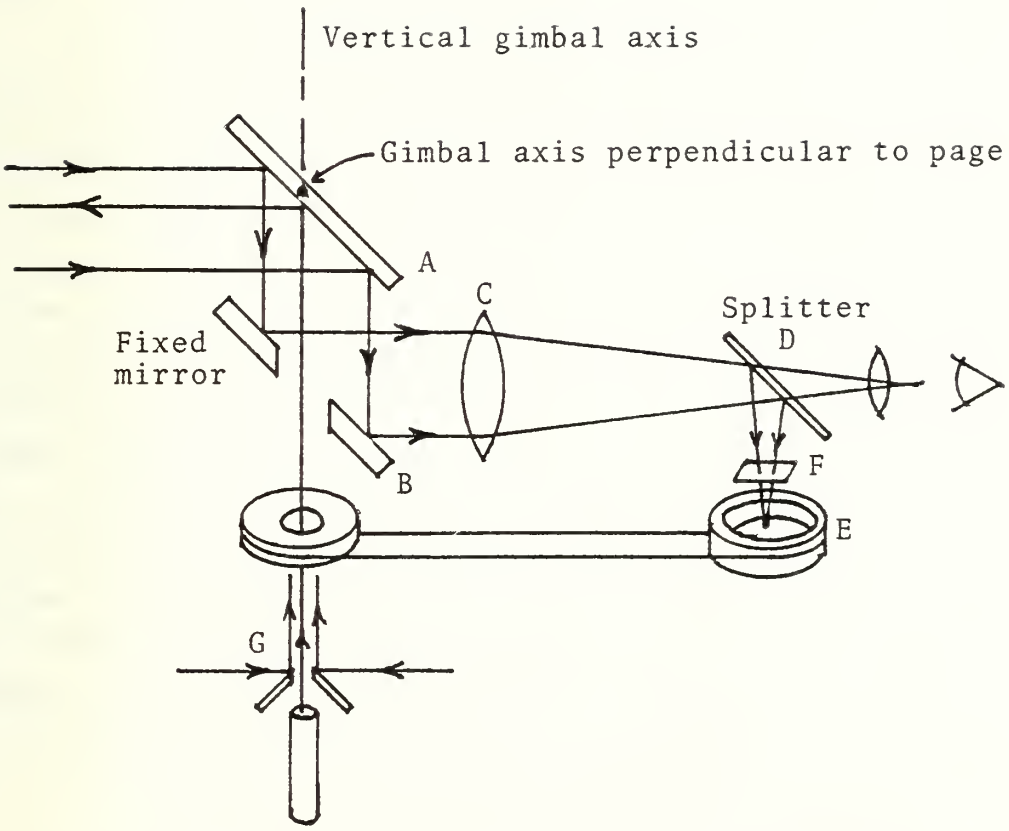

Fig. V-18. Optical tracking system for gyro-platform.

The incoming beacon light then is focused by a lens C and reflected in the splitter mirror, D, onto a quadrant photocell at E. This photocell is mounted in bearings and driven by a wire drum coupling to rotate 1:1 with the motion of the gyro system about the vertical gimbal axis. This motion is necessary to preserve proper orientation of the detector for up-down and right-left gimbal deflections. The splitter D allows about 1% of the light to be viewed through the eyepiece, for alignment. Rough tracking during approach to lock-on is done by a separate finder telescope mounted on the gyro rotor frame. An interference filter passing .6328 μm is provided at F to reduce background signal.

Three outgoing laser beams of different wave lengths are rendered parallel and close together by the two mirrors at G. They are separated by a few mm. Use of mirror A for both outgoing laser and returning beacon beams makes the system almost independent of misalignment. As long as the vertical beams are parallel, other alignments are very non-critical.

The analog error signal circuit is utilized for control. Each quadrant photocell signal and the sum of all quadrants is amplified and rectified. The right-left difference signal and the up-down difference signal are then each divided by the sum signal from all four quadrants, to cancel scintillation effects. The scintillation-corrected right-left and up-down signals are utilized as proportional error signals to correct the gyro position. The up-down and right-left signals are also differentiated and added through a variable attenuator to the error signals for the quadrants at 90°, to produce damping. The output of the adders are power amplified and used to drive the two-phase torque motor power driver circuits. A joy-stick control adds a signal to allow manual control in the approach to lock-on. When the lock-on occurs, the beacon spot is located within the center third of the finder scope field.

The optical receiver telescopes are normally mounted on

top of the gyro frame, with counterweights below. A photo of the system is shown in Fig. V-19. In use, the complete unit is ordinarily covered with a 7'x7'x6' high aluminum shed, on the boat deck of the ACANIA. This provides for a 90° swing of the optical beam. The shed is manually rotated when large shifts in ship orientation require it. An operator is required to recapture lock-on, if the beam is interrupted for more than a few seconds.

The receiver and transmitter apertures are located approximately 15 ft. from the undisturbed water surface. The equipment for data processing the receiver signals is located in the "dry lab" immediately below the boat deck. Received detection signals, other than the tracking signals, are amplified to one volt level to reduce pick-up noise before transmission via coax cable, to the data processing equipment below.

4. Ship-Motion Problems

a) Fan Scan System

Determination of C_n from log intensity fluctuation depends on maintenance of a constant input intensity. For data taken with one path-end on shipboard, the ship motion becomes a problem. For a CW or a chopped beam, a slight motion of the beam relative to the receiver moves the Gaussian beam cross-section relative to the receiver, modulating the received intensity. A number of tests were made utilizing the gyro platform and tracking beam. However, motion was still a problem and the apparent C_n^2 was increased by the motion. The problem has been solved by going to a different chopping method. In this method the beam profile is spread into a horizontal fan, with vertical width 1/3 to 1/10 of the horizontal spread. This beam is then oscillated in the vertical direction across the receiver at a frequency of about 2500 Hz. The receiver detects a series of peaks. Vertical motion of the ship changes the relative timing of the peaks but the detector always passes through the peak intensity. The horizontal motion of the ship is usually less than the vertical motion. The

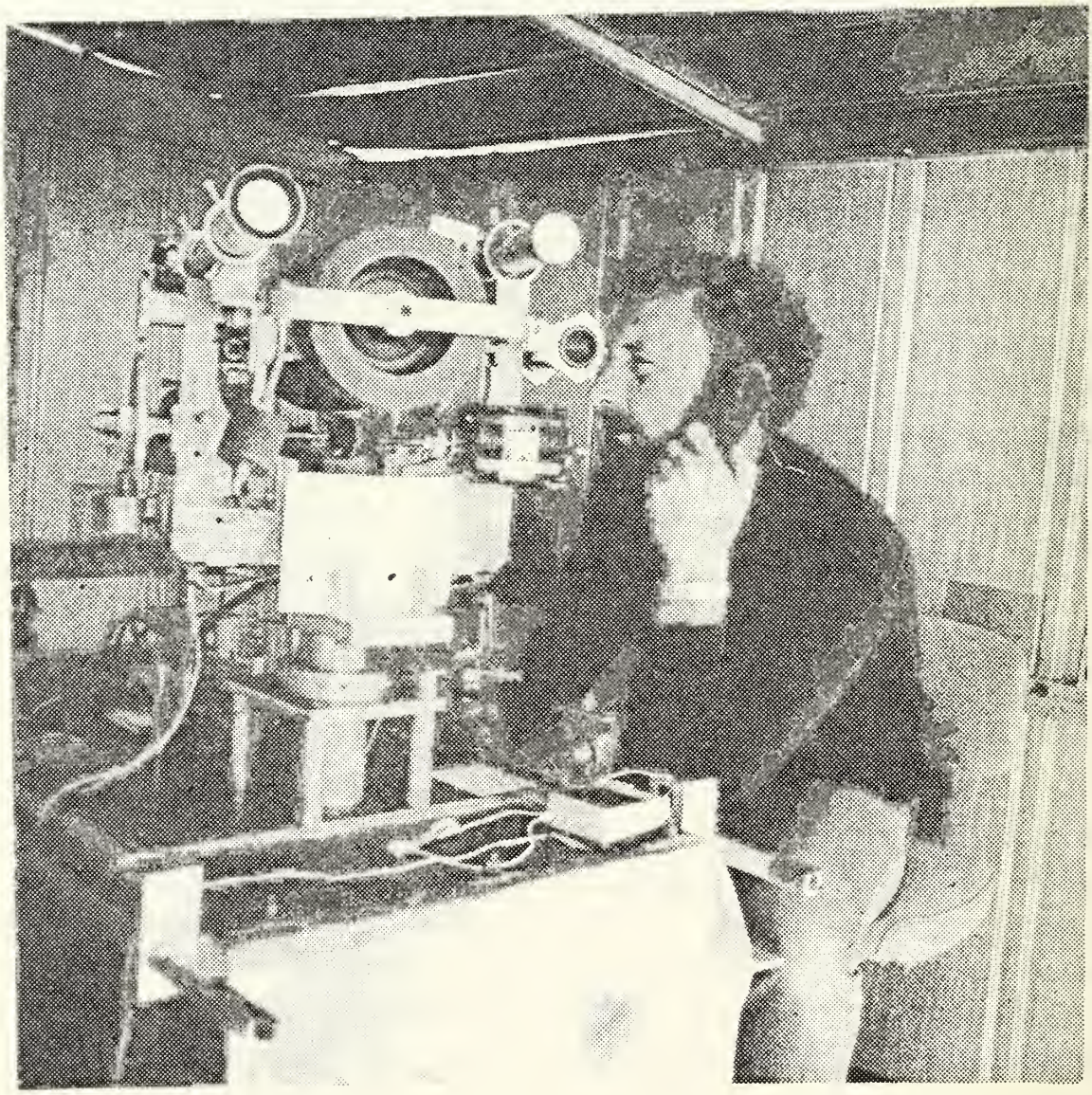

Fig. V-19. Gyro System.

horizontal beam width is 5 to 10 times wider than formerly with non-fanned beams so that the effects of horizontal motion are essentially eliminated. The 2500 Hz frequency provides 5000 samples per second, fast enough to "freeze" the turbulence.

The optical system is shown in Fig. V-20. Beams from two (or more) lasers are reflected to closely spaced parallel paths by the mirrorsat A. These beams strike a deformable cylindrical mirror at B. This consists of a front surface aluminized microscope cover slide, bent by a pad pressed by a micrometer screw against the back. The screw allows changing the horizontal width of the beam. Each of the three beams falls on the cylindrical axis of the deformable mirror. After that reflection, the beams then are reflected by an oscillating mirror, to move perpendicular to their wide beam pattern.

b) Fan Scan Demodulation

The land-based fan-scanned beam is detected on shipboard by gyro-mounted receivers. The detected pulses are approximately Gaussian in shape and have a time duration of the order of 40 μsec. The optics and circuitry for the receiving end is functionally the same as the chopped-beam system described above. The principal difference lies in the demodulator. This demodulator is referred to as the "fan-scan" demodulator. The output pulse from the PAR is fed into a peak detector circuit. The output of the peak detector is a pulse which follows the input pulse up to its peak value. The peak value is then held (stretched) for a predetermined time which is of the order of half the total time between successive pulses. The stretched pulse is fed into the sample-and-hold circuit, just as with the chopped beam circuitry. All other aspects of the demodulator circuitry are similar to the chopped beam case, including the formation of the main trigger pulse at the beginning of the received pulse. The controllable stretch time used with the peak detector is also initiated by the trigger pulse.

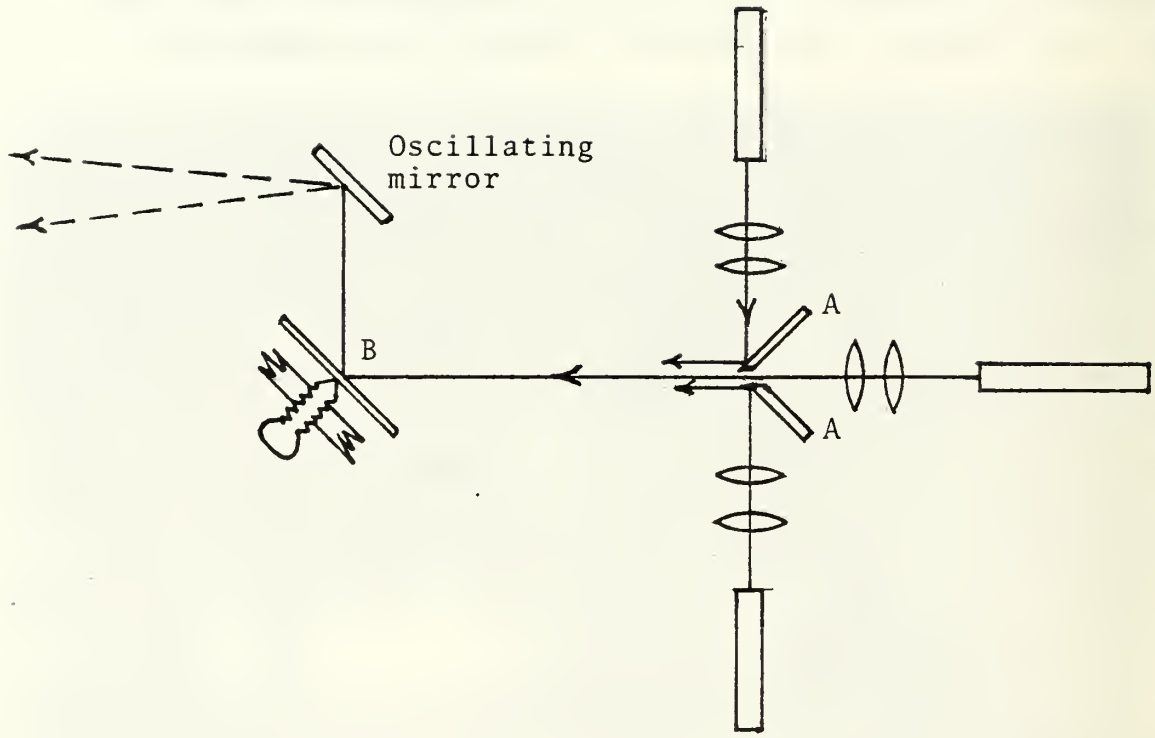

FIG. V-20. "FAN-SCAN" TRANSMITTER OPTICAL SYSTEM.

5. Aperture Averaging and Saturation

The optical turbulence structure parameter C_n^2 is often inferred from measurements of the local irradiance reaching a detector from a distant laser source, using the theoretical relationship given in Section III, relating the log-intensity (or log-amplitude) of the received signal to the wavelength, to the range, and to C_n^2, assumed to be constant along the propagation path. The theoretical relationships hold for a spherical wave (similar relationships are available for plane waves), a path length sufficiently short that the variance, σ^2, is below the critical value of 0.6 for the onset of saturation, and for a point detector. It has been long recognized that the variance will be modified by an aperture of finite size; the imaging of the received wave onto a small detector integrates the wave over the aperture of the receiving optics, obliterating the effects of spatial fluctuations of scale less than the receiver diameter. Since scintillation measurements frequently accompany optical measurements of other kinds, it is frequently desirable to use common input optics, which may be large compared to the spatial scales of interest in scintillation. In this case a correction should be made to the measured C_n^2 to reduce the value obtained with a finite aperture to that appropriate to an infinitely small detector.

The temporal irradiance fluctuations are related (by the Taylor Hypothesis) to the spatial irradiance fluctuations, which are described by the transverse correlation length ρ_ℓ. This quantity is a function of path length and wavelength. With a detector of finite diameter D the variance of log-amplitude σ_s^2 observed will vary with the ratio D/ρ_ℓ. For $D/\rho_\ell > 1$ the fluctuations at different parts of the aperture will tend to be uncorrelated, and some cancellation will occur. In this case the measured log-intensity variance will be less than that for an ideal point detector by a factor

$$A = \frac{\sigma_s^2}{\sigma_{so}^2}$$

which is then the necessary correction for C_n^2. Theoretical studies have thus far been unable to provide a readily applicable form for this correction factor. Lutomirski and Yura (73) have given the expression

$$A = \left(\frac{4}{\pi D^2}\right)^2 \frac{C_I(|\underline{P}_1 - \underline{P}_2|)d^2\underline{P}_1 d^2\underline{P}_2}{C_I(o)}$$

where $C_I(\rho)$ is the irradiance covariance, which reaches the limiting values of A = 1 (no aperture averaging effect) for $\rho >> D$, and $A \simeq 4(\rho_\ell/D)^2$ for $\rho_\ell << D$. For small scintillation in homogeneous turbulence the correlation length can be written $\rho_\ell \simeq (Z/k)^{\frac{1}{2}} = .399\ (\lambda z)^{\frac{1}{2}}$. For intermediate values $\rho_\ell \simeq D$, calculation of A requires a knowledge of $C_I(\rho)$, which is not usually available. Lutomirski and Yura recommend use of a semi-empirical form

$$A = \frac{1}{1 + (D/2\rho_\ell)^2}$$

for this range. Fried (Fried, 67-1) has calculated an aperture averaging factor of the same form, in terms of the log-amplitude covariance and the log-amplitude variance, and has used available experimental data to tabulate it as a function of log-amplitude variance and normalized aperture diameter, for infinite plane wave propagation. This correction has been applied in a number of experiments in the literature, but checks of its validity have shown very mixed success. A direct determination of the aperture correction factor and a comparison with the Fried value was carried out under the conditions of the NPS experiments.

The quantity to be measured was the log-intensity variance as a function of detector aperture diameter. Tests were carried out over two time periods; first in 1974 with the equipment in use at that time for CW measurement of scintillation, and again in 1975/76 using the chopped-beam mode of measurement developed for use with the fan-scan system described above. In the 1974 experiment background compensation was provided by a second detector assembly mounted at an angular offset slightly greater

than the angular acceptance of the detector. Each detector was a UDT PIN-10 photodiode with collecting lens, defining aperture and field lens, to minimize fluctuations due to image wander over the detector surface. The technique developed for determination of the aperture averaging correction factor for this equipment was applied to the chopped-beam system. Except where otherwise specified, the remainder of this section will refer to the chopped beam equipment.

To compensate for changes in the atmospheric conditions during the period of the data collection, a fixed aperture reference detector was used in close proximity to the variable aperture detector. The reference detector was a UDT PIN-5DP photodiode with one inch collecting optics. The variable aperture detector was a TI SL69 silicon avalanche photodetector, whose high sensitivity allowed measurement down to very small apertures. Each detector system was fitted with collecting optics and field lens. The 4.9 cm diameter objective of the variable detector was preceded by an interference filter and an 18 leaf iris adjustable from 1.5 to 42 mm. A 5mW He/Ne laser operated in the fan-scan mode described in Section V. C 4 was used as source, and the log-intensity variance obtained with the PIP pulse height analyzer and HP-9810 calculator which prints out the values of the variance, C_n and C_n^2. For shipboard use the receiver was mounted on the gyrostabilized platform. The experimentation involved accumulation of the log-intensity probability density distributions for the signal and reference detectors averaged over the same time interval. Ideally, each variable aperture measurement should be compared with that of a "point" detector. In fact the reference detector must have aperture large enough to maintain a satisfactory signal to noise ratio. Experience in the early measurements and verified with the later equipment indicated that the variance σ_{sD}^2 did not approach an asymptotic value as D became small, but either passed through a minimum or displayed erratic behavior below a critical diameter. To determine the detector size best approximating the

"point detector", several series of measurements were made with decreasing variable aperture referred to a standard fixed aperture detector.

At each measurement time a determination was made of the value of C_n^2 obtained with the test detector at aperture D, and with the reference detector at aperture D_o. The quantity G(D) was then defined to refer the results to the same detector at the same time.

We define $C_n\left[V,(D,t)\right]$ as the value of C_n measured with the variable aperture detector V at time t, and $C_n\left[F,(D_o,t_o)\right]$ as the value from the Fixed detector with aperture D_o at time t_o; then the quantity G(D) is defined as

$$G(D) = \frac{C_n\left[V\ (D_o,t)\right]}{C_n\left[V\ (D,t)\right]}$$

the ratio of simultaneous measurements with the same detector. This can be computed from the measured quantities as follows:

$$G(D) = \frac{C_n\left[V\ (D_o,t)\right]}{C_n\left[V\ (D,t)\right]} = \frac{C_n\left[V\ (D_o,t_o)\right]}{C_n\left[F\ (D_o,t_o)\right]} \cdot \frac{C_n\left[F\ (D_o,t)\right]}{C_n\left[V\ (D,t)\right]}$$

For each measurement series the G(D) factor was normalized to the largest diameter used, and plotted against diameter normalized to $(z/k)^{\frac{1}{2}}$, the approximate expression for ρ_e used by Lutomirski and Yura. The value of aperture diameter best approximating the "vanishingly small detector" was chosen as the minimum of the curve, or the break point in the absence of a minimum. A correction factor equivalent to the Fried factor or A defined above was then computed as

$$\frac{\sigma_s^2}{\sigma_{so}^2} = \text{Ⓗ} = A = \left[\frac{G(D)}{\{G(D)\}_{min}}\right]^2$$

As pointed out in Section II, the theoretical expression for irradiance log-amplitude variance in terms of wavelength, path length and structure parameter is valid only for small fluctuations such that $\sigma^2 \lesssim .64$. Kerr (Kerr, 1972) has shown that the onset of saturation and the maximum saturated variance of the log amplitude are independent of wavelength. Above the onset of saturation the variance reaches a flat maximum value, and then decreases under conditions of supersaturation. As no adequate theoretical description of the saturation regime exists, determination of C_n by scintillation becomes impossible at the onset of saturation. In fact values of log-intensity standard deviation as low as 0.3 have been reported in the supersaturated regime. For this reason care must be taken in the interpretation of scintillation measurements. The table below shows the critical range at which saturation will invalidate scintillation measurements of C_n^2, evaluated for the laser wavelengths used in the NPS experiments, under conditions of "typical" turbulence at $C_n = 5 \times 10^{-8}\ m^{-1/3}$ and high turbulence with $C_n = 20 \times 10^{-8}\ m^{-1/3}$.

Table V-C-1. Range for Saturation of Scintillation

	Range at indicated λ			
C_n ($m^{-1/3}$)	λ = .4880 μm	λ = .6328 μm	λ = 1.06 μm	λ = 10.6 μm
$5\ 10^{-8}$	$3.19\ 10^3$m	$3.78\ 10^3$m	$5.25\ 10^3$m	$22.7\ 10^3$m
$20\ 10^{-8}$	706.8 m	833.8 m	$1.15\ 10^3$m	$4.99\ 10^3$m

From this table it can be seen that scintillation at visible wavelengths is a viable technique to ranges of about 3 to 4 kilometers under normal to light turbulence conditions. For operation over longer paths over the sea, as for example, in combination with MTF measurements, it has been necessary to operate at infrared wavelengths.

D. Extinction

1. Alignment, Monitoring, Detection, and Calibration

Measurement of extinction can be accomplished by either of two general methods. In one, a beam of radiation is transmitted and the entire beam captured by a receiving optical system. This system requires rather large optical systems for transmission and reception over long paths. It is also vulnerable to deflection of the optical beam out of the receiver system by beam wander due to turbulence, or beam displacement due to long term atmospheric refraction from vertical temperature gradients. The alternative system involves transmission of a divergent beam, with sufficiently broad a pattern at the receiver that the receiver optics lie within an essentially uniform intensity region at the center of the pattern. The intensity in such a beam decreases as the square of the distance from the source, provided that it is at a distance large compared to the Rayleigh range, and that the distance is measured from the apparent "crossover" of the divergent beam leaving the transmitter. This latter system has been used for measurements reported here.

The transmitter system is shown in Fig. V-21. The laser beam emitted from the source laser is converged with a short-focus lens to a crossover. A pinhole sufficient to include most of the Gaussian beam profile is located at this crossover. It is provided with lateral motion adjustments as well as adjustment parallel to the beam axis, in order to locate the pinhole at the beam crossover. A rotating chopper disc just beyond the crossover chops the beam at about 4 kHz. The beam diverges beyond the crossover through a small-angle prism used as a splitter. The light reflected from the splitter falls on a photocell to monitor the transmitted beam. The deflected beam has the same lateral cross-section distribution of light intensity as the transmitted beam. A prism is used as the splitter to avoid problems with interference between the light reflected from the front and back face of the splitter. The splitter prism is adjustable in rotation in two directions, in order to locate the beam center on

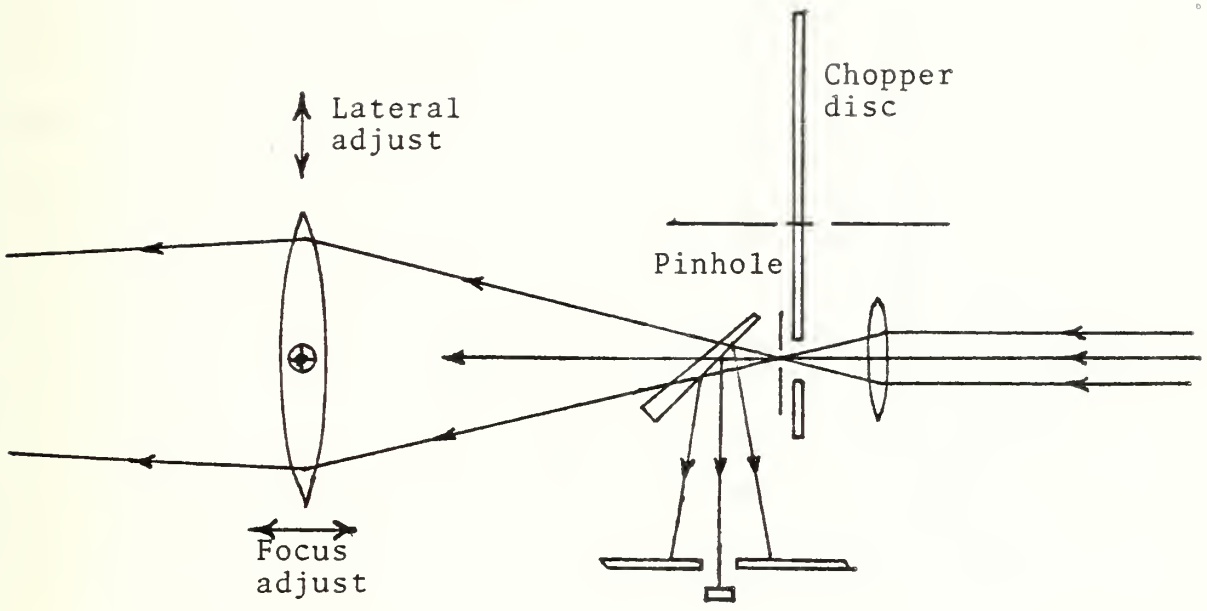

FIG. V-21. TRANSMISSION AND MONITORING SYSTEM FOR EXTINCTION.

the monitoring photocell. The light transmitted through the splitter prism falls on a lens to render the beam nearly parallel. The position of this lens is adjustable in distance from the crossover and its lateral position is adjustable in the other two directions. All of these motions are provided with micrometer screws so that the position can be accurately reproduced. The motion parallel to the axis controls the divergence of the beam. The beam is diverged by converging to a second crossover in front of the transmitting system. The position of this crossover is measured carefully during calibration since the inverse square law decrease in intensity is determined by the distance from this crossover. The lateral motions of the lens control the direction of transmission of the beam.

The system is calibrated on a precisely measured range length, between two buildings on the NPS grounds. The ratio of intensity received by the receiver to that measured by the monitor is utilized in the calibration. Both signals have been chopped by the same chopper and have the same beam cross-sectional profile. The center of the monitor beam is located by rocking the splitter mirror in both directions to find the maximum intensity as measured by the monitor. In the data reported here, the center of the transmitted beam at the distant receiver was located by displacing the transmitting lens in the two lateral directions to locate the center of the transmitted pattern. To accomplish this, the received signal is demodulated at the distant receiver and used to frequency modulate an audible signal which is then transmitted by the intercom radio to the operator at the transmitter end of the optical path. This permits the operator to adjust the lateral motion screws by direct audible feedback. In practice, scintillation of the light beam often makes adjustment difficult.

Modifications are in progress to improve the ability to locate the center of the transmitted beam at the distant receiver. The new system uses a counter-rotating optical wedge-scanning

system to deflect the transmitted beam sinusoidally in time through a small angle, at a rate of about 20 Hz. A trigger signal is telemetered to the receiving end at the beginning of each half scan cycle. The received optical signal is displayed on an oscilloscope with sweep initiated by the trigger. The sweeps in opposite directions are displayed in terms of the time since the trigger pulse for each direction. When the beam is centered, the two displayed cross-sectional intensities coincide. Scintillation causes these to vary in amplitude but not in time, so the centering can be accomplished in spite of scintillation. This system gives a quick check of centering and provides for precise readjustment when needed. Guidance to the operator at the source end is relayed by voice from the receiver end. The scanner is provided with a quick rotation capability to shift it from up-down scan to right-left scan. Removal of the scan device also does not deflect the optical beam, so the same test scanner can be used, when needed, for each of the visible and near IR lasers.

The receiving system consists of a 10" diameter Dall-Kirkham telescope focal length imaging directly onto a detector. The system is provided with a splitter to separate the middle and far IR, from the visible and near IR. However, the middle and far IR sources are not yet in operation. At present the detector is a GE silicon avalanche multiplier detector with a diameter of mm. This detector is operated at an internal gain of 50. Uniformity over the active area was measured and found to be constant within 2%. The receiver is equipped with a rapid-change filter system to sequentially utilize four different interference filters, to match the transmitting lasers. The filters used are 1.06 μm, .4880 μm, and .6328 μm. The fourth filter space is open. The detector and amplifier chain are calibrated and checked during a data sequence, by comparison with the signal provided by illumination of the detector within the detector head by a GaAs LED, operated on a pulsed signal at the same pulse rate and shape as the chopped signal from the distant

sources. The output of the LED and the sensitivity of the Si avalanche detector are temperature sensitive, so the detector head is thermally insulated and held at constant temperature by thermostatic control. The pulse current to the LED is measured digitally and regulated to be held constant. The signal amplifier chain gain is then adjusted to be constant, although the observed gain, if different, can be inserted into the calculation of extinction.

In switching from one wavelength to another, the general range of signal in the amplifier and demodulator is held within a predetermined range by switching the input resistor at the photocell.

2. Signal Demodulation

The receiving-end circuitry for extinction measurements is identical with that used for scintillation measurements with the chopped beam.

On the transmitting end, the chopped beam is partially reflected by a small angle prism onto a photovoltaic silicon pin diode, as described in detail earlier in this report. The resulting voltage pulse, which appears across a temperature insensitive resistor, is amplified by a PAR 113 amplifier to no greater than 7 volts peak value. This pulse is then fed into a simplified demodulator circuit. This circuit dispenses with the sample-and-hold circuit such as used on the receiving-end circuitry. Instead, the input pulses are capacitatively coupled to the input of the signal sample-and-hold circuit. The above input is diode-clamped to a small adjustable bias voltage which effectively clamps the background portion of the pulse to ground. The demodulated signal obtained is the "monitor" signal for the amplitude of the transmitted optical signal. For the red 0.6328 μm laser, which is very stable, the monitor output is read on a digital voltmeter to the nearest 10 millivolts out of about 7 volts. For the less stable lasers, the 0.4880 μm and the 1.06 μm,

the mean monitor output is determined by a probability density analyzer determination of the mean signal, with circuitry similar to that at the receiving-end of the optical path. Measurement of the monitor signals are made over the same time interval in which the received signal is measured at the far end of the optical path.

3. Data Reduction

Measurement of the absolute light intensity at the receiver is complicated by the scintillation caused by atmospheric turbulence. However, the same system, that is used to determine the standard deviation of the log intensity fluctuation for scintillation, can be utilized to obtain the mean intensity. The probability density curve for the logarithm of the intensity is obtained in the same manner as for scintillation and the data reduced as before. The process of obtaining the best fit Gaussian distribution not only yields the standard deviation, sigma, but also the mean of the logarithm of the intensity, $\overline{\ln I}$. In Section V. C 1, the quadratic regression coefficients, a and b are given by:

$$a = -1/2\sigma^2 \qquad \text{and} \quad b = \bar{x}/\sigma$$

so:
$$\bar{x} = b\sqrt{-1/2a}$$

where
$$\bar{x} = \overline{\ln I}$$

The quantity $\overline{\ln I}$, the mean value of ln I, is not the same quantity as $\bar{I}$, the mean of the linear intensity values. The latter is needed for extinction calculation. It is obtained from $\overline{\ln I}$ by the expression:

$$\bar{I} = \exp\left(\overline{\ln I} + \sigma^2/2\right)$$

Measurement of the extinction coefficient for the atmosphere over a long path requires a calibration of the same system over a short path, to determine the constants of the system. The intensity at the far end of a range of length z_o is such that

$$I z_o^2 = ST = S e^{-\mu z_o}$$

where z_o is the range, measured from the transmitting source laser beam crossover, T is the transmission coefficient of the atmosphere, S is the source brightness and μ is the extinction coefficient of the atmosphere.

For a calibration range, z_c, much shorter than the long range, z_o

$$I_c z_c^2 = S e^{-\mu z_c} \cong S$$

provided the calibration range conditions are such that the extinction coefficient μ is small, so that $\mu z_c \cong 0$.
Then

$$T = \frac{I z_o^2}{I_c z_c^2} = e^{-\mu z_o}$$

Calling $I_o = I_c z_c^2 / z_o^2$

Then: $T = I/I_o = e^{-\mu z_o}$

and: $\mu = -(\ln T)/z_o$

Since the observed intensities during calibration and during field measurements are drastically different, the system has to be calibrated with very different gain values. In order to make these changes in gain with precision, the bulk of the gain change is accomplished by changing the input dropping resistance which generates the signal from the photocell current. This also keeps the potential difference at the cell constant and avoids nonlinearities in the photocell. The primary input resistors were calibrated on precision circuits and their values, R_c, during calibration and R, during the field measurement, entered into the following expression:

$$T = \frac{I}{I_o} = (Sig/Mon_s) \cdot (Mon_c/Cal) \cdot (LED_c/LED_s) \cdot (R_o/R) \cdot (z_o/z_c)$$

Sig. is the magnitude of $\bar{I}$ from the data reduction unit.

Cal. is the similar signal at the receiver during calibration.

Mon_s is the source monitor signal during extinction measurement.

Mon_c is the source monitor signal during calibration.

LED_s is the signal measured in the field through the complete detection data reduction system, for the LED light input.

LED_c is the signal measured similarly during calibration.

R is the primary signal dropping resistance during measurement.

R_o is the primary signal dropping resistance during calibration.

z_o is the range from the crossover during measurements.

z_c is the range from the crossover during calibration.

The value of T is then converted to a value of μ by means of

$$\mu = - (\ln T)/z_o$$

For the red, 0.6328 μm, laser, the monitor signal is steady enough that no difficulty is experienced in reading the demodulated signal visually on a digital voltmeter. For the blue, 0.4880 μm and the IR, 1.06 μm, lasers, the source output intensity fluctuates. For these lasers the mean source intensity (Values of Mon_c and Mon_s) are determined by operating a probability density data reduction unit at the source, identical to that used at the receiver. The assumption that the source fluctuation is Gaussian seems justified in terms of the fit to the ideal Guassian curve that is observed.

4. Subtraction of Absorption

a. General

Measurement of extinction as described in the preceding section determines the absorption coefficient for total light loss from the laser beam. The parameter of interest in

this work is the light loss due to fog or aerosol scattering. For wavelengths larger than about one micron, molecular absorption begins to be appreciable and must be subtracted from the measured total attentuation coefficient. The molecular absorption is quite well known for much of the wavelength spectrum of interest, and the data is available in the form of the McClatchey code. (McClatchey,1973; 1977)

b. McClatchey Code

The McClatchey code is a computer program to calculate optical extinction in the atmosphere due to molecular absorption. This calculation rests on the detailed molecular energy-level structure as described below. It may be used in either of two ways: (1) high resolution, including the case of an essentially monochromatic laser or (2) low resolution for application to broadband radiation, obtained by averaging over a specified range of wavelengths.

The data for this calculation is an exhaustive collection (on tape) of over 100,000 line tabulations, each entry containing the frequency, intensity, half width, energy of the lower state of the transition, vibrational and rotational identifications of the upper and lower energy states, isotopic identification, and molecular identification. We have acquired the computer code and the data-base for use on the NPGS IBM 360, Model 67 computer system.

To use the program, we specify the wavelength, pressure, temperature, and molecular abundance (in molecules/cm^2) of each of the species responsible for absorption: CO_2, N_2O, CO, CH_4, O_2, O_3, and H_2O. The program responds with the appropriate transmittance. It does not include the effect of either molecular scattering or the absorption or scattering by aerosols. If L is the path length and τ is the calculated transmittance, then the extinction due to molecular absorption is $\mu_m = \frac{1}{L} \ln \frac{1}{\tau}$. The data base covers absorption in the range just below 1 μm to 100 μm.

5. Prediction of Extinction from Nephelometer Data

A nephelometer measures the distribution of aerosol drop sizes. Assuming a known complex-valued refractive index for the aerosol material, a straightforward calculation gives the aerosol extinction coefficient μ_a. The total extinction coefficient is the sum of μ_a and the molecular extinction coefficient, μ_m, which is calculated from Rayleigh scattering theory in the visible, and from Rayleigh scattering plus the McClatchey molecular absorption code in the infrared. Calculations of the expected extinction will be made for each wavelength utilized for the fog/aerosol spectrum during extinction runs in FY78. Similar calculations were made by NOSC for data taken in the run test run during FY77.

6. Nephelometer Measurements

Determination of the fog/aerosol particle size spectrum is planned for fiscal 78. This will be carried out at the time of extinction measurements, by the fog group at NPS. Two Knollenberg nephelometers have been acquired and are being put into service. (Type ASAS, 0.15 to 3 μm, and type CSAS, 0.5 to 20 μm; Knollenberg, 1976).

Joint work has also been carried out with NOSC, San Diego, in which an aircraft from NOSC, equipped with Knollenbergs was flown along the optical path from Pt. Pinos to Marina, across Monterey Bay, to sample the particle size spectrum at the same

time that extinction was measured along the same general path. This test run is reported in the results Section, VI. C. Similar runs are also planned for fiscal 78, as well as a run in the vicinity of San NIcolas Island as part of the CEWCOM 78 program.

E. DF Laser

In the time period 1974 - 75 a major sponsor-required objective of the NPS program was the verification of the wavelength variation of MTF, with particular interest in the MTF at CO_2 and DF laser wavelengths. To further this objective development of a small DF laser system was initiated. To satisfy the requirements for MTF measurements, the laser was to be CW, have stable output intensity and wavelength, and be operable at safe radiation levels at the receiver end over land-land and sea-land paths of a few kilometers. As no DF laser was commercially available, development of a suitable laser head was constracted to the Aerospace Corporation, with the system to be completed at NPS. Total system development was carried out in the time period June 1975 to June 1977.

The NPS DF laser is a small scale CW flowing gas electric discharge chemical laser. The active molecule, which may be either deuterium fluoride or hydrogen fluoride, is produced by injection of either deuterium or hydrogen into a rapid but subsonic gas flow containing atomic fluorine. Due to the rapid relaxation of the excited molecules, the active region extends for only a few millimeters downstream from the injection point. The location and width of the lasing region are determined by the flow speed and the inlet partial pressures of the fuel and diluent gases. The laser is in its conception, a low cost laboratory-type of CW laser producing on the order of one watt output power spread over a number of discrete wavelengths, or the order of 100 milliwatts with careful selection of a single molecular (vibration-rotation) transition. The input gas consists of a mixture of sulphur hexafluoride with helium and oxygen. This mixture flows axially through a high density electrical

discharge, in which the helium is ionized to maintain the discharge, and the sulphur hexafluoride (SF_6) is dissociated by electron impact to provide free fluorine. This excitation mechanism involves storage and the transport of gases which are not especially toxic or hazardous. The laser optical cavity, the discharge channel, the associated ballast resistor and the gas mixing and flow controls are mounted on and under a wheeled table approximately three by two feet by thirty inches high, weighing not more than one hundred pounds. The laser beam leaves this system directly through a partially transmissive resonator window in multiline operation, or by off-axis reflection from an intra-resonator diffraction grating in single line operation.

The electrical power input of 350 mA at 17.5 kV is provided by a Hipotronics 20 kV 500 mA laboratory power supply; cooling is provided with a closed cycle distilled water flow of 500 gallons per hour. The required gas through-put is obtained with a Kinney KDH-130 pump throttled to 40 liters/sec. Safety regulations require the removal from the effluent gas of the noxious products of reaction of the SF_6, O_2, and D_2; this is accomplished with a soda lime trap before the pump, backed up by the pump oil. For safety reasons, the laser system has been assembled in a roof-top room with outside access. From this location the beam can be directed to the Coast Guard Wharf in Monterey while satisfying eye and chemical safety regulations around the transmitter. The laser has been operated single-line and multiline with both DF and HF.

Optimized multiline HF output to date is 6.5 watts, 85% reflectance output mirror. Singleline HF operation using a diffraction grating as output reflector allowed tuning over fifteen lines from 2.6 μm to 3.0 μm, with line powers from 90 to 600 watts. Multiline DF operation gave an optimized 2.5 watt output.

In DF, singleline operation allowed tuning over eighteen

lines between 3.55 μm and 4.05 μm, with a maximum power of 240 m Watts, and a best operation at 3.8007 of 160 m Watts.

Changing mode of operation, for example from multiline DF to singleline DF requires interchanging optical elements within the laser cavity, requiring a major realignment of the cavity optics. This is a laboratory operation, not practical under field conditions.

The laser as it now operates is suitable for MTF measurement from land-to-land, or, with sufficient mounting effort, from ship-to-land. It is not suitable for extinction or pulse mode scintillation.

VI. Results

A. MTF

1. Curve Shape

a. General

As discussed previously in section V.A.1 the MTF can be expressed as a function of angular frequency, f, in terms of the Fried expression (Fried, 1966):

$$M = \exp\{-21.49\, C_n^2\, z_o\, f^{5/3}\, \lambda^{-1/3}[1 - \alpha\, (\frac{f\lambda}{D})^{1/3}]\}$$

where

M = MTF
z_o = range
f = angular spatial frequency
α = 1 for short term, near field.
λ = wavelength
D = aperture diameter
α = 0 for longterm

This expression predicts the shape for both the long exposure MTF and the average short exposure MTF, with alpha equal to zero, or unity respectively.

1b. Long Exposure MTF

A set of long exposure MTF curves are shown in Figs. VI-A-1 to VI-A-4. Each of these is for a different wavelength from 0.4880 to 10.6 μm as indicated. The points are the actual data points and the solid curve is plotted using the Fried model, with alpha equal to zero. For each curve, the known wavelength and range have been utilized in the calculation. The value of C_n has been used as a fitting parameter, with a best fit calculation made for each point. The average of these C_n values has been used to plot the curve and that value used as a measure of C_n as described in detail in section VI A.2 . Several hundred such curves are also shown in the data compendium in Appendix B. These long exposure MTF curves, although simpler than the short exposure to obtain, are subject to the possibility of additional broadening, if there is some accidental motion of the receiving optics, or if there is some motion of the source. The data can be obtained only for land-to-land measurements

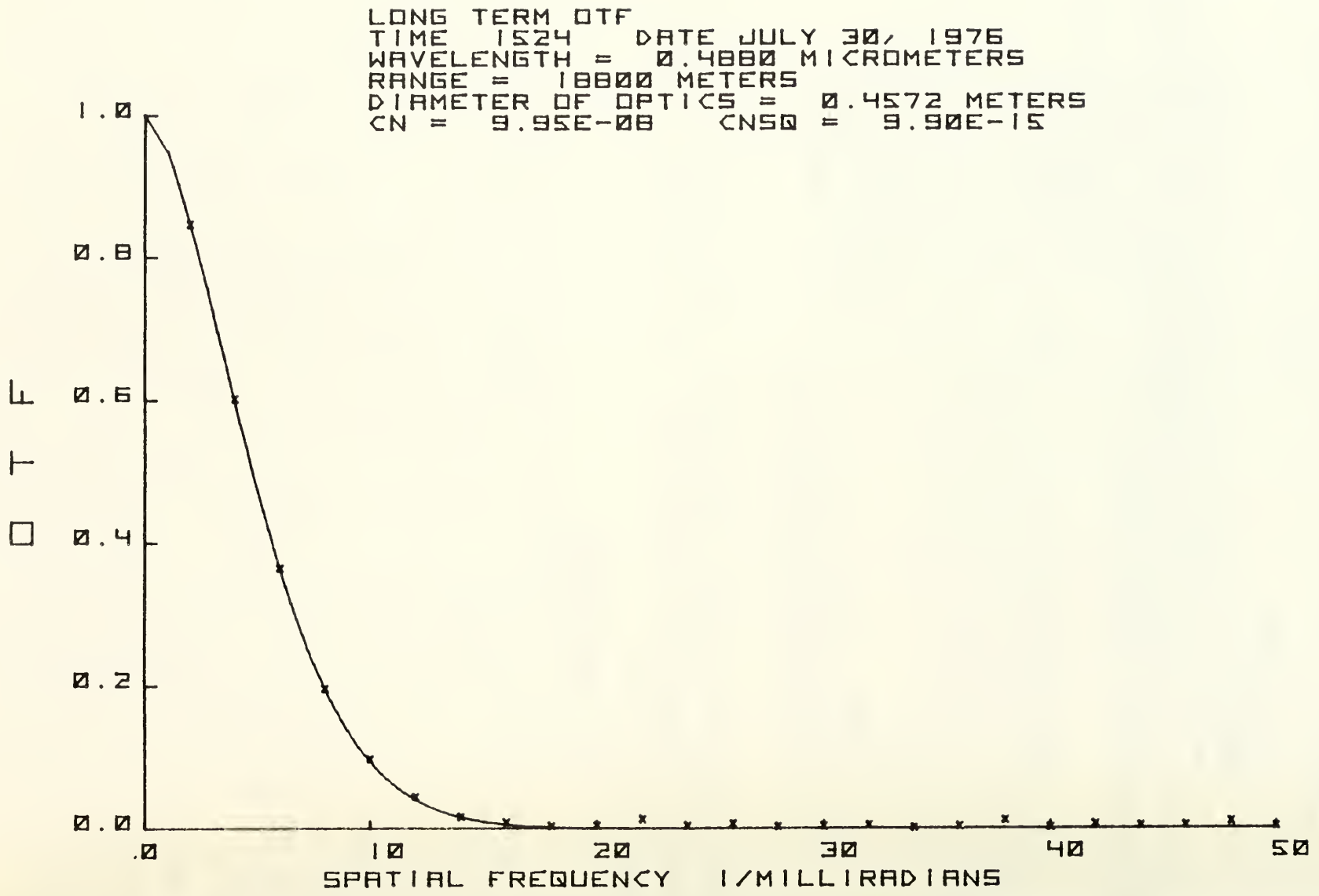

FIG. VI-A-1. OTF OF THE ATMOSPHERE

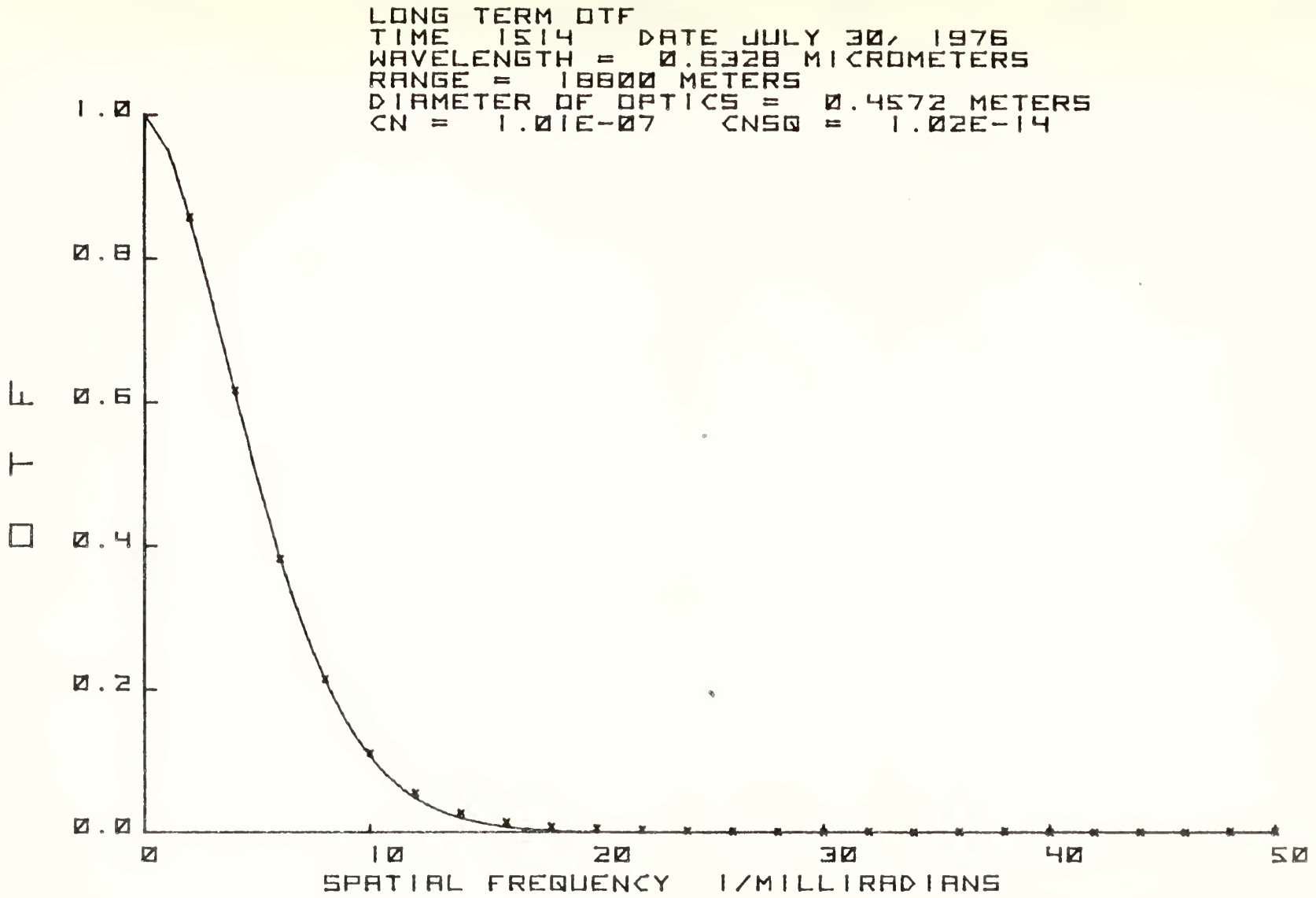

FIG. VI-A-2. OTF OF THE ATMOSPHERE

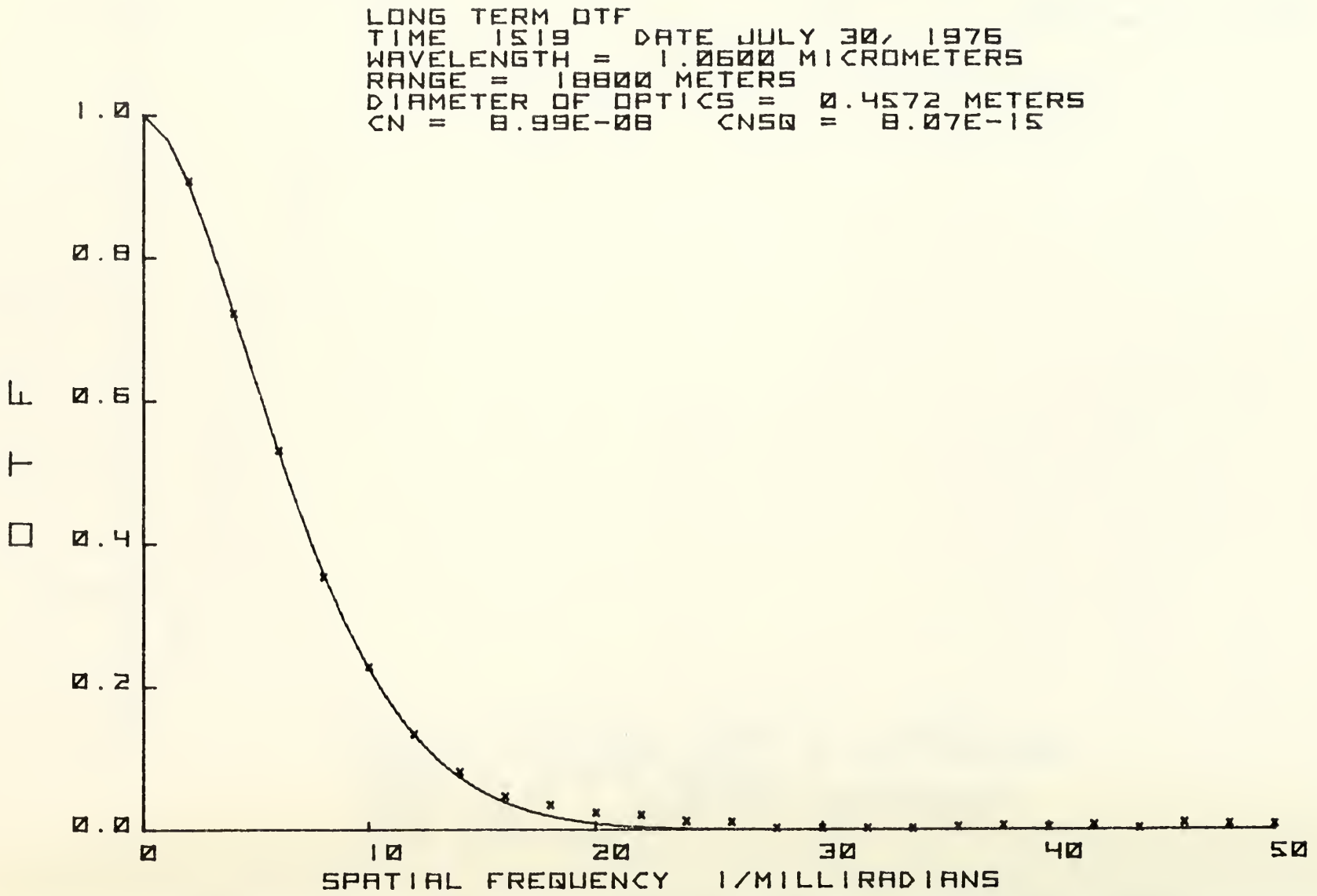

FIG. VI-A-3. OTF OF THE ATMOSPHERE

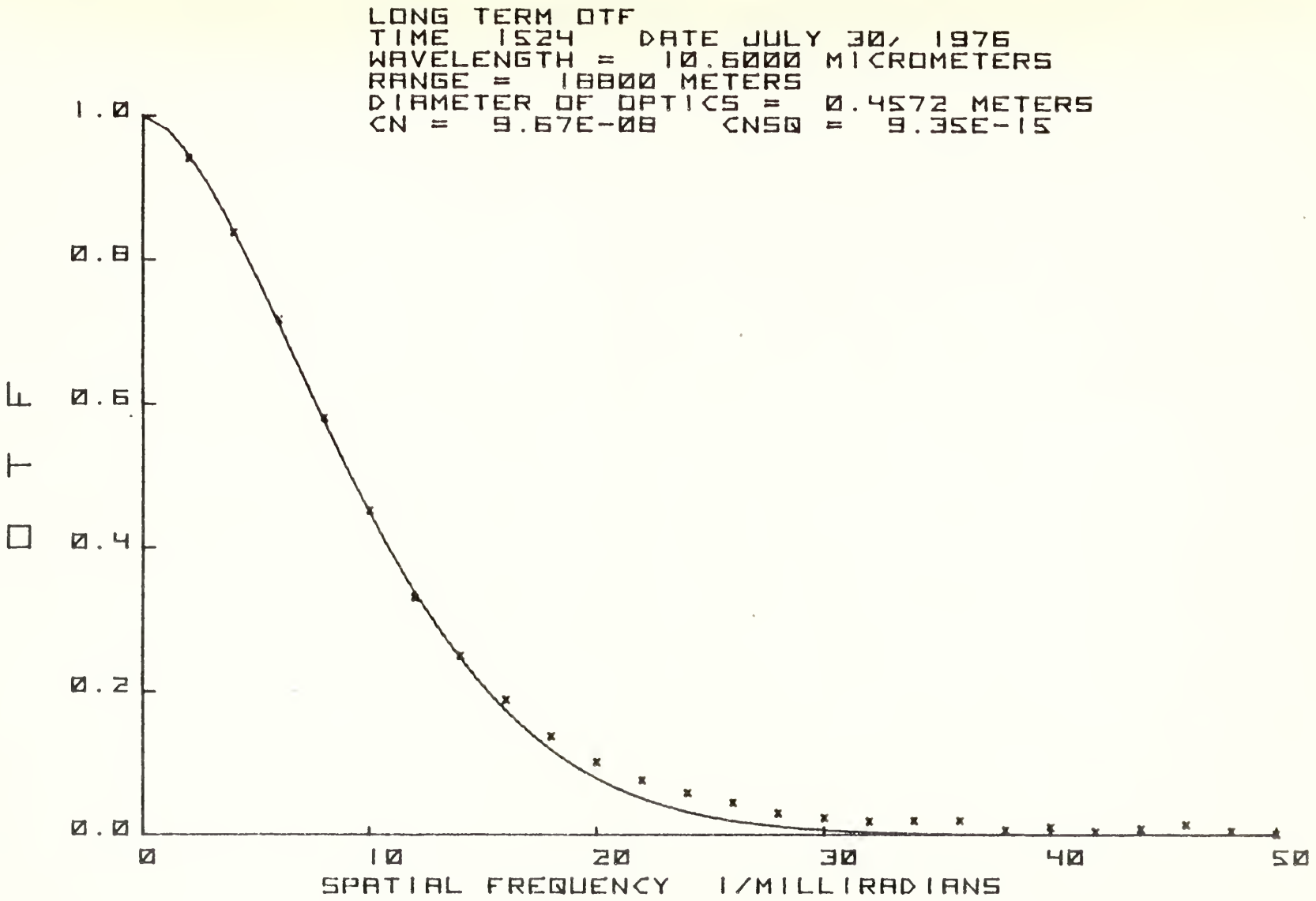

FIG. VI-A-4. OTF OF THE ATMOSPHERE

because the instability of sources or receivers on shipboard preclude making such measurements. Even for land-to-land, some difficulty is experienced when the wind is from such a direction as to blow slightly into the optical path opening in the instrument vehicle. The turbulence in the opening can cause intermittent forces on the telescope. The resulting telescope motion though small, is large enough to increase the image wander and broaden the long term line-spread function, leading to reduced MTF. As a result the long term MTF will tend to fall slightly on the low side of the true MTF. The main result of this is primarily to slightly increase the value of C_n deduced from the MTF.

Disturbance to the telescope due to a sudden jar from contact of personnel in the instrument van with the telescope is detectable in the frequency spectrum of the wander displacements. Under such conditions the natural frequency of vibration of the telescope support structure shows up strongly at about 9 Hz. Data showing this effect has been discarded. (See section V-A-1.)

The fit of the data to the Fried model curves in Figs. VI-A-1 to VI-A-4 and in the data compendium, is excellent. These curves indicate that the Fried model is adequate to express the MTF behavior for the long-exposure case.

1c. Average Short Exposure MTF

A set of average short exposure MTF curves is shown in Figs. VI-A-5 to VI-A-8 for four different wavelengths. These are the short exposure MTF curves obtained from the same primary data as for the long exposure curves of Figs. VI-A-1 to VI-A-4. Additional curves appear in the data compendium, Appendix B.

The Fried theoretical model for the short exposure case predicts a higher MTF at all spatial frequencies than for the long exposure. After the initial decrease in MTF with frequency at low frequencies, the model predicts a minimum in the MTF, followed by a rise in MTF at high spatial frequencies as the diffraction limit is approached at $f = f_o = D/\lambda$. The theoretical curve does not include direct effects of diffraction, but it is valid only up to the diffraction limit, beyond which no experimental information can be obtained in any case. The shape of the MTF curve depends on the value of the parameter, α, as well

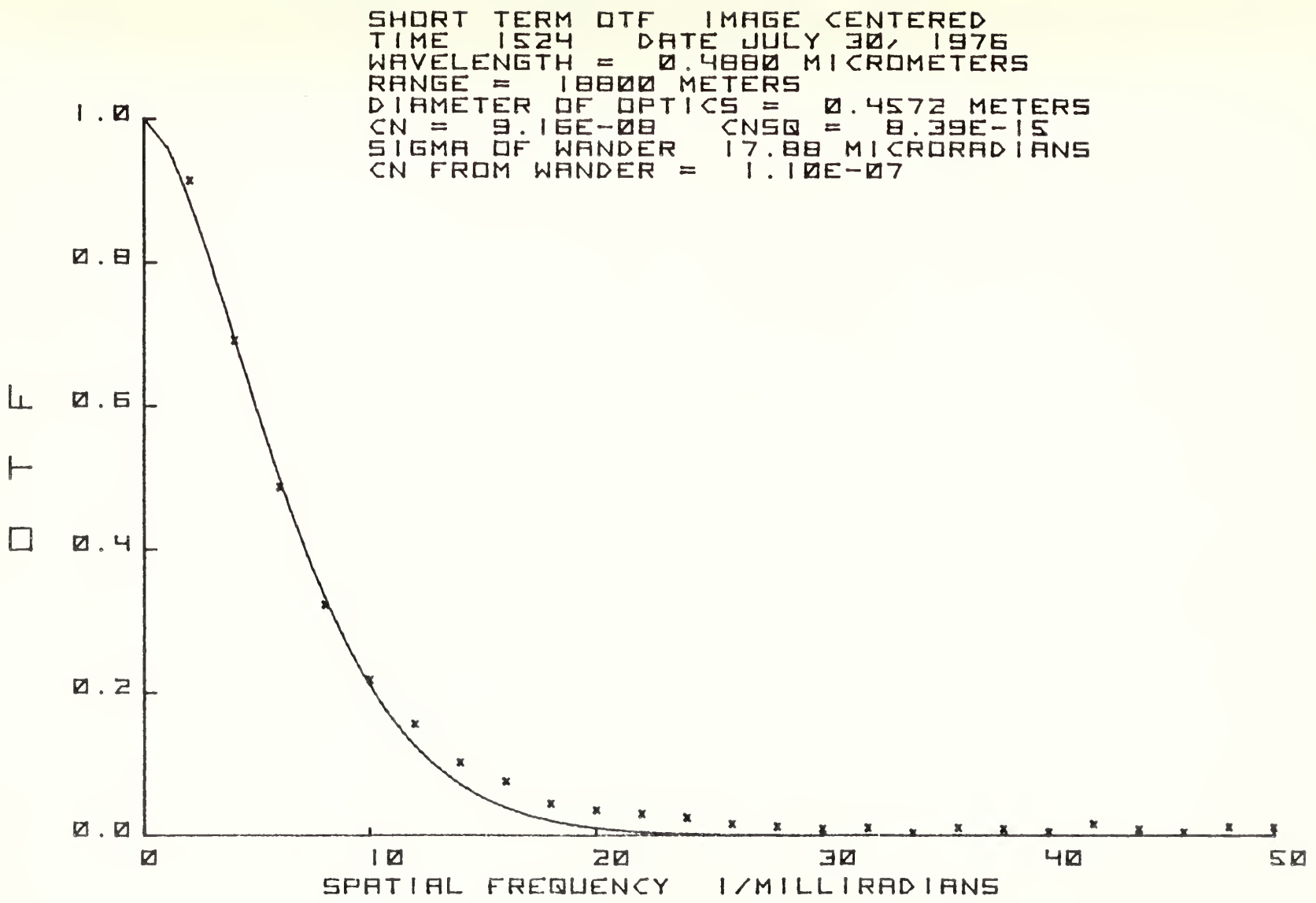

FIG. VI-A-5. OTF OF THE ATMOSPHERE

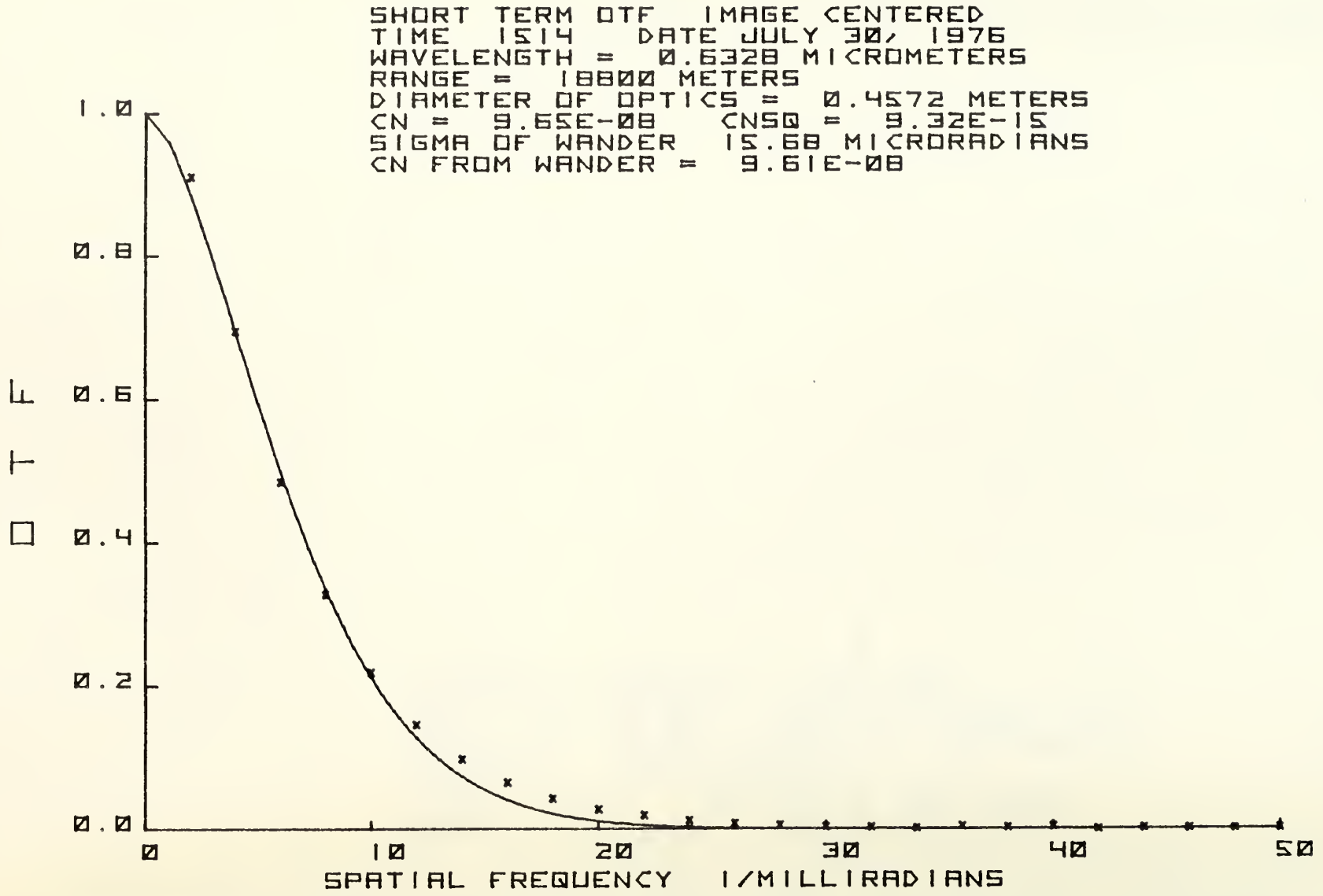

FIG. VI-A-6. OTF OF THE ATMOSPHERE

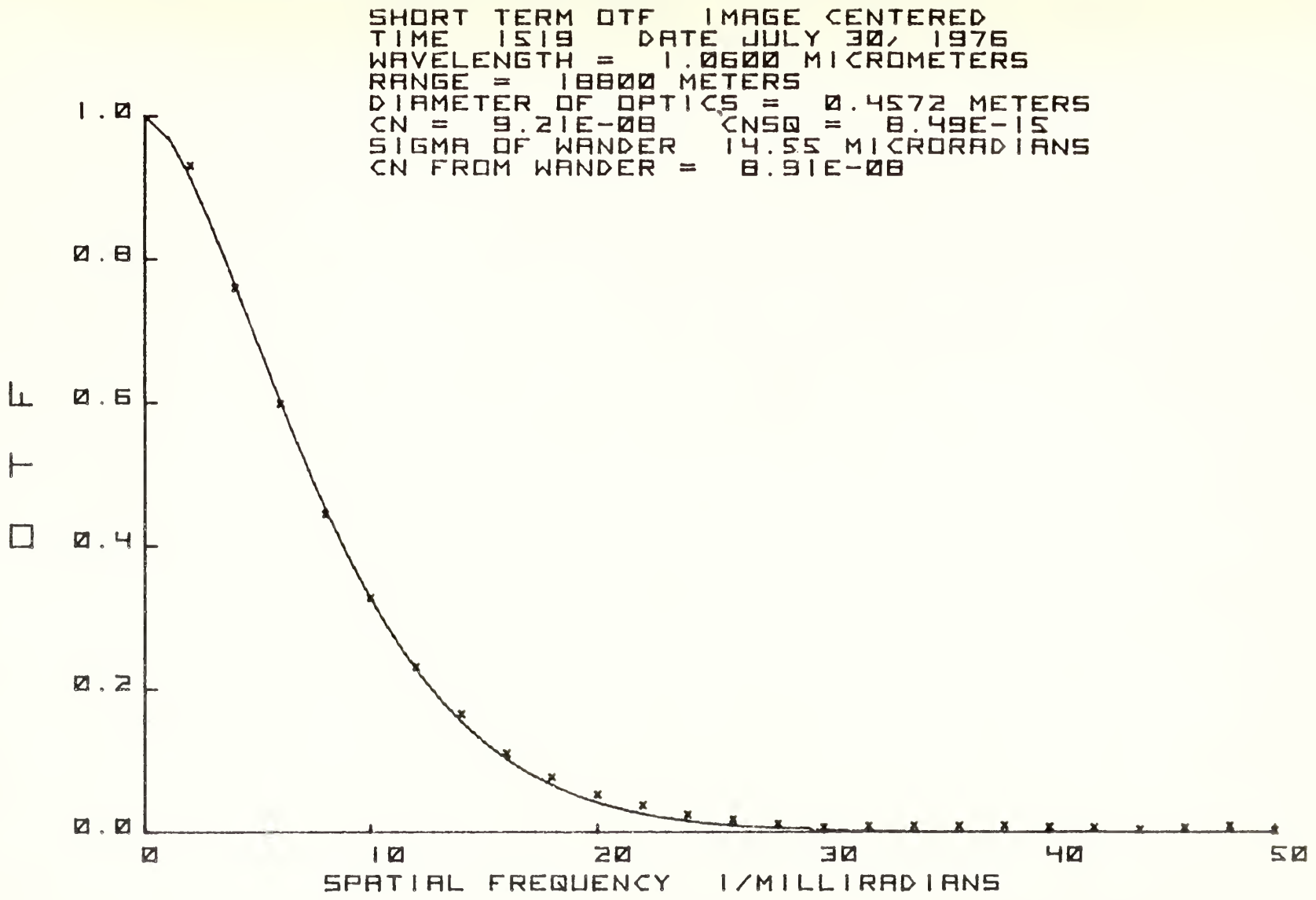

FIG. VI-A-7. OTF OF THE ATMOSPHERE

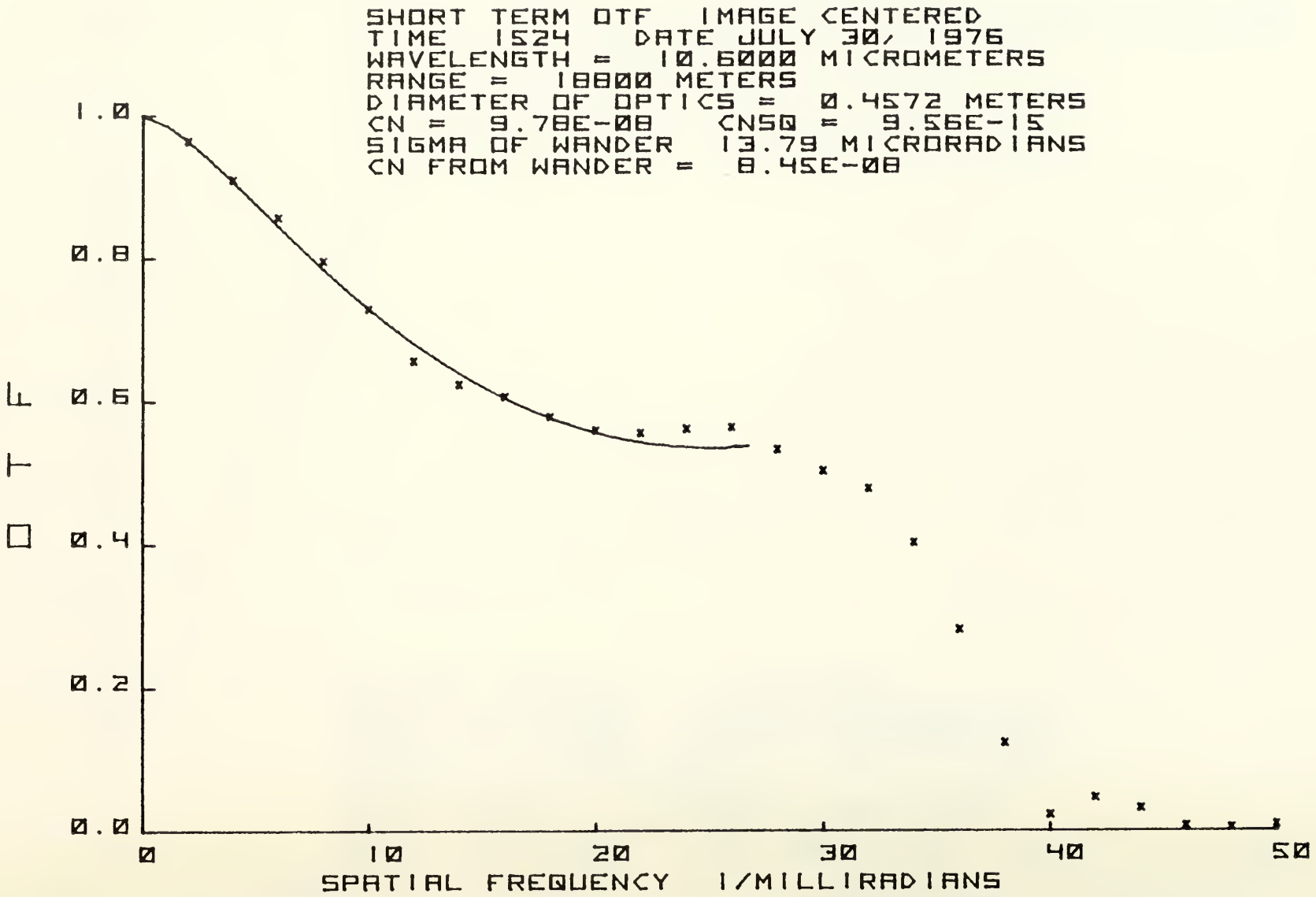

FIG. VI-A-8. OTF OF THE ATMOSPHERE

as on the product of the variables $C_n^2 z_o \lambda^{-1/3}$; and on the value of the diffraction limit D/λ. The quantity α has been used as unity*. Two sets of curves of MTF as a function of spatial frequency are shown in Fig. VI-A-9 for three different turbulence levels in terms of C_n and for the two wavelengths 3.8 μm and 10.6 μm, for a range of 18.8 km. As can be seen in these curves, decreasing the wavelength, or increasing C_n, cause the MTF to drop rapidly toward zero in the mid-range frequencies.

For the three shorter wavelengths, with MTF's shown in Figs. VI-A-5 to VI-A-7 for the short exposure case, the term $C_n^2 z_o \lambda^{-1/3}$ is sufficiently large that the MTF reaches essentially zero before the frequency range of turn-up of the theoretical curves. Expressed differently, the diameter of the optics is large enough, compared to the coherence length, that the turn-up at high spatial frequency is not observed. For this case, the Fried model seems adequate to express the short exposure MTF.

For the curve of Fig. VI-A-8, for 10.6 μm, the term $C_n^2 z_o \lambda^{-1/3}$ is small enough that the MTF is still substantially above zero at midrange spatial frequency. The experimental curve of MTF follows the Fried theory well at low spatial frequency and for a short range of frequency beyond the minimum of the theoretical curve. Beyond that point the experimental points fall off toward zero as the diffraction limit is approached at 43 cycles per milliradian. Behavior similar to this has been observed for all of the 10.6 μm short-term curves. Two other examples are shown in Figs.VI-A-10 and VI-A-11 showing two extremes of behavior. In the first of these figures, the drop off initiates at about 50% of the diffraction limit. In the second figure, the MTF follows the

*For the wavelengths shorter than 10.6 μm used here, the value of α is very close to unity. For 10.6 μm, α is about 0.95 by the Fried model for an unobstructed aperture. More recent theoretical models (Tavis, 1976) indicate α nearer unity for a circular obscuration such as used here. α has been used as unity in all the data reduction reported here.

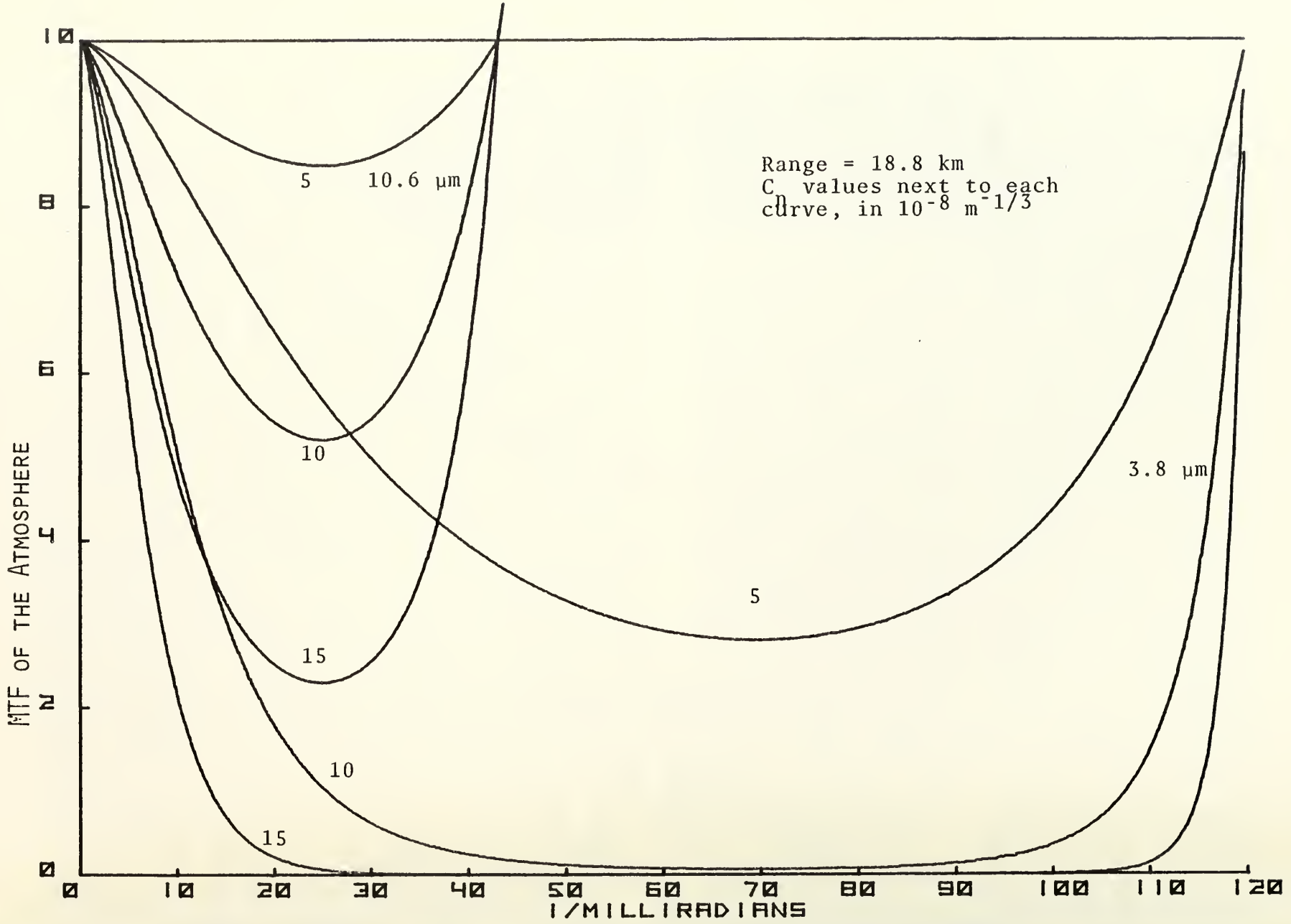

FIG. VI-A-9. MTF FOR TWO WAVELENGTHS AND THREE TURBULENCE LEVELS, NEAR DIFFRACTION LIMIT.

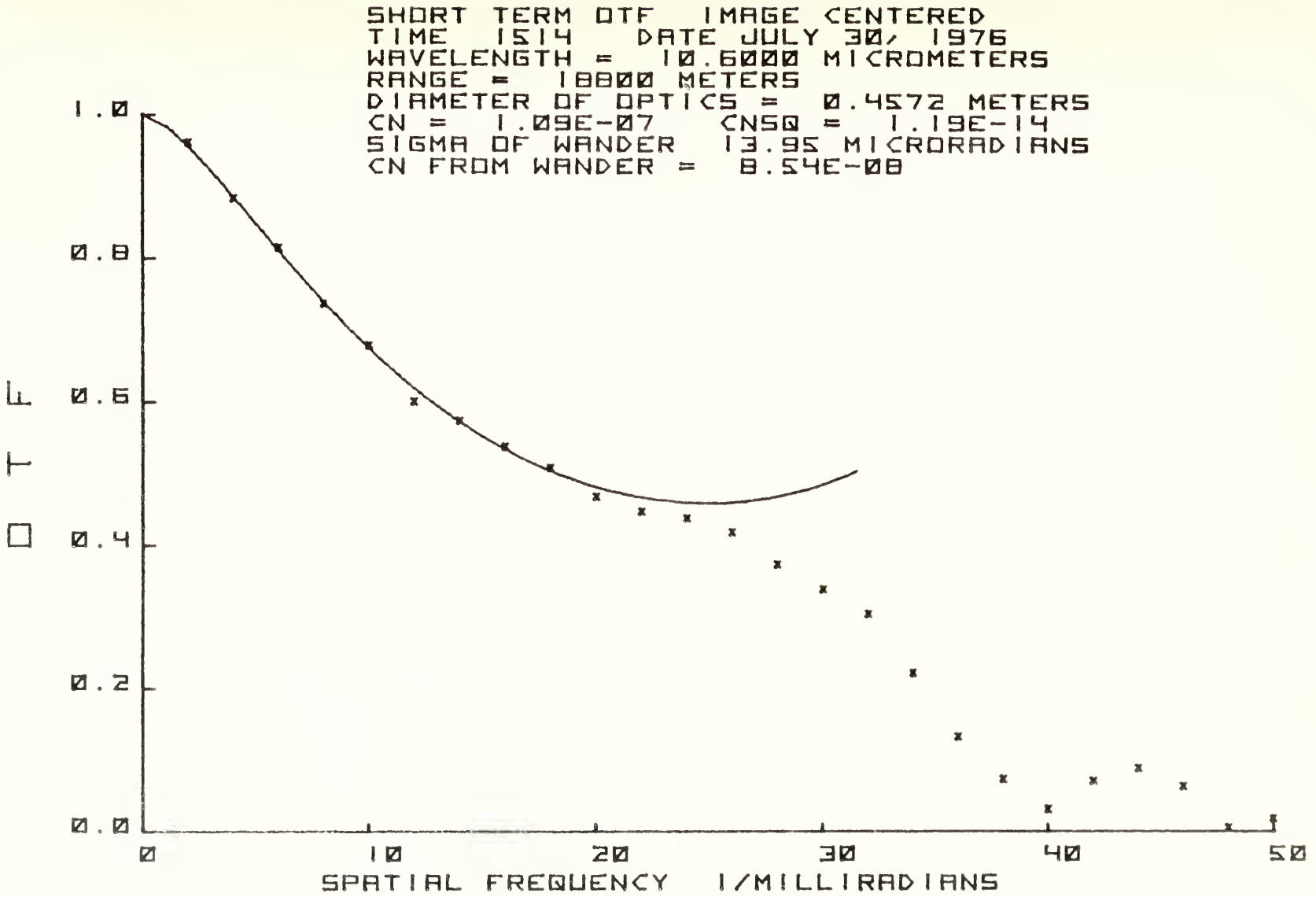

FIG. VI-A-10. OTF OF THE ATMOSPHERE

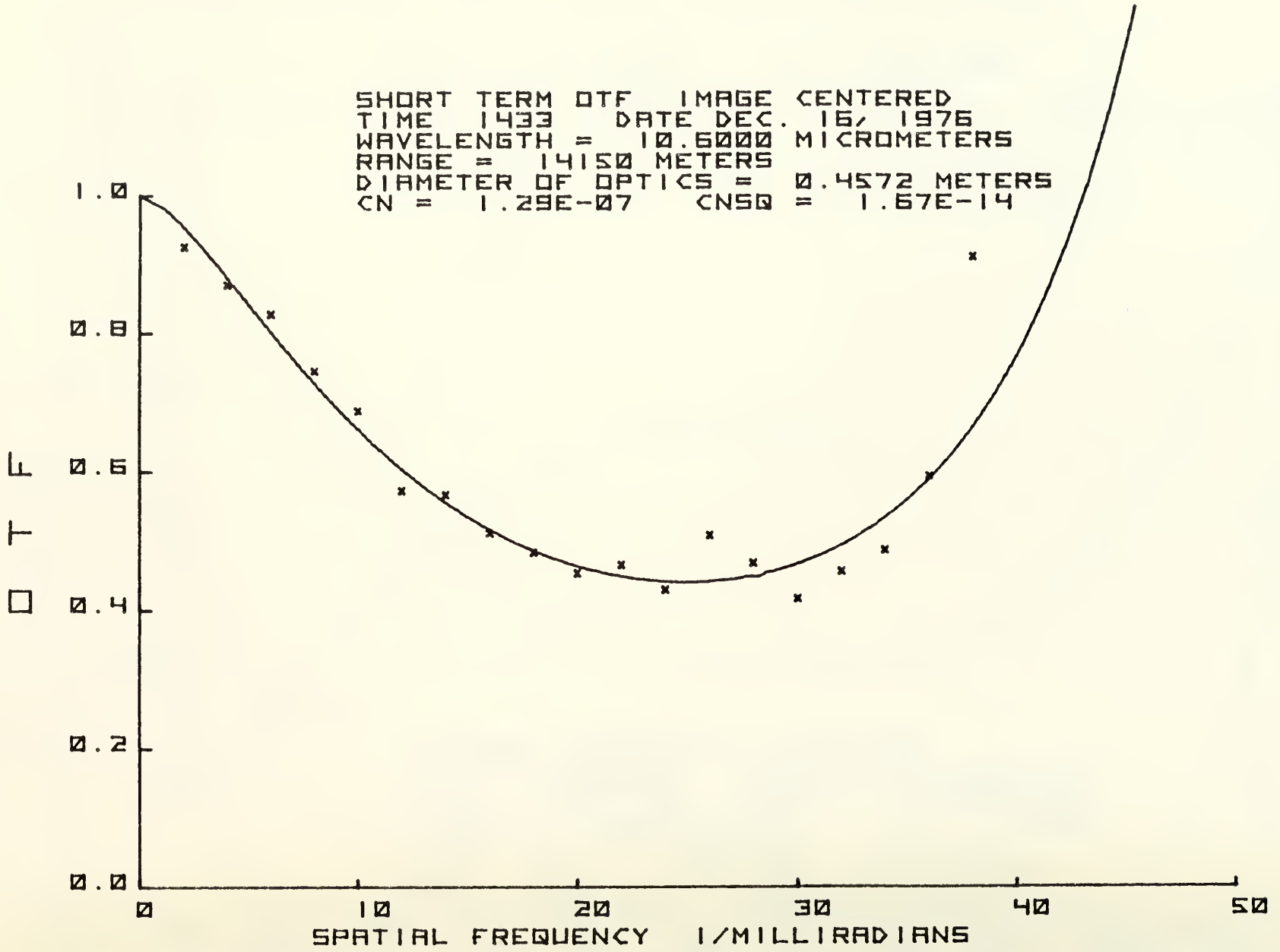

FIG. VI-A-11. OTF OF THE ATMOSPHERE

Fried model nearly to the diffraction limit. In that curve the final drop-off was lost in noise, as indicated by the high last point. An additional example of the short-term MTF curve shape for 10.6 μm is shown later in Fig. VI-A-17 in connection with other data. Other examples are also shown in the data compendium, Appendix B.

The observed MTF curves for 10.6 μm are realistic out to about 40 cycles per milliradian. Beginning there the MTF is terminated in the computer with a Hanning-type roll-off between there and the diffraction limit at 43 cycles per milliradian. This cut off of the tail of the MTF at high spatial frequencies is necessary to prevent problems with the noise which becomes dominant near the diffraction limit because of division by zero, that would occur there in the process of unfolding the instrument function. The noise generated in the process, if not cut-off, interferes with reinversion of the MTF to obtain the line spread function.

The experimentally observed curve of the short-term MTF for 10.6 μm, in the vicinity of the minimum and beyond, is very sensitive to precision in the unfolding of the instrument MTF. An error of a few percent in the spatial frequency scale calibration can substantially alter the curve shape. Nevertheless the minimum and the subsequent turn-up of the curve seem reproducible. Most of the curves start the drop-off toward zero at a spatial frequency in the vicinity of 60% to 70% of the diffraction limit. For lack of a better model a simple cosine-squared roll-off seems adequate to express this approach to zero.

Although the shape of the high spatial frequency part of the short-term MTF curves for 10.6 μm is sensitive to the spatial frequency scale calibration, the value of C_n^2 required for curve fit is relatively insensitive to that calibration. Values of C_n^2 are more dependable than the variation in curve fit might qualitatively imply.

Use of the Fried model, with the above modification for the high spatial frequency region, seems adequate for application in most cases. If detailed behavior is needed in the very high spatial frequency region, near the diffraction limit, it may be necessary to make a direct measurement under the prevailing conditions. However, it seems likely that the uncertainty about the upper frequency region will usually be of little importance, because that region is always multiplied at least by the diffraction limited MTF curve, approaching zero at the high frequency end. Often other MTF degradations will further reduce the MTF in that region.

VI.A.2 Internal Consistency Between Short Exposure and Long Exposure MTF, and Image Wander

a. Average Short Exposure vs. Long Exposure MTF

The internal consistency between measurements of average short exposure MTF and long exposure MTF can be expressed in terms of comparison of the C_n values deduced from these measurements. In Fig. VI-A-12. C_n from average short exposure MTF is plotted as a function of the C_n value obtained from the long exposure MTF for the same line-spread data. The points are for a large variety of weather conditions. They also include four different wavelengths, 0.4880, 0.6328, 1.06, and 10.6 μm, and several different ranges between 4 km and 20 km. The points fall close to the line of unity slope, indicating that measurements of C_n by either technique would give essentially the same value of C_n.

2b. Image Wander

The shifts of the center of area of the individual line-spread functions, in obtaining the short exposure average, also yield a measure of C_n. The standard deviation, σ, of these shifts, termed the image wander, or the wave front tilt, yields C_n from the expression, previously discussed in section V.A.1.d:

$$C_n = 1.046\ \sigma\ D^{1/6} z_o^{-1/2}$$

The image wander has been calculated with this expression for most of the land-to-land short exposure measurements. A few runs have been discarded due to telescope motion, indicated by a frequency spike in the frequency analysis of the displacements required to center the line spread functions. Values of C_n obtained from the wander appear in the data printed on each of the short exposure MTF curves. (In some cases the plotter was programmed to print the wander results on the associated long term curve plot.)

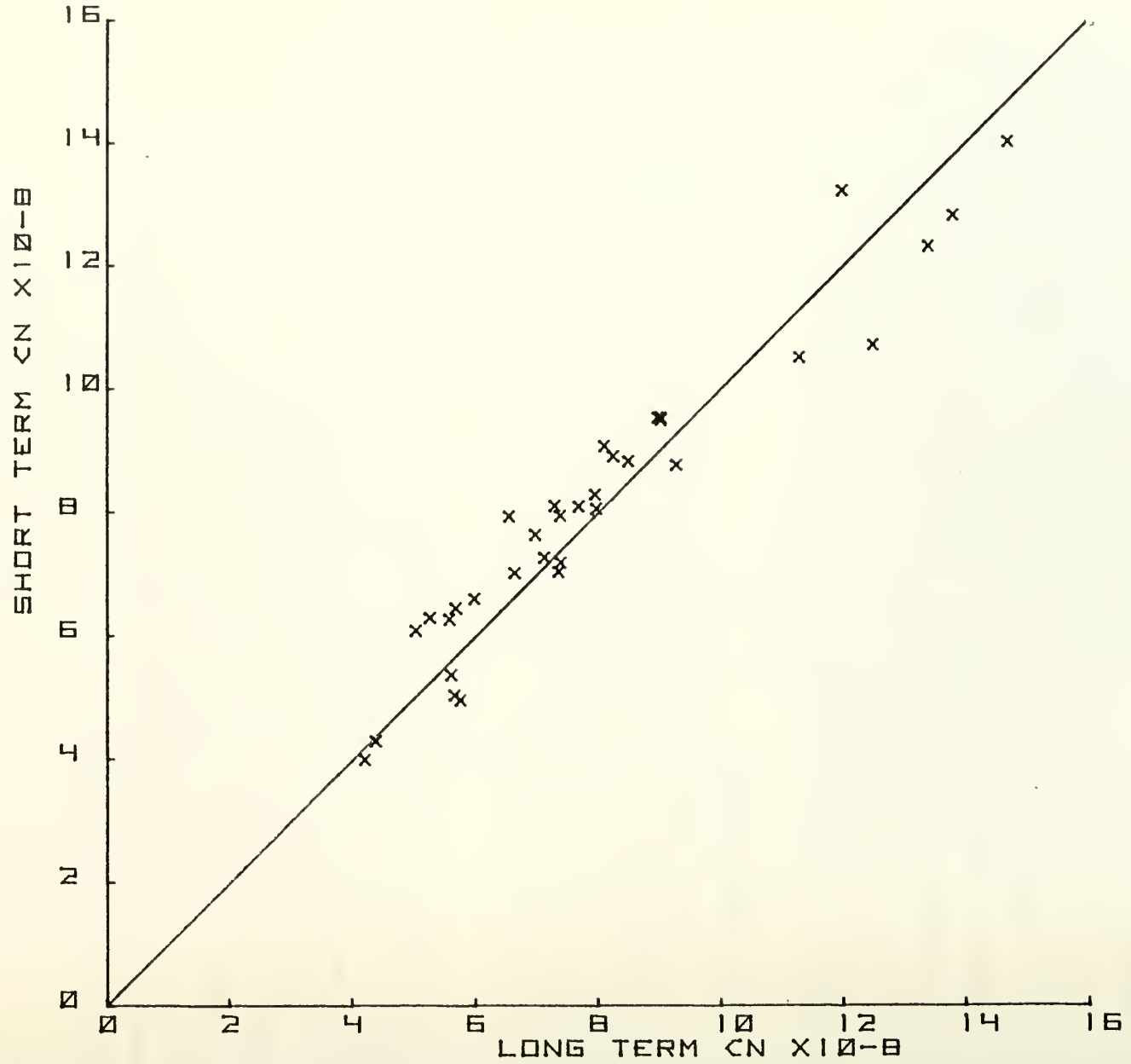

Fig. VI-A-12. C_n from Short-Term MTF vs. C_n from Long-Term MTF.

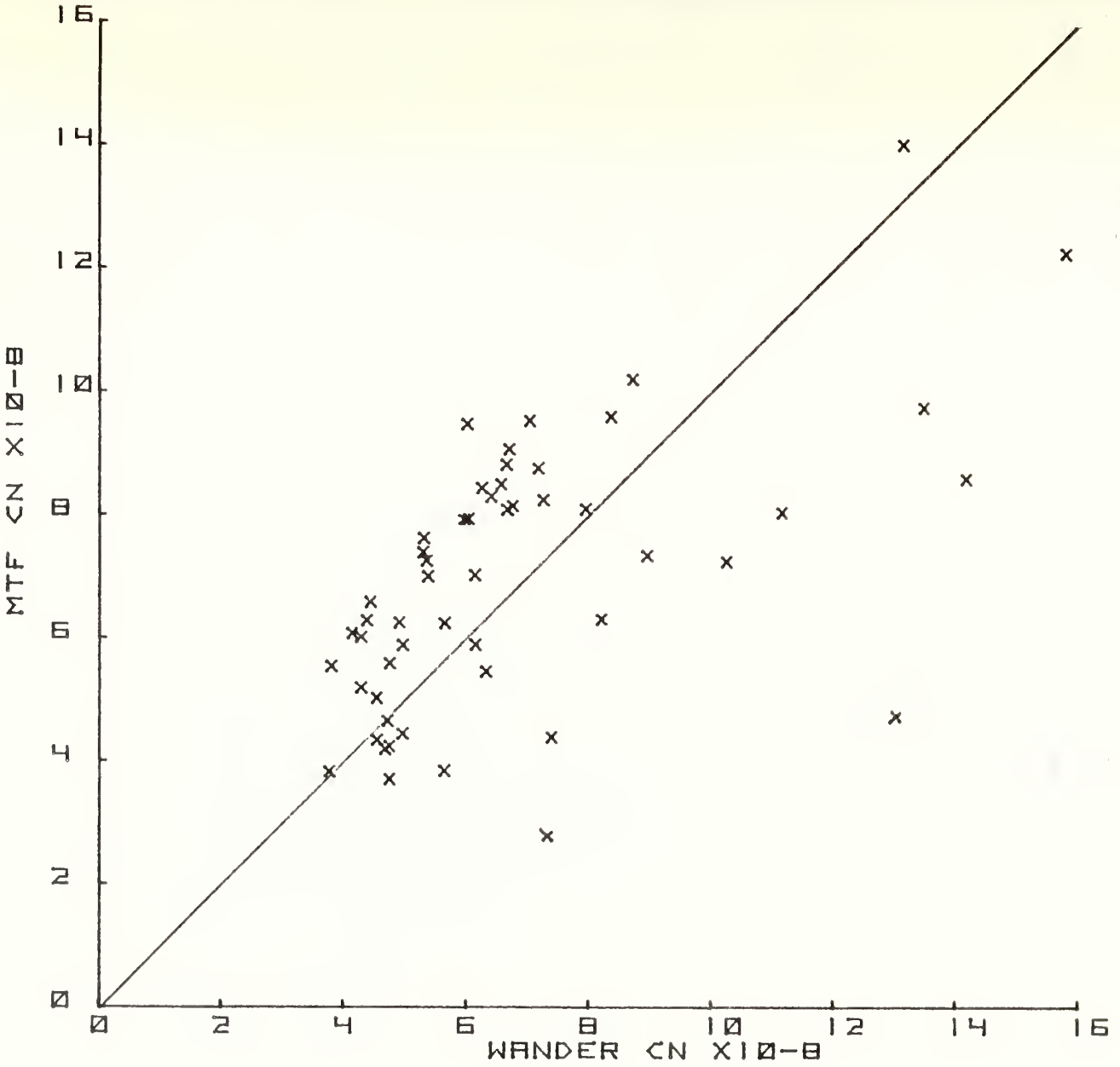

Fig. VI-A-13. C_n from Short-Term MTF vs. C_n from Wander

2c. Consistency of Image Wander with Short Exposure MTF

In general the values of C_n obtained from image wander have been consistent with the values of C_n from average short exposure MTF measurements. Results from a sequence of measurements taken over a period of five days, in February, 1975, are shown in Fig. VI-A-13. The range was 4.03 km from Holiday Inn to Hopkins Marine Station. All the measurements were made at 0.6328 μm. The weather varied from storm conditions with a southwest wind over the adjoining land to 15 knots of steady wind from the northwest. This was the same data group used in the comparison of the NPS instrument with the Lincoln Laboratory shearing interferometer. The points in Fig VI-A-13 are grouped around the line of unity slope indicating reasonable consistency of the results from the two methods.

There are a few data points relatively far from the line of Fig. VI-A-13, indicating too large a value of C_n from wander. These occurred when the wind was blowing from the southwest, over the land, before passing over the water of Monterey Bay, with large gusts apparent in the storm conditions prevailing. As the optical path was fairly close to shore in this case, it seems possible that large scale vortices generated by obstacles on land did not have time to come to equilibrium, as needed to provide a Kolmogorov distribution. An excess of large scale vortices would lead to a high value of wander.

The possibility that the large wander observed in the experiments described above could be due to instrumental effects is quite remote. Motion of the telescope would be detected by the frequency spike that then occurs in the temporal spectrum of wander. The telescope was also well sheltered from the wind in these experiments.

Although wander and short exposure MTF usually give good agreement, other occasions than the above have also occurred in which large differences of C_n have been observed. A further example is shown in Figs. VI-A-14 to VI-A-17. The curves shown there are long term and short term MTF, with wander values, for two different wavelengths, 0.6328 μm,

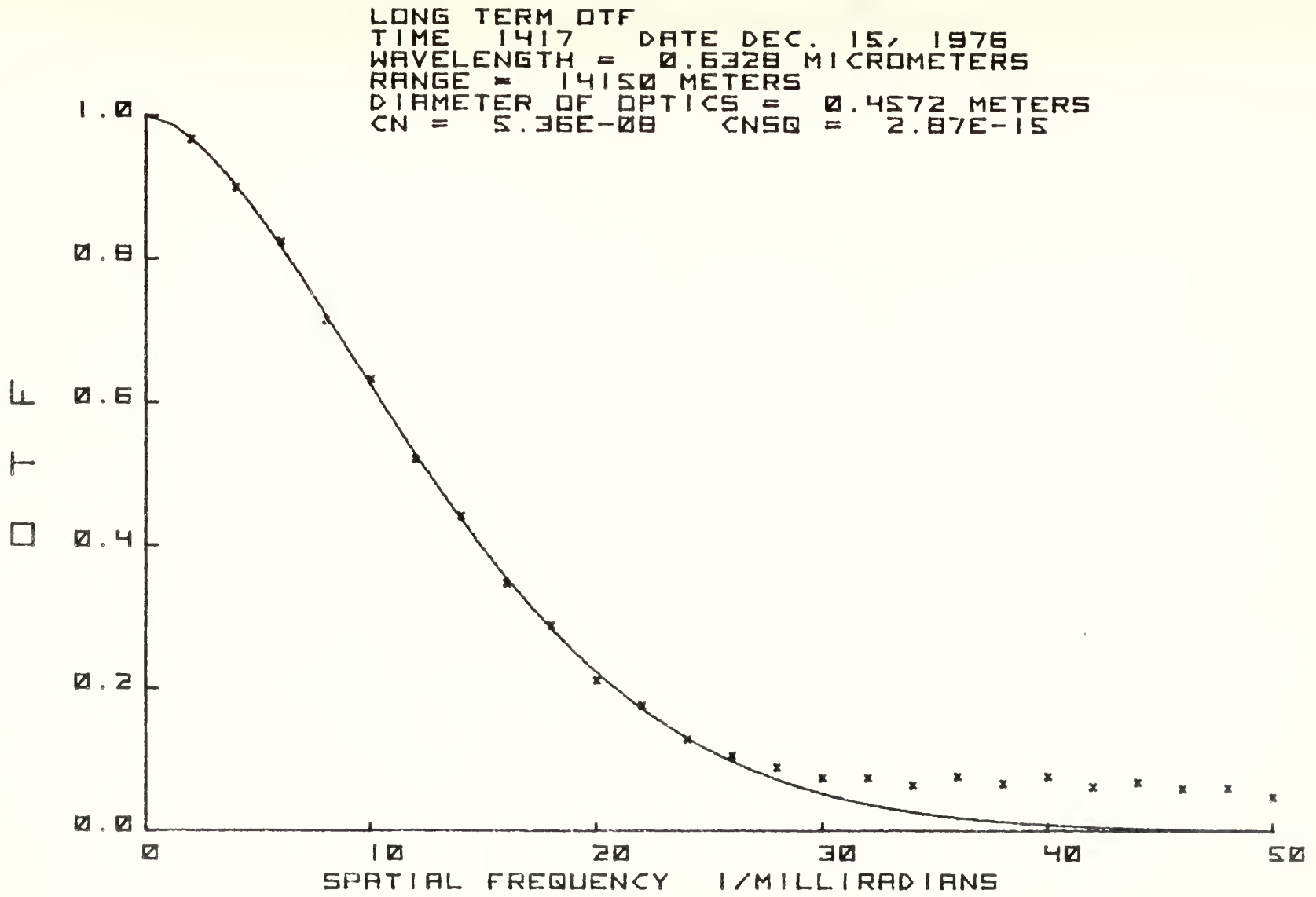

FIG. VI-A-14. OTF OF THE ATMOSPHERE

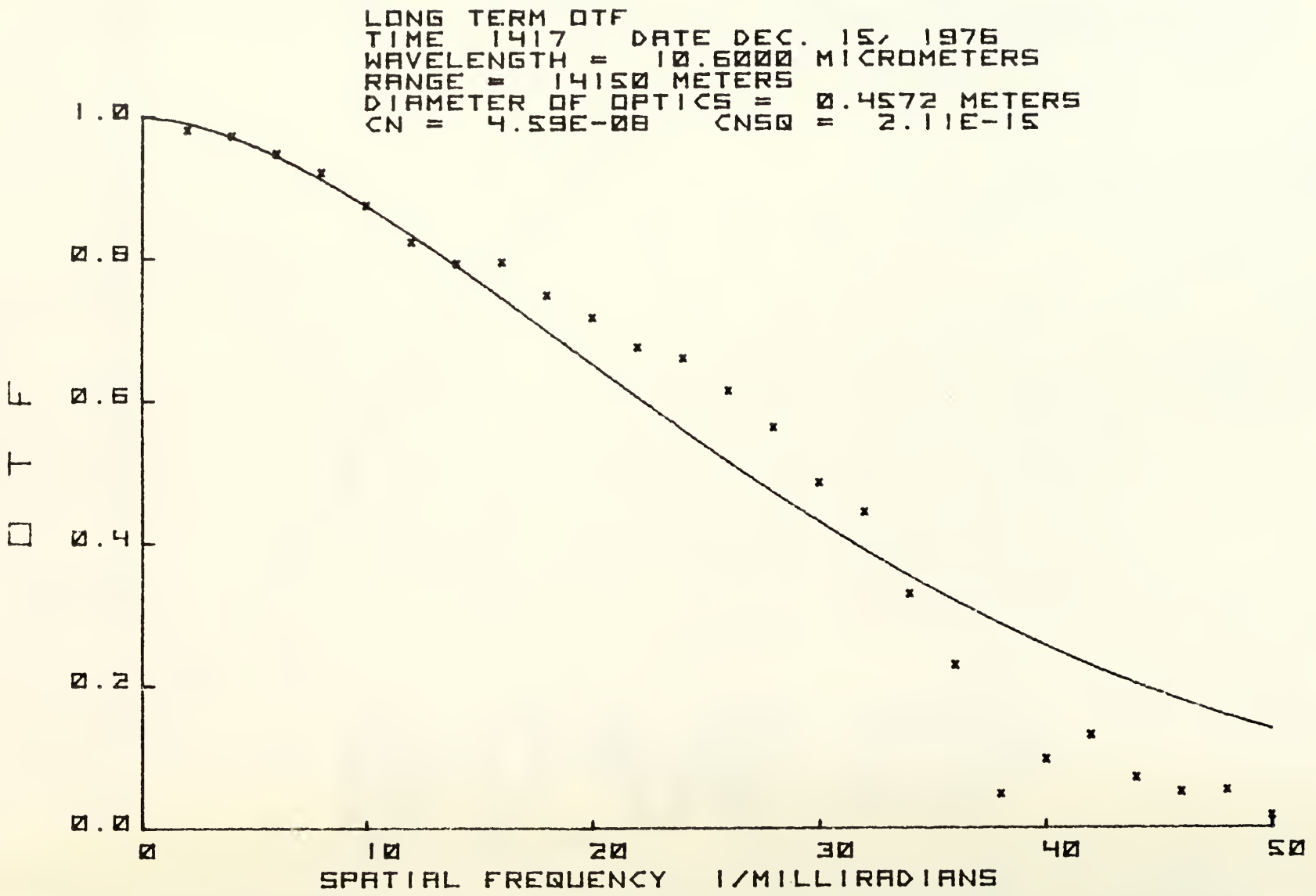

FIG. VI-A-15. OTF OF THE ATMOSPHERE

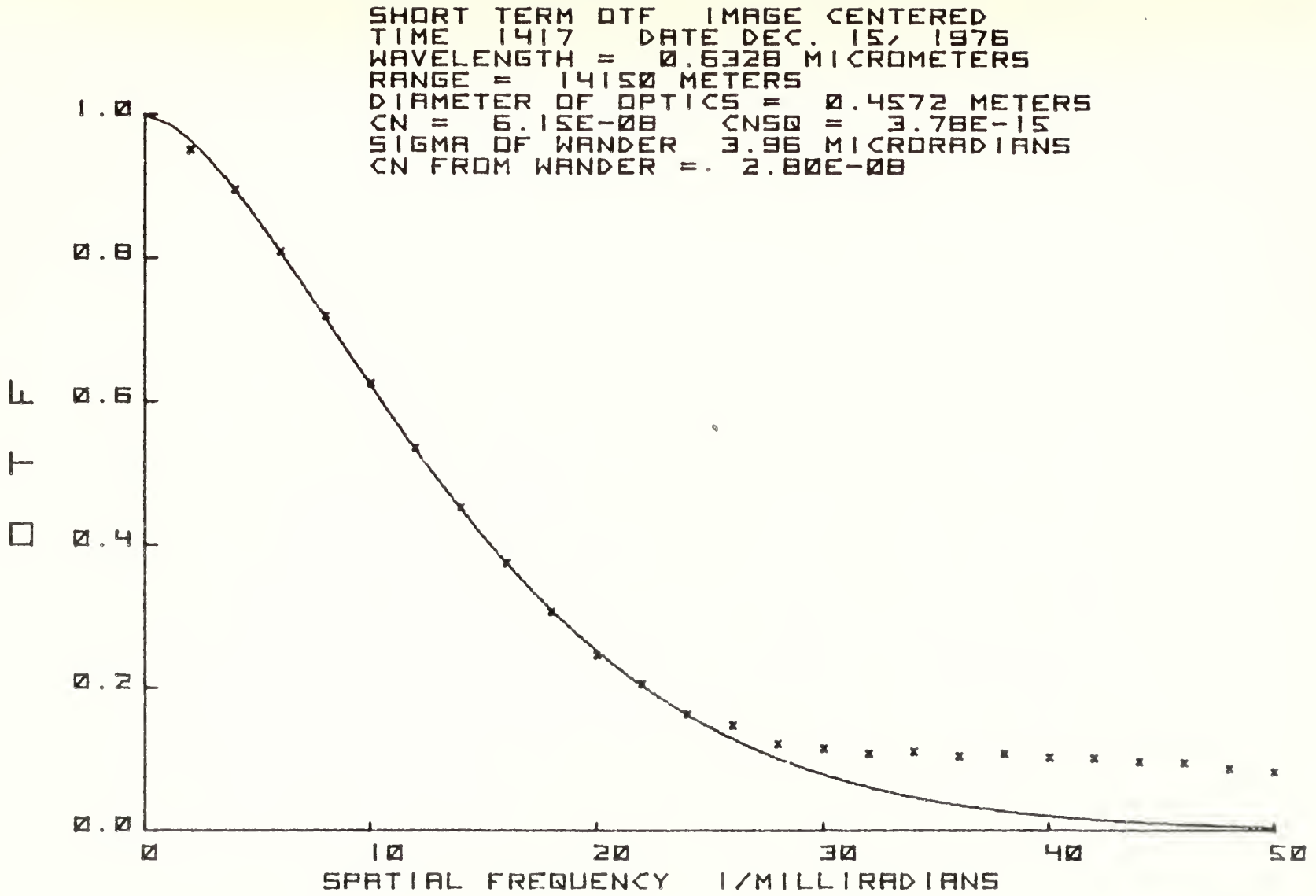

FIG. VI-A-16. OTF OF THE ATMOSPHERE

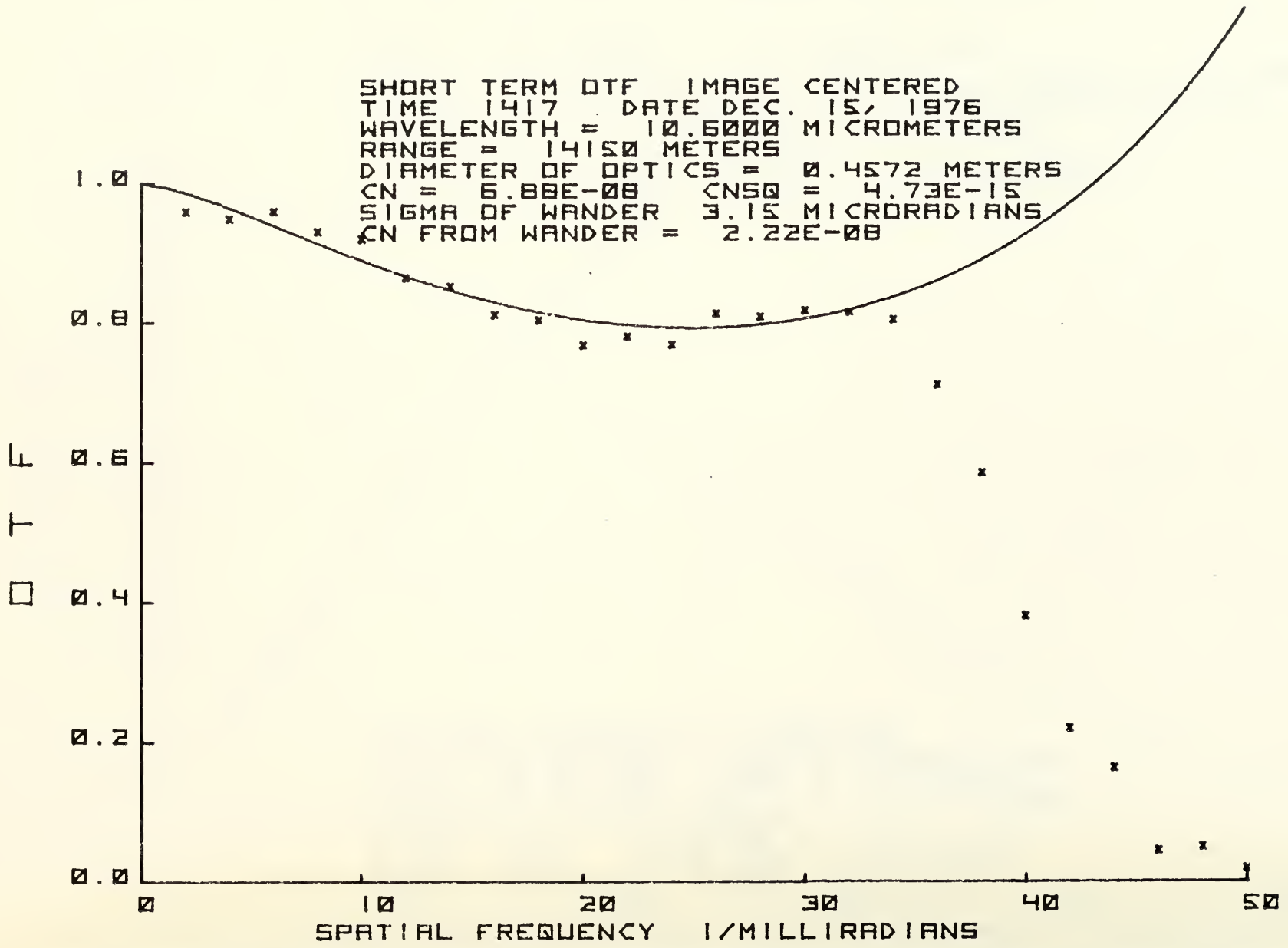

FIG. VI-A-17. OTF OF THE ATMOSPHERE

and 10.6 μm. The MTF was measured simultaneously at these two wavelengths, with a dichroic splitter in the detection system to separate the two wavelengths. The results for the two wavelengths are not identical because the data sampling used slightly different line spread function sequences, but the two values of wander are reasonably close, at 2.80×10^{-8} and $2.22 \times 10^{-8} m^{-1/3}$, respectively, for 0.6328 and 10.6 μm. However the short-term MTF measurements for these wavelengths yielded 6.15×10^{-8} and 6.88×10^{-8} respectively. The corresponding long-term MTF values of C_n were 5.36×10^{-8} and $4.59 \times 10^{-8} m^{-1/3}$. These are lower than the short-term, as expected, consistent with the low wander values. These data were taken on an optical path from the sand plant to Pt. Pinos (14.15 km) with the optical path very near the water at the center of the path. At high tide the curvature of the earth caused a clearance from the water at path center of only one meter. This could be even smaller with a temperature gradient increasing upward. On several occasions during these runs ocean waves obstructed the optical beam. Under these conditions it seems likely that the large scale vortex end of the Kolmogorov distribution may be truncated, leading to the small wander values. Unfortunately micrometeorological data is not available to establish this with certainty.

From the collection of measurements made in the course of this work it is concluded that usually the wander can be predicted from a value of C_n determined from the MTF. However circumstances exist in which the wander can be substantially larger or smaller than predicted by that means. Usually these deviations occur under conditions in which the validity of the Kolmogorov distribution on the large scale vortex end might be questioned.

VI. A.3 Wavelength Variation and Overall Internal Consistency

The wavelength variation of MTF is more readily verified than the variation of MTF with other paramaters, because it is possible to make measurements at several wavelengths within a short enough period of time that C_n can remain essentially constant. The slit scanning telescope was equipped with a dichroic splitter so that measurements could be made simultaneously at 10.6 μm and at any one of the three shorter wavelengths. A number of such runs have been made in the course of this project. The results of a representative set of data taken in this manner at four different wavelengths are listed in Table VI-A-1 , in terms of the values of C_n to give fit to the MTF, or derived from wander. The data was taken in a period of ten minutes. The table indicates not only the wavelength consistency, but also the consistency between long-term MTF, short-term MTF and wander derived C_n values. Some of the detailed curves of this set have already been presented in Figs. VI-A-1 to VI-A-8 and in Fig. VI-A-10 . The remaining curves can be found in the data compendium, Appendix B. The standard deviations of the various measurement methods and wavelengths are shown in the table. The standard deviation of C_n for all the measurements is 8.6%. This sort of consistency isoften observed, although occasionally the wander results for C_n fall outside of this range, as discussed earlier.

Another similar group of measurements taken in a short period of time is tabulated in Table VI-A-2 . The overall standard deviation of C_n in this group of measurements is 12.5%. From the consistency shown in the above two tables, and the results reported in earlier sections it can be concluded that the Fried formulation is adequate to predict the behavior of long-term and short term MTF and to predict the wander in many cases, with some caution in the latter because of occasional deviations.

Table VI-A-1.

Values of C_n, in units of 10^{-8} $m^{-1/3}$, from MTF and Wander

Range 18.8 km, 0.457 m. Optics

30 July, 1976

Time	Fig. No. VI-A-	Wavelength µm	C_n, long-term MTF	C_n, short-term MTF	C_n from wander	mean	σ	%
1514	10	10.6	8.45	10.9	8.54			
1519	-	10.6	9.30	10.4	8.24	9.53	.74	7.8
1524	4,8	10.6	9.67	9.78	8.45			
1514	2,6	0.6328	10.1	9.65	9.61	9.79	.27	2.7
1519	3,7	1.06	8.99	9.21	8.91	9.04	.13	1.4
1524	1,5	0.4880	9.95	9.16	11.0	10.04	.75	7.5

Overall mean C_n = 9.46, sigma = .81, 8.6%

Table VI-A-2

Values of C_n, in units of 10^{-8} $m^{-1/3}$, from MTF and Wander

Range 18.8 km, 0.457 m. Optics

30 July, 1976

Time	Wavelength µm	C_n, long-term MTF	C_n, short-term MTF	C_n from wander	mean	σ	%
1344	10.6	12.1	14.8	10.8	12.6	2.0	16
1344	1.06	14.5	13.2	11.7	13.1	1.4	11
1355	0.6328	13.8	10.9	15.2	13.3	2.2	13
1401	0.4880	13.5	10.8	12.1	12.1	1.4	11

Overall mean C_n = 12.78, sigma 1.60, 12.5%

VI.A. 4. Variation of MTF with Range and Path Weighting of C_n^2 and Comparison with C_n^2 from Scintillation and C_T^2.

Test of the variation of MTF with range is more difficult than that for the variation with wavelength, or for short term vs. long term, because of the difficulty of obtaining conditions in which C_n^2 is uniform along the path, while varying the path length. Although, on an optical path across the water under open ocean conditions, one has the possiblity of finding a time when C_n^2 is constant in path position and constant in time, in practice these occurrences are not common, nor is it easy to know that such conditions exist. In order to optimize the chance of having such conditions, a number of trips with the ACANIA were carried out in which the ACANIA was stationed off Pt. Pinos from early afternoon until about an hour before sunset, during which a well-established and fairly constant northwest wind was blowing. An optical path was established from Pt. Pinos to the shore of Monterey Bay, with the ACANIA just off that path and downwind of it. The ACANIA was usually initially placed approximately at the center of the optical path. The ACANIA measured the values of C_T^2 at several heights above the water. When possible, the ACANIA was also moved along the path to get values of C_T^2 at various points on the range. C_T^2 was also measured at the telescope end of the optical path on Pt. Pinos. In almost every case the C_n^2 values, determined from C_T^2, near the telescope were decidedly higher than over the water, because of thermal input and wind disturbance on the small amount of land lying under the first part of the optical path. As a result of these complications, it has been only possible to determine that the behavior is consistent with a reasonable interpretation of the distribution of C_n^2 along the optical path.

An example of conditions in which C_n^2 was reasonably constant is provided by the data of 22 September 1977 collected in Fig. VI-A-18. During that day the sky was overcast at an altitude of several thousand feet and a steady wind of about 7 knots was blowing from the west-northwest. This direction was approximately 45 degrees from the perpendicular to the optical path. The wind

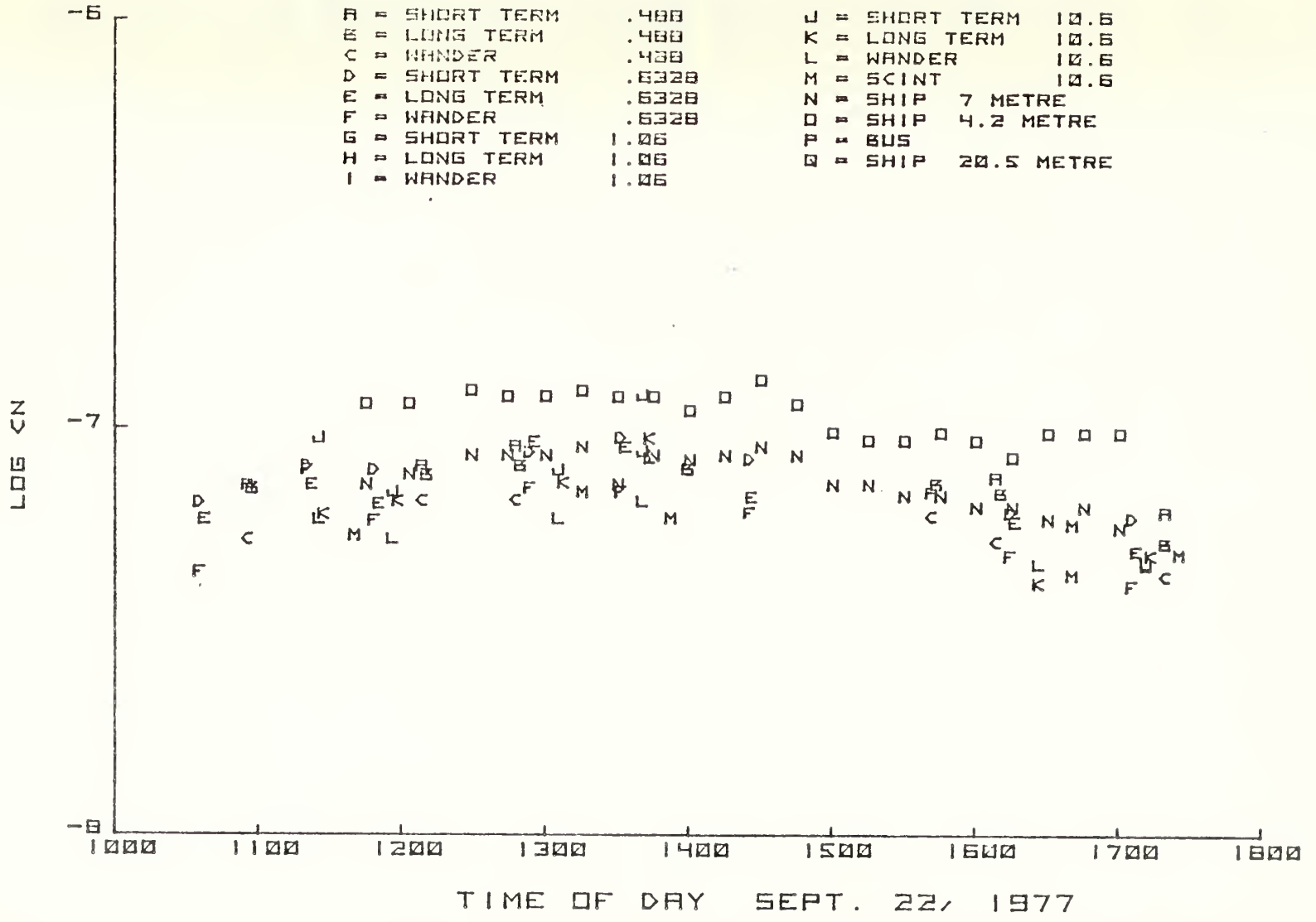

Fig. VI-A-18. Log C_n vs Time of Day for a Variety of Types of Measurement.

was fairly uniform at all points along the optical path as judged by the roughness of the sea surface. The path was from Pt. Pinos to Marina, a distance of 13.16 km. The ship was located at about the path midpoint. The values of C_n obtained by all the methods are essentially constant and agree within about 15 %. Seventeen different types of observations are plotted.

In contrast to the data discussed above, the results of similar measurements made on 21 September, Fig. VI-A-19 show a large scatter in the values of C_n measured by different methods and at different locations. On that day the weather was clear, with sun shining on the ground in the vicinity of the instrument bus. The wind was light and erratic along the optical path as evidenced by patches of wind ripples that changed location along the surface of the water under the optical path.

Still a different set of situations pertained on 16 and 17 December 1976. These runs show the effects of path weighting which emphasizes the region near the telescope for the MTF derived C_n but emphasizes the center of the path for the scintillation derived C_n.

On December 16, 1976 the wind was from the west flowing across Pt. Pinos to the bus at about 2 to 8 kts. The sun was shining. The C_n measured thermally at the bus was about 20×10^{-8} while that measured on the ACANIA was about 7×10^{-8}. The C_n near the bus was high because of the wind blowing across the hot asphalt of the road going around the point. Fig. VI-A-20 for December 16, 1976 shows the C_n measured from scintillation to be about ½ that measured from MTF. This is because the path weighting of C_n for MTF is largest near the optics end of the path (the bus end) while the path weighting of C_n for scintillation is largest in the middle of the path where C_n was small.

On December 17, 1976, the wind was from the east in the morning. That is, the wind was offshore at the laser end but onshore at the bus end. This would give a higher land value of C_n at the laser, and a lower value of C_n at the bus. The wind shifted to the northwest at 1100 and increased to 7-10 kts by 1300. Fig. VI-A-21 shows C_n measured from scintillation to be higher

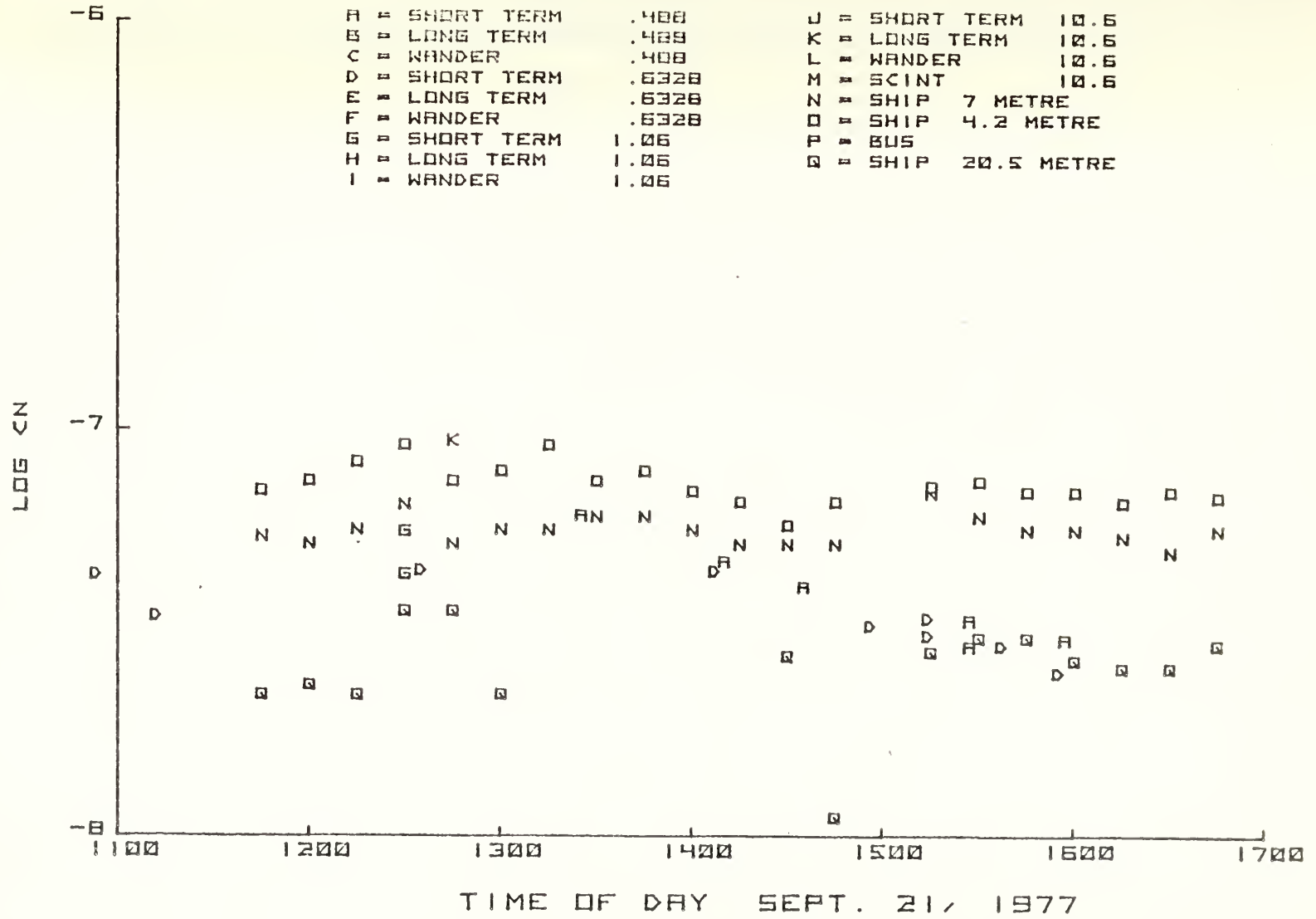

Fig. VI-A-19. Log C_n vs Time of Day for a Variety of Types of Measurement.

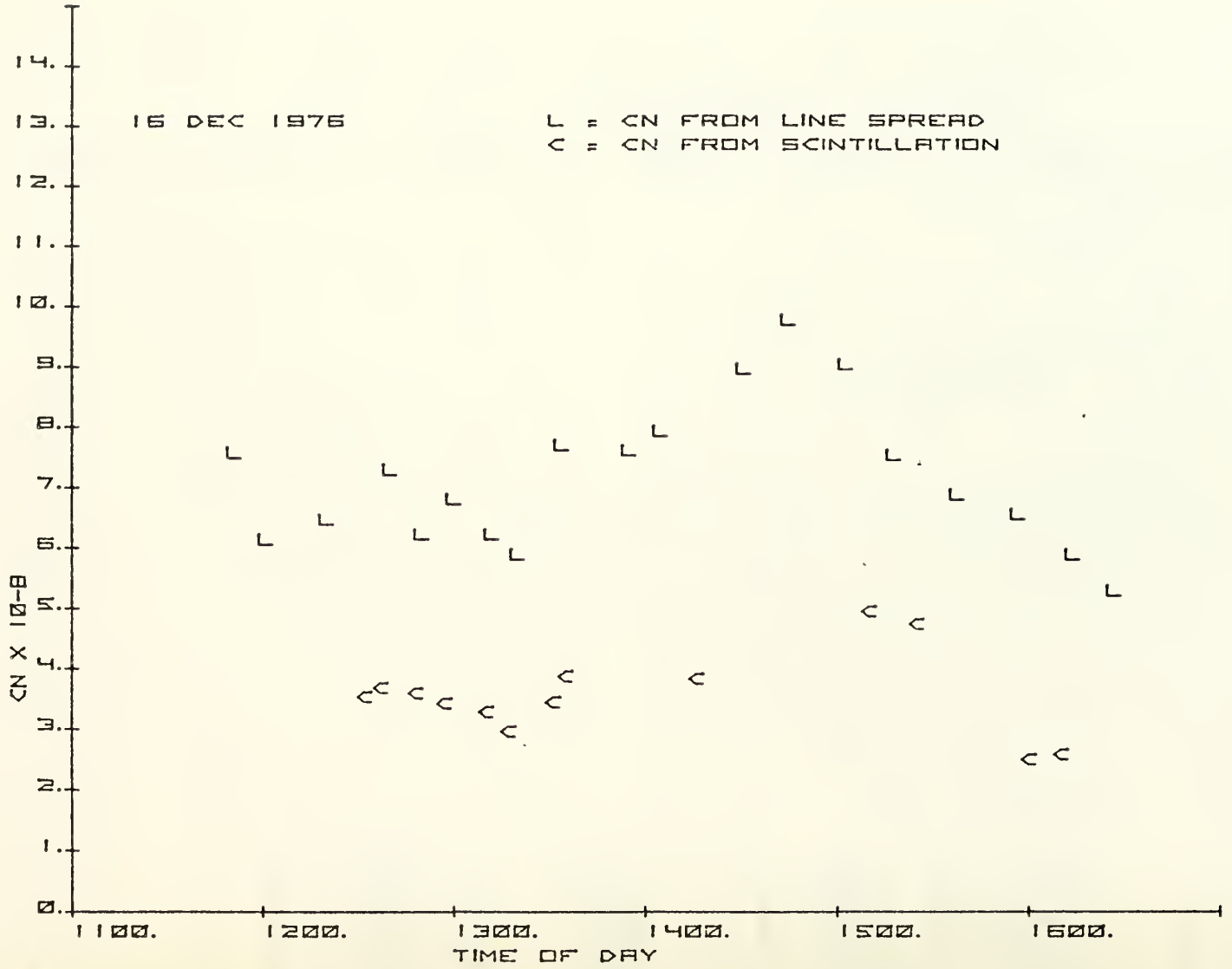

Fig. VI-A-20. C_n from MTF and C_n from Scintillation vs. Time of Day, 16 Dec.,1976.

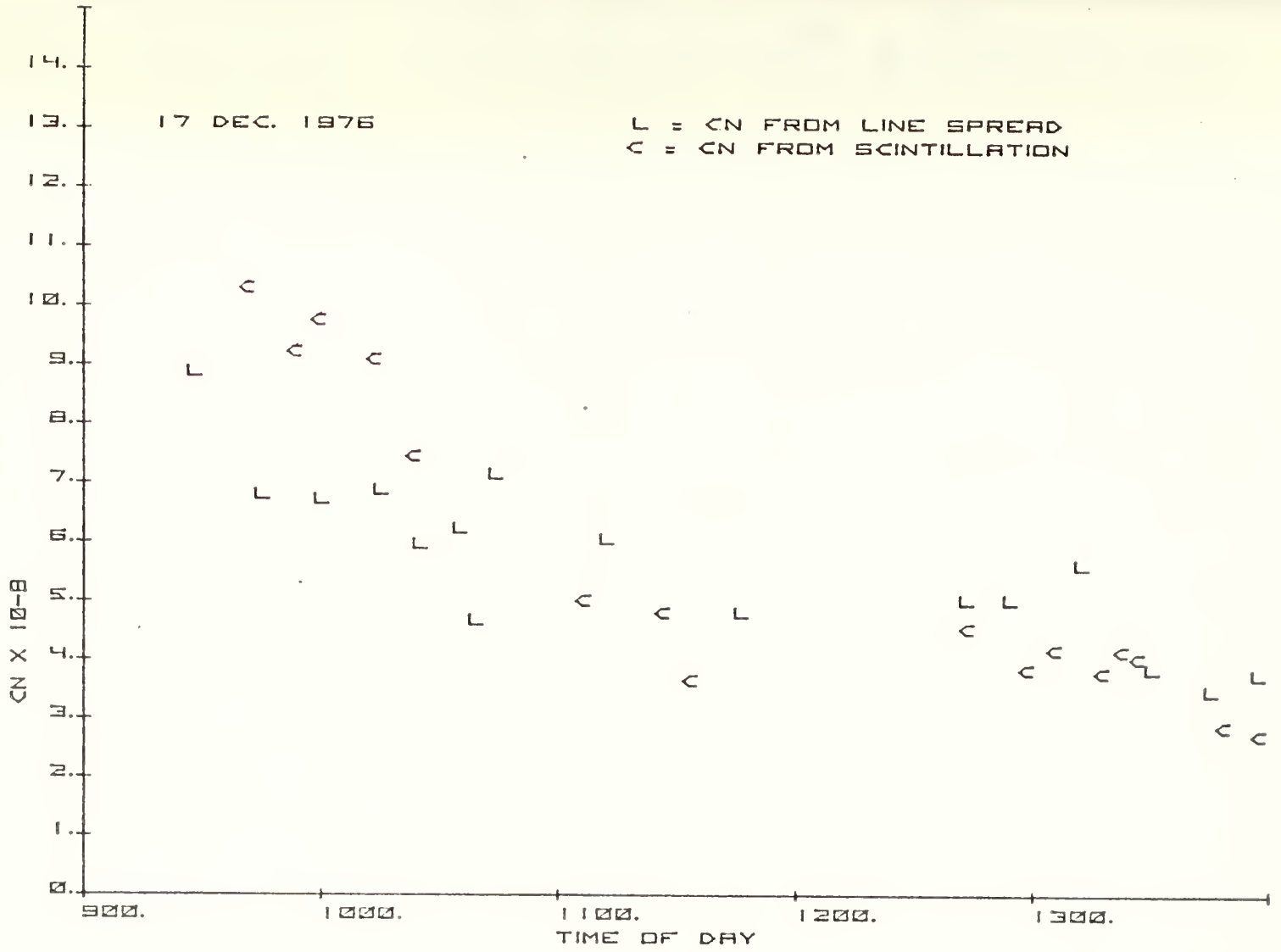

Fig. VI-A-21. C_n from MTF and C_n from Scintillation vs. Time of Day, 17 Dec. 1976.

in the morning when the wind was offshore than the C_n measured from MTF. The two values of C_n become approximately equal when the wind shifted to the northwest at approximately 1100.

The examples given above to illustrate the relative path-position weighting of C_n^2 show a consistency of the observations with the predicted weighting. Many other examples can be cited within the body of data attached in Appendix B. Although it has not been possible to demonstrate a true fit between the data and the expected path-position weighted C_n^2, no cases of violation of the predicted behavior have been observed. The difficulty of demonstrating a true fit has been simply the difficulty of knowing the values of C_n^2 at a large number of points along the optical path. This could better be done over land, but would be an expensive experiment. The very good fit of other aspects of the Fried model also lend credence to the expectation that the path weighting is as predicted by that model.

Finally it should be pointed out that determination of an effective weighted C_n^2 from MTF values obtained with a slit scanning imager such as that employed here provides the basis for predicting the behavior of an imager, or a beam forming optical system regardless of the form of the weighting factor. The observed MTF has responded to whatever the weighting factor is, just as does any other imager under test.

VI. A. 5. Comparison of MTF from Slit Scanner and Shearing Interferometer

In order to provide a confirmation of the MTF results, as measured by the NPS slit scanning imager, an experiment was carried out to compare the results of that technique with MTF results obtained with a shearing interferometer. A group from Lincoln Laboratory* brought a version of the Kelsall shearing interferometer (Kelsall, 1973) to Monterey for a one-week experiment, in February, 1975. The two instruments were set up to view a single HeNe laser source (0.6328 μm) along the 4.03 km path across the southern end of Monterey Bay from the Holiday Inn in Seaside to the Hopkins Marine Station in Pacific Grove. This particular optical path often does not have representative open ocean conditions due to land effects on the western end of the path. However, the two instruments viewed the same atmospheric conditions, even though the values of C_n^2 probably varied considerably along the path. The receiving apertures were located as close together as possible, with centers about 0.3 m apart. The optical path was horizontal and about 6 m above the water. The laser beam was diverged to give a spot diameter about 50 meters wide at the receivers. The latter were located at the western end of the path, in an unheated storage area of a building at the Hopkins Marine Station Laboratory.

The receiver optical system of the shearing interferometer was a 7 inch diameter Questar telescope with a 2 1/4 inch diameter central obscuration. The NPS 10 inch diameter slit scanning imager was masked to duplicate the 7 inch diameter aperture and central obscuration of the shearing interferometer, in order that the two systems would have identical input optics.

Runs were made for identical time periods. These were 20.5 seconds in duration, representing 512 scans of the NPS

*We are indebted to D. Kelsall, E.S. Cotton, L.C. Marquet, and W. Stiehl of Lincoln Laboratory for their cooperation in carrying out this experiment.

instrument, at that time operating at 25 Hz repetition rate. (2^n scans are needed to permit fast Fourier transform frequency analysis). The shearing interferometer obtained interferograms at a higher repetition rate of about 120 Hz. Both systems observed the atmosphere for a period of about one millisecond per repetitive cycle.

A comparison of the results obtained by the two methods is presented in Fig. VI-A-22. The values plotted are the values of C_n required to produce the best fit of each MTF curve to the Fried model for short exposure MTF (Fried, 1966). This model has been discussed earlier in Sections III. B and V.A.1 . For most of the curves of MTF, for the shearing interferometer, the high spatial frequency region of the curves was obscured sufficiently by noise to make the differences between the two techniques indiscernible. The best fit MTF calculation was, for both methods, based on low spatial frequency data, for points at lower spatial frequency than the 1/e point for the curves. The small differences that might occur due to differences between MTF and OTF thus do not appear.

The points in Fig.VI-A-22 lie sufficiently close to a line of slope unity to give some confidence that the two methods are measuring essentially the same quantity.

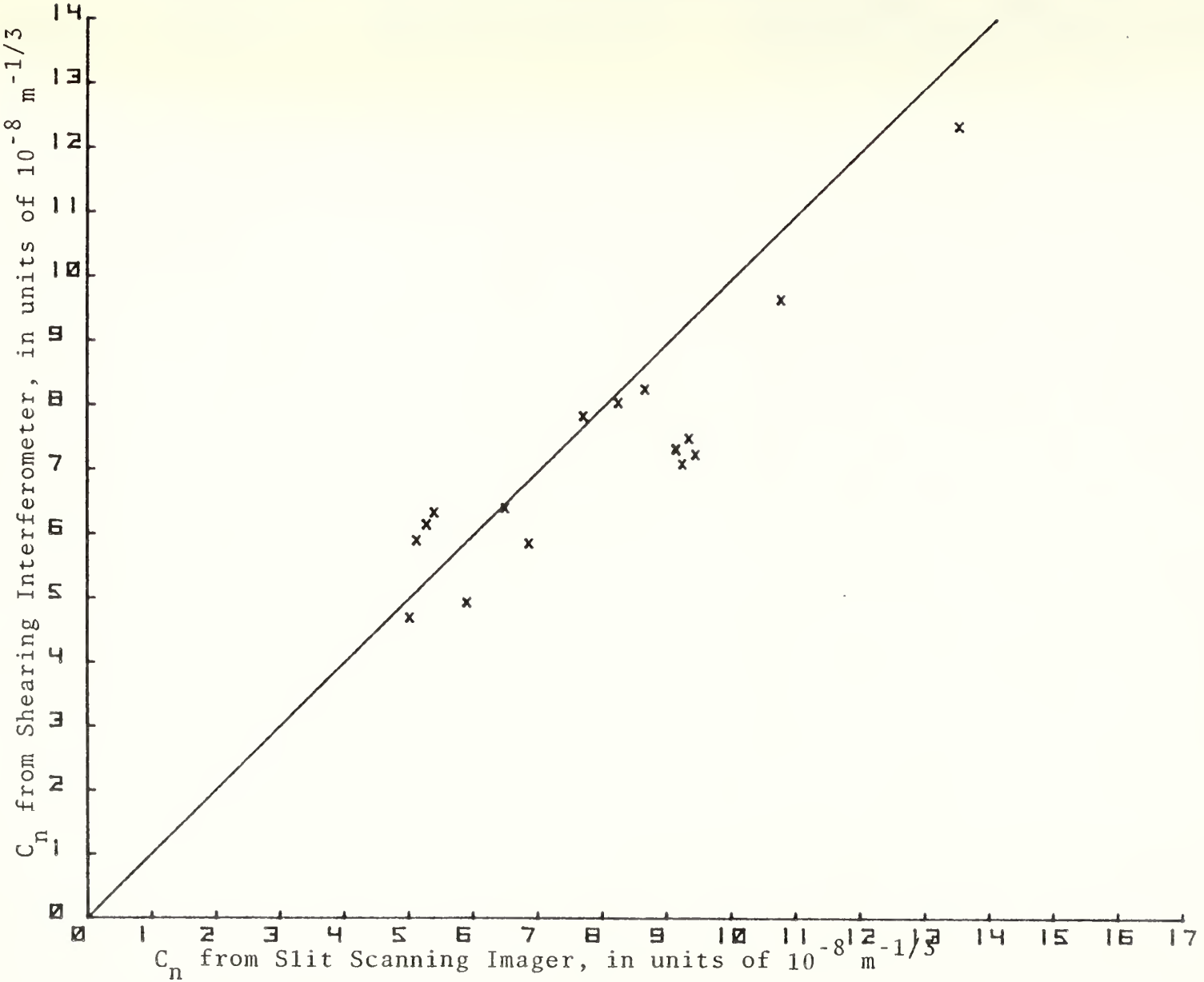
C_n from Shearing Interferometer, in units of 10^{-8} $m^{-1/3}$
0 1 2 3 4 5 6 7 8 9 10 11 12 13 14
C_n from Slit Scanning Imager, in units of 10^{-8} $m^{-1/3}$
0 1 2 3 4 5 6 7 8 9 10 11 12 13 14 15 16 17

Fig. VI-A-22. C_n from Shearing Interferometer vs. C_n from Slit Scanning Imager.

VI. A 6. Isotropy of Optical Turbulence

Most of the MTF data reported in this report have been taken with the slit of the slit-scanning telescope moving in the horizontal direction. This was chosen as the preferred direction primarily because point laser source targets are occasionally located on shipboard. The lateral motion of a source of the ship is smaller in the horizontal direction than in the vertical direction, making the tracking problem easier to handle. To settle the question, whether the usual assumption that the optical turbulence is isotropic, is correct or not, the new 8 inch diameter Celestron portable MTF system was built with its detector scanning system able to rotate so as to scan in either the horizontal or vertical directions. A number of tests have been made in the field, mostly for path lengths of about 13 km. No discernible difference has been observed in the line-spread function for horizontal vs. vertical scan, indicating that the assumption of isotropic behavior is correct.

VI. B. Scintillation

1. Aperture Averaging

Initial aperture averaging tests with the CW scintillation equipment were carried out on a 286 m indoor range with artificial turbulence, and indicated that significant aperture averaging occurred with apertures smaller than the first Fresnel Zone, using a He/Ne laser as source. Measurements were made with apertures 3.5, 9, 18 and 23 mm diameter, and relative values computed using the 3.5 mm aperture as reference. Results for five data sequences and a composite of the results are shown in Fig. VI-B-1. On the basis of these preliminary results full scale over-sea experiments under regular measurement conditions were carried out on October 22 and 27, 1973, on a 4.05 km path across Monterey Bay (Schroeder, 1973). The measurements were made using the comparison technique described in Section VI. C.2, with a 23 mm aperture detector as reference.

October 22, 1973

Conditions were clear but with rather strong southerly winds. Deviations between log-intensity variance values obtained with reference and test detectors were found in addition to the effect of changing diameter and the temporal variations. Rather than the ratio of variances, the difference $\sigma_{\ell I}(D) - \sigma_{\ell I}(Ref)$ was found to be a consistent measure of the aperture averaging effect, and is shown plotted versus D in Fig. VI-B-2. The data show a consistent rise to a maximum at 4.8 mm.

October 27, 1973

Conditions were sunny, with light variable winds, predominately from the North-West. Again the quantity $\sigma_{\ell I}(D) - \sigma_{\ell I}(23\ mm)$ was found to show consistent behavior with a maximum value at D = 4.8 mm. (Fig. VI-B-3)

These results indicated that for this equipment a 4.8 mm aperture showed the maximum variance; i.e., best approximated the ideal point detector. For this diameter correction appeared

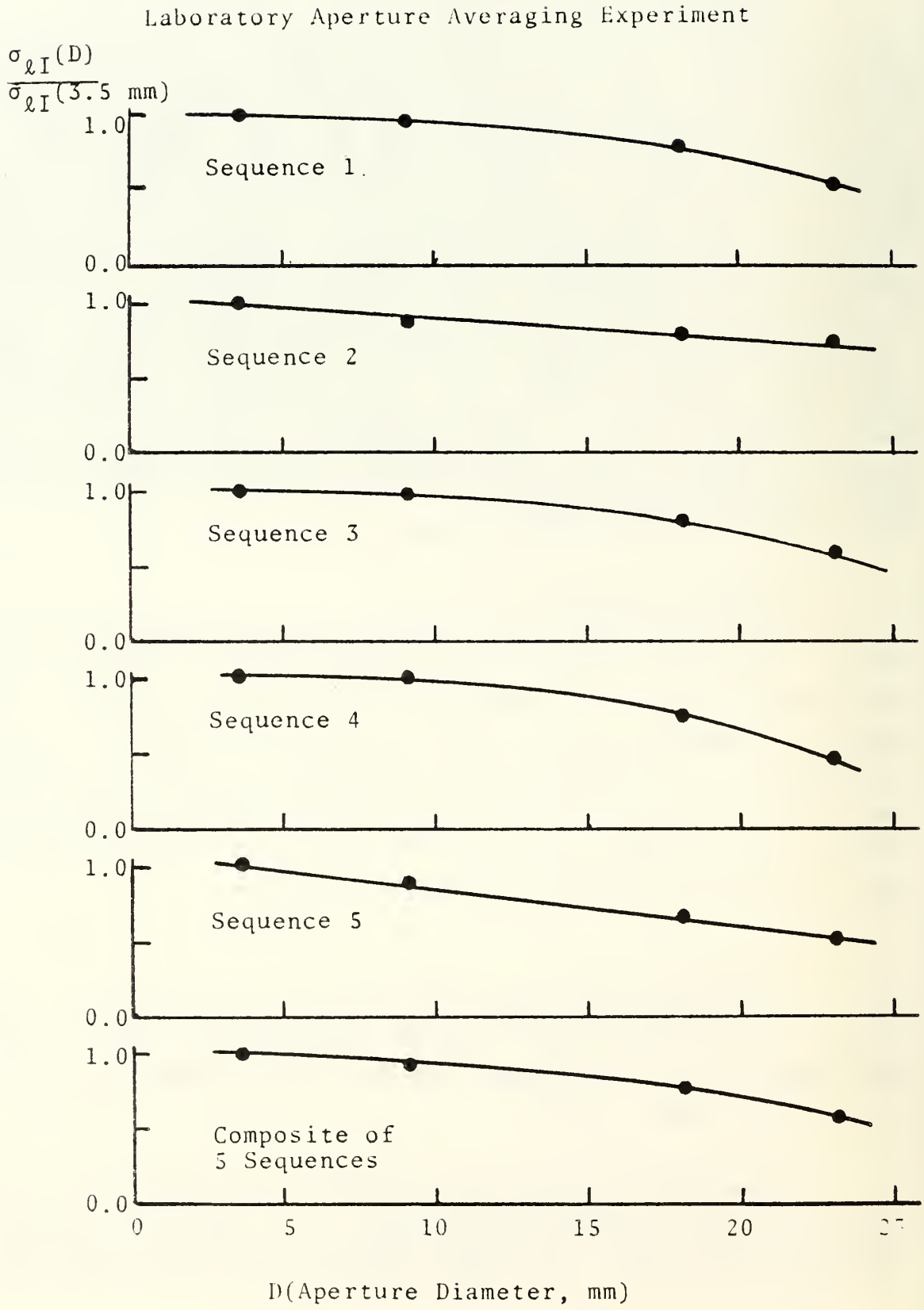

FIG. VI-B-1. LABORATORY APERTURE AVERAGING EXPERIMENT

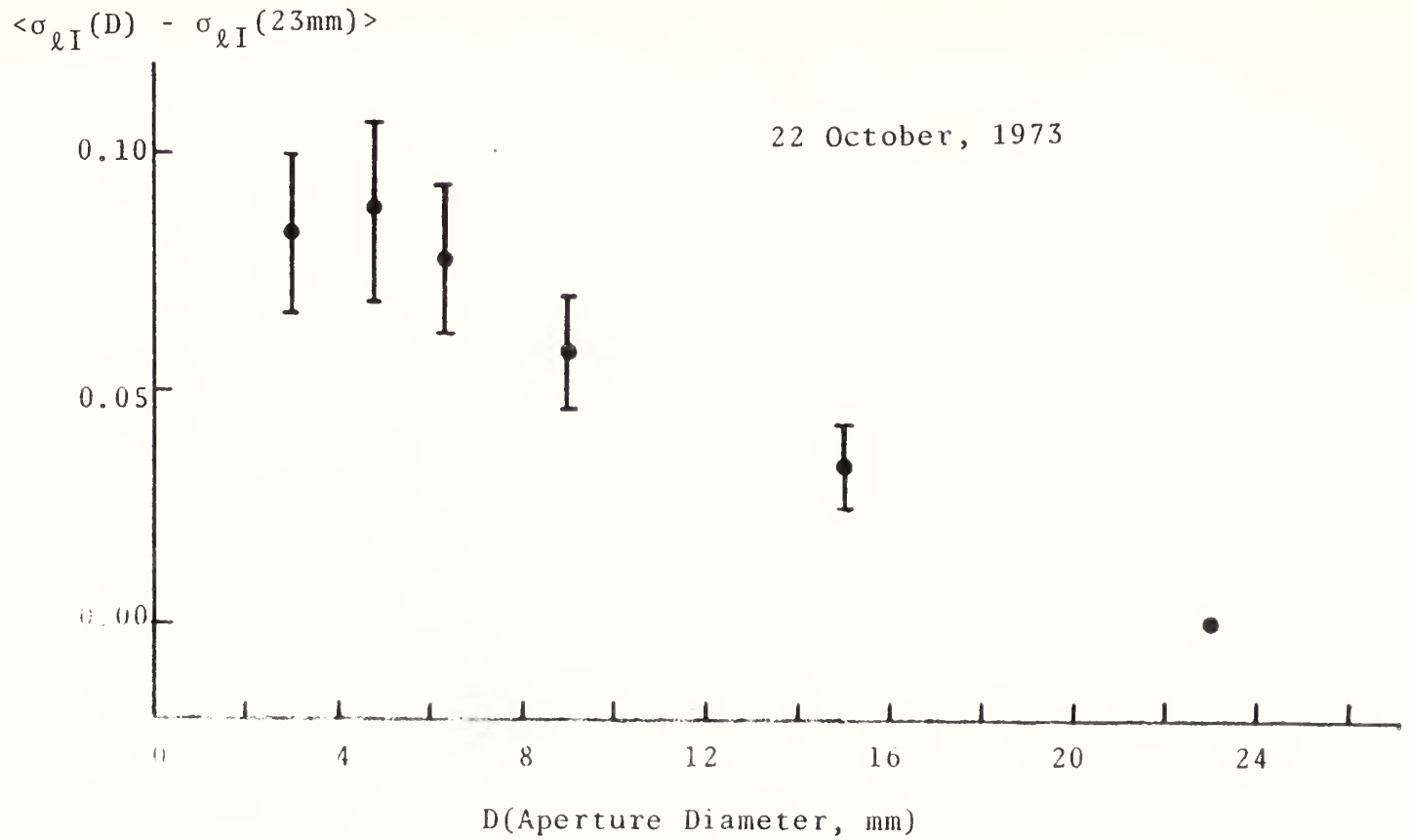

Fig. VI-B-2. Average value of $\sigma_{\ell I}(D) - \sigma_{\ell I}(23mm)$ vs aperture diameter, for 22 October, 1973

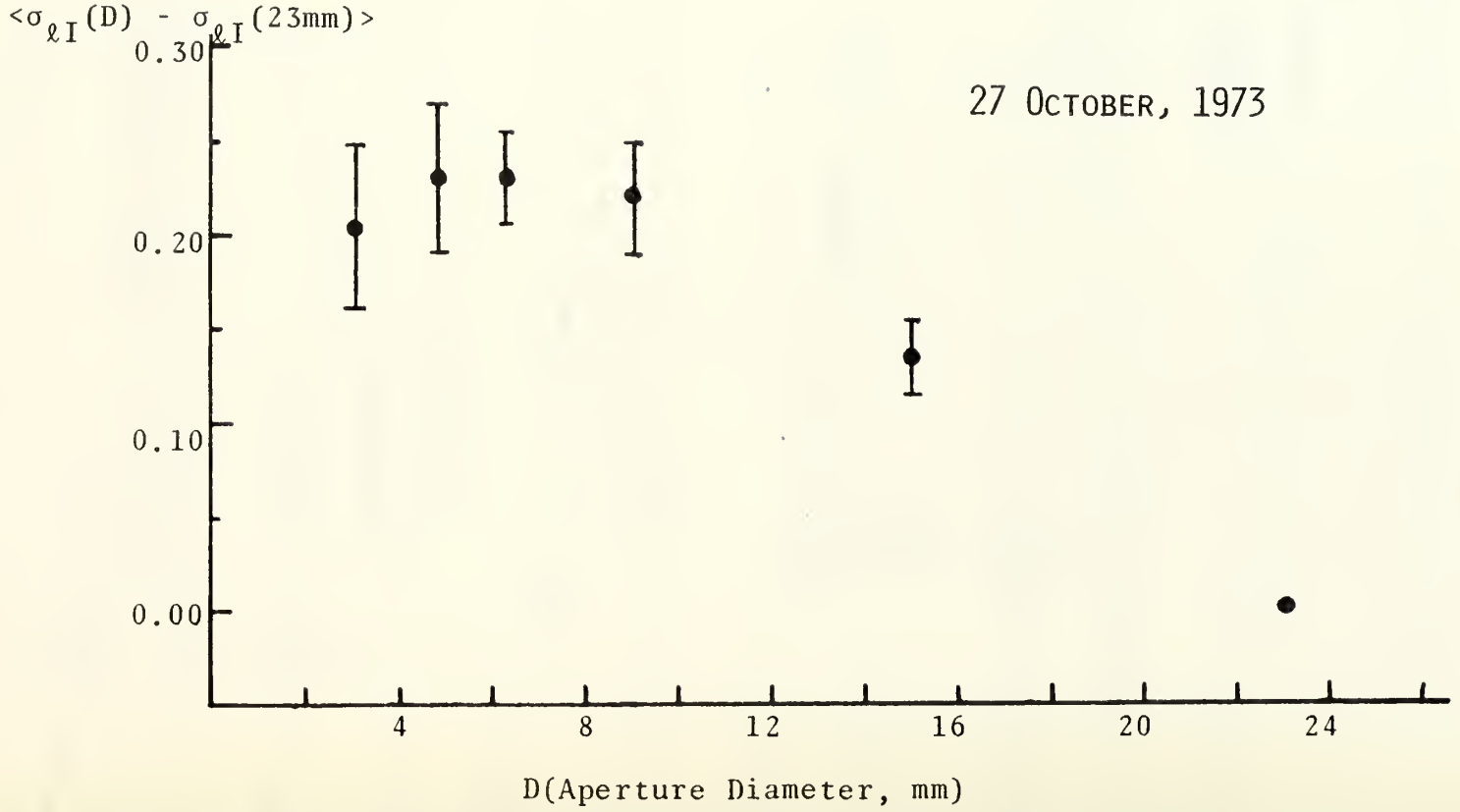

Fig. VI-B-3. Average value of $\sigma_{\ell I}(D) - \sigma_{\ell I}(23mm)$ vs aperture diameter, for 27 October, 1973.

to be unnecessary, and whenever possible the CW scintillation apparatus was operated with this aperture. The correction factor $\sigma_{\ell I}(O)/\sigma_{\ell I}(D)$ was dependent on $\sigma_{\ell I}$ but not consistent with previously published models. An empirical interpolation procedure using data from NPS experiments together with published data of Fried, Mevers and Keister (Fried, 1967- 3) was devised for apertures up to one inch in diameter.

Further measurements of aperture averaging effects were made using the chopped-beam scintillation equipment, to extend the results previously obtained with the CW system. Measurements were carried out over five different ranges under different path conditions listed below. A summary of experiments is shown as Table VI-B-1.

a) "Corridor"; a doubled path through a basement corridor, with a total path of 280 meters. The ventilation system and heating ducts provided a reasonable level of turbulence; the irradiance distribution was found to be log-normal. This range was used only for preliminary measurements.

b) Navy Annex; a 336 meter path over a level road surface without local eddy effects from buildings.

c) Spanagel-Coast Guard Wharf; a convenient check-out location with transmitter on the roof of Spanagel Hall at NPS, and detectors in the equipment bus in the parking lot at the Coast Guard Wharf, Monterey (see map, Fig. VI-B-4). The surroundings of the optical path were very irregular, with downward slant from about 70 meters to 10 meters, one third over water, the remainder over buildings and roads. The experiments over this 2335 meter path were found to be under conditions of saturated scintillation.

d) Holiday-Hopkins; a land-to-land range 97% over water, with the transmitting equipment in the parking lot at the Monterey Holiday Inn, and the receiving and processing equipment in the instrumentation bus on the point at the Hopkins Marine Station.

e) Pt. Pinos-ACANIA; a variable length sea-land range with the transmitters on the instrumentation bus on the shoreline at

TABLE VI-B-1. SUMMARY MATRIX OF EXPERIMENTS CONDUCTED

Date	Location	Path Length (m)	Detectors	1(Apt Ave) 2(W/Freq Anal)	Aperture Diameters (mm)
(7-8) Feb 76	Corridor	280	(V)Avalanche/ (F)PIN-5DP (No Field Lens)	1	22.6, 20, 17 14, 12, 10, 7, 6 5, 4, 3, 2
10 Feb 76	Corridor	280	"	1	22.6, 20, 17 14, 12, 10, 7, 6 5, 4, 3, 2
(5-6) Mar 76	Spanagel Roof Coast Guard	2335	(V)Avalanche/ (F)PIN-5DP (W/Field Lenses)	1	24.3, 20, 16, 12 7, 6, 5, 4, 3, 2
11 Mar 76	Holiday Inn-Hopkins Lab	4230	(V)Avalanche/ (F)HgCdTe (No Field Lens)	1	41.7, 24.3, 14
30 Mar 76	Pt. Pinos-ACANIA	1600	(V)Avalanche/ (F)PIN-5DP (W/Field Lenses)	1	38, 31, 24.3 17, 10
2 Apr 76	Pt. Pinos-ACANIA	1600	"	1	40, 30, 20, 10
(7-9) Apr 76	Corridor	280	"	1,2	40, 30, 20, 15 10, 7, 5, 3, 2, 1.5
20 Apr 76	Navy Annex	336	"	1,2	40, 30, 20, 15 10, 7, 5, 3
27 Apr 76	Pt. Pinos-ACANIA	1650	"	1	40, 35, 30, 25 20, 16, 13, 10 5, 4
29 Apr 76	Pt. Pinos ACANIA	1442	"	1,2	40, 35, 30, 25 20, 16, 13
30 Apr 76	Pt. Pinos-ACANIA	1625	"	1,2	40, 16, 13, 10, 5

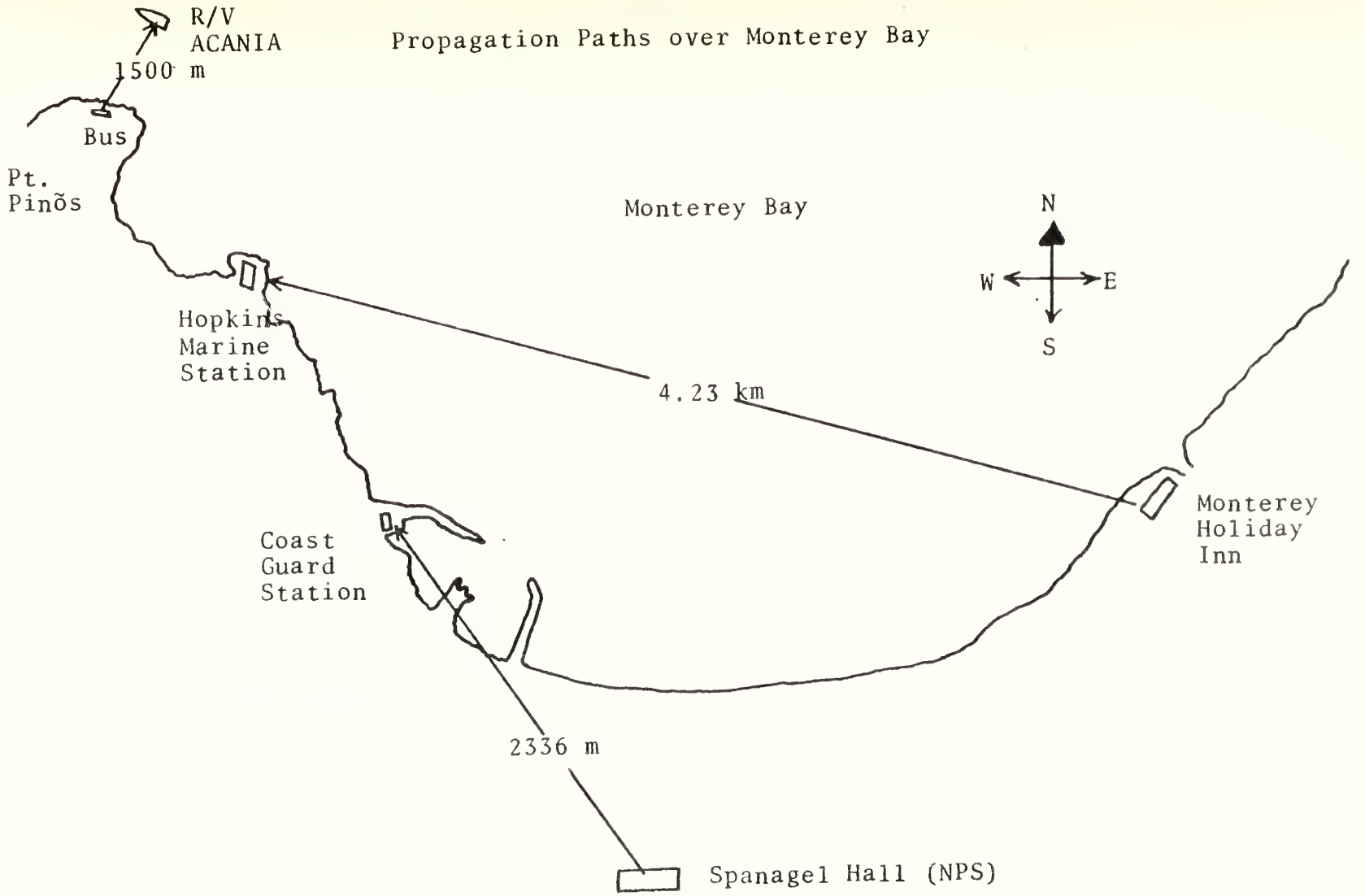

Fig. VI-B-4 Propagation paths used for aperture averaging studies

Pt. Pinos and the receiving and processing equipment on board the R/V ACANIA, using the gyro-mounted platform.

Corridor experiments were carried out on 7 February, 10 February and 7-9 April, 1976. Each data set required several hours of experimentation; data were taken mostly during the night-time hours when conditions should be most stable. However, $\sigma_{\ell I}$ did vary appreciably during some data periods. The data taken during the period 2235, 7 February to 0515, 8 February are tabulated in Table 2, showing the log-intensity standard deviation for the fixed and variable detectors, G(D), and G(D) normalized to its minimum value. The average $\sigma_{\ell I}$ over this time was .33. Data from the period 1655 to 2240, 10 February 1976, are shown tabulated in Table 3. Here the log-intensity standard deviation varied from .398 to .454, with a mean of .428. This implies a C_n in the vicinity of 3×10^{-7} $m^{-1/3}$.

Similar data were obtained during the night-time hours of April 8/9, 1976, with a range of $\sigma_{\ell I}$ from .057 to .098, and C_n in the vicinity of 6×10^{-8} $m^{-1/3}$, with an average $\sigma_{\ell I}$ of .084. The summarized results for these three experiments are shown in Fig. VI-B-5, showing G(D) plotted against normalized aperture diameter. These results immediately indicated that aperture averaging could be a significantly large effect for larger apertures and shorter paths. The averaging factor shows a minimum at a reduced diameter of approximately unity, with somewhat erratic behavior at lower reduced diameters. Aperture averaging is most important at low levels of turbulence, $G(D)_{min}$ and $G(D)/G(D)_{min}$ rising toward unity as $\sigma_{\ell I}$ increases.

An overland experiment was carried out over the Navy Annex path during the period 2128 to 2345, 20 April 1976. During this period the fan-scan transmitter was used; the temperature averaged 12°C, with light or no wind and clear sky. C_n was in the range of 8 to 10×10^{-8} $m^{-1/3}$, with $\sigma_{\ell I}$ averaging .162. The results were qualitatively similar to those previously described, but with $G(D)_{min}$ of .67.

TABLE VI-B-2

7-8 February, 1976

D (mm)	$\sigma_{\ell I}[V(D,t)]$	$\sigma_{\ell I}[F(D_o,t)]$	G(D)	$G(D)/[G(D)]_{min}$
22.6	.218	.426	1.000	2.17
20	.251	.419	.854	1.86
17	.258	.414	.821	1.78
14	.228	.325	.729	1.58
12	.258	.361	.716	1.56
10	.265	.331	.639	1.39
7	.267	.273	.523	1.14
6	.280	.276	.504	1.10
5	.292	.267	.468	1.02
4	.306	.281	.470	1.02
3	.308	.277	.460	1.00
2	.324	.306	.483	1.05

TABLE VI-B-3

10 February, 1976

D (mm)	$\sigma_{\ell I}[V(D,t)]$	$\sigma_{\ell I}[F(D_o,t)]$	G(D)	$G(D)/[G(D)]_{min}$
22.6	.431	.431	1.000	1.55
17.0	.465	.433	.930	1.44
12.0	.541	.401	.740	1.14
7.0	.579	.398	.686	1.06
6.0	.701	.454	.647	1.00
5.0	.676	.441	.651	1.01
4.0	.599	.426	.710	1.10
3.0	.716	.426	.594	.92

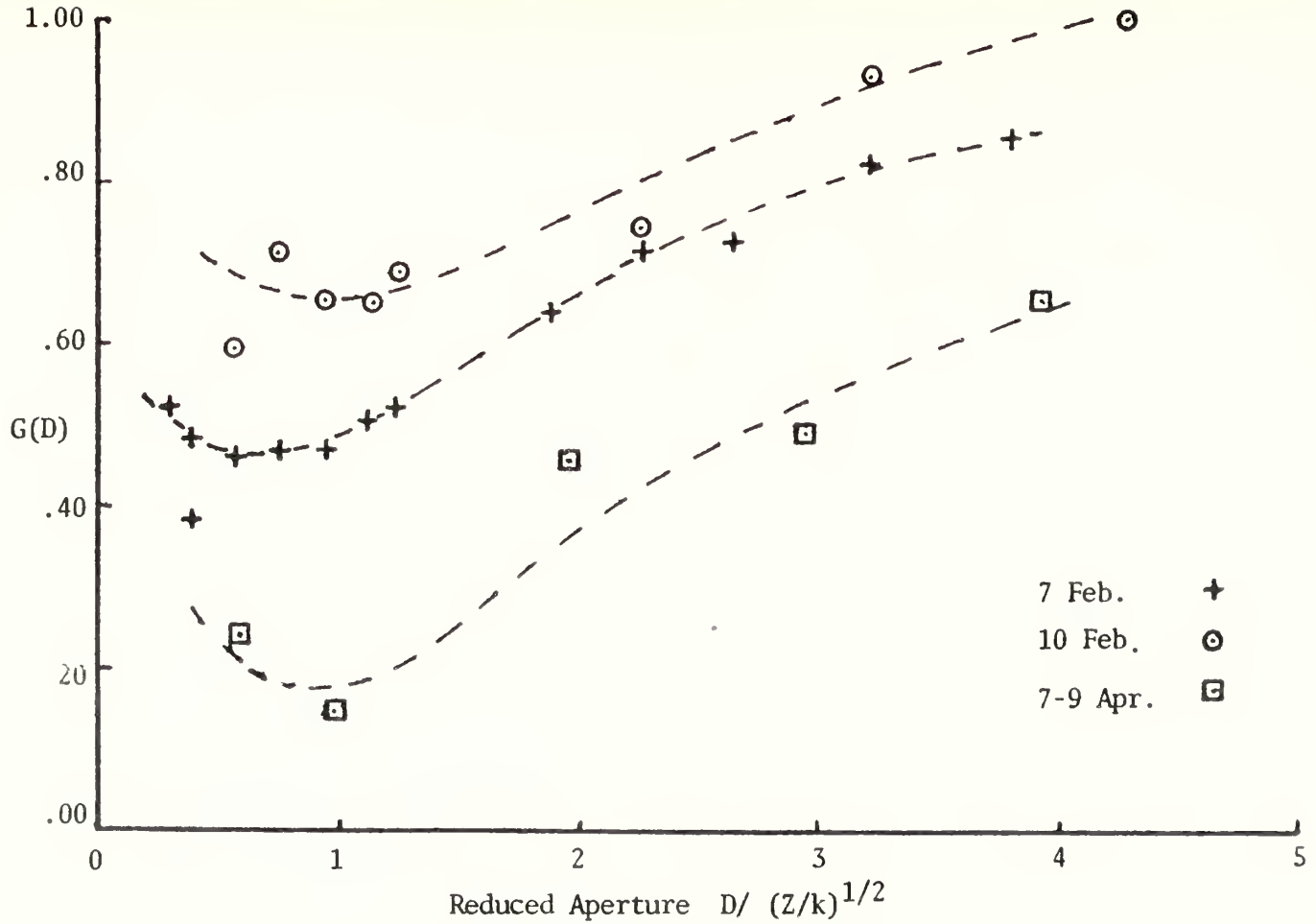

Fig. VI-B-5. Aperture factor vs reduced aperture.

An experiment was carried out from Spanagel Hall to the Coast Guard Wharf overnight on March 5 to 6, 1976, under high turbulence conditions, with an average $\sigma_{\ell I}$ of 1.01. Measured values of G(D) shown in Figure VI-B-6indicate that aperture averaging is essentially insignificant under such saturated conditions at least for apertures up to the 24.3 mm used.

Over water experiments were carried out on the Holiday Inn-Hopkins path on 11 March 1976, and on the ACANIA-Pt. Pinos path on 30 March, 2 April, 27 April, 29 April and 30 April 1976, with path lengths of 1600 meters on all days except the 29th, when the range was reduced to 1442 m. On 30 March and 27 April, operating conditions on the ACANIA were difficult, with moderate to high seas, and both lock of the gyroscopic platform and tracking from shore were erratic. Data for these runs did not fit with data from the remaining measurements. Data for 30 March are shown as Fig. VI-B-7. All data for the remaining measurements are consistent with the conclusions of the corridor measurements, and are shown summarized in Fig. VI-B-8, together with the Holiday-Hopkins data.

A comparison of the values of the correction factor calculated from these measurements, with that of Fried (67-1),is given as Fig. VI-B-9 for the laboratory data and Fig. VI-B-10for the measurements at sea. The Fried semi-empirical curve is drawn for $C_{\ell}(O) = 2^{-5}$, i.e.,$\sigma_{\ell I} = .68$, the smallest value listed by Fried. Extrapolating the Fried data, the measurements appear to give excellent agreement with the Fried model for $C_{\ell}(O)$ of $2^{-6.5}$. Thus, the Fried correction can be used as an empirical correction for the range of apertures and log-intensity variances used to date in the NPS experiments. However, the NPS data show some systematic differences from the previous theory, which should be noted:

1) the corrections do not approach an asymptotic value at zero aperture diameter, but show an "optimum" detector aperture at $D/(Z/k)^{\frac{1}{2}} = 1$.

Spanagel Roof to Coast Guard Parking Lot, (5-6) March 1976
Saturation Conditions for $\sigma_{\ell 1}$

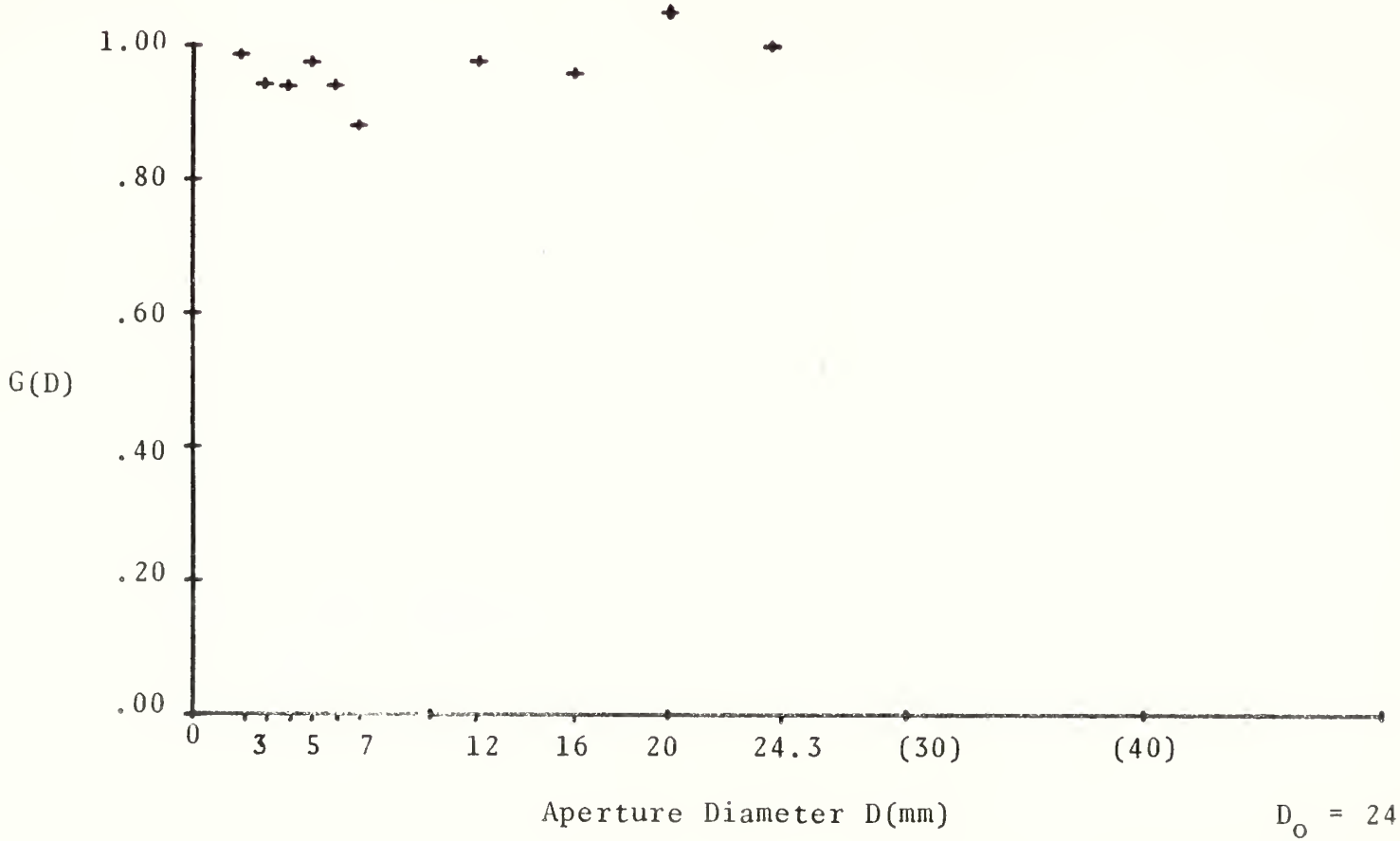

D_o = 24.3 mm
D_{min} = 2 mm

Fig. VI-B-6. G(D) vs aperture diameter D, 5-6 March, 1976

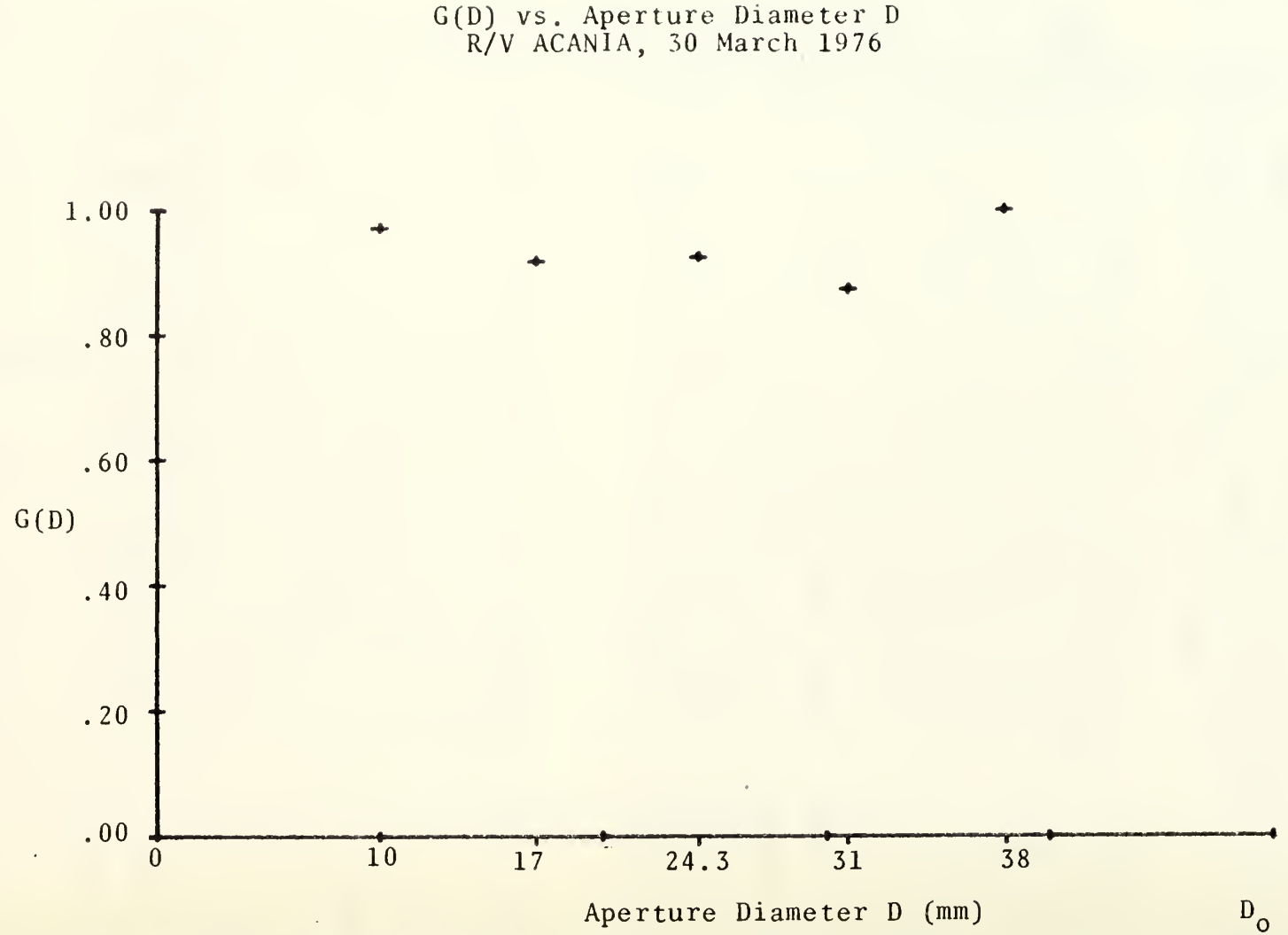

Fig. VI-B-7. G(D) vs aperture diameter D, 30 March, 1976

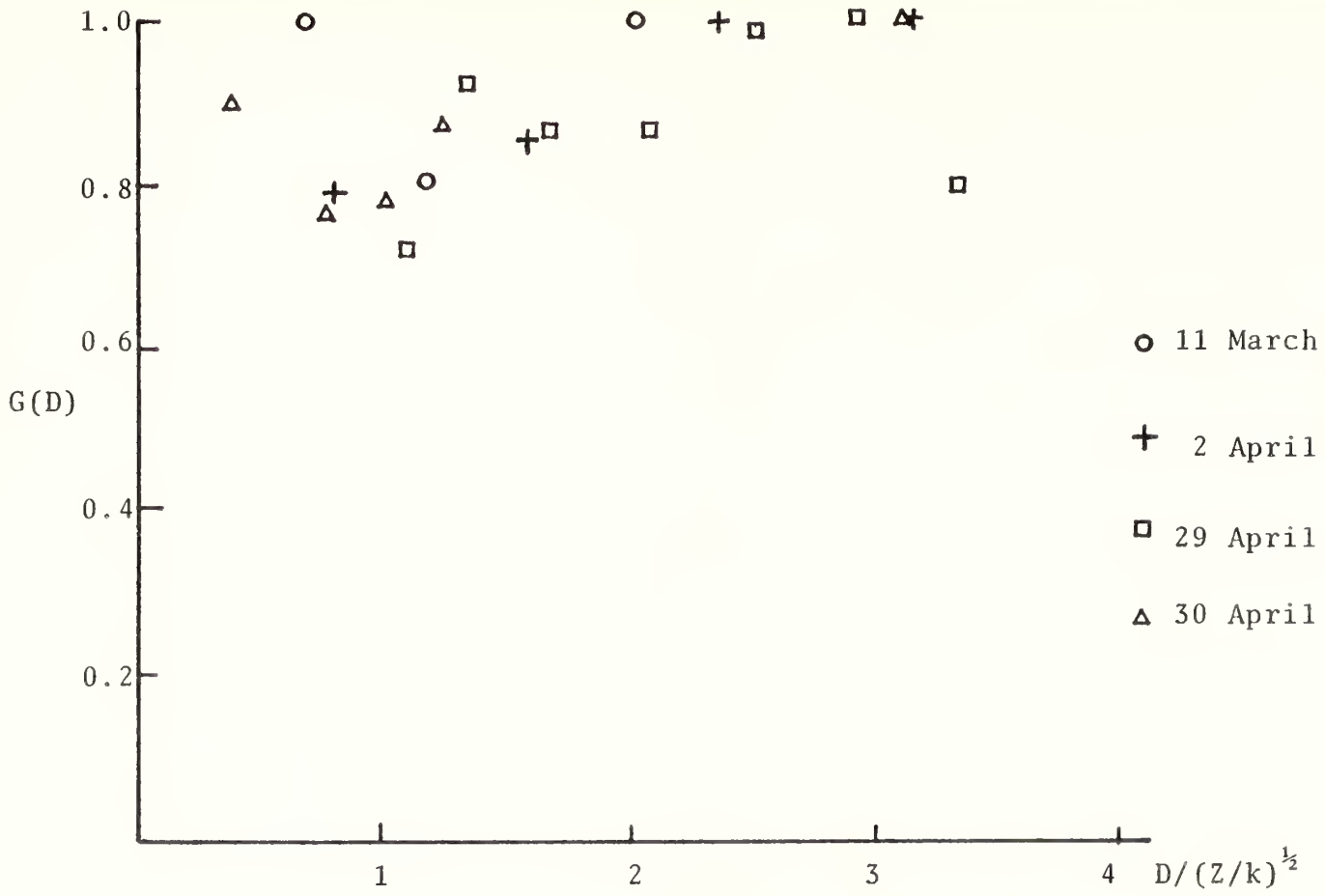

Fig. VI-B-8. G(D) as a function of reduced aperture.

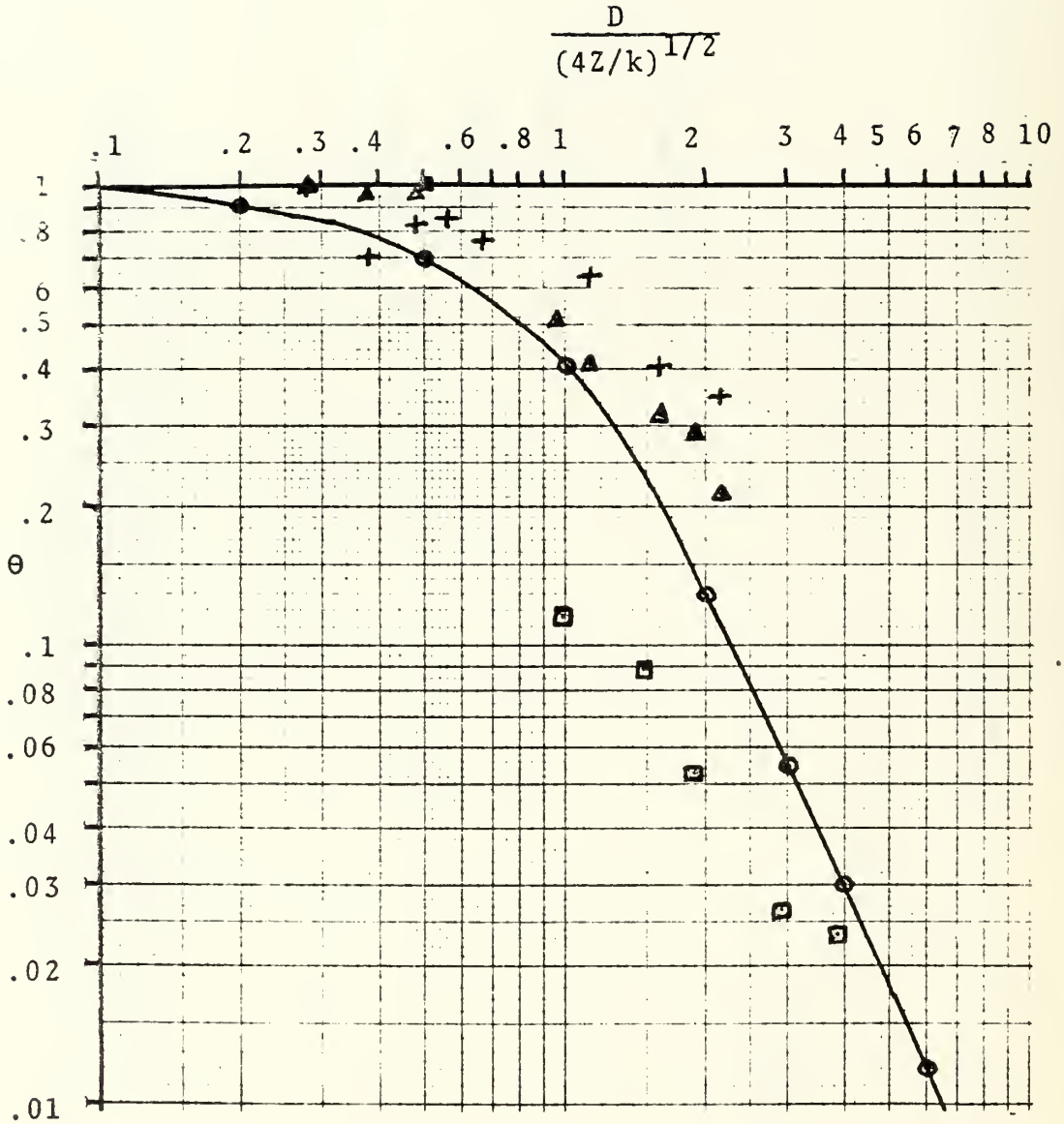

△ 7 Feb (Corridor)

⊡ (7-9) Apr (Corridor)

⊙ Fried's Theoretical for $C_{\ell}(0) = 2^{-5}$

\+ 10 Feb (Corridor)

Fig. VI-B-9. Empirical vs Theoretical Θ vs. $\frac{D}{(4Z/k)^{\frac{1}{2}}}$

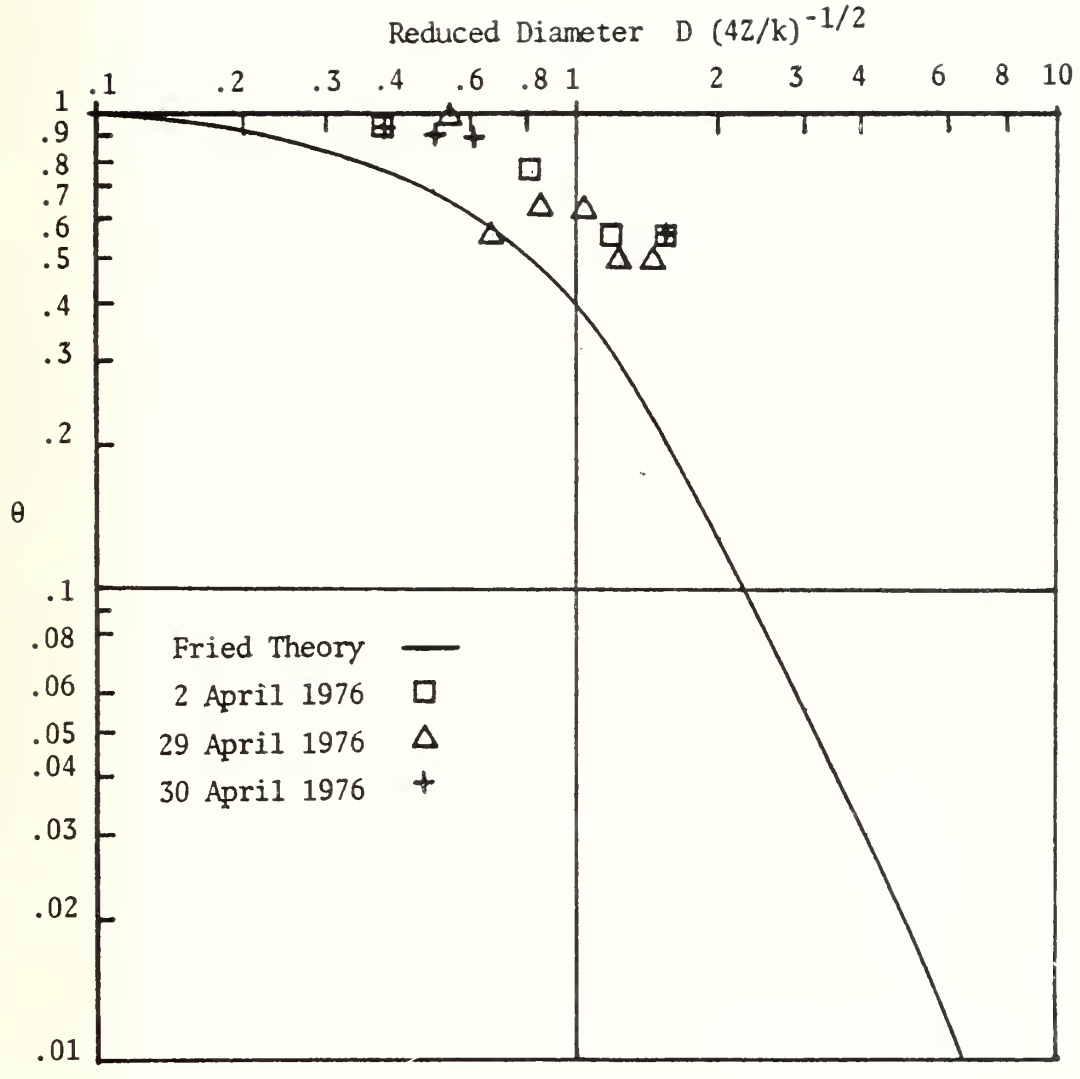

Fig VI-B-10. θ (D) = $G(D)_{min}$ / G(D) vs Reduced Aperture.
Data taken at sea.

2) For the range of measurements used, the correction factor becomes less important as the log-intensity variance increases, with only small correction needed in the saturation regime. This variation is contrary to that deduced by Fried.

3) The data obtained on the indoor range at very low turbulence levels show a correction ($1/\mathcal{H}$) much greater than the remainder of the data. This inconsistency is not yet understood.

VI. B. Scintillation

2. Wavelength Effects

The theoretical relationship used for evaluation of C_n^2 from scintillation involves a factor of $k^{7/6}$. Since the relationship is based on a "small fluctuation" theory, it ceases to be valid as $\sigma_{\ell I}$ becomes comparable to unity, the variance of the log-intensity beginning to saturate at values about .65. The upper limit of validity for each wavelength of interest was given for conditions of moderate and high turbulence in V. C.5.

Measurements of scintillation have been made at wavelengths of .4880, .6328, 1.06 and 10.6 μm. In most cases only one or two of these have been used as consistent with the range and expected turbulence conditions. An observation of the joint influence of range and wavelength was made in May 1975. Concurrent measurements were made of scintillation at .6328 μm on board the R/V ACANIA, moored 2011 meters off Pt. Pinos, and at 10.6 μm Fort Ord to Pt. Pinos, over a range of 10.27 km. Fig. VI-B-11. shows results obtained over the period from 1900 hours, 22 May, to 0600 hours, 23 May. The values of C_n obtained at the two wavelengths are shown to agree within a factor of two. While the visible measurements tend to give higher values than the infrared, they are not consistently higher, and the differences are more probably associated with the greater coastline influence over the shorter path than with the technique of measurement used.

A specific experiment to test the wavelength dependence was carried out on 10 and 11 March 1976, using all four wavelengths over the same range, 4229 meters, from the Holiday Inn to the Hopkins Marine Station. Fig. VI - B-12 displays the results of 10 March obtained at .6328 μm and 10.6 μm over the same path. The values of $\sigma_{\ell I}$ for the visible were consistently in the range 0.5 to 0.7, somewhat below the expected threshold for the onset of saturation, while $\sigma_{\ell I}$ for the infrared was in

Fig. VI-B-11. Scintillation, Monterey Bay, 22 May, 1975

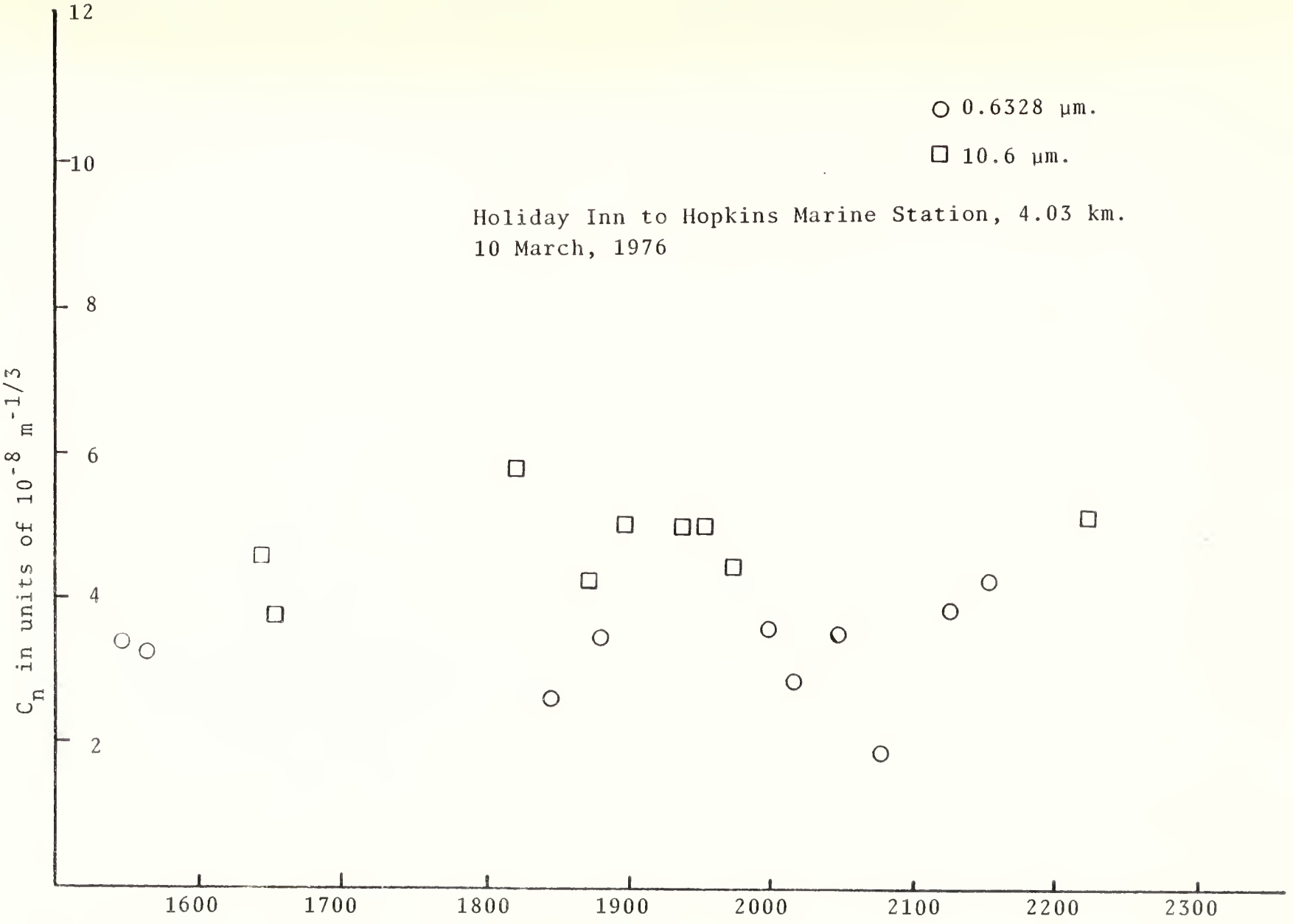

Fig. VI-B-12. C_n vs time for two wavelengths

the range 0.1 to 0.2. The .6328 μm points appear to fall regularly below the 10.6 μm points, which may indicate slight tendency to saturate.

The entire range of wavelengths was used on the afternoon and evening of 11 March, during which time C_n apparently increased by about a factor of 10. The results are shown in Fig. VI-B-13. Only three values were obtained for blue, over a short time range. All the other wavelengths appeared to track the rise consistently, except that the red (.6328 μm) appeared to saturate at the higher values of C_n. At 2200 hours and 2305 hours the values of C_n at .6328 μm were registered at 1.14 and 1.16 respectively, values similar to those reported in saturated cases (Lutomirski et al, RAND Report, 1973). In the range below saturation, multiwavelength experiments indicate that values of $\sigma_{\ell I}$ in scintillation yield values of C_n essentially independent of the wavelength used for the measurement.

3. Saturation of Scintillation

In addition to the evidence of saturation described in the previous section, a further experiment to confirm the saturation effect was carried out between the R/V ACANIA and a shore station at Pt. Pinos, during a period of nearly constant conditions on 28 August 1975. During the afternoon period from 1300 to 1655 on this day, only small changes were observed in C_T^2 and weather conditions remained almost constant. The ACANIA was stationed successively at a number of offshore positions ranging from 610 to 2871 meters from the shore station. Measurements of scintillation were made at similar positions both outward bound and returning. To separate the saturation effect from the effect of range, the measured values of $\sigma_{\ell I}$ are shown in Fig. VI -B-14 plotted against the 11/12 power of range; the theoretical range dependence should then result in a linear plot assuming C_n^2 remains constant. This figure shows that $\sigma_{\ell I}$ attains a maximum value of .95, remaining approximately constant from

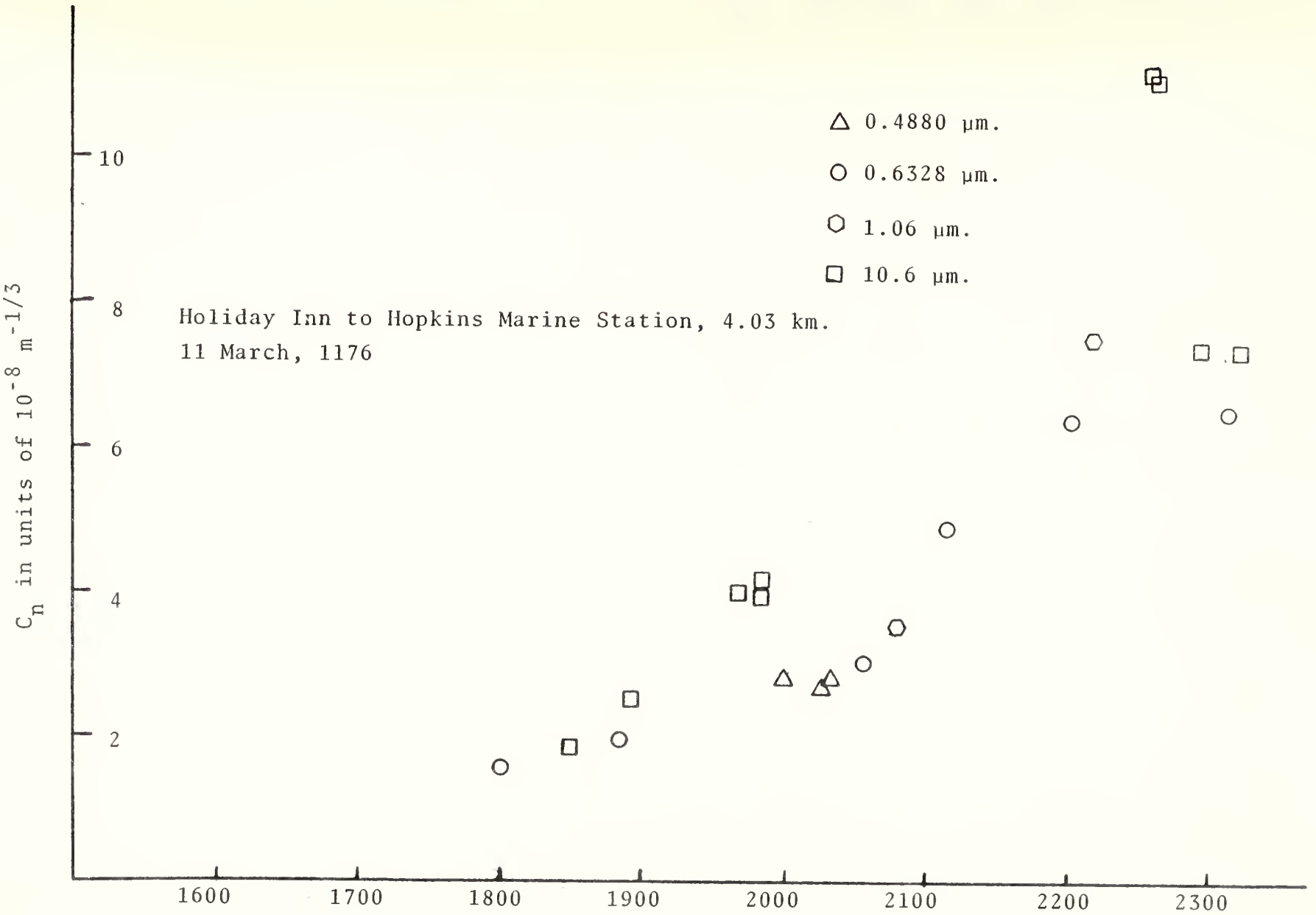

Fig. VI-B-13. C_n as a function of time for four wavelengths.

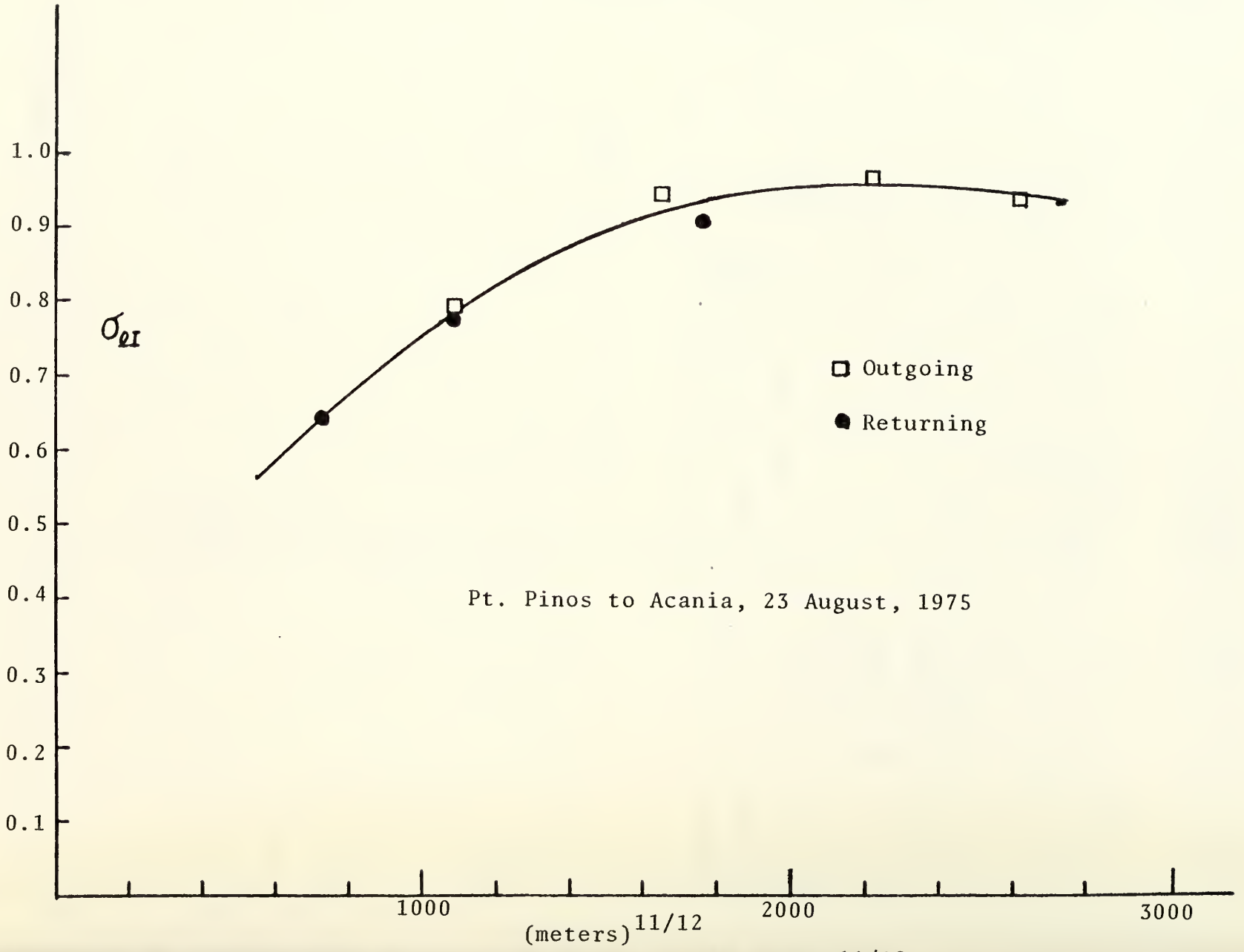

Fig. VI-B-14. Standard deviation of log-intensity vs (range)$^{11/12}$

1600 $m^{11/12}$ to 2600 $m^{11/12}$. Values obtained on the outward and return legs of the ships path agree closely, indicating that the experiment was not disturbed unduly by temporal changes in condition.

In view of these measurements it is believed that the wavelength dependence is adequately described by current theory, and that onset of saturation occurs approximately as predicted. The choice of wavelength suitable to range and conditions can therefore be made with confidence. It is realized however, that path weighting of C_n^2 could invalidate scintillation measurement of C_n^2 in inhomogeneous turbulence. In all later experiments scintillation measurements have been restricted to such wavelengths that valid results might be expected over the paths used. In addition, $\sigma_{\ell I}$ is monitored continually during the experiments, and values nearing .9 treated with suspicion.

4. Temporal Frequency Spectra of Scintillation

The temporal frequency spectrum of scintillation has been predicted by Tatarski (1) on the basis of the Taylor hypothesis, i.e., the assumption that the turbulent refractive index field may be considered frozen in time and convected across the beam with the mean wind speed. This gives a characteristic frequency $f_o = v/2\pi p_\ell$ where p_ℓ is the intensity correlation length; in the usual small fluctuation approximation $\sigma^2_{\ell I} << 1$, $p_\ell = \sqrt{z/k}$, this gives $f_o = v/2\pi\sqrt{z/k}$. Clifford (2) has calculated the temporal frequency spectrum for spherical waves, giving the asymptotic forms

$$\phi(f) = .245\ (\sigma_{\ell A}{}^2)(1/f_o)\ [1 + 0.119\ \Omega^{4/3}]$$

$$\phi(f) = 2.81\ (\sigma_{\ell A}{}^2)(1/f_o)\ \phi^{-8.3}$$

where $\phi = f/f_o$ and $f_o = \bar{v}/(2\pi\lambda z)^{\frac{1}{2}}$.

This spectrum is subject to the filtering action of a finite aperture due to the convective drift time across the aperture, which causes a rapid roll-off at frequencies above $f' = 2\bar{v}/D$.

Experimental measurements of the scintillation frequency spectrum have been made in conjunction with a number of measurements (A.F. Schroeder, M.S. Thesis, NPS, 1973; H.R. Hall, M.S. Thesis, NPS, 1976). These fall into two groups, corresponding to the time periods, June through December 1973, and January through April 1976. During the first of these periods frequency analysis was carried out on sample scintillation data obtained across Monterey Bay between the Holiday Inn and Hopkins Marine Station. Spectral measurements were made using a wave analyzer with 10 Hz resolution on recorded log-intensity data. Power spectra were obtained by planimeter integration of the single frequency amplitude curves. The instrumentation had a low frequency cut-off at 20 Hz, and a high frequency limit of 1 kHz. During the second period analysis was carried out by playing back the recorded log-intensity signal into an EMR Schlumberger 1510 Digital Spectrum Analyzer, covering the frequency range 10 Hz to 2.56 kHz, with a sampling time of 25.6 seconds. Spectral power density

was obtained on a relative scale of 0 to -60 db.

Sample data taken in the first period are shown in Figs. VI-B-15,16. Fig. VI-B-15 is characteristic of wind speed of 8 m/sec, with f_o of 65 Hz for the characteristic frequency, and the wind speed for Fig.VI-B-16 was estimated at .5 m/sec, with f_o at 4 Hz. Both demonstrate the power-law variation with frequency predicted for f f_o; this is shown in the logarithmic plot of Fig. VI-B-17. However, the index of -4/3 differs from the Clifford prediction of -8/3. Both wind speeds show qualitatively the effect of aperture filtering in the depression of the high frequency components in the spectrum with increasing aperture diameter. However, for the range of apertures used the modification of the spectrum due to the windspeed dependence of the roll-off frequency dominates the aperture effect. Higher windspeeds favor higher frequency components.

Measurements carried out using the pulsed scintillation source and detection demodulation circuitry, during April 1976, showed the spectrum to be similar to that obtained with the CW equipment. The measurements were extended to the 2 kHz range, the limit of the demodulator, which introduced a sharp noise spike at 1.92 kHz. The data during this time period also demonstrated a power-law fall off in the frequency range out to about 500 Hz, with index in the vicinity of -2, with a relatively small amplitude plateau out to 1.5 kHz markedly dependent on the aperture diameter. Sample data are shown as Fig. VI-B-18 and Fig. VI-B-19.

In summary, the frequency spectrum of log-intensity fluctuations is dominated by the frequency range below 500 Hz. This spectral range is not greatly changed by use of a pulsed source rather than CW, and shows only minor effect of varied aperture size over the range of apertures used by NPS. This statement should be tested for extension to larger apertures if the 18-inch telescope were to be used as a scintillation receiver. The spectrum also displays a rather flat tail which extends to 1 to 1.5 kHz, which is of relatively small magnitude and much more susceptible to aperture averaging.

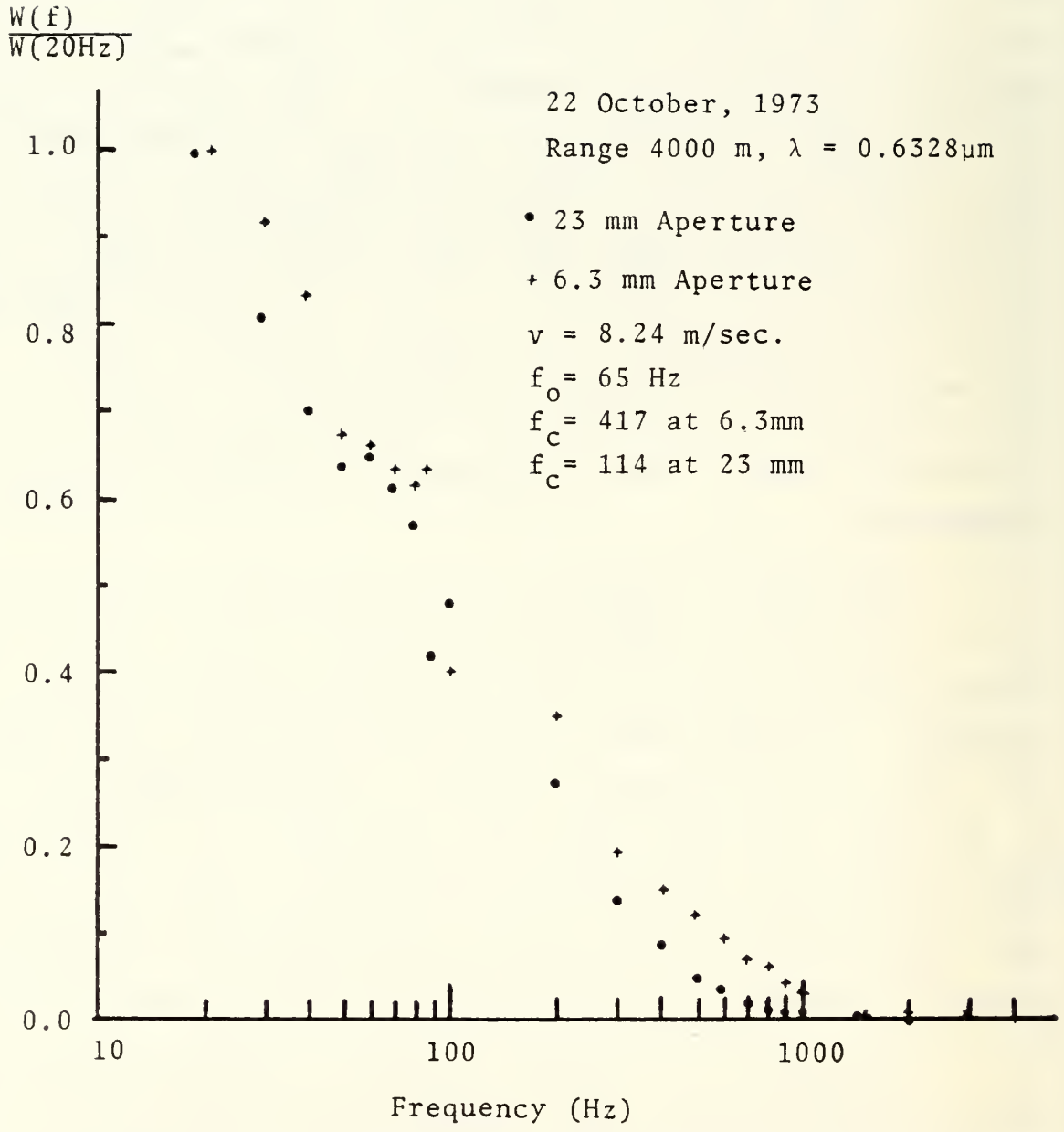

Fig. VI-B-15. Relative Spectral Power vs. Frequency for Scintillation, Wind Velocity 8 m/sec.

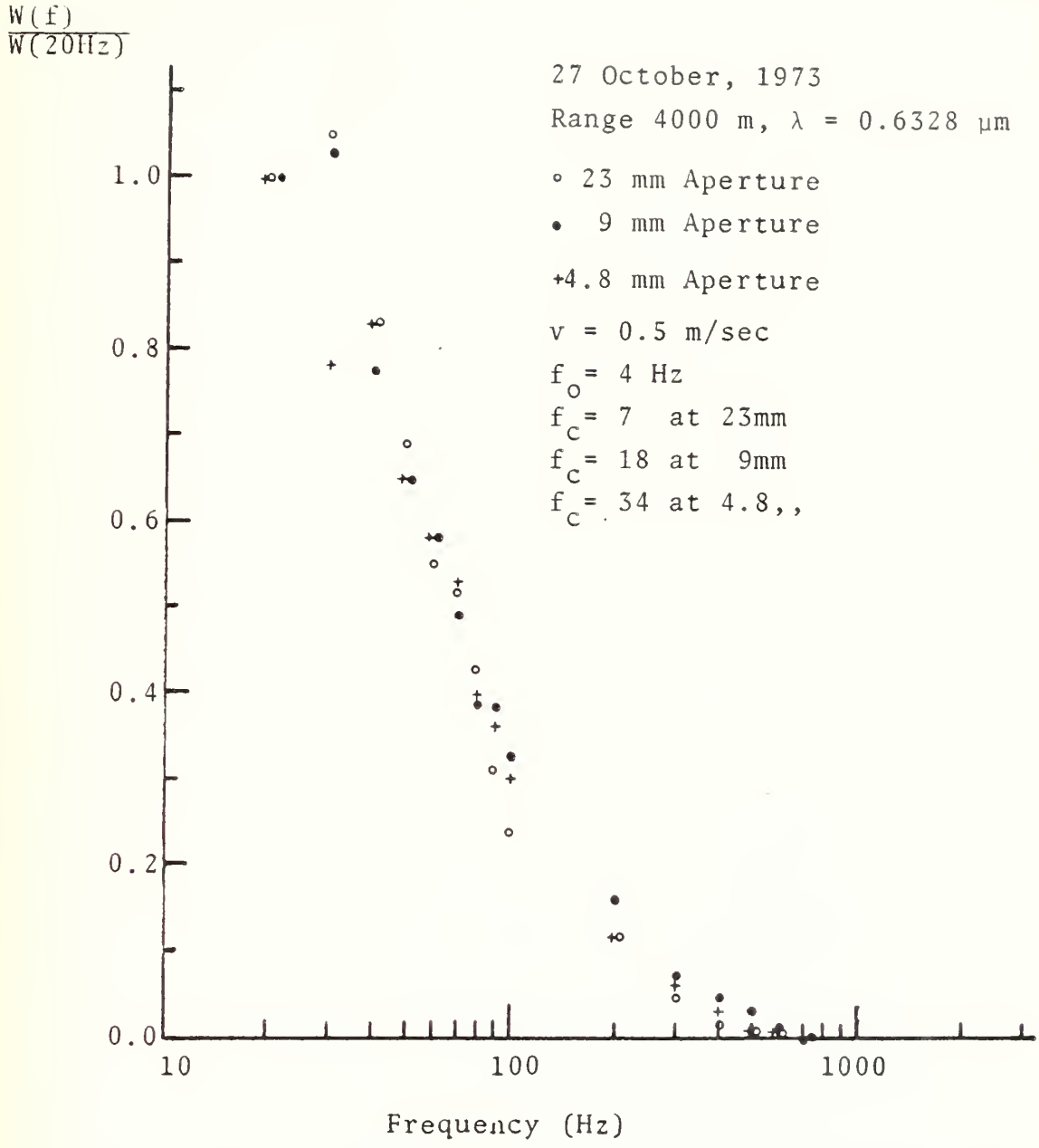

Fig. VI-B-16. Relative Spectral Power vs. Frequency for Scintillation, Wind Velocity 0.5 m/sec.

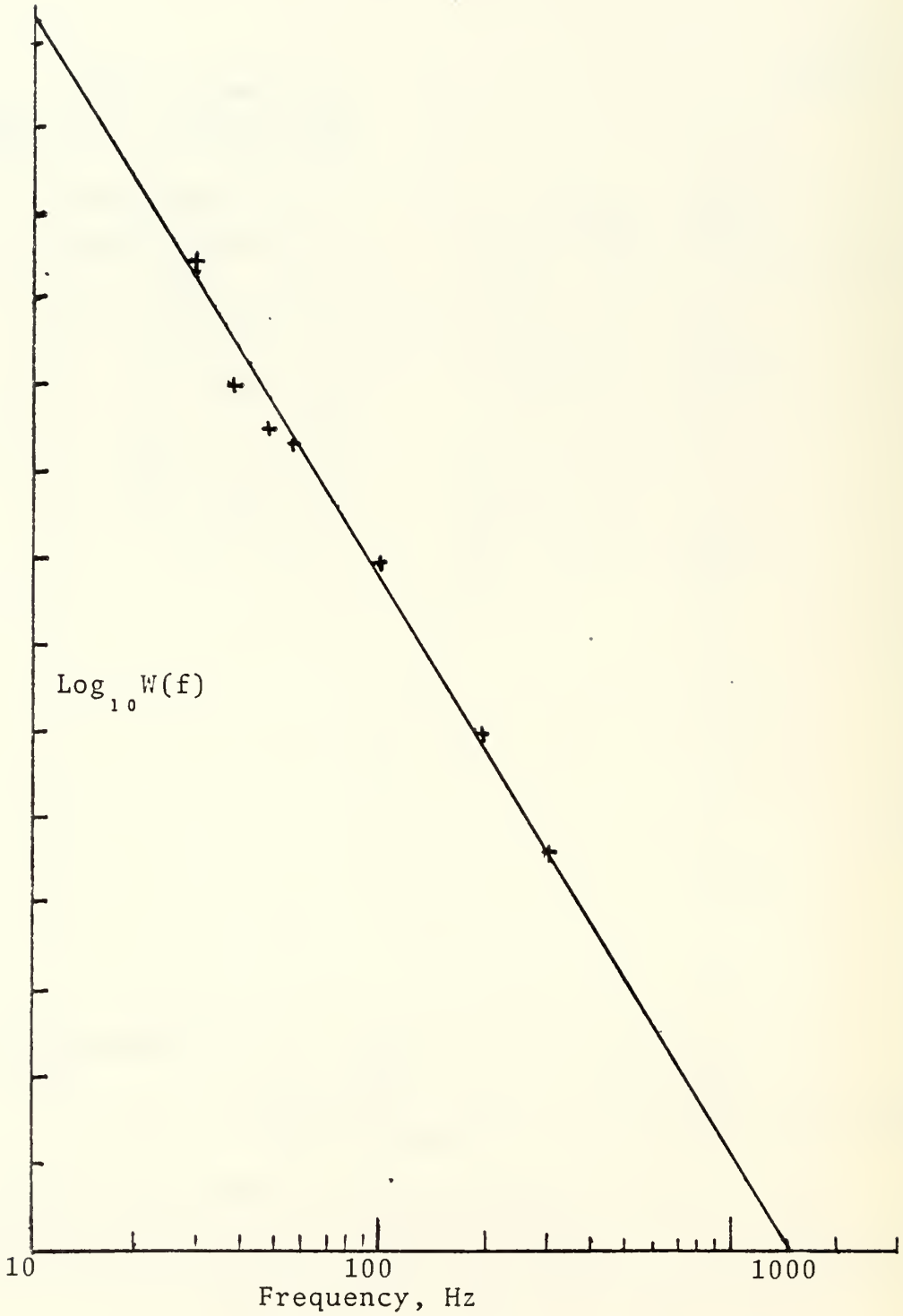

Fig. VI-B-17. $Log_{10} W(f)$ as a function of frequency.

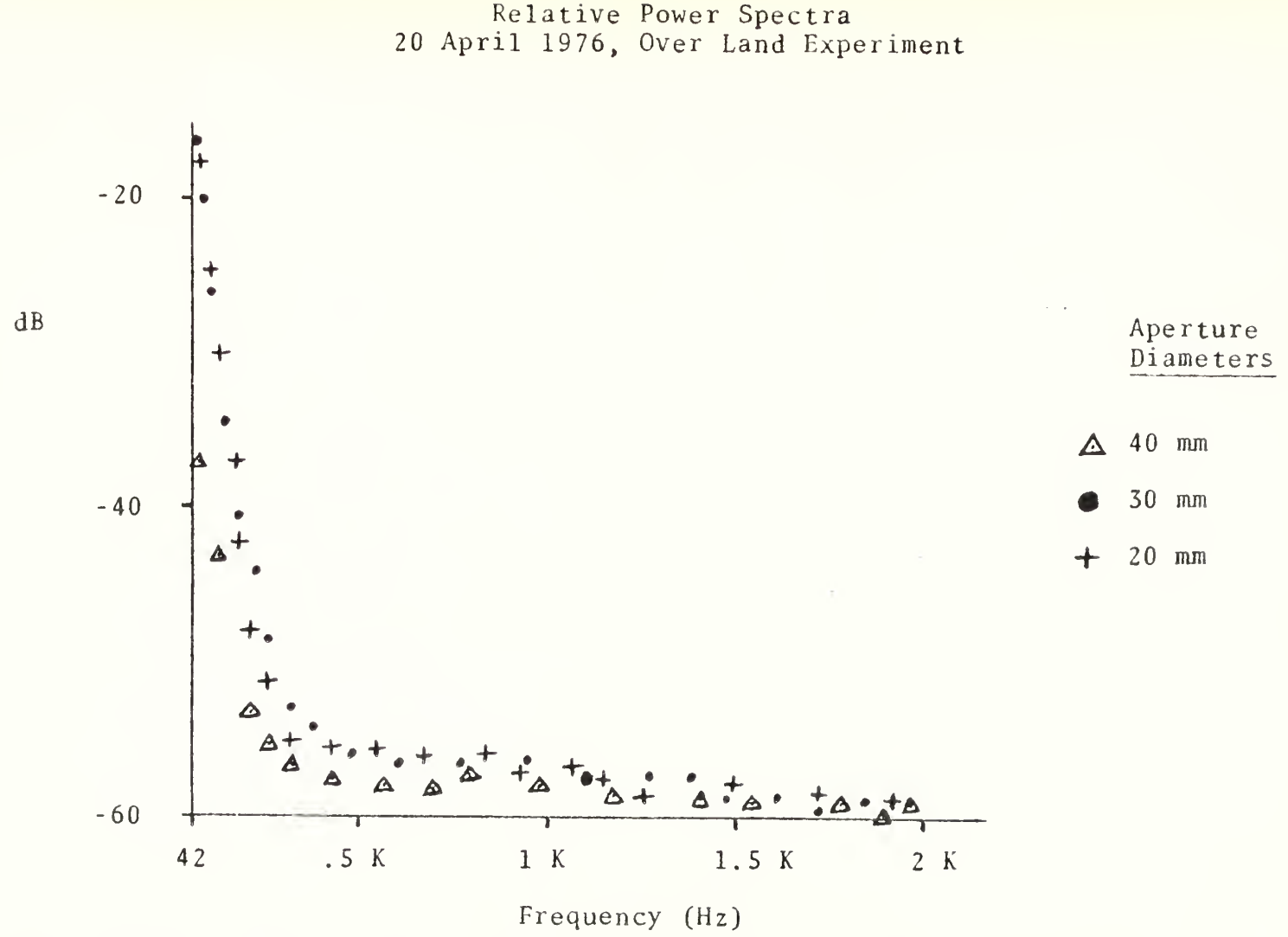

Fig. VI-B-18. Temporal Frequency Spectra for Several Aperture Diameters.
(Continued in Fig. VI-B-19 for Smaller Aperture Diameters)

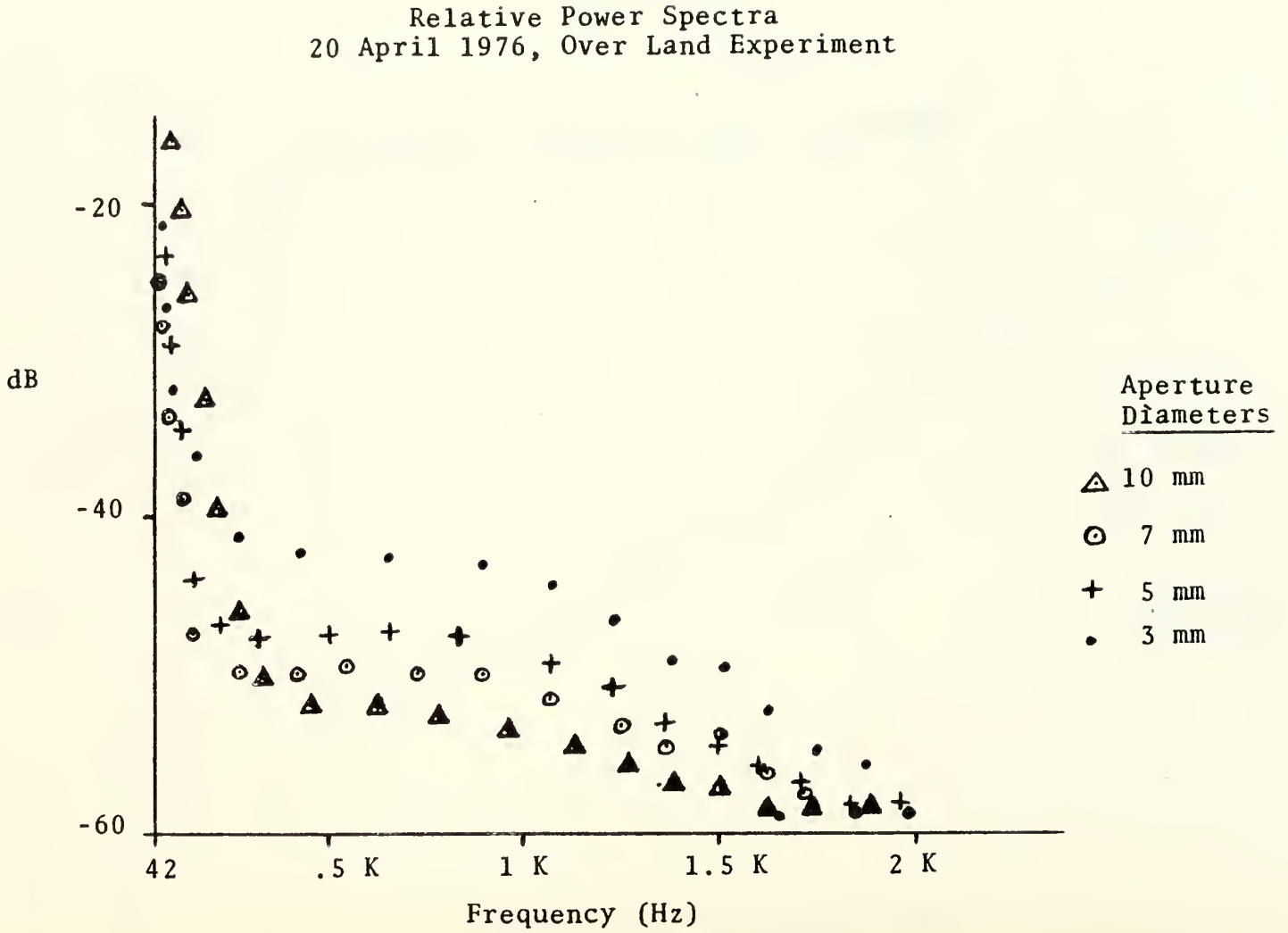

Fig. VI-B-19. Temporal Frequency Spectra for Several Aperture Diameters (See also Fig. VI-B-18 for Larger Diameters.)

VI. B. 5. Scintillation C_n^2 vs C_T^2

The theoretical relationship between the temperature structure parameter C_T^2 and the optical structure parameter C_n^2 is deduced from the temperature dependence of the refractive index, and is given by

$$C_n^2 = \left(\frac{79 \times 10^{-6} P}{T^2} \right)^2 C_T^2 .$$

This expression is used to deduce the optical turbulence parameter from the local temperature fluctuations. The optical value of C_n^2 is deduced from the statistics of irradiance fluctuations in a laser beam projected over a long path, using one of the relationships

$$\sigma_{\ell I}^2 \begin{cases} = 1.24\ C_n^2\ k^{7/6}\ z_o^{11/6} & \text{(for plane waves)} \\ = .52\ C_n^2\ k^{7/6}\ z_o^{11/6} & \text{(for spherical waves)} \end{cases}$$

Implicit in this formulation are assumptions regarding spatial homogeneity and isotropy of the turbulence and the geometry of the beam. Consistent agreement between scintillation and thermal determinations of C_n^2 could only be expected under atmospheric conditions in which the strength of turbulence was constant along the path. Initial experiments were carried out to test the correlation between the methods, (Haagensen, 1973) and at later times discrepancies between the values were used to diagnose non-uniform conditions, leading to conclusions regarding path-weighting of turbulence, described elsewhere in this report.

In a series of experiments over Monterey Bay, thermal measurements either on the beach at one end of the path, or on board the R/V ACANIA at the midpoint of the path were compared with scintillation over the 4.05 km path between the Monterey Holiday Inn and the Hopkins Marine Station. Under conditions of "normal" turbulence ($C_n \simeq 5 \times 10^{-8}\ m^{-1/3}$) close agreement

was found between thermal and optical methods. Table VI-B-4 shows sample results over a two hour period; a comparison in graphical form is shown as Fig. VI-B-20. As a test of the influence of wind speed on the consistency of results, scatter plots were made of optical (C_{nO}) versus thermal (C_{nT}) turbulence parameter, shown as Fig. VI-B-21 to Fig. VI-B-22. Grouping the results by wind speed showed very strong correlation (93% of all points within one standard deviation) for moderate wind speeds, and very poor correlation (23% of all points within one standard deviation) for low wind speed. Fig. VI-B-23 shows a scatter plot of all the data. It is apparent that the discrepancies occur at low wind speeds, at which the air flow tends to be poorly developed and patchy, and probably reflect the lack of uniformity along the path. The data of Fig. VI-B-22 show some indication of saturation of scintillation, since most of the discrepancies lie below the equivalence line. As discussed in Section V. C.5, the measured values of C_{nO} correspond to the critical value for onset of saturation for .6228 μm radiation over paths of 5 km. Under the conditions of these experiments it is not feasible to distinguish the effects of inhomogeneity of turbulence from saturation of scintillation.

Table VI-B-4. Comparison of C_{nO} from Scintillation with C_{nT} from Thermal Fluctuation.

Time	C_{NO}	C_{NT}
1220	---	3.21
1225	2.87	2.80
1230	2.50	3.02
1235	---	3.56
1240	2.18	2.51
1245	2.55	2.80
1250	2.55	3.22
1255	2.66	3.60
1300	2.71	3.73
1305	2.98	3.11
1310	3.30	4.02
1315	3.57	2.80
1320	4.36	5.01
1325	4.15	12.00
1330	----	4.02
1335	3.25	4.50
1340	3.41	3.45
1345	---	3.53
1350	3.25	15.00
1355	---	5.01
1400	---	3.02
1405	3.00	2.03
1410	2.87	2.52
1415	2.93	3.73
1420	2.77	3.54
1425	---	3.01
1430	2.23	3.70
1435	2.34	3.00
1440	2.18	3.55

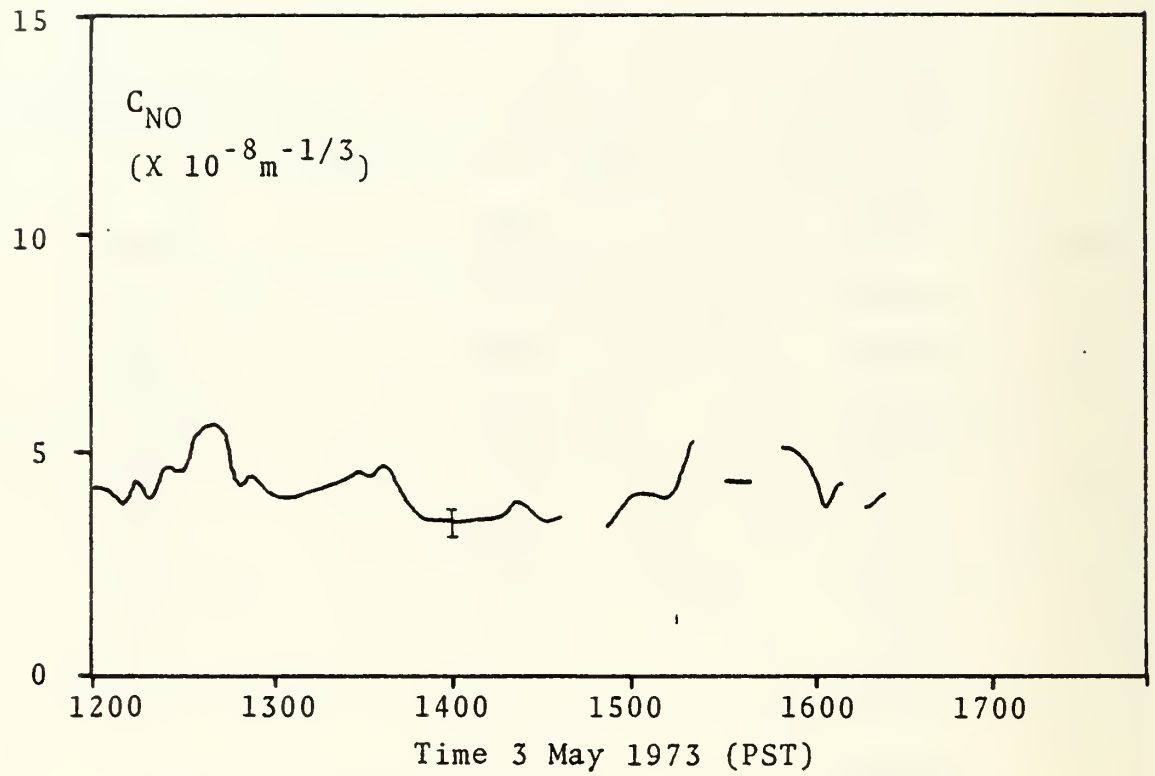

Optical Measurements of C_N versus Time of Day.

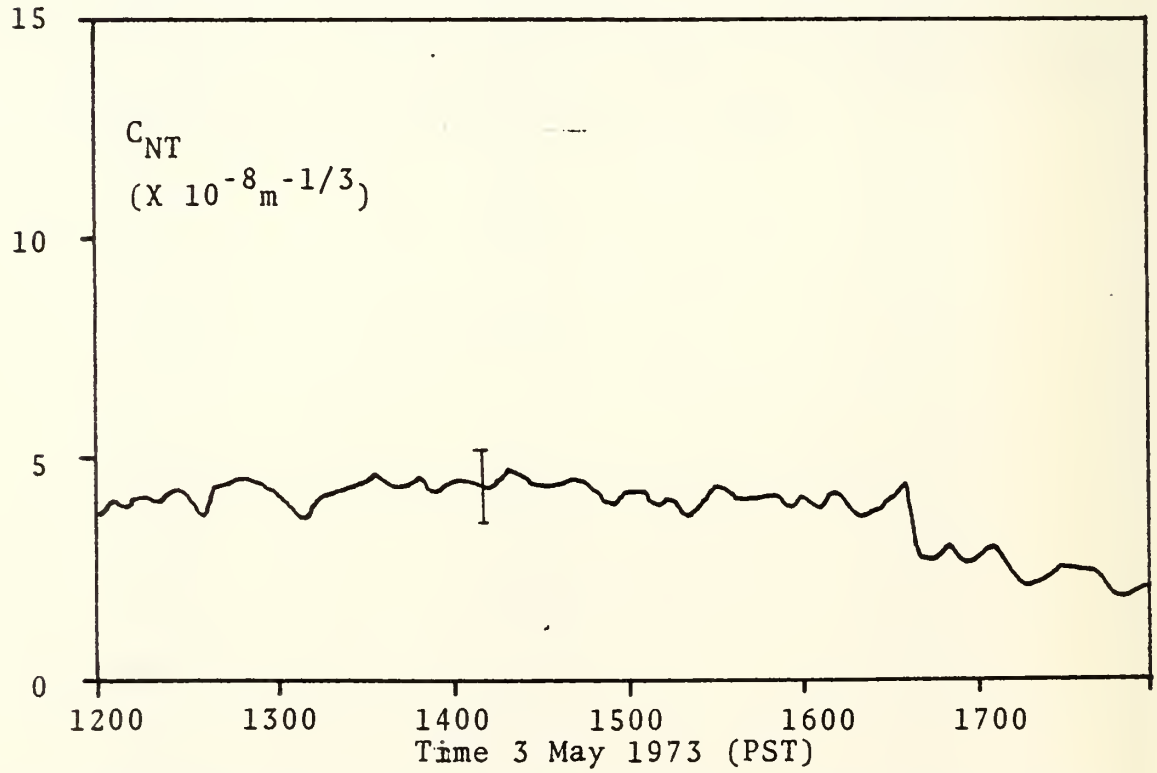

Fig.VI-B-20 Meteorological Measurements of C_N versus Time of Day.

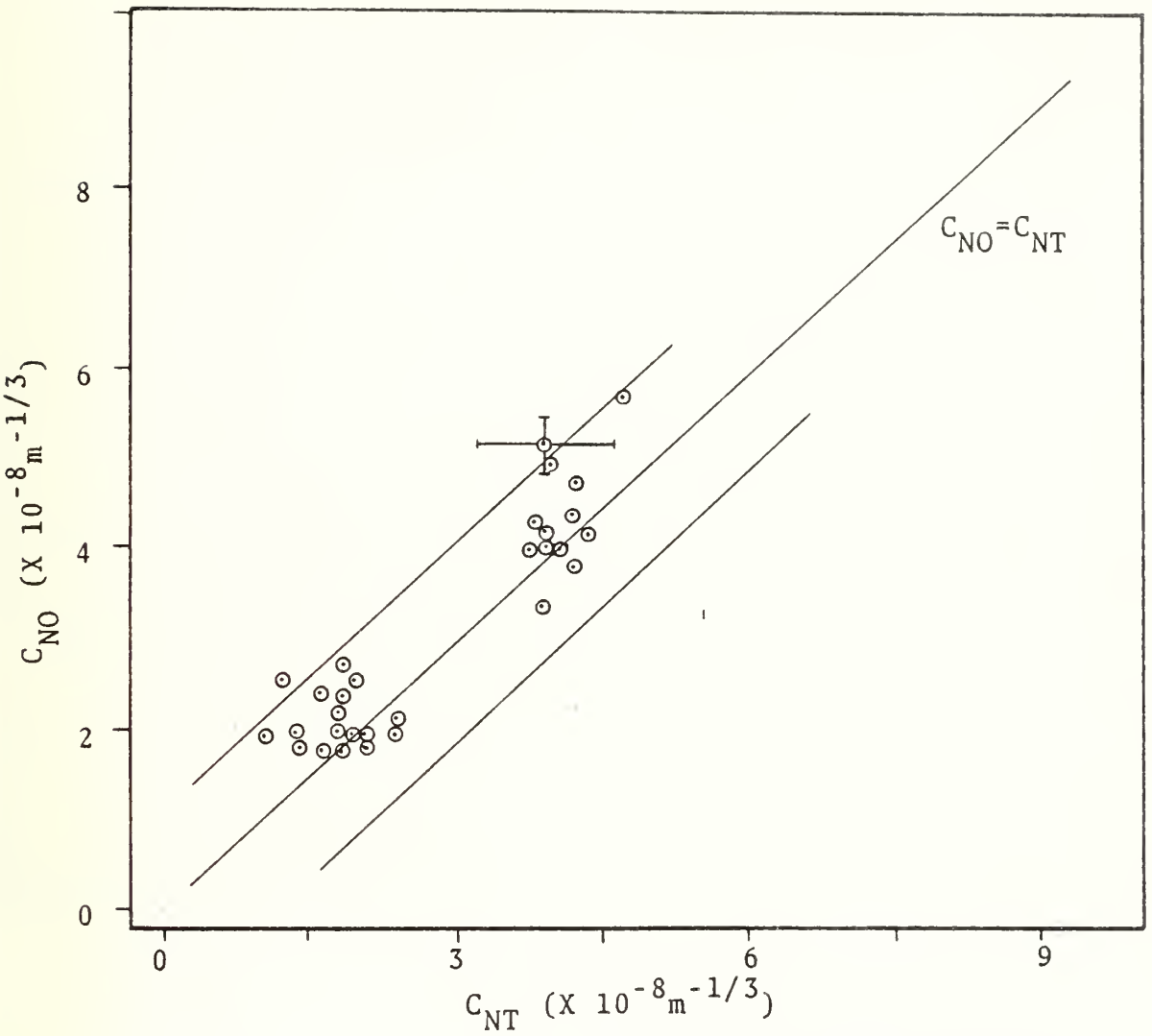

Fig. VI-B-21. Optical Measurements of C_N versus Meteorological Measurements of C_N.

Data taken when the mean wind speed was greater than 6 MPH.

Data taken over Monterey Bay on the third of May.

Ninety-three per cent of all data points are within one standard deviation experimental error of the C_{NO}-C_{NT} equivalence line.

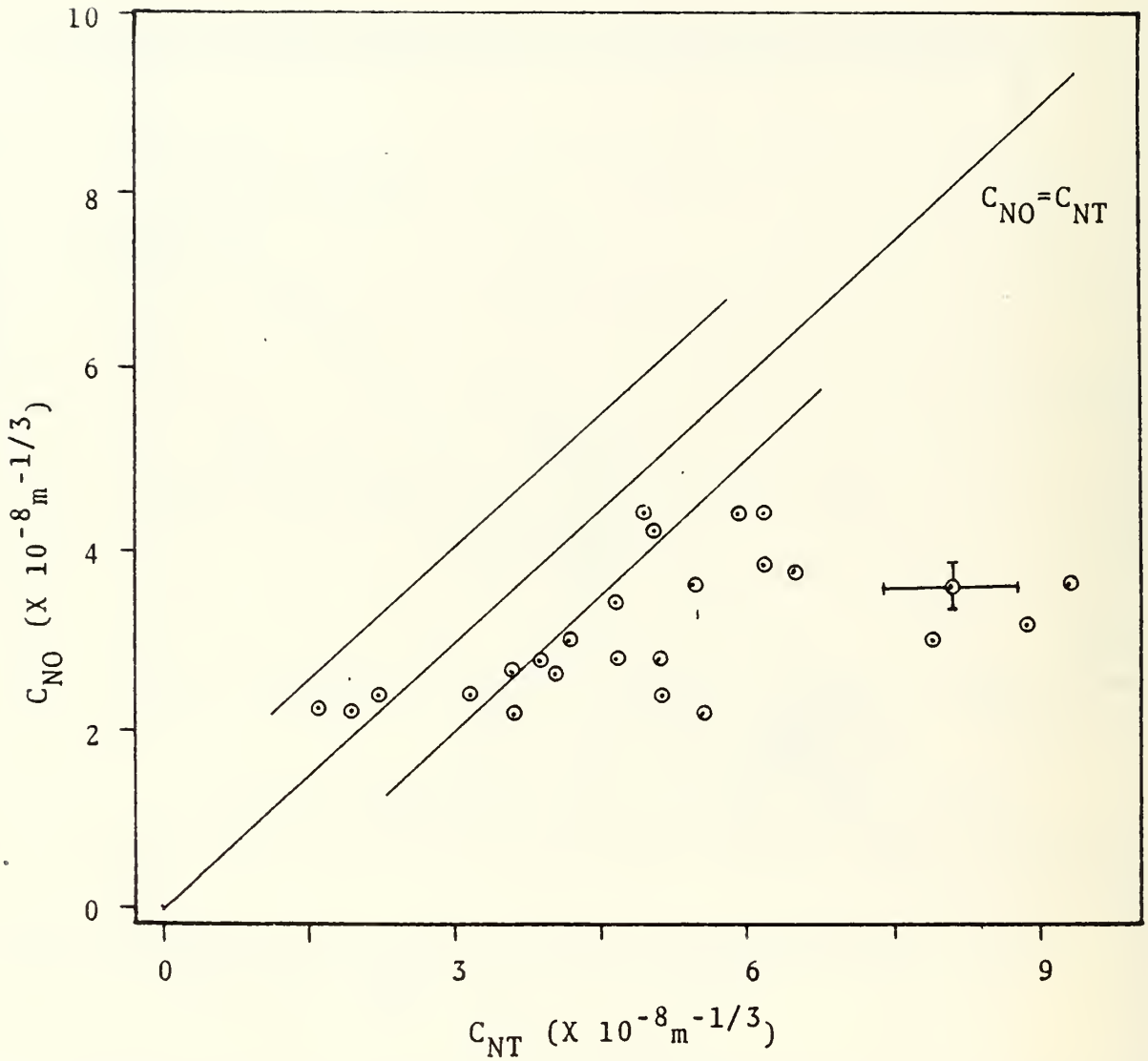

Fic. VI-B-22. Optical Measurements of C_N versus Meteorological Measurements of C_N. Data taken when the mean wind speed was less than 3 MPH.

Data taken over Monterey Bay on the third of May.

Twenty-three per cent of all data points are within one standard deviation experimental error of the C_{NO}-C_{NT} equivalence line.

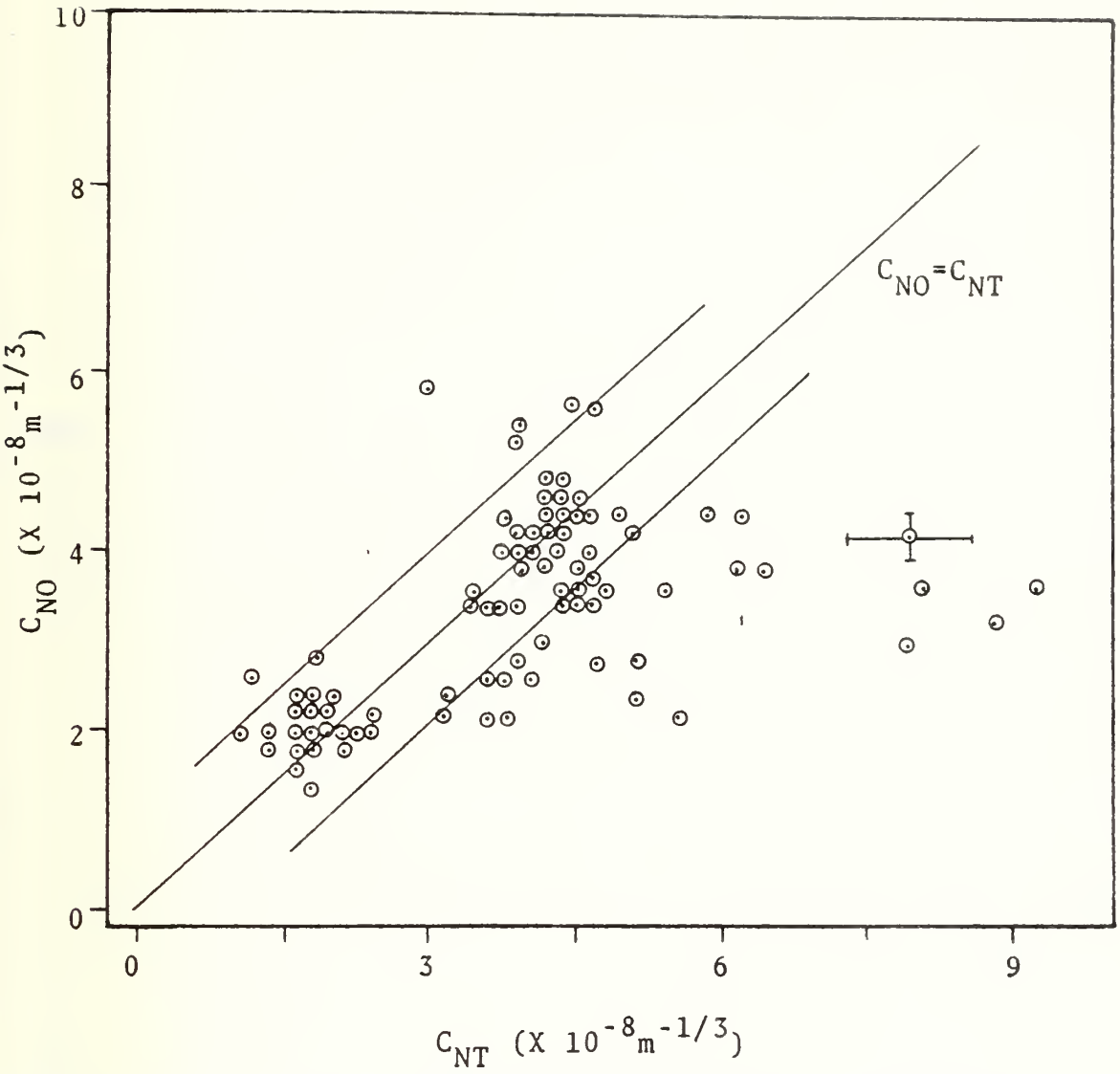

Fig. VI-B-23. Optical Measurements of C_N versus Meteorological Measurements of C_N.

Data taken on the third of May over Monterey Bay.

Sixty-three per cent of all data points are within one standard deviation experimental error of the C_{NO}-C_{NT} equivalence line.

VI. B. 6. Variation of C_n^2 with height

Prediction of optical propagation characteristics from meteorological measurements is based on the validity of the semi-empirical boundary layer theory and the relation of the meteorological quantities to the optical. The validity of the scaling relationships at the air-sea interface was tested by comparisons of C_n^2 and C_T^2 measured simultaneously at two vertical levels above Monterey Bay.

A semi-empirical relationship between C_T^2 and vertical height has been given by Wyngaard, Izumi and Collins (Wyngaard, 1971) based on similarity theory. Since C_n^2 is directly proportional to C_T^2, verification of the predicted scaling lends confidence in both the boundary layer theory and the relationship between C_n^2 and C_T^2. The predicted scaling law is

$$\frac{C_T^2(1)}{C_T^2(2)} = \frac{C_n^2(1)}{C_n^2(2)} = \left[\frac{h(2)}{h(1)}\right]^x$$

where the index x takes the value 4/3 under unstable meteorological conditions (upward heat flux) and approaches 2/3 when conditions are neutral.

Experimental measurements were made on a 4.05 km path across Monterey Bay, using two Helium-Neon lasers mounted on different floor levels at the Monterey Holiday Inn, at heights of 4.9 meters and 12.3 meters above mean water level. The beam diameters at the detectors were maintained at 3.7 millimeters, with careful alignment so that no mixing of the beams occurred. The two detector systems were mounted on different floor levels of the Hopkins Marine Station, so that the beams travelled horizontally. Each detector package consisted of two PIN detectors with narrow acceptance angle optics offset by a slightly greater angle to provide background compensation by subtraction in a differential amplifier. The signals from the two levels, after background

compensation, were log-converted and stored simultaneously on FM tape for later analysis. During the period of data recording, (1943 to 2221 PDT, 18 October 1973) the R/V ACANIA was at anchor at the mid-point of the propagation path while the meteorological group recorded air and sea water temperatures and macroscopic meteorological parameters. During the data period the wind was from the south at 3 to 5 knots, with waves about two feet high with two foot swells. Fig. VI-B-24 shows the log-intensity standard deviation at the two levels as measured with the two initially matched detectors. Three periods of regular behavior of the $\sigma_{\ell I}$ values were selected for comparison; (a) 2105 to 2137, (b) 2140 to 2206 and (c) 2209 to 2221. During the first two periods the two levels showed rather similar responses, while in period (c) the two behaved differently with time. The shipboard measured values of temperature gradient showed an almost constant value indicating unstable conditions during the periods (a) and (b), with a rapid fall-off indicating an approach to neutral conditions following 2200, coinciding with an increase in cloud cover. Table VI-B-5 shows the values of log-intensity standard deviation, and the ratio of log-intensity variances compared with the 4/3 and 2/3 powers of the height ratio. Periods (a) and (b) show agreement to within 2% and 4% respectively with the predicted 4/3 power variation, while period (c) agrees to within 4% with the 2/3 power law expected for neutral conditions (Schroeder, 1973), (Cooper, 1974).

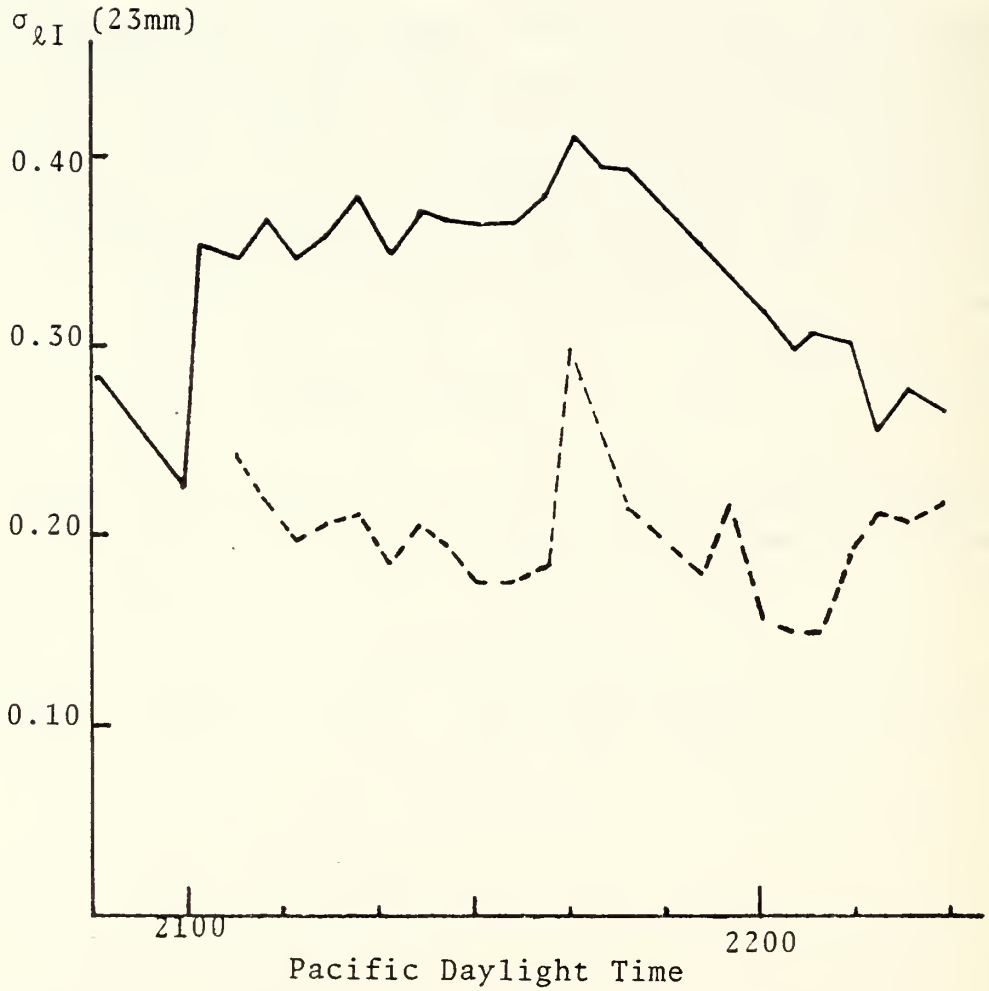

Fig. VI-B-24. Standard deviation of log intensity vs. time

—— 40 ft above ocean surface

--- 16 ft above ocean surface

	Period (a)	Period (b)	Period (c)
$\sigma_{\ell I}$ at h(1) = 16 ft.	0.360	0.349	0.271
$\sigma_{\ell I}$ at h(2) = 40 ft	0.192	0.192	0.204
$(h(2)/h(1))^{4/3}$	3.44	3.44	
$(h(2)/h(1))^{2/3}$			1.85
$\sigma_{\ell I}^2(1)/\sigma_{\ell I}^2(2)$	3.51	3.30	1.77

TABLE VI-B-5

HEIGHT DEPENDENCE OF STANDARD DEVIATION OF LOG-INTENSITY, $\sigma_{\ell I}$, FOR 30 MINUTE PERIODS AT 2105, 2140, AND 2290.

VI. C. Comparison of Extinction Results with NOSC Aircraft

Development of the extinction equipment had reached the point by September 1977, that a field test run seemed warranted, even though only three of the five planned wavelengths were then available. The run was carried out also because the opportunity occurred to perform a joint experiment with NOSC*, San Diego, in which their aircraft measured the aerosol spectra in the vicinity of our optical path during the extinction measurements.

The optical path employed was from Marina to Pt. Pinos, across Monterey Bay, with a path length of 13.16 km. The path is shown in Fig. III-1 . The tests were scheduled to take place on four days, 6-9 September 1977. Unfortunately, heavy fog on all or part of the optical path prevented both optical work and flight of the aircraft for the first three days. On the fourth day, 9 September, the fog thinned sufficiently for flight with the aid of radar guidance provided by the NPS Department of Electrical Engineering. The optical transmission was also high enough for optical work after initial line-up.

The optical system was aligned and calibrated on a building-to-building range on the NPS grounds prior to moving the equipment to Marina and Pt. Pinos. After the move of the equipment to the field sites, the fog prevented intitial optical line-up until just before the aircraft flight. The hurried alignment and compressed flight schedule combined to lead to drift of the beam center positions during the run for two of the laser sources, the 0.4880 μm and the 1.06 μm lasers. These both have cavity mirrors that drift with temperature and hence need external adjustment. The beam centers also move with these adjustments. The resulting drift led to unacceptable performance during the aircraft flight time. A system for quick alignment test and

*We are indebted to Doug Jensen, Herbert Hughes, of NOSC, San Diego, for their efforts in carrying out this experiment.

correction has since been developed, as described in Section V.D.1. This should correct the problem in future runs.

The 0.6328 μm laser was more stable, and acceptable extinction data were obtained. The transmission of the atmosphere was low at 0.6328 μm at the time of the run, varying between a low of 3% and a high of 8.5%. Optimum precision occurs for transmissions in the vicinity of 30-50%, but useful results can be obtained with lower transmissions such as occurred that day. The corresponding values of extinction coefficient range from 0.27 km^{-1} to 0.19 . The values obtained are plotted as a function of time of day in Fig. VI-C-1.

The aircraft nephelometer spectra were reduced at NOSC and the anticipated extinction coefficient values calculated for 0.6328 μm using the MEGATEK computer code (Stone, 1976). Those results are also plotted as a function of time in Fig. VI-C-1. The aircraft nephelometer data were taken during aircraft flights parallel to the optical path but above it at an altitude of 75 ft. above the water surface. The optical path was slightly sloping from a height of about 20 ft. at Pt. Pinos to about 60 ft. at Marina. The aircraft passes took about five minutes, and the optical data was roughly synchronized to this timing. The density of the haze was unusually uniform. The aircraft made a climbing run from a low of 50 ft. to about 500 ft. during which essentially no change in the particle spectrum was observed. The particle spectrum was also essentially constant along the length of the optical path.

The two plots of extinction vs. time vary together but differ by a factor of about 1.8. The cause of this difference is at present not known. Some uncertainty exists in the composition of the aerosol particles. NOSC reports that an increase due to salt concentration in the particles could perhaps reduce this difference to a factor of 1.6. Errors in the optical measurement are most likely in the direction of giving too low a value, i.e.,

COMPARISON OF CALCULATED EXTINCTION COEFFICIENTS BY NOSC AND MEASURED COEFFICIENTS BY THE NAVAL POST-GRADUATE SCHOOL VERSUS TIME

$\lambda = 0.6328\ \mu m$ $\quad n = 1.33 - j\ 1.05 \times 10^{-8}$

Upper Curve: Naval Postgraduate School Measured Extinction Data
Lower Curve: NOSC Calculated Extinction Data From Measured Aerosol Size Distributions

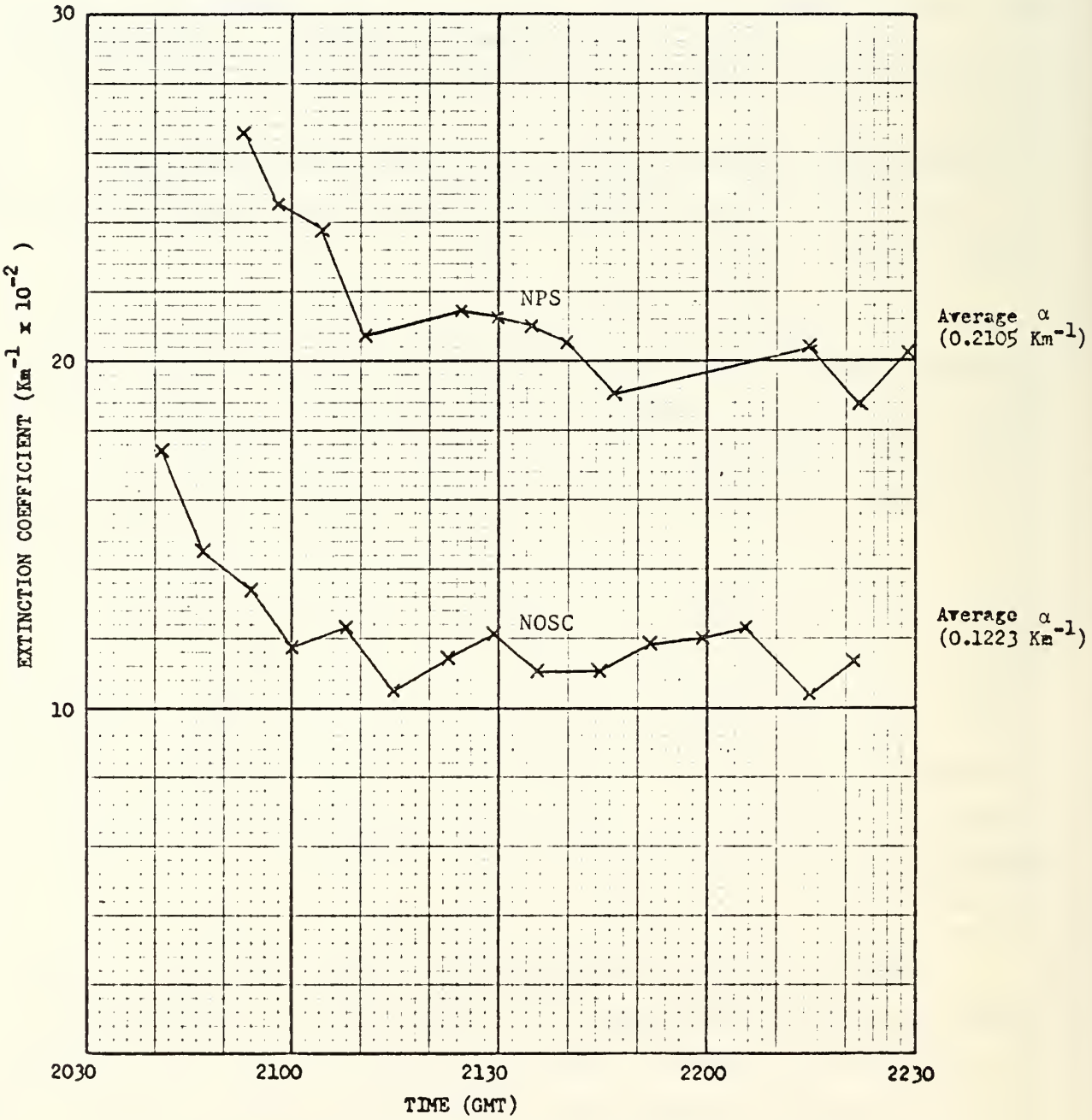

Fig. VI-C-1. Measured Extinction across Monterey Bay, and Extinction Calculated from Aerosol Spectrum, Plotted as a Function of Time.

loss of light for causes other than atmospheric extinction - dirty optics, misalignment, etc. This experiment is scheduled for repetition in the near future, with additional wavelength measurements available.

VII. References

Born, 1970; Born, M. and Wolf, E., Principles of Optics, Fourth Edition, Pergammon Press, 1970.

Collins, 1971; Collins, S.A., and Damon, E..K., RADC TR-71-124, 1971.

Cooper, 1974; Cooper, A.W., Crittenden, E.C. Jr., and Schroeder, A.F., Height Dependence of Optical Scintillation Over the Ocean, Digest of Technical Papers, Optical Soc. of America Topical Conference on Optical Propagation through Turbulence Rain and Fog, Boulder, CO, July 9-11, 1974.

Davidson, 1977-1; Davidson, K.L., Houlihan, T.M., Fairall, C.W., and Schacher, G.E., Observational Results on the Temperature Structure Function Parameter, C_T^2, Adjacent to the Ocean, Naval Postgraduate School Report, NPS 63-77-001, 29 December 1977.

Davidson, 1977-2; Davidson, K.L., Fairall, C.W., Houlihan, T.M., and Schacher, G.E., Observed Height and Stability Dependence of Turbulent Kinetic Energy Dissipation in the Atmospheric Marine Boundary Layer, Naval Postgraduate School Report, NPS 63-77-002, 29 December 1977.

Elliott, 1977; Elliott, R.A., Dunphy, J.R., and Kerr, J.R., Statistical Tests of Distributional Hypotheses Applied to Irradiation Fluctuations, Optical Society of America Topical Conference on Optical Propagation through Turbulence Rain and Fog, Boulder, CO, 9-11 August, 1977.

Fried, 1965; Fried, D.L., Statistics of a Geometric Representation of a Wavefront Distortion, Jour. Optical Soc. of Am. 55, 11, 1427, 1965.

Fried, 1966; Fried, D.L., Optical Resolution through a Randomly Inhomogeneous Medium for Very Long and Very Short Exposures, Jour. Optical Soc. Am., 56, 10, 1372, 1966.

Fried, 1967-1; Fried, D.L., Aperture Averaging of Scintillation, Jour. Optical. Soc. Am., 57, 2, 169, February 1967.

Fried, 1967-2; Fried, D.L., Propagation of a Spherical Wave in a Turbulent Medium, Jour. Optical Soc. Am., 57, 2, 175, 1967.

Fried, 1967-3; Fried, D.L., Mevers, G.E. and Keister, M.P. Jr, Measurements of Laser Beam Scintillation in the Atmosphere, Jour. Optical Soc. Am., 57, 6, 787, 1967.

FrieHe, 1975; Friehe, C.A., La Rue, J.C., Champagne, F.H., Gibson, C.H., and Dreyer, G.F., Effects of Temperature and Humidity Fluctuations on the Optical Refractive Index in the Marine Boundary Layer, Jour. Optical Soc. Am., 65, 12, 1502, 1975.

Goodman, 1968; Goodman, J.W., Introduction to Fourier Optics, Chapter 6, McGraw-Hill, 1968.

Griem, 1964; Griem, H., Plasma Spectroscopy, p. 176, McGraw-Hill, 1964.

Haagensen, 1973; Haagensen, B.C., Laser Beam Scintillation in the Marine Boundary Layer, Naval Postgraduate School M.S. Thesis, June 1973.

Hall, 1976; Hall, H.R., Aperture Averaging Effects on Scintillation and the Temporal-Frequency Power Spectrum, Naval Postgraduate School M.S. Thesis, 1976.

Hufnagel, 1964; Hufnagel, R.E., and Stanley, N.R., Modulation Transfer Function Associated with Image Transmission through Turbulent Media, Applied Optics, 10, 1652, 1971.

Kelsall, 1973; Kelsall, D., Optical Seeing Through the Atmosphere by an Interferometric Technique, Jour. Optical Soc. Am., 63, 1472, November 1973.

Kerr, 1972; Kerr, J.R., Experiments on Turbulence Characteristics and Multiwavelength Scintillation Phenomena, Jour. Optical Soc. Am., 62, 9, 1040, September 1972.

Knollenberg, 1976; Knollenberg, R.G., Three New Instruments for Cloud Physics Measurements, The Forward Scattering Probe, and the Active Scattering Aerosol Spectrometer, p. 554, Preprint Volume of the International Conference on Cloud Physics, American Meteorological Society, Boulder, CO, July 26-30, 1976.

Korff, 1973; Korff, D., Analysis of a Method for Obtaining Near Diffraction Limited Information in the Presence of Atmospheric Turbulence, Jour. Optical Soc. Am., 63, 971, August 1973.

Livingston, 1975; Livingston, P.M., Trusty, G.L., Ruhnke, L.H., and Mooradian, G., Optical SATCOM, Joint NRL/NELC Optical Satellite Communication Atmospheric Propagation Test Plan, April, 1975.

Lutomirski, 1971; Lutomirski, R.F., and Yura, H.T., Propagation of a Finite Optical Beam in an Inhomogeneous Medium, Applied Optics, 10, 1652, 1971.

Lutomirski, 1973; Lutomirski, R.F., Huschke, R.E., Meechan, W.C., and Yura, H.T., Degradation of Laser Systems by Atmospheric Turbulence, Rand Report R-1171-ARPA/RC, 1973.

Lutomirski, 1974; Lutomirski, R.F., and Yura, H.T., Imaging of Extended Objects through a Turbulent Atmosphere, Applied Optics, 13, 431, 1974.

Magnus, 1949; Magnus, W. and Oberhettinger, F., Special Functions of Mathematical Physics, p. 141, Chelsea Publishing Co., New York, 1949.

McClatchey, 1973; McClatchey, R.A., Benedict, W.S., Clough, S.A., Burch, D.E., Calfee, R.F., Fox, F., Rothman, L.S. and Garing, J.S., Atmospheric Absorption Line Parameters Compilation, AFCRL-TR-73-0096, January 26, 1973, Environmental Research Paper #434.

McClatchey, 1977; McClatchey, R.A., Atmospheric Absorption Line Parameters Computer Code Tape, May 31, 1977.

Ochs, 1969; Ochs, G.R., Bergmann, R.R., and Snyder, J.R., Laser Beam Scintillation over Horizontal Paths from 5.5 to 145 Kilometers, Jour. Optical Soc. Am., 59, 2, 231, 1969.

Ochs, 1976; Ochs, G.R., Wang, T., Lawrence, R.S., and Clifford, S.F., Refractive Turbulence Profiles Measured by One-Dimensional Spatial Filtering of Scintillations, Applied Optics, 15, 10, 2504, October 1976.

Schroeder, 1973; Schroeder, A.F., Laser Scintillation Properties in the Marine Boundary Layer, Naval Postgraduate School M.S. Thesis, December 1973.

Stone, 1976; Stone, W.A., MIE and SCATCO: Programs to Compute the Scattering, Extinction, and Absorption Properties of the Optical Properties through Particle Distributions,

MEGATEK Corporation, San Diego, CA, Report R2005-070-F-1, 1 November 1976.

Tatarski, 1961; Tatarski, V.I., Wave Propagation in a Turbulent Medium (McGraw-Hill Book Co., Inc., New York, 1961;) The Effects of the Turbulent Atmosphere on Wave Propagation, (U.S. Department of Commerce, NTIS, Springfield, VA, 1971).

Tavis, 1976; Tavis, M. T., and Yura, H. T.,Short-Term Average Irradiance Profile of an Optical Beam in a Turbulent Medium, Applied Optics, 15, 11, 2922, Nov., 1976.

Wyngaard, 1971; Wyngaard, J., Izumi, Y., and Collins, S.A., Behavior of the Refractive-Index-Structure Parameter near the Ground, Jour. Optical Soc. Am., 61, 1646, 1971.

Yura, 1973; Yura, H.T., Short-Term Average Optical Beam Spread in a Turbulent Medium, Jour. Optical Soc. Am., 63, 567, 1973.

VIII. Appendixes

Appendix A

For a beam projection system the predicted average beam cross-section on the target is calculated from the atmospheric MTF and the properties of the laser and the pointer/tracker, as follows. For a linear system, the MTF of the entire system is the MTF of the atmosphere times the Fourier transforms of the line-spread functions of the laser output pattern, and of the optics (defocus, diffraction, and aberration broadening), as indicated in Fig. VIII-1. The line-spread function of the laser output pattern is obtained from its radial distribution by integrating to obtain the intensity falling in a vertical slit of width delta x and a distance x from the center of the pattern as shown in (a), (b), and (c) of Fig. VIII-1. (If the output laser pattern is elliptical, instead of circular, the situation can be handled by finding a line-spread function in the x and y directions instead of just the x direction). The Fourier transform of the line-spread function is then calculated to give a curve such as (d) of Fig. VIII-1. The Fourier transform of the entire system, as indicated in (g) of Fig. VIII-1 is obtained by multiplying the line-spread function transform (d) by the MTF of the atmosphere (e), and by the transform for the optics, (f). Taking the inverse Fourier transform of (g) yields the line-spread function for the entire system, as indicated in (h) of Fig. VIII-1. This line-spread function can be converted to a radial distribution function by application of the Abel transform, described below, to yield a curve such as the solid curve in (i) of Fig. VIII-1. The original radial distribution is shown as the dotted curve in (i) for comparison with the atmospheric and equipment broadened distribution function. The fractional energy falling within a given radius is then calculated by integrating with respect to r to give a curve such as (j) of Fig. VIII-1.

The calculation outlined above can be carried out in a few seconds in an on-line data processer that is coupled to the

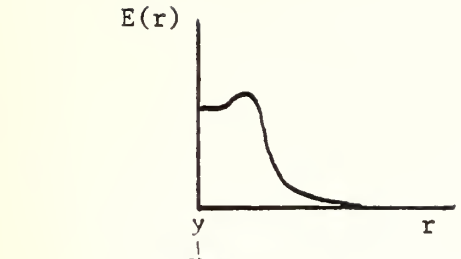

(a) Radial distribution of laser output pattern. Intensity E(r) as a function of radius, r, (or angle, r/z)

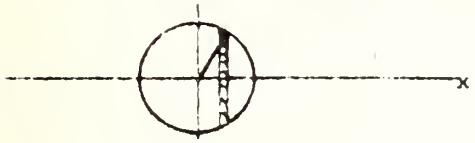

(b) Integration to produce the line spread function Intensity vs x is the area of the hatched strip

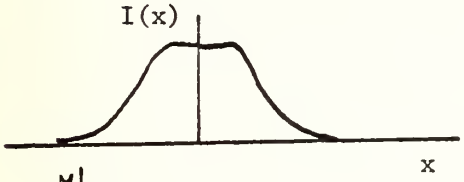

(c) Line spread function, intensity vs.x

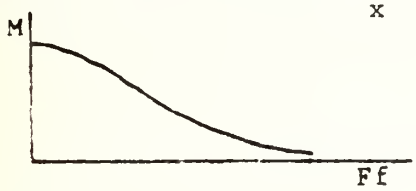

(d) Fourier transform of the line spread function

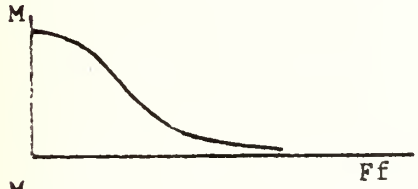

(e) MTF of the atmosphere

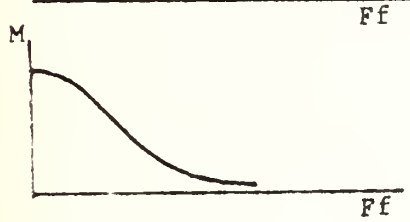

(f) Fourier transform for diffraction, defocus, and aberration broadening

(g) System transform. The product of curves (d), (e), and (f)

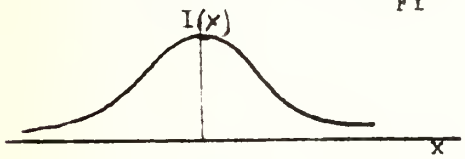

(h) Line spread function for all the effects on the system. Inverse Fourier transform of curve (g).

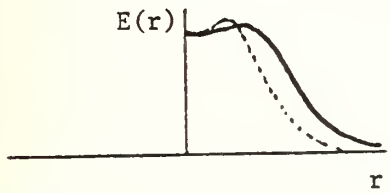

(i) Radial distribution of intensity for the complete system. Abel transform of curve (h). The dotted curve is the original geometrical divergence, curve (a), for comparison

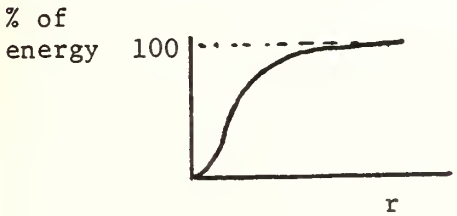

(j) The fraction of energy, in % of total, within a given radius ,r.

Fig.VIII-1.The processes involved in calculating a real system spot distribution.

line scan MTF equipment developed at the NPS. Any of the curves of Fig. VIII-1 can be provided as output plots in a few minutes of plotting time.

The Abel transform (Griem, 1964; Magnus, 1949) referred to above, is the process by which a line-spread function in one-dimension is converted to a two-dimensional point spread function. This is possible, provided that it is known that the point spread function is radially symmetric. The line-spread function is obtained by integrating the image function E(r) along the slit direction (y direction).

$$I(x) = \int_{-\infty}^{\infty} E(r)\,dy = \int_{-\infty}^{\infty} E(x^2 + y^2)\,dy$$

The Abel transform allows us to reverse this process. It is accomplished by carrying out the calculation indicated by:

$$E(r) = -\frac{1}{\pi} \int_{r}^{R} \frac{I'(x)\,dx}{x^2 - r^2}$$

where:

$I(x) = 0$ for $x > R$

$I'(x)$ is the x derivative of $I(x)$

DISTRIBUTION LIST

Director 2
Air Force Geophysics Laboratory, AFSC
L. G. Hanscom AFB, Massachusetts 01731
ATTN: John Garing

Commander 2
Air Force Weapons Laboratory, AFSC
Kirtland AFB, New Mexico 87117
ATTN: Dr. Barry Hogge

Commander 4
Atmospheric Sciences Laboratory
White Sands Missile Range, New Mexico 88002
ATTN: Dr. Howard Holt (DELAS-BL-DD)
Mr. James Lindberg (DELAS-BL-ASAP)
Mr. Tom Pries

Defense Documentation Center 2
Cameron Station
Alexandria, Virginia 22314

Commander 1
Naval Air Systems Command, Headquarters
Washington, D. C. 20360
ATTN: Mr. M. H. Schefer (AIR-370C)

Commander 1
Naval Electronic Systems Command, Headquarters
Washington, D. C. 20360
ATTN: Mr. Albert D. Ritter (PME107-52A)

Naval Environmental Prediction Research Facility 2
Monterey, California 93940
ATTN: Mr. Paul Lowe
Dr. Andre' Goroch

Commander 1
Naval Oceanographic Command
National Space Technology Laboratories
Bay St. Louis, Mississippi 39520

Naval Oceanograhic Office 1
Library (Code 3330)
Washington, D. C. 20373

Naval Postgraduate School 4
Monterey, California 93940
ATTN: Prof. Kenneth L. Davidson, Dept. of Meteorology (Code 51Ds)
Prof. Dale F. Leipper, Dept. of Oceanography (Chairman, Code 58Lr)
Library (Code 0212)

Distribution List (Cont'd.)

Commanding Officer
Naval Missile Center
Point Mugu, California 92042
ATTN: Library (Code N0322) — 2

Naval Ocean Systems Center
San Diego, California 92152
ATTN: Dr. Jergen Richter — 3

Chief of Naval Research
Department of the Navy
800 N. Quincy Street
Arlington, Virginia 22217
ATTN: Mr. W. J. Condell, Jr. (ONR-421) — 3

Director
Naval Research Laboratory
Washington, D. C. 20375
ATTN: Dr. L. F. Drummeter (Code 5510)
Dr. J. C. Kershenstein (Code 4109K)
Dr. J. M. MacCallum (Code 4109)
Library — 4

Commander
David W. Taylor Naval Ship Research & Development Center
Bethesda, Maryland 20084
ATTN: Library — 1

Commander
Naval Sea Systems Command
Washington, D. C. 20362
ATTN: Lt. Michele M. Hughes (PMS-405-35/4 copies)
Toshio Tasaka (SEA-0341) — 5

Commander
Naval Surface Weapons Center, Dahlgren
Dahlgren, Virginia 22448
ATTN: W. Taczak — 2

Commander
Naval Surface Weapons Center, White Oak
Silver Spring, Maryland 20910
ATTN: Dr. B. Katz (Code 213) — 2

Director of Libraries
U. S. Naval War College
Newport, Rhode Island 02840 — 1

Institute for Defense Analyses
400 Army-Navy Drive
Arlington, Virginia 22202
ATTN: Lucien M. Biberman (STD)
Robert E. Roberts (STD) — 2

Distribution List (Cont'd.)

Office of the Under Secretary of Defense for Research & Engineering 1
Room 3D139, The Pentagon
Washington, D. C. 20301
ATTN: Col. E. W. Friday, Jr. (Dep. Under Secretary for Tactical Warfare Programs-Rm. 3E1044)

Chief of Naval Material 2
Department of the Navy
ATTN: R. E. Gaylord (MAT-03E)
Glen Spalding (MAT-08T245)

Chief of Naval Operations 1
Department of the Navy
Room 4C 470, The Pentagon
Washington, D. C. 20350
ATTN: Mr. Bill Triggs (OP-35E)

Professor M.A. Plonus 1
Department of Electrical Engineering
Northwestern University
Evanston, IL 60901

Dr. Philip A. Selwyn 1
DARPA
1400 Wilson Blvd.
Arlington, VA 22209

Dr. Douglas Jensen 1
Code 5322
Naval Ocean Systems Center
San Diego, CA 92132

Professor E. C. Crittenden 18
Code 61Ct
Naval Postgraduate School
Monterey, CA 93940

U 185353

DUDLEY KNOX LIBRARY - RESEARCH REPORTS
5 6853 01071859 6
U185353